The Local Glaciers and Ice Caps on Greenland:

Their Mapping, Separation from the Ice Sheet and their Climate Sensitivity

---

Dissertation

zur

Erlangung der Naturwissenschaftlichen Doktorwürde

(Dr. sc. nat.)

vorgelegt der

Mathematisch-naturwissenschaftlichen Fakultät

der

Universität Zürich

von

Philipp Rastner

aus

Italien

Promotionskomitee

Prof. Dr. Andreas Vieli (Vorsitz)
Dr. Frank Paul (Leitung der Dissertation)
Dr. Tobias Bolch
Dr. Horst Machguth
Dr. Claudia Notarnicola

Zürich 2014

Summary

Most glaciers all over the world have been receding and wasting away since the middle of the 20th century, which can mainly be related to the global temperature increase, and thus have contributed substantially to global sea-level rise. Accurate estimates of this contribution were so far nearly impossible, because a globally complete glacier inventory was lacking. This was also the case for the local glaciers and ice caps (GIC) on Greenland that are often connected to the ice sheet and its outlet glaciers. There was thus a requirement to both accurately map all GIC on Greenland, and separate them in a consistent way from the ice sheet. The overall aim of this thesis was therefore the creation of a Greenland Glacier Inventory (GGI), and investigation of its use for the analysis of glacier mass changes and other applications. The results of this work provided the basis for a wide range of studies by the glaciological community in support of the fifth IPCC assessment report (AR5). This thesis was conducted within the framework of the EU FP7 project ice2sea and the ESA-funded Glaciers_cci project, both having also aimed at making a timely contribution to AR5.

The GGI was derived from freely available Landsat satellite scenes (72 in total) and a Digital Elevation Model (DEM) that were used for mapping and separating glaciers, respectively. Time-consuming manual corrections were required for adjusting glacier outlines in regions with debris cover, shadow, perennial snow fields, icebergs, and sea ice. To serve the different needs of the scientific community, all GIC have been classified into three levels describing the strength of their connection to the ice sheet (CL0, CL1, CL2; i.e. no, weak, and strong connection). Considering only entities larger than 0.05 km^2, all CL0 and CL1 GIC have a total area of 89720 $\pm$2781 km^2, which is a 50% larger value than the mean of the most recent previous estimates. Including also glaciers with a strong connectivity (CL2) adds 40355 $\pm$1251 km^2 for a total of 130076 $\pm$4032 km^2 and 20300 entities by number.

It was further investigated whether the manual corrections could be reduced by applying so-called 'object-based image analysis' (OBIA). This approach summarizes pixels into objects, and allows classifying them spectrally and according to their neighbourhood relationships. For example, icebergs surrounded by water are excluded while unmapped lakes on a glacier (surrounded by ice) are included in the glacier classification. A first time application of this approach to glacier mapping revealed a substantial reduction of the post-processing workload and a 3 to 12% improvement in mapping accuracy compared to the classic pixel-based mapping.

The GGI was used to determine the sea level contribution of the GIC separately from the ice sheet. For this purpose, elevation changes obtained from the Ice, Cloud, and Elevation Satellite (ICESat) over the 2003 to 2008 period were restricted to the GGI extent. Overall, a mean surface lowering of 0.45 m a^{-1} $\pm$0.11 m a^{-1} (CL0 & 1) was found, resulting in an overall mass loss of about 27.9 $\pm$10.7 Gt a^{-1} for the CL0 and CL1 glaciers, and about 40.9 $\pm$16.5 Gt a^{-1} for all GIC.

In a final study, the correlation of mass changes with the climatic regime or trends in temperature (*T*) and precipitation (*P*) were analysed. Both *T* and *P* were obtained from re-analysis-driven RACMO2 Regional Climate Model data. A significant correlation of 0.69 and 0.59 was found with mean annual *T* and *P*, indicating that observed elevation changes can be largely explained by the climatic sensitivity on this regional scale. The mass-balance sensitivity was obtained by dividing the mass budget by the respective changes in *T* for each sector, yielding high values in the south-east (>1 m w.e. a^{-1} K^{-1}) and lower ones for the rest of Greenland (<0.28 m w.e. a^{-1} K^{-1}).

This thesis demonstrates the application of satellite data and geoinformatics for the investigation of GIC over large regions. The GGI, with its classification of GIC according to their connectivity to the ice sheet, was in this regard a milestone for this thesis and for related global-scale studies.

Zusammenfassung

Viele Gletscher und Eiskappen (GEK) der Erde haben sich seit Mitte des 20. Jahrunderts, besonders aufgrund erhöhter Globaltemperaturen zurückgezogen und so zu einem Anstieg des Meeresspiegels geführt. Eine genaue Abschätzung dieses Beitrages ist jedoch schwierig, da viele kontinentale Eismassen bis vor kurzem noch nicht erfasst waren. Dies traf auch auf die GEK in Grönland zu, welche zusätzlich oft mit dem Eisschild oder deren Auslassgletscher verbunden sind. Es war deswegen von besonderem Wichtigkeit einmal die Kartierung der GEK und zweitens die Trennung der GEK auf konsistenter Basis von dem Eisschlild umzusetzen. Das primäre Ziel dieser Arbeit war die Erstellung eines Grönländischen Gletscherinventares (GGI) um weitere Applikationen wie die Ableitung von zum Beispiel Gletscheroberflächen-veränderungen zu ermöglichen. Die Resultate dieser Dissertation waren auch die Basis für eine große Anzahl weiterer Studien und im besonderen auch die des fünften IPCC Berichts (AR5). Diese Arbeit wurde im Rahmen des EU FP7 Projekts ice2sea und des ESA Projekts Glaciers_cci finanziert, die beide auch einen markanten Beitrag zum letzten IPCC Bericht lieferten.

Das GGI wurde basierend auf frei verfügbaren Landsat Satellitenbildern (72 Szenen) kartiert. Die Unterteilung in einzelne Gletscher erfolgte auf Grundlage eines digitalen Geländemodells. Zeitaufwändige manuelle Korrekturen waren oft notwendig um Gletscherbegrenzungslinien in Gebieten mit hoher Schuttbedeckung, Schatten, ganzjährigen Schneefeldern, Eisbergen und Meereis zu verbessern. Um die diversen Ansprüche der Gletscherforschung abzudecken, wurden allen GEK eine Konnektivitätsklasse (CL0, CL1, CL2; nicht verbunden, leicht verbunden, stark verbunden), die deren Verbindung mit dem Eisschild beschreibt, zugewiesen. Aus den Ergebnissen dieser Studie konnten 20300 GEK gezählt werden mit einer Gesamtgletscherfläche von 130076 ±4032 km^2 oder 89720 ±2781 km^2 ohne die CL2 GEK. Dies entspricht einer 50% größeren Gletscherfläche als das Mittel der bisherigen bekannten Abschätzungen.

Weiters wurde untersucht, ob die manuellen Korrekturen mit der objektorientierte Klassifikation (OBIA -Object Oriented Image Analysis) reduziert werden können. Bei dieser Methode werden Pixel zu Objekten zusammengefasst und in Klassen, aufgrund der spektralen Eigenschaften und räumlicher Nachbarschaftsanalysen, eingeteilt. Zum Beispiel, Eisberge umgeben von Wasser müssen ausgeschlossen werden, wohingegen nicht erfasste Seen auf einem Gletscher (also umgeben von Eis) in the Gletscherklasse mit einbezogen werden müssen. Es zeigte sich, dass die Genauigkeit von OBIA die der PBIA von 3-12% übersteigt und manuelle Korrekturen reduziert.

Das GGI wurde auch verwendet um deren Beitrag zum Meeresspiegelanstiegs zu beziffern. Dafür wurden Höhenveränderungen der GEK mithilfe des "Ice, Cloud and land Elevation Satellite" Satelliten (ICESat) für die Zeitperiode 2003-2008 abgeleitet. Ein mittlerer Höhenverlust von 0.45 m a^{-1} ±0.11 m a^{-1} (CL0 & 1) konnte so beziffert werden. Dies entspricht einem Massenverlust von 27.9 ±10.7 Gt a^{-1} für CL0 und CL1 und 40.9 ±16.5 Gt a^{-1} für alle GEK.

In der finalen Studie wurde analysiert, ob die Massenänderungen mit dem klimatischen Regime oder mit den Trends in Temperature (*T*) und Niederschlag (*N*) (abgeleitet vom RACMO2 Klimamodell) zusammenhängen. Die Ergebnissen zeigten eine signifikannten Zusammenhang mit der mittleren *T* (0.69) and dem mittleren *N* (0.59). Massenveränderungen können somit besonders mit der Klimasensitivität der GEK erklärt werden. Zudem wurde die Massenbilanz Sensitivität (Massenbudget/Temperaturveränderung) berechnet. Hierbei wurden hohe Raten im Südosten (>1 m w.e. a^{-1} K^{-1}) und niedrige im Rest von Grönland (<0.28 m w.e. a^{-1} K^{-1}) errechnet.

Diese Dissertation zeigt, dass Satellitendaten und Geoinformationstechnologie für die Untersuchung von GEK in großen Gebieten verwendet werden können. Das GGI und die Einteilung der GEK in verschiedene Konnektivitätsebenen war hierbei ein Meilenstein nicht nur in dieser Arbeit sondern auch für weltweite Studien.

Contents

List of Figures

List of Tables

Abbreviations

AAR	Accumulation Area Ratio
ASTER	Advanced Spaceborne Thermal Emission and Reflection Radiometer
ASTER GDEM	ASTER Global Digital Elevation Model
DCW	Digital Chart of the World
DEM	Digital Elevation Model
DN	Digital Number
DSM	Digital Surface Model
DSZ	Dry Snow Zone
DTM	Digital Terrain Model
ECMWF	European Centre for Medium range Weather Forecasting
ECV	Essential Climate Variable
EL	Equilibrium Line
ENVI	Remote Sensing Software Package
EOSDIS	NASA's Earth Observing System Data and Information System
ESA	European Space Agency
ETM,	Enhanced Thematic Mapper
ETM+	Enhanced Thematic Mapper Plus
FCC,	False Colour Composite
GCM	Global Climate Model
GCOS	Global Climate Observing System
GTOS	Global Terrestrial Observing Systems
GDB	Glacier Database
GEUS	Geological Survey of Denmark and Greenland
GGHydro	Global Hydrographic Dataset
GGI	Greenland Glacier Inventory
GHOST	Global Hierarchical Observing Strategy
GIC,	Glaciers and Icecaps
GIMP	Greenland Mapping Project
GIS	Geographic Information System
GLAS	Geoscience Laser Altimeter System
GLIMS	Global Land Ice Measurements from Space
GLOVIS	USGS Global Visualization Viewer
GPS	Global Positioning System
GRACE	Gravity Recovery and Climate Experiment
GrIs	Greenland Ice sheet
GTN-G	Global Terrestrial Network for Glaciers
HIRHAM	Atmospheric regional climate model
HIRLAM	High Resolution Limited Area Model
ICSI	Commission of Snow and Ice
IDL	Interactive Data Language
IPCC	International Panel on Climate Change
KNMI	Royal Netherlands Meteorological Institute
LDCM	Landsat Data Continuity Mission
LPZ	Lower Percolation Zone
MAR	Modèle Atmosphérique Régional
METI	Japan's Ministry of Economy, Trade and Industry
MMU	Minimum Mapping Unit
MODIS	Moderate Resolution Imaging Spectroradiometer
MRS	Multiresolution Segmentation
MSS	Multispectral Scanner

NASA	National Aeronautics and Space Administration
NCAR	National Center for Atmospheric Research
NCEP	National Centers for Environmental Prediction
NDSI	Normalized Difference Snow Index
NDSM	Normalized Difference Surface Model
NetCDF	Network Common Data Form
NSIDC	National Snow and Ice Data Center
OBIA	Object Oriented Image Analysis
OLI	Operational Land Imager (Landsat 8)
PBIA	Pixel Based Image Analysis
PSFG	Permanent Service of Glaciers
RACMO2	Regional Atmospheric Climate Model version 2.1
RCM	Regional Climate Model
RGI	Randolph Glacier Inventory
RMSE	Root-Mean-Square Error
RS	Remote Sensing
SAR	Synthetic Amplitude Radar
SIZ	Superimposed Ice Zone
SLR	Sea Level Rise
SPIRIT	Stereoscopic survey of Polar Ice: Reference Images and Topographies
SPOT	Systeme Pour l`Osservatoire de la Terre
SRTM	Shuttle Radar Topography Mission
SuZ	Slush Zone
SWIR	Short Wave Infrared
TANDEM-X	TerraSAR-X add-on for Digital Elevation Measurements
TIN	Triangulated Irregular Network
TIR	Thermal Infrared
TM	Thematic Mapper
TOAR	Top of the Atmosphere Reflectance
TSL	Transient Snow Line
TTS/WGI	Temporary Technical Secretary of the WGI
UNEP	United Nations Environmental Programme
UNFCCC	United Nations Framework Convention on Climate Change
UPZ	Upper Percolation Zone
USGS	United States Geological Survey
UTM	Universal Transversal Mercator
VFP	Viewfinder Panorama Digital Elevation Model
VNIR	Visible and Near Infra-Red bands
WGI	World Glacier Inventory
WGMS	World Glacier Monitoring Service

Part I

Synopsis

1. Introduction

1.1 Motivation

Climate change is widely recognised as a major environmental threat that mankind is facing in the 21st century (Stocker et al., 2013). Increased and higher variability of temperature and thus enhanced melting of snow and ice all around the world are well proven evidences (UNEP, 2011). Glaciers and ice caps (GIC) are located in most mountains and the Arctic regions on Earth and their shrinkage and vanishing has impacts on different scales. On a local scale they affect the local hydrological cycle, irrigation, the landscape and the natural hazard situation (Bolch et al., 2011; Frey et al., 2010; Huggel et al., 2004; Quincey et al., 2007). On a regional scale they affect the hydrological cycle of major water catchments (Huss, 2011), whereas at a global scale, future sea-level rise (SLR) is the most investigated effect (Gardner et al., 2013; Machguth et al., 2013; Meier et al., 2007; Radić and Hock, 2011; Raper and Braithwaite, 2006). As glaciers react very sensitively to small changes in climate they are considered as the best natural indicators of climate change (Haeberli, 2005; Oerlemans, 1994).

Glaciers have thus been selected as an Essential Climate Variable (ECV) by the Global Climate Observing System (GCOS) (GCOS, 2003) implementation plan for the United Nations Framework Convention on Climate Change (UNFCCC) (World Meteorological Organization, 2004). Correspondingly, monitoring strategies were developed within international efforts such as the Global Terrestrial Network for Glaciers (GTN-G) of GCOS (Haeberli et al., 2007). The core of the tiered strategy is to measure selected glaciers in detail for process understanding and a large number of glaciers more roughly (e.g. length changes) to get a regionally more representative signal. These annual in-situ measurements were combined with decadal updates of glacier inventories that are preferably derived by remote sensing. Although field measurements have the advantage of high accuracy, they are not cost- and time-effective in remote regions. Here remote sensing is of advantage due to the repeated and comparably fast and robust analysis of large areas with sufficient spatial detail (Raup et al., 2007).

Glacier inventories provide the basis for the investigation of glacier changes and their characteristics. The inventories have also been used for estimating glacier volumes (e.g. Haeberli and Hoelzle, 1995; Huss and Farinotti, 2012; Linsbauer et al., 2012), the determination of volume changes with the geodetic method (e.g. Gardelle et al., 2013; Kjaer et al., 2012; Paul and Haeberli, 2008; Rignot and Mouginot, 2012; Schiefer et al., 2007) and for the projection of future glacier mass change to determine their contribution to SLR (Giesen and Oerlemans, 2013; Marzeion et al., 2012; Pfeffer et al., 2014; Radić and Hock, 2011). The uncertainty in projections of future SLR was so far dominated by uncertainties in the distribution of continental ice (all ice bodies on land) (e.g. Radić and Hock, 2011; Raper and Braithwaite, 2006), and that key processes determining loss of ice (e.g. by calving) were not fully understood (Vaughan et al., 2013). A key drawback was that the regions with the largest ice cover (e.g. the Arctic) and thus the potentially highest sea level contribution had the largest gaps in their glacier inventories. For this and other reasons (e.g. GCOS, 2003) several projects have been launched in the recent past by the European Space Agency (ESA) and the European Union to collect information on glaciers (outlines and changes) using satellite data, for example the projects GlobGlacier (Paul et al., 2009a), Glacier_cci (Paul et al., 2012, 2013a) and ice2sea (Vaughan et al., 2013). One ultimate goal, based on these projects and on the Working Group I of the Fifth Assessment Report (AR5) of the Intergovernmental Panel on Climate Change (IPCC) was creating a globally complete glacier inventory (Pfeffer et al., 2014).

One major gap in the global inventory was the total area covered by local GIC on Greenland independent of the ice sheet. Hence, for global-scale applications this missing part was assessed by rough extrapolation schemes (Radić and Hock, 2011), its complete exclusion (Raper and Braithwaite, 2006), or a separate treatment (Lemke et al., 2007). With the Landsat archive now being freely available from glovis.usgs.gov (Wulder et al., 2012) and procedures for the compilation of glacier inventories being well established (Andreassen et al., 2008; Bolch et al., 2010; Le Bris et al., 2011; Frey et al., 2012; Jiskoot et al., 2012; Paul et al., 2011a; Racoviteanu et al., 2009), a good opportunity to map all local GIC on Greenland was in place. Nevertheless, the situation on Greenland is challenging, due to the difficult conditions for glacier mapping (e.g. icebergs, seasonal snow and cast shadow). The challenge is even greater from a semantic point of view, as two types of ice coverage exist that are interacting: a) the Greenland ice sheet (GrIs) with its outlet glaciers and b) the local or peripheral GIC that are or are not in touch with the ice from a) (Weidick and Morris, 1998). This implies that a glacier inventory for Greenland has also to develop a classification scheme that allows the local GIC to be separated consistently from the ice sheet.

Even though methods for mapping of clean ice and snow from optical satellite data using the classical pixel-based image analysis (PBIA) are well established and provide accurate results, there are shortcomings when it comes to more complex terrain where glacier parts are covered by debris or shadow, terminate in (ice-covered) lakes, or one in contact with icebergs (Paul and Kääb, 2005; Paul et al., 2013b; Racoviteanu et al., 2009). These points are in particular problematic for large-scale inventories, as time-consuming manual corrections are required. Object-based-image analysis (OBIA) is a classification technique which uses in addition to the classification based on spectral characteristics, also spatio-contextual information such as shape, texture and neighbourhood relationships (Blaschke, 2010; Blaschke and Strobl, 2001; Narumalani et al., 1998) that can help to reduce the workload of manual corrections considerably. A study which assesses the strengths and weaknesses of OBIA and PBIA for glacier mapping in challenging terrain has so far not been performed. In particular, a reduction of workload in post-processing might be achieved by this technique.

A glacier inventory for the local GIC on Greenland could be a key to distinguishing the mass changes obtained for the whole of Greenland using low-resolution gravimetry data (e.g. Schrama et al., 2011; Velicogna, 2009; Wouters et al., 2008) from those obbtained from the GIC (Paul, 2011). As in-situ mass balance measurements are sparse on Greenland, remote sensing data provide means to determine regional variations in mass balance. As frequently-used Digital Elevation Models (DEMs) from two points in time are not available for most of Greenland, altimetry data from the ICESat GLAS sensor are an alternative. They are freely accessible (Schutz et al., 2005; Zwally et al., 2002) and provide a reasonably good spatial coverage in the South and a good one in the North of the ice sheet and the surrounding GIC. However, due to the missing inventory of the local GIC, the mass budget has so far only been estimated for the ice sheet and a selection of local GIC (van den Broeke et al., 2009; Ettema et al., 2009; Sørensen et al., 2011; Velicogna, 2009). Combined with the glacier outlines from the inventory, mass changes for the GIC on Greenland can be calculated.

Combining the elevation change data from ICESat over GIC with climate variables such as temperature and precipitation would enable a relation to be found between mass changes and climate change. However, weather and climate-station data are sparse on Greenland and mostly located at low elevations and along the coastline (Ahlstrøm et al., 2008; Steffen and Box, 2001). The local GIC in contrast, are located in remote and high mountains areas and inland so that other ways of obtaining climate information must be found. Here, Regional Climate Models (RCM) driven by re-analysis data at the lateral boundaries can be considered. Though terrain representation in RCMs is often poor and uncertainties are high, they provide quantitative and spatially-distributed estimates of the regional climate of the past and the future on a physically

consistent basis (Laprise, 2008). Given that terrain differences can be considered (e.g. using a regionalized lapse rate) and that spatial averaging of values can be performed in a consistent way, such a comparison might reveal why the local GIC on Greenland show this spatial variability, even if trends in climate are similar in several parts of Greenland. The comparison of observed trends in temperature with observed changes in mass, gives an observed mass-balance sensitivity (Braithwaite et al., 2013), which is a key parameter for studying glacier-climate relations.

1.2 Objectives and research questions

Considering the above research challenges and opportunities, the main research questions of this thesis are:

What is the current status and the characteristics of the local GIC on Greenland?

Can a consistent way of separating the local GIC from the ice sheet be found?

Can the glacier-mapping process be improved with object-based image analysis (OBIA) to reduce the amount of manual correction during post-processing?

What is the regionalized mass change of the local GIC on Greenland and its overall contribution to sea-level rise?

Can the variability in observed mass changes be explained by differences in the climatic regime or recent trends in temperature and precipitation?

The above research questions will be addressed by creating first a complete glacier inventory for Greenland using optical satellite data and a DEM. One part of the work is specifically investigating the performances of OBIA and PBIA for glacier mapping. Surface elevation changes are derived from ICESat altimetry data in combination with the glacier outlines and a DEM. Converting them to mass changes includes re-analysis data that are downscaled by an RCM to incorporate a temperature-dependent firn-compaction model. Climate models (and weather station data for validation) are also used to investigate the climate sensitivities of the glaciers. The integration of all datasets is completed within a Geographical Information System (GIS from ESRI), digital-image-processing software (ENVI and eCognition) and script-based programming (IDL).

1.3 Organization of the thesis

The thesis is structured in three main parts:

Part I presents a synopsis of the relevant scientific background. It is subdivided into six chapters: After this more general introduction (Chapter 1) the scientific background relating to the research questions and methods is provided in Chapter 2. This includes a short overview on glaciers, remote sensing, digital elevation models, regional climate models and the study region. Chapter 3 focuses on a more detailed description of the here-applied methods and datasets and the study site Greenland. A summary of all research papers is given in Chapter 4. In Chapter 5 key findings of this thesis are discussed and evaluated in a broader context. In the final Chapter 6 the main conclusions in view of the initial research question are given, and a short outlook on potential future applications is presented.

Part II contains full versions of the research articles constituting the main part of the thesis. Their general approach and related research papers are depicted in Fig. 1.1.

The thesis is based on four papers of which three are already published in peer-reviewed journals.

Paper I describes the creation of the Greenland Glacier Inventory; Paper II compares the two different approaches for glacier mapping; Paper III deals with the derivation of surface elevation changes of all local GIC on Greenland, and Paper IV finally analyses the possible climatic reasons for these changes. Paper I and II are connected by the glacier mapping theme and Paper IV is based on the results of Paper III. Both Papers III and IV rely on the glacier outlines from Paper I.

Part III consists of appended material such as the CV, personal bibliography, and acknowledgements.

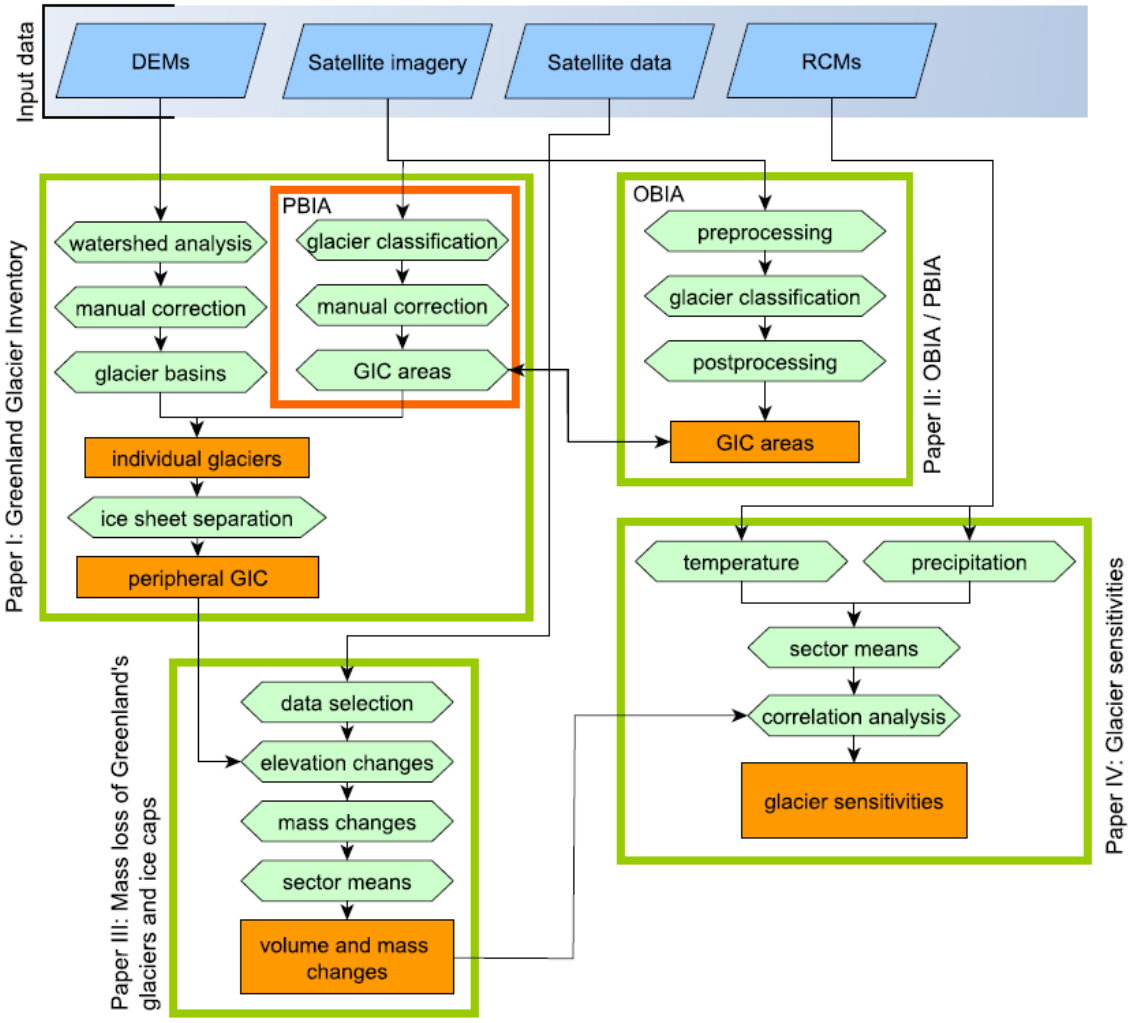

Figure 1.1 Schematic overview of the main elements of this thesis, their connections and structure, as well as the grouping of topics into different research papers.

2 Thematic and scientific background

2.1 Glaciological background

This chapter introduces the glaciological background for the various applications performed in this thesis. The chapter starts with the formation of a glacier, followed by a description of different glacier zones and glacier mass balance terms, also from a remote sensing perspective. Finally, an overview of international glacier-monitoring strategies and the available glacier datasets is given.

2.1.1 Formation of a glacier

Glaciers can be defined as a perennial mass of ice, and possibly firn and snow which originate from the recrystallization (or metamorphism) of snow or other forms of solid precipitation and showing evidence of past or present flow (Cogley et al., 2011). Glaciers form in regions with sufficient snow accumulation and temperatures low enough for the snow to remain during the summer. Once deposited, the snow crystals are transformed into rounded grains by evaporation, mechanical destruction (wind, compression) and cycles of melting and refreezing. This process also increases its density (see Table 2.1). After one year of metamorphosis snow is called firn. Air can still circulate through firn but its density is already higher than that of settled snow. Further compression by subsequent snow layers will change the firn into ice, which is by definition not permeable for air and has a density of about 900 kg m^{-3}. The speed of the metamorphosis depends on the climatic regime and the availability of percolating melt water. Once ice has been formed, it flows down slopes when located in the respective topography under the force of gravity, where ice is lost by melting and calving (Cuffey and Paterson, 2010).

Table 2.1: Typical densities for different stages of metamorphosis after Cuffey and Paterson (2010).

Type	Density (kg m^{-3})
Fresh snow	50-70
Settled snow	200-300
Firn	400-830
Glacier ice	830-917

The climatic regime is characterised by the local temperature and precipitation which are also the main factors that determine the global distribution of glaciers and ice caps (GIC). GIC can be found in the Arctic and Antarctic and along mountain regions, such as in the Andes, the Alps, the Himalayas, the Rocky Mountains, and the Coastal Mountains of Alaska and British Columbia, Norway and New Zealand. Their occurrence depends on the elevation of the equilibrium line (see section 2.1.2) and a given topography, which must be higher than the equilibrium line, to allow snow to accumulate at high altitudes where temperature is low. While temperature has a distinct decrease from low to high elevations and latitudes, the precipitation pattern is often rather complex, even on a local scale. The mean annual amount of precipitation is also dependent on the climatic zone and thus the global circulation pattern (Haeberli and Alean, 1985).

Temperature and precipitation also determine the climatic characterisation of a glacier (e.g. Ohmura et al., 1992). Glaciers located in coastal regions with high amounts of precipitation are of the maritime type having a high mass turnover (Fig. 2.1). For glaciers at mid-latitudes snow

accumulates predominantly during winter time as temperature during summer months are often too high for precipitation falling as snow. In monsoon-type climates large amounts of precipitation fall in summer while winter is the dry season. Accumulation at high elevations occurs in parallel with ablation, as mountains are sufficiently high (Kaser and Osmaston, 2002). Glaciers located in cold-dry regions are of continental type. Melt rates and mass turnover are low and accumulation can occur throughout the year (Anderson et al., 2010; Braithwaite and Zhang, 2000; Dyurgerov, 2003; Oerlemans and Reichert, 2000).

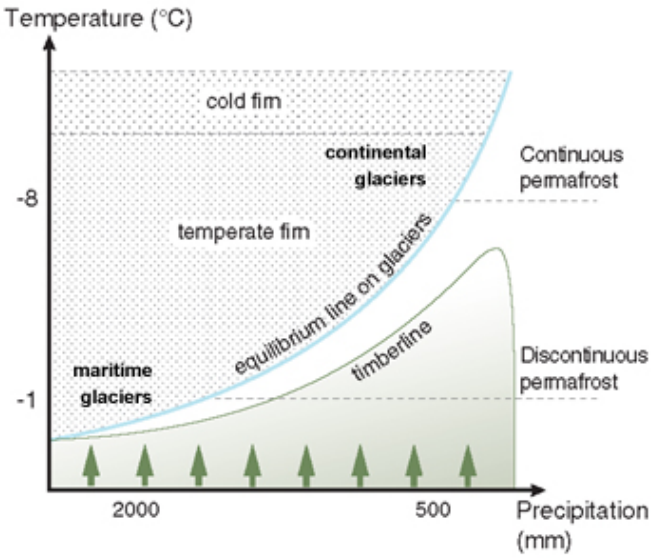

Figure 2.1: The climate type of a glacier is determined by precipitation (annual or winter amounts) and air temperature (annual or summer) at their equilibrium line. Modified cryospheric diagram from UNEP (2007).

2.1.2 Glacier zones

Glaciers can be divided into distinct zones that are described in more detail below (cf. Fig. 2.2). The entire sequence of zones can only be found in very cold climates without melting conditions throughout the year (e.g. the central parts of Greenland before the summer of 2012). The extent of the zones varies from year to year according to weather conditions.

The upper-most part of a glacier might have a dry snow zone (DSZ in Fig. 2.2) where no melting occurs. This zone can rarely be observed on the local GICs on Greenland (Williams et al., 1991). The percolation zone follows further down. This zone can be subdivided into an upper- (UPZ) and a lower percolation zone (LPZ). In the UPZ a limited amount of surface melt occurs and water can percolate a certain distance into snow before it refreezes again so that ice layers or lenses are formed there. The LPZ is characterised by snow that has been warmed to 0°C. Melt water in this zone also percolates into the deeper firn layers from previous years. Towards the lower boundary of the LPZ, a water-soaked slush zone (SuZ) can sometimes be found. This can be identified from satellite images (Fig. 2.4) (Hall et al., 1988). The lower boundary of the LPZ is marked by the transient snow line (TSL), which is due to the strong contrast between snow and the often much darker ice, also well-defined in satellite images. Below the TSL, water on the surface can refreeze, forming ice layers in the so-called superimposed ice (SIZ) zone. The TSL represents the boundary between firn and ice on a glacier surface at the end of the melt season, given that no SIZ is present. The lower end of the SIZ is the location of the equilibrium line (EL) which separates zones with mass gain (accumulation) from the zone with mass loss (ablation). The EL can rarely be observed as a line at the same elevation across the entire width of the glacier due to local topographic and climatic variations in accumulation and ablation. Thus, the

equilibrium line altitude (ELA) is the average altitude of the EL. Accumulation is due to solid precipitation, avalanches or snow drift, ablation is due to melting and calving (Benson, 1962; Cogley, 2012; Cuffey and Paterson, 2010). Mass balance is zero at the EL, negative below the EL and positive above it.

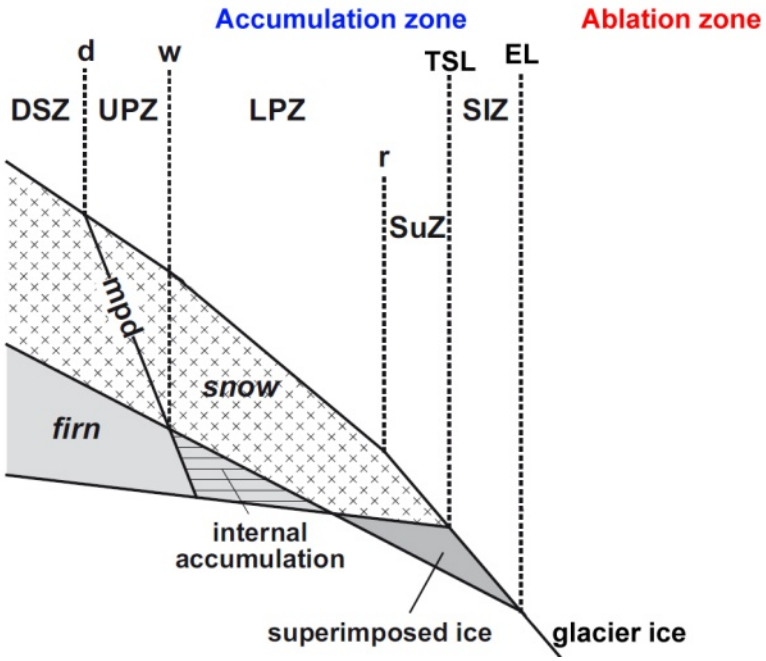

Figure 2.2: Different snow zones in the accumulation region of a glacier. From top to bottom: dry-snow zone (DSZ), upper percolation zone (UPZ), lower percolation zone (LPZ), slush zone (SuZ) and superimposed ice zone (SIZ). The zones are separated by the dry-snow line (d), wet-snow line (w), runoff limit (r), transient snowline (TSL) and equilibrium line (EL) which separates the ablation zone from the accumulation zone (modified after Cogley, 2012).

All of the zones mentioned above have different surface reflectivities due to variable grain size and liquid water content. While pure snow reflects solar radiation in the visible part of the electromagnetic spectrum (VIS) (400 – 700 nm) by almost 100% (Fig. 2.3), snow that is contaminated with dust or soot has a much lower reflectance. Ice can be seen spectrally as snow with very large grain size and always contains a certain amount of impurities. It thus appears much darker in the VIS than snow (Fig. 2.3). From the near-infrared (NIR) (750 nm – 900 nm) onwards, the reflectance of snow decreases and the sensitivity of the reflectance on impurities decreases as well (e.g. Hall et al., 1988). On the other hand, the sensitivity of its reflectance onto grain size increases (Dozier, 1989). As water has a very low reflectance in the NIR, glacier ice that is covered by liquid water also has a very low reflectance (Paul et al., 2005). In the short wave infrared (SWIR) range (1500 nm – 1700 nm), reflectance of snow and ice is very low, in particular for glacier ice with its large grain sizes (Zeng et al., 1984). This strong difference in the reflectance characteristics of ice and snow in the VIS and SWIR, is the basis for automated glacier mapping (cf. section 2.2.2)(Dozier, 1989; Kargel et al., 2005; Racoviteanu et al., 2009).

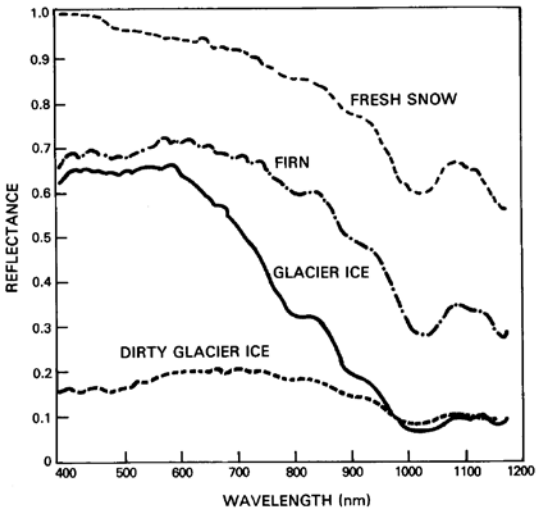

Figure 2.3: Curves of spectral reflectance for different surface materials. Reflectance of snow is higher than of firn and ice, but all decrease from the VIS to the NIR (Hall and Martinec, 1985).

Owing to the different spectral characteristics of the snow and bare-ice zone of a glacier, these two zones can often be easily distinguished from space. Assuming a small SIZ a separation of the accumulation from the ablation region is possible (Bippus, 2011; Rabatel et al., 2008). However, sometimes a water-saturated snow zone blurs this separation (Fig. 2.4). In years with very negative mass balances, polluted firn layers from previous years might be visible that belong to the ablation region (Gross et al., 1977). Depending on their reflectance, it might be possible that these polluted firn layers are difficult to separate from snow, so that accumulation and ablation regions cannot be clearly distinguished in such years (König et al., 2001).

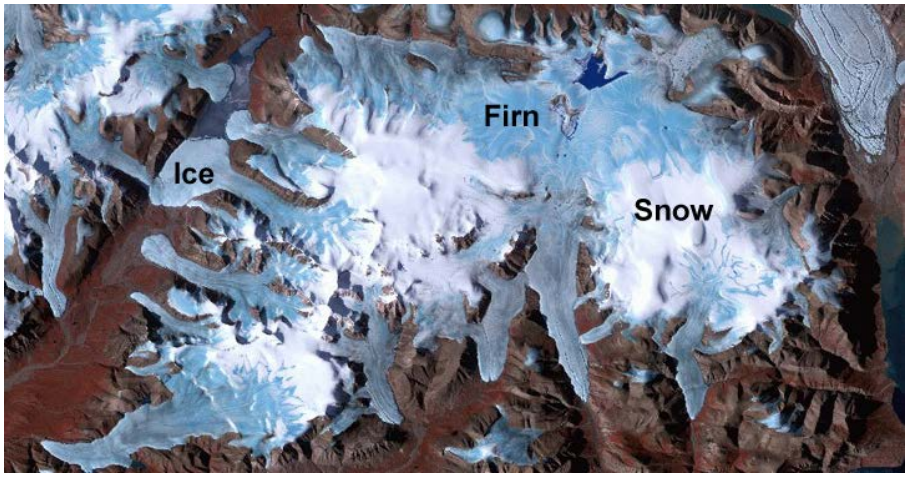

Figure 2.4: Ice, water saturated firn/snow and snow as seen on glaciers and ice caps on Ellesmere Island, Canadian Arctic with bands 3, 2, 1 (as RGB) from the Terra ASTER sensor (image acquired on (19.07. 2000). ASTER scene provided by GLIMS, image source: www.globglacier.ch.

2.1.3 Glacier mass balance and measurement methods

Mass balance can be defined as the mass loss subtracted from the mass gain over a year for a point on a glacier, a glacier section or an entire glacier (Cuffey and Paterson, 2010). It is determined by the sum of all processes that add mass to and remove mass from the glacier. Snow, avalanches, snow wind drift and internal accumulation from refrozen melt water or rain contribute to mass gain (or accumulation), whereas melting, evaporation, calving or basal melting

beneath the glacier remove mass (ablation). The mass balance (or budget) at the glacier surface is the direct result of the climatic conditions in the respective year and has thus a high correlation with the prevailing atmospheric conditions.

Measuring mass balance in the field is laborious and thus only performed on individual (mostly smaller) glaciers (e.g. Cogley, 2009a; WGMS, 2012; Zemp et al., 2009). The annual mass balance is measured over a hydrological year, starting at the beginning of the accumulation season until the end of the ablation season (stratigraphic method). At best, the mass balance is measured once or twice a year in the field using the glaciological method (Kaser et al., 2003). The geodetic method provides the overall volume loss over a decadal time scale by comparison of the topography from two points in time determined by repeated mapping (Bamber and Rivera, 2007; Gardelle et al., 2012; Rignot et al., 2003). The latter method also includes mass loss due to internal or basal melt (or calving) that cannot be measured at the surface and changes in zones that are difficult to access in the field (crevasses, avalanches, steep slopes). The geodetic method at a high temporal resolution can be used for calibration of the glaciological method (Zemp et al., 2013). Mass change can afterwards be obtained by multiplication with an assumed average density (e.g. 850 kg m^{-3}), but this can introduce major uncertainty (Huss, 2013; Li and Zwally, 2011).

Since 2003 mass changes can also be determined by repeated measurement of the Earth's gravity field using the satellites from the GRACE mission (e.g. Jacob et al., 2012). The coarse spatial resolution (about 300 km) and the difficulties of separating different mass change signals limit this method to large regions with continuous ice cover (Schrama et al., 2011; Velicogna, 2009; Wouters et al., 2008). It works well for the two ice sheets (e.g. Shepherd et al., 2012) but less so for the GIC on Greenland. For these much smaller features, repeat determination of elevation changes at point locations from spaceborne altimetry sensors such as the ICESat Geoscience Laser Altimeter System (GLAS) has proven to provide useful results (e.g. Bolch et al., 2013; Gardner et al., 2013; Kääb, 2008; Kääb et al., 2012; Neckel et al., 2014). The key issue here is to find reasonable ways of applying the point measurements to the entire glacier (e.g. Kääb et al., 2012).

Mass balance can also be calculated for a glacier or an entire mountain range using models that are driven by time series of atmospheric variables (Hock et al., 2009; Machguth et al., 2009; Marzeion et al., 2012) or converting glacier variables such as a change in length or ELA into mass change (Leclercq and Oerlemans, 2011; Paul et al., 2007). Modelling has the advantage of extending measured mass balances in space and time, but requires careful validation or calibration of the models applied.

In Greenland most in-situ mass-balance measurements take place on the ice sheet rather than on local GIC (compare Fig. 1 in Machguth et al. (2013) for a graphical overview) (Ettema et al., 2009; Hanna et al., 2008; Weidick, 1984; Weidick et al., 1995). Only one long term mass balance series exists from Mittivakkat glacier in Eastern Greenland (see Fig. 2.14 for location) since 1995 (Mernild et al., 2011). The mean annual net mass balance of this glacier is –0.97 ±0.75 m w.e. a^{-1} (1995/96–2010/11), with a mean winter balance of 1.18 ±0.19 m w.e. a^{-1} and a mean summer balance of –1.94 ±0.38 m w.e. a^{-1} (1995/96–2007/08) (Mernild et al., 2013). Information on mass changes of GIC on Greenland is therefore sparse, including volume changes obtained by the geodetic method. In consequence, repeat altimetry data from spaceborne sensors such as ICESat GLAS provide the only way to retrieve such information over larger regions.

2.1.4 International glacier monitoring strategies

The monitoring of glacier-specific parameters and changes using in-situ data and remote-sensing techniques are important components of the Global Hierarchical Observing Strategy (GHOST).

The idea of GHOST is to measure a large number of variables at a few locations and a few variables regularly at a large number of places (World Meteorological Organization, 1997). The related measurements within GHOST are organised into a system of tiers that can be summarised for glaciers as follows (e.g. Haeberli et al., 2002): Tier 1 emphasises observations across different environmental gradients, like transects through different mountain ranges. Tier 2 focuses on extensive glacier mass balance and flow studies within major climatic zones. At Tier 3 sites a reduced observational network (index stakes) is used to determine regional glacier volume changes. Tier 4 measurements (length changes) are performed at a much higher number of sites to increase spatial and temporal representativeness including long-term observations. Finally, observations at Tier 5 are related to repeated compilation of glacier inventories at time-scales of a few decades for regional-scale change assessment, up-scaling of the other observations and other applications. A starting point for Tier 5 was the compilation of national glacier inventories initiated during the International Hydrological Decade (1965 – 1974) and completed with the World Glacier Inventory (Haeberli et al., 1989). With satellite data becoming freely available glacier outlines were produced by an international consortium under the brand "Global Land Ice Measurement from Space" (GLIMS) (http://glims.org/). The related GLIMS glacier database is designed to augment glacier baseline information to facilitate global-scale glacier monitoring, glacier change studies, hazard detection and free exchange of data. Furthermore, data fusion and GIS-based modelling (Bishop et al., 2004; Raup et al., 2007) were established. While the World Glacier Monitoring Service (WGMS) aims at maintaining and fostering the active collection of information on ongoing fluctuations in glacier mass, volume, area and length from field measurements and aerial photography, GLIMS is in charge of collecting the satellite component (Tier 5) with a focus on generating glacier outlines and glacier inventories. The GLIMS database is hosted by the National Snow and Ice Data Center (NSIDC) and all three form the Global Terrestrial Network for Glaciers (GTN-G). Strategies for global glacier monitoring are proposed and discussed within GTN-G and its associated bodies.

2.1.5 Global distribution (datasets) of glaciers

Despite the demand for a globally complete glacier inventory (GCOS, 2003; Lemke et al., 2007; Raper and Braithwaite, 2006), such a dataset was not available at the required level of detail until recently. In consequence, worldwide glacier coverage had to be estimated and extrapolated for several global scale applications such as the past and future contribution of glaciers to sea-level rise (Hock et al., 2009; Meier et al., 2007; Radić and Hock, 2011), river runoff at continental scales (Huss, 2011) and determination of global glacier-climate interactions (Marzeion et al., 2012). While several important glacier parameters can be calculated using the World Glacier Inventory (WGI) (Evans and Cox, 2005; Haeberli and Hoelzle, 1995), the determination of area change requires precise outlines including flow divides for separation of individual glaciers (see section 3.3).

The global glacier databases currently available can be roughly distinguished into three types: point, raster and vector (see comparison in Fig. 2.5). The point type is basically a tabular listing of all glaciers (names, coordinates, meta-data) and includes the WGI (Haeberli et al., 1989) and its extended version the WGI-XF (Cogley, 2009b). The vector type includes the digital chart of the world (DCW) which was digitised from large-scale topographic maps (Danko, 1992), and the glacier outlines from the GLIMS database that are mainly compiled from satellite data (Raup et al., 2007). Finally there is the Global Hydrographic Data (GGHYDRO) raster dataset (Cogley, 2003) that has been widely used as it is globally complete, but which has only a 1 by 1 degree spatial resolution (Fig. 2.5). So all datasets differ in coverage, level of detail, available data entries, periods of acquisitions and in regard to their formats (point, vector, raster).

According to Ohmura (2009), the WGI in 2009 covered 46% of the worldwide estimated glacier area of 540 ±30 x 10^3 km^2 (Dyurgerov and Meier, 2005). The GLIMS database covered 34% and

26% is covered jointly by both datasets, resulting in an overall coverage of 54%. Before this thesis was started, large data gaps prevailed in the Canadian and Russian Arctic, in India as well as Greenland. This latter gap was closed by this thesis (Paper I) with the compilation of an inventory for all GIC on Greenland. The DCW on the other hand was until recently, probably the most complete, albeit an inaccurate dataset due to rough base data. In its entirety, the DCW comprises 20 themes with raster and vector data of different quality, including a hydrological layer with information about the permanently ice-covered regions. Finally, the GGHYDRO dataset stores the relative amount of glacier coverage per 1 by 1 degree cell.

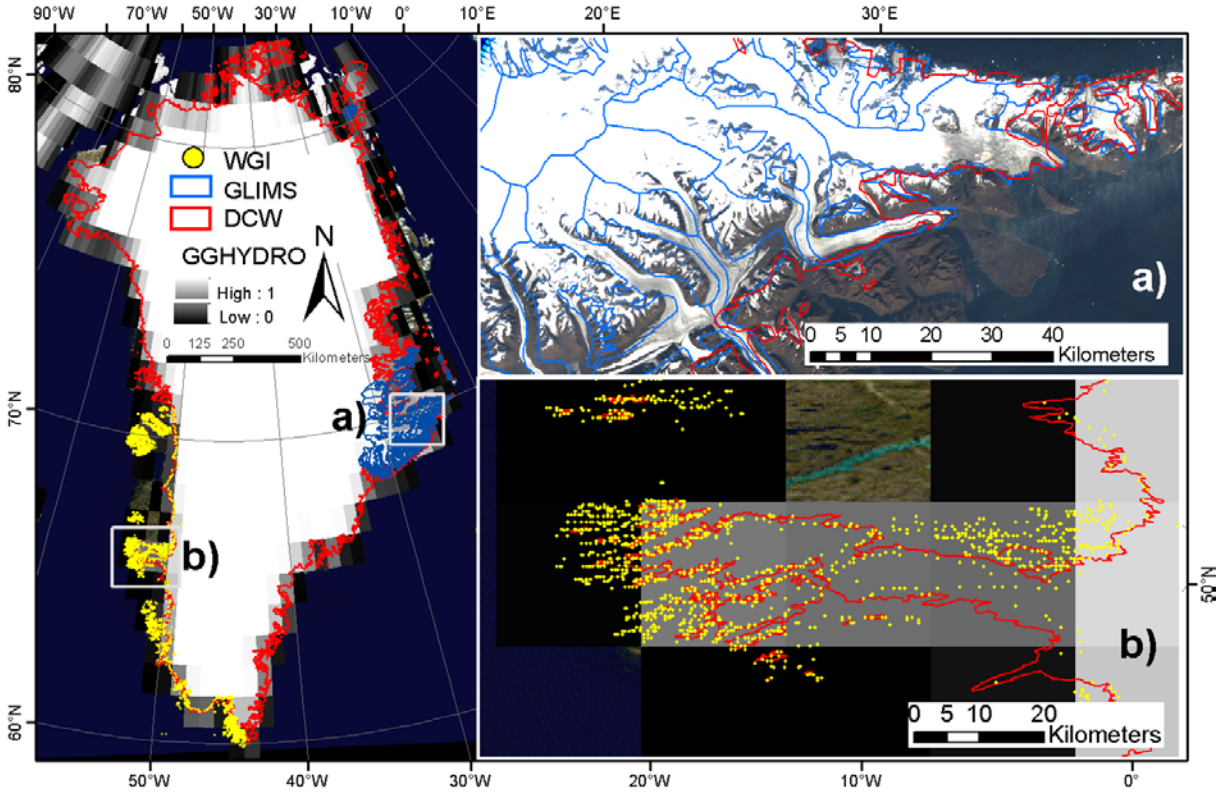

Figure 2.5: State of the GLIMS- the WGI- the DCW and the GGHYDRO glacier database for Greenland as of November 2013. Greenland's local GIC are only covered by the DCW, however, in an inaccurate manner. GLIMS data is only partially available as the WGI (inset a). The latter data source as well as the GGHYDRO are available as point information and as grid (inset b) and thus unusable for glacier change detection (sources: GLIMS glacier viewer, NSIDC and Global Glaciology at Trent University)

2.2 Remote Sensing

Remote Sensing (RS) is a methodology for measuring the physical properties of an object at the Earth's surface without touching it (Lillesand, 2006; Richards and Jia, 2006; Schowengerdt, 2006). Sensors mounted on airborne or spaceborne platforms measure the quantity of energy reflected by an object for specific electromagnetic wavelengths. RS thus offers powerful tools to investigate characteristics of objects spatially and temporally. Two basic principles of satellite systems can be distinguished: Passive and active sensors. The latter emit their own source of energy (microwave) whereas the former take advantage of the solar energy reflected and emitted by the earth's surface.

Remote sensing imagery can be distinguished according to different types of resolution (Lillesand, 2006; Richards and Jia, 2006; Schowengerdt, 2006). The spectral resolution is defined

by the number of spectral bands and the spectral width of each band. Satellite sensors can range from a few (multi-spectral) to more than 100 bands (hyperspectral). The spatial resolution is the smallest ground area resolved in an image. A pixel (picture element) approximates the spatial resolution of the instrument (Pellikka and Rees, 2009). If the spatial resolution of the instrument is smaller than the object size, it can be traced in the image. In cases of strong contrast, also objects smaller than the pixel size can be recognised as they influence the spectral information in a mixed pixel (e.g. Fisher, 1997). The temporal resolution refers to the revisiting time of a satellite, which is determined by the repetition cycle of orbits (geostationary or polar orbiting), the swath width of a sensor and the geographic location on Earth (e.g. stronger overlap towards higher latitudes). Geostationary satellites, in general, weather and telecommunication satellites, rotate around the Earth at about 36000 km height with the Earth's rotation. This enables a high temporal resolution but a low spatial resolution. In contrast, polar orbiting satellites have a smaller swath width and a lower temporal resolution, but a much higher spatial resolution than geostationary satellites. The radiometric resolution is the ability of a sensor to differentiate intensities (brightness value) in an individual band. The quantified values can range from 2, to 8 or 14 bits corresponding to 4, 256 or 16384 discrete grey values, represented by so-called digital numbers (DN) in integer format. To accommodate the broad range of land surface reflectances and avoid sensor saturation (e.g. over snow), some sensors (e.g. ASTER and ETM+) allow correction of the gain settings of individual bands for the time of satellite overpass (e.g. low over land surfaces with ice and snow and high over forest). The 8-bit sensors of the Landsat TM visible bands were often saturated over snow when facing direct sunlight.

2.2.1 Platforms and Sensors

This section introduces some background of the platforms and sensors used in this thesis. A description of how and for what purpose they were used is given in section 3.1.1. Further platforms for mapping the GICs on Greenland such as SPOT 5 (Korona et al., 2009) or the Indian Remote Sensing satellite (IRS) (details available at: http://www.isro.org/) exists, but they were not considered explicitly here.

The Landsat Program from the National Aeronautics and Space Administration (NASA) and the U.S. Geologic Survey (USGS) is the most famous satellite mission in history that records images of the Earth's surface between 81° North and South. The program started in 1972 with the launch of Landsat 1 and is still continuing with the recent launch of Landsat 8. The Landsat mission thus constitutes a unique long-term time series of Earth observation data which is extremely useful for studing changes of the landscape (Wulder et al., 2012) such as glaciers. Unless otherwise cited, the information in this paragraph is derived from the Landsat website (http://landsat.usgs.gov/index.php, accessed November 2013). Landsat 4, launched in 1982, was mounted with the first Thematic Mapper (TM) sensor with a higher spectral (blue and short – wave infrared (SWIR) bands) and spatial resolution (30 m) than the previous Landsat 3 Multi Spectral Scanner (MSS) sensor with 75 m resolution and only 5 spectral bands. Landsat 5 was launched in 1985 and operated until the end of 2011, 20 years longer than its designated lifetime. Landsat 6 (1993) failed to reach orbit so that in 1999 Landsat 7 was launched with the new Enhanced Thematic Mapper Plus (ETM+) sensor that included a 15 m resolution panchromatic band (Fig. 2.6). In May 2003, the scan line corrector of the ETM+ sensor failed and caused striped data gaps. In consequence, the nearly 20-year-old Landsat TM sensor was reactivated and used more frequently. In order to provide continuity with the Landsat imaging dataset, NASA and the USGS initiated the Landsat Data Continuity Mission (LDCM) which was after the successful launch in February 2013 renamed to Landsat 8. Landsat 8's Operational Land Imager (OLI) improves on past Landsat sensors by providing a 12-bit quantisation of data allowing for a better discrimination of otherwise saturated pixels and improved spectral discrimination of land cover. Landsat data are available in different processing levels from the website glovis.usgs.gov. The best processing level is the standard Terrain correction (Level 1T) that requires a DEM

(Global Land Survey Digital Elevation Model (GLSDEM) and/or Shuttle Radar Topography Mission (SRTM)) and enough ground control points to be available. The lowest is the Systematic Correction (Level 1G) which has only been corrected with a mean geoid but without a DEM.

The Terra satellite is in a sun-synchronous orbit and has different types of sensors on board. The two that are used in this thesis are the Advanced Spaceborne Thermal Emission and Reflection Radiometer (ASTER) and the Moderate Resolution Imaging Spectroradiometer (MODIS) instrument. ASTER provides high resolution images in 14 different channels such as the VNIR (Visible and Near Infra-Red), the SWIR (Short Wave Infrared) and the TIR (Thermal Infra-Red) (Fig. 2.6). The spatial resolution of the respective images ranges from 15 m (VNIR), to 30 m (SWIR) to 90 m for the TIR (http://asterweb.jpl.nasa.gov/, accessed November 2013). A big advantage of the ASTER sensor is its ability to acquire three-dimensional stereoscopic images (from an along-track sensor with a nadir and backward looking telescope) which is very useful for generating high resolution DEMs (Kääb et al., 2002; Toutin, 2008) (see section 2.3.1 for more details regarding DEM generation). ASTER imagery also comes in two different levels. The Level-1B Registered Radiance at the Sensor (RRS) product contains radiometrically calibrated and geometrically co-registered data for the acquired channels of the three different telescopes of Level-1A data. The Level-1B data set is produced by applying the radiometric calibration and geometric correction coefficients to the Level-1A (https://lpdaac.usgs.gov/products/aster_products_table/ast_l1b, accessed January 2014); however, orthorectification is not performed (the related product has to be ordered).

The MODIS instrument was launched in 1999 on board the Terra satellite and three years later also on board the Aqua satellite. The MODIS sensor has 36 bands with two bands at 250 m resolution, five bands at 500 m and 29 bands at 1 km resolution. The Level 1A product provides the geolocation and Level 1B a cloud mask. Several higher-level MODIS land and atmosphere products are produced by the MODIS Adaptive Processing System that is available at http://modis.gsfc.nasa.gov/data (accessed January 2014). MODIS data, with their global coverage nearly every two days, provide information for large-scale (global) applications with high dynamics (cloud cover, sea ice cover, fire detection etc.).

ASTER and MODIS imagery can be downloaded by registered users from the NASA's Earth Observing System Data and Information System (EOSDIS) at http://reverb.echo.nasa.gov.

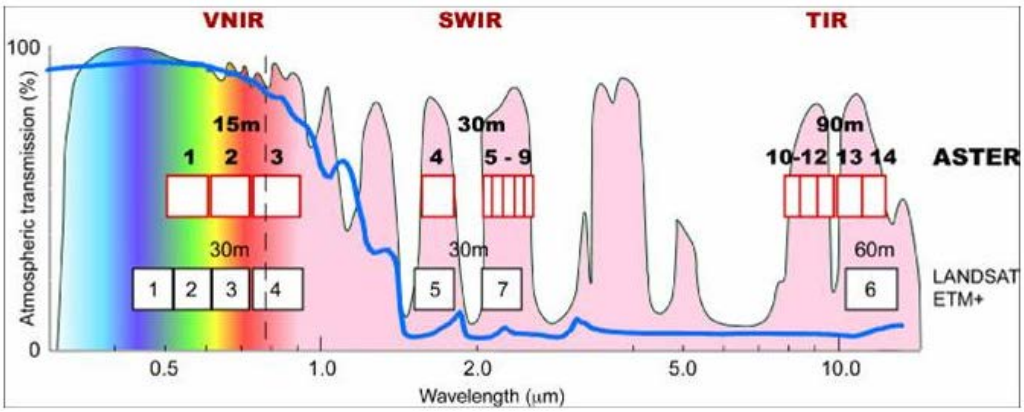

Figure 2.6: ASTER and Landsat ETM+ bands superimposed on a generalised curve of atmospheric transmission. ASTER bands are shown as red squares and Landsat ETM+ bands as black squares along with their respective spatial resolution and spectral bandwidth. The blue line represents the spectral reflectivity of snow. Electronic source: http://asterweb.jpl.nasa.gov/images/spectrum.jpg, accessed January 2014.

The Ice, Cloud, and Elevation Satellite (ICESat) was a satellite mission for measuring ice sheet elevation change, cloud and aerosol heights, as well as land topography and vegetation characteristics. It was launched in 2003 into a near-circular, near-polar orbit and worked until 2009. ICESat's Geoscience Laser Altimeter System (GLAS) emitted infrared and visible laser pulses at 1064 and 532 nm with footprints of about 70 m and a sampling frequency of about 170 m (Schutz et al., 2005; Zwally et al., 2002). It has been shown in several studies that ICESat-derived elevation changes could not only be derived for the relatively large GIC in Arctic-regions (Kropáček et al., 2013; Moholdt et al., 2010; Rinne et al., 2011; Sørensen et al., 2011; Wenlu Qi and Braun, 2013), but also for the much smaller glaciers located in the steep terrain of mid-latitude mountain ranges (Gardner et al., 2013; Kääb et al., 2012; Neckel et al., 2014). Moreover, they served as vertical and horizontal references in remote regions where ground-truth-data for validation are lacking (Nuth et al., 2013; Pieczonka et al., 2013). ICESat data has been used for many other applications and can be freely downloaded from: http://nsidc.org/data/icesat/data.html.

2.2.2 Pixel-based glacier mapping

The classification of glaciers from optical satellite data is usually carried out at pixel level. The pixel-based image analysis (PBIA) utilises the spectral information stored in each pixel in the individual image bands and classifies each pixel on the basis of the variability of reflectance values in each band (Lillesand, 2006).

The images recorded by a satellite sensor can, however, contain geometric errors and the measured digital numbers of the pixels may limit the ability to interpret or quantitatively process and analyse the digital data. Radiometric variability that is not related to spectral properties of the surface can arise from scattering/diffraction of light in the atmosphere, whereas geometric errors can arise from poor orthorectification in steep terrain (e.g. when using a low-quality DEM), as well as from uncontrolled motion of the satellite (Richards and Jia, 2006).

Hence, prior to the classification process satellite imagery should be geometrically and atmospherically corrected. For glacier mapping the latter step is not a must as the conversion to physical values of spectral reflectance (e.g. Hall et al., 1987) does not provide a better classification because a) a threshold has to be chosen anyway, b) ratio images compensate the radiometric corrections, and c) the result is in close agreement with methods using physical values (Burns and Nolin, 2013; Paul and Kääb, 2005). If, however, several satellite scenes from different sensors and dates are to be processed at a time with a unique threshold (standardisation) a conversion into physical values is recommendable (Burns and Nolin, 2013; Liu et al., 2013; Racoviteanu et al., 2009).

A variety of mapping algorithms have been developed in the last few decades to map clean ice and snow (König et al., 2001; Paul and Kääb, 2005). All glacier mapping algorithms utilise the high reflection of snow and ice in the visible part and the low reflection in the shortwave part of the electromagnetic spectrum. For instance, the simple ratio of a NIR and SWIR by Hall et al. (1987) was originally developed to distinguish between ice- and snow-covered areas on a glacier, but was later also used to classify glaciers (Bayr et al., 1994; Jacobs et al., 1997; Paul et al., 2002). Another approach is the calculation of the Normalized Difference Snow Index (NDSI) (NDSI = (GREEN – SWIR) / (GREEN + SWIR)) that was proposed by Dozier (1989) to map snow cover and was later used for both snow (Hall et al., 1995) and glacier mapping (Sidjak and Wheate, 1999). Rott (1994) tested a RED / SWIR ratio based on atmospherically corrected spectral reflectance values. Bolch and Kamp (2006) found a better performance of the NIR / SWIR ratio than the RED / SWIR ratio for the Bernina Group in the Swiss Alps. Paul and Kääb (2005) compared several of these approaches and concluded that the ratio RED and SWIR yield the best results in the steep terrain of Baffin Island. The NIR / SWIR ratio had problems in

mapping snow or ice in cast shadow, where the NDSI performed somewhat better. The classification of snow and ice is done by a selection of an appropriate threshold. The thresholds applied to the simple RED / SWIR ratio vary slightly from scene to scene but are mostly between 1.6 and 2.2. Due to its high efficiency and easy usage, band ratio techniques have become a quasi-standard for glacier mapping today (Andreassen et al., 2008; Aniya et al., 1996; Bolch et al., 2010; Le Bris et al., 2011; Falaschi et al., 2013; Frey et al., 2012; Paul et al., 2009a).

Debris-covered glacier areas are part of a glacier and have thus to be included in the class "glacier" (Raup and Khalsa, 2010). Their automatic mapping, however, is difficult due to similar reflectances of debris and the surrounding terrain. Several approaches, which can be seen as complementary to PBIA, have been developed to map debris-covered glacier parts from non-spectral information. These include the application of artificial neuronal networks (Bishop et al., 1999), the usage of thermal bands (owing to the cooling effect of the underlying ice, thin supraglacial debris (<2 cm) can be several degrees colder than debris without ice underneath (Foster et al., 2012; Mihalcea et al., 2008; Taschner and Ranzi, 2002), geomorphometric DEM analysis considering terrain slope (debris mainly accumulates on flat parts of a glacier) (Bishop et al., 2001; Bolch and Kamp, 2006; Bolch et al., 2007; Paul et al., 2004; Racoviteanu and Williams, 2012) or the combination of geomorphometric parameters and temperature information (Bhambri et al., 2011; Bolch et al., 2007; Buchroithner and Bolch, 2007; Rastner et al., 2014).

Besides the challenges in mapping debris-covered glaciers, it is also difficult to map glaciers correctly in cast shadows. They are common in rough mountain terrain (e.g. South-east Greenland) but also in the very far north of Greenland due to low solar angle. Although band ratio techniques work also in shadowed areas most of the time (Hall et al., 1987), inaccuracies in the glacier outlines are unavoidable. Paul and Kääb (2005) applied an additional threshold onto the blue band to improve mapping of glaciers in shadowed areas. The usage of a DEM (see next section for details), to mask these regions (Gao and Liu, 2001) is another possibility when a high quality DEM is available (which was not the case for Greenland).

The mapping of glaciers is further impeded by water surfaces and semantic differences**.** For example, a clear lake on a glacier is not mapped (although it should be) whereas a turbid lake in front of a glacier is mapped (but should not be). Huggel et al. (2002) applied a so-called Normalized Difference Water Index (NDWI) (NIR-BLUE/NIR+BLUE), which basically maps all water surfaces in a scene. Such an additional classification of water is recommendable if a large number of water bodies are present in the scene, but water classification with the NDWI is sometimes confused in regions with shadows.

Finally, after the automatic mapping is completed, a 3 by 3 kernel filter can be applied (Paul et al., 2002) to homogenise the final class "glacier" by removing small snow patches, closing gaps from debris cover (e.g. a medial moraine) and reduce noise in regions of cast shadows (Falaschi et al., 2013; Racoviteanu et al., 2009). Subsequently, the binary image is converted into a vector format (e.g. a polygon shapefile) for its final manual post-processing. This step is in general the most laborious and time-consuming. Commission errors (clouds, snow patches, lakes, icebergs, sea ice) and omission errors (debris-cover, ice in shadow, supraglacial lakes) can be identified by visual interpretation of false colour composite (FCC) images displayed in the background using a Geographic Information System (GIS). Thereby, different band combinations help in identifying specific objects. For example, an FCC of the RED-GREEN-BLUE bands (true-colour) is most helpful for the identification of ice in shadow, the combination of the NIR-RED-GREEN bands enhances contrast over ice and snow and enables identification of lakes and finally the SWIR-NIR-RED RGB is helpful for separating ice from rock/debris, or snow/ice from clouds. If the minimum mapping unit (MMU) of a glacier is applied, a fast approach is to reject all polygons that have a size smaller than the MMU. In addition, this might help to reduce the number of wrongly mapped seasonal snow pixels. For glacier inventories, the MMU is often set to >0.01

km² (Andreassen et al., 2008; Falaschi et al., 2013; Paul et al., 2011a) or >0.02 km² (Le Bris et al., 2011; Frey et al., 2012) however, for the Greenland Glacier Inventory (GGI) and other studies like the inventory of Western Canada it was set to 0.05 km², or more (Bolch et al., 2010; Rastner et al., 2012).

2.2.3 Object-based image analysis

Progress in computer technology in recent decades led to the development of an image classification technique called object-based image analysis (OBIA). This approach groups single pixels according to some common properties in single objects. The objects can afterwards be classified based on their spectral characteristics, but also based on their spatial-contextual information such as shape, texture and neighbourhood relations (Blaschke, 2010). OBIA thus offers interesting opportunities for the mapping of glaciers, in particular when it comes to the automatic detection of typical omission and commission errors. When seen in their context, they can be assigned to the correct class and the workload for manual correction can be grately reduced. Several software packages offer object-based classification algorithms, for example IDRISI, ERDAS Imagine, ENVI, SPRING, MADCAT and eCognition. In this thesis eCognition was used and therefore all further descriptions are related to this software package.

Independent of the software used, the mapping process in OBIA can be divided into three key processing steps: a) image segmentation, b) classification, and c) post-processing. These steps are explained in more detail in the following.

Segmentation: A fundamental first step of image classification with OBIA is the segmentation of the satellite scene in the beginning. Segmentation is the subdivision of an image into separate regions represented by basic unclassified image objects called image object primitives. The most common segmentation procedure in eCognition is multiresolution segmentation (MRS) which, for a given number of image objects, minimizes the average heterogeneity and maximizes their respective homogeneity. The MRS segmentation is used for: (a) extracting features that are characterized not purely by spectral characteristics but also by shape homogeneity and (b) extracting land cover or man-made features from remote-sensing imagery. A careful selection of the three segmentation parameters scale, shape and compactness (Fig. 2.7) as well as an appropriate weighting of the input bands is of utmost importance in MRS to create object primitives. The special challenge is to get the objects as large as possible and at the same time small enough to represent the structures of interest (Baatz et al., 2005; Trimble, 2011).

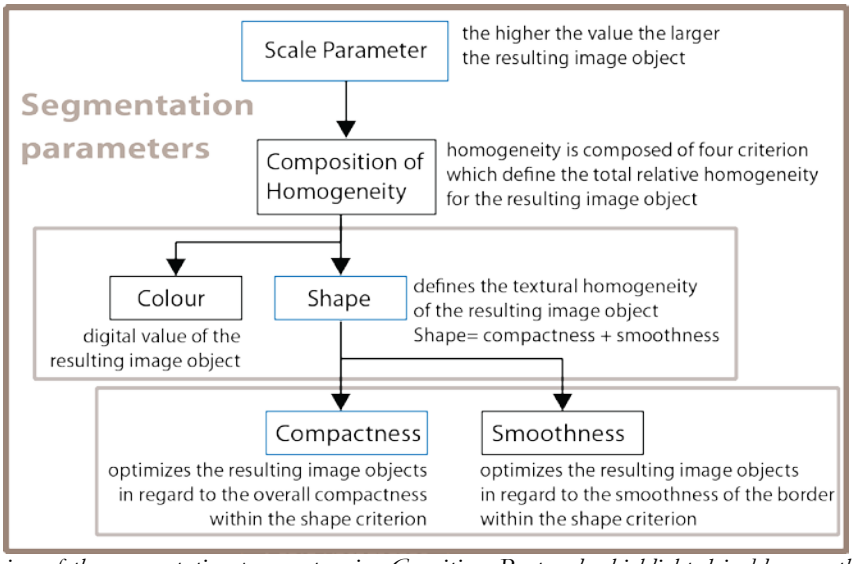

Figure 2.7: Overview of the segmentation parameters in eCognition. Rectangles highlighted in blue are the ones with direct user input. Modified after Definiens (2007).

The scale parameter is a theoretical term determining the maximum heterogeneity allowed for the resulting image objects (Trimble, 2011). By modifying the scale parameter it is possible to influence the size of the image objects. The example in Fig 2.8 shows the influence of the scale parameter based on only three image layers and a scale of 10, 30 and 60 (in a, b, and c, respectively). As can be seen, the objects get larger with increasing scale parameter. By comparing the results of the segmentation it is recognisable that: in a) the objects are small enough to catch the spectral variability of the features on the ground whereas in b) and c) the objects are already so large that features with differing spectral reflectance are merged together. For example, ice and debris are merged together (arrows 2 & 3) and in c) lakes and soil are merged (arrow 4). Using these objects would result in poor accuracy and time consuming manual correction. In contrast, in a) the objects are slightly too small for the post-processing of lakes, i.e. one lake is represented by two objects (arrow 1). These are typical problems (under- and over-segmentation) resulting from the segmentation step (Liu and Xia, 2010). This is a particular OBIA problem when small details (at the extent of a few pixels) have to be classified. On the other hand, considering too small objects at the initial stage of segmentation reduces the possibility of mapping medial moraines or extended debris-covered glacier tongues as specific objects.

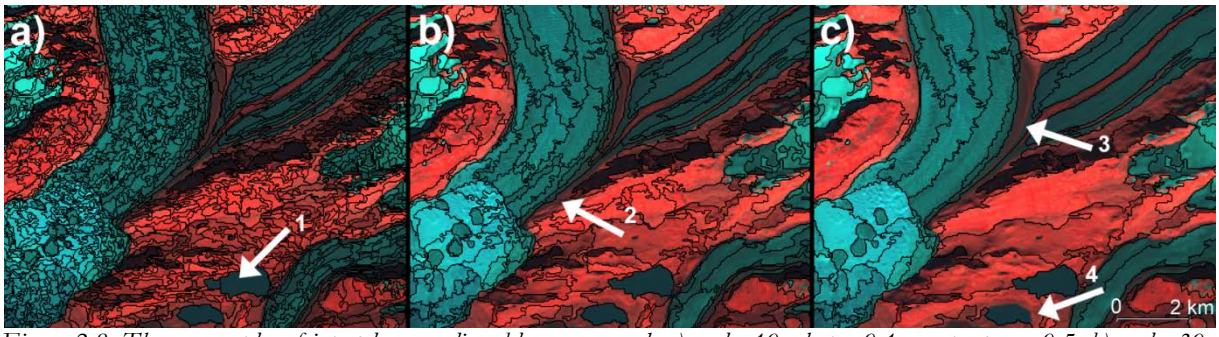

Figure 2.8: Three examples of input layer scaling: blue, green, red; a) scale: 10, shape: 0.1, compactness: 0.5, b) scale: 30, shape: 0.1, compactness: 0.5 c) scale: 60, shape: 0.1, compactness: 0.5. The arrows mark objects discussed in the text: arrow 1 two objects are assigned to one lake, arrows 2, 3 and 4: one object includes different surface types. Location: Watkins range-Greenland.

The shape criterion is helpful in avoiding highly fractured image objects that result from strongly textured data. Modifying the shape criterion indirectly influences the colour criterion that is related to the percentage the spectral values of the image layers contribute to the entire homogeneity criterion. The shape criterion cannot have a value higher than 0.9, as without the spectral information of the image, the resulting objects would not be related to the spectral information at all (Definiens, 2007; Trimble, 2011).

In a raster the ideal compact form of an object is a square. The compactness criterion minimizes the deviation from the ideal compact form. This criterion is also a relative weighting against the smoothness criterion which is used to optimize image objects regarding the smoothness of their boundaries. The compactness criterion is used when working with very heterogeneous data to prevent the objects from having frayed borders (Definiens, 2007; Trimble, 2011).

In Fig. 2.9 four images are shown where at first the compactness is kept stable and the shape is increased from 0.5 to 0.9 (a & b), and then the shape is unchanged (0.1) and the compactness is increased from 0.1 to 0.9 (c & d). Figures 2.9 a) and b) illustrate that when the shape is increased, the objects lose their relation to the spectral information from the image as objects start to include different spectral surfaces (Fig 2.9b: arrows 2 & 3). A high degree of compactness on the other hand, increases the number of objects having a relatively strong dependence on spectral contrast. At the same time, objects become very frayed.

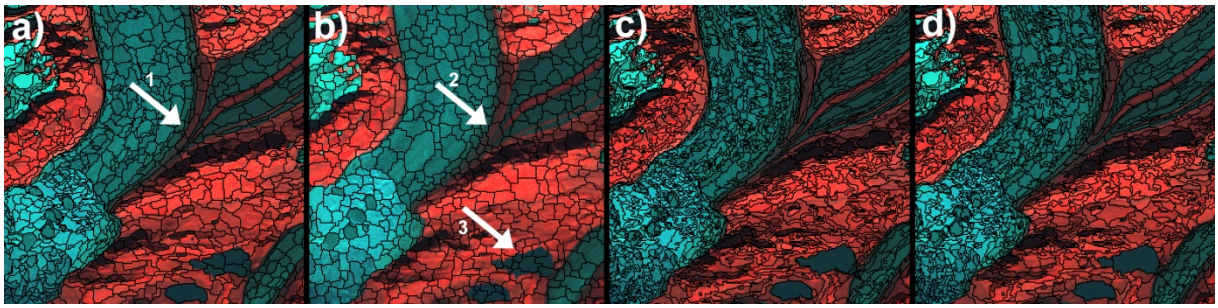

Figure 2.9: In a) objects with shape 0.5 and in b) objects with shape 0.9 are shown. Compactness is kept stable at 0.1 for a) and b). In c) shape is kept stable at 0.1and the compactness is increased from 0.1 to 0.9 in d). The arrows mark objects discussed in the text: arrow 1 shows appropriate objects for medial moraine, arrows 2 and 3: one object includes different surface types. Location: Watkins range-Greenland.

During the segmentation process it is possible to weight one or several input image layers. The higher the weight assigned to an image layer is, the more of its information will be used during the segmentation process. Figure 2.10 shows schematically how the weighting of different input bands influences the creation of objects. Those created with a scale value: 20, shape: 0.1, and compactness: 0.5 are visible in b), by only weighting the image bands GREEN, RED and NIR (weighting: 1). Figure 2.10c is the result when additionally including slope information (weighting: 3), and Fig. 2.10d considers slope and thermal information. From b) to c) to d) the number of objects decreases. However, Fig. 2.10b, includes problematic objects that sometimes do not represent ground features well (arrow 1). Including slope information leads to usable objects over a glacier surface, as distinct boundaries are obtainable along lateral moraines (arrow 2) and at the glacier terminus. The objects become even more distinct when the thermal channel is included (arrow 3), as the debris might be cooled by the ice underneath (Dobhal, 2011; Nakawo et al., 1993; Tangborn and Rana, 2000) d) and thus has a different temperature.

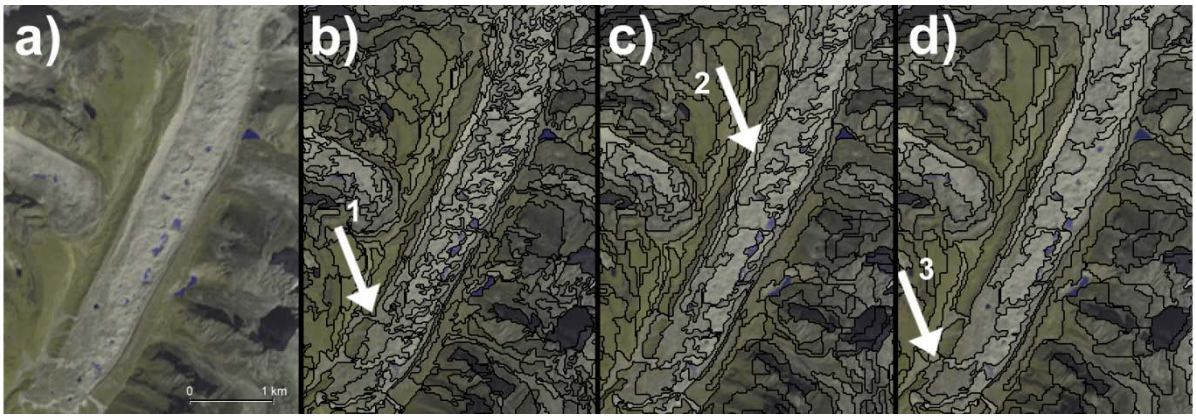

Figure 2.10: Segmentation example for the weighting of different input bands. In b) three image bands are used for the segmentation. In c) slope is included and in d) the temperature information. Including slope and temperature information enables the creation of appropriate objects for the segmentation. Location: Everest region - Himalaya.

Image classification: Image classification is based upon contiguous, homogeneous image regions (objects) generated by the initial image segmentation. For each object, class descriptions are calculated (spectral values, size, form, texture, neighbourhood, etc.) to determine whether an image object can be a member of a class or not. The classification is then carried out in two ways: a) by a nearest neighbour classifier or b) by fuzzy functions defined for selected features and calculated for each segment. During the classification each object is step-wise assigned to a class and the relations to other classes as formulated in the specific class descriptions are transferred to the image objects. The final outcome of the classification is a network of classified image objects

with their corresponding attributes (Baatz et al., 2005; Kressler et al., 2005; Trimble, 2011).

Post-processing: OBIA is a very useful environment for post-processing of classification results. Due to the fact that each object "knows" the objects surrounding it, simple rules can be developed allowing the automatic improvement of the classification result. For example, commission errors can be eliminated and omission errors assigned to the correct class. Several post-processing tools were tested in Paper II, revealing that best results were obtained by the creation of a simple loop and (shape) neighbourhood relationships. A detailed description of these tools is given in section 3.4.4.

2.3 Digital Elevation Models

A Digital Elevation Model (DEM) and also a Digital Terrain Model (DTM) is a digital representation of the Earth's surface, normally with elevation values (z coordinate) given for a regular grid (i.e. equidistant spacing of values in the x and y direction) (Mark, 1975) (other definitions of DEMs can be found in Burrough and McDonnell (1998) and in Li et al. (2005). While a DEM describes the "bare ground" of the Earth without vegetation or man-made structures a, Digital Surface Model (DSM), describes the "real surface" with all objects located on it such as buildings, cars, trees etc. Most of the time (and in this thesis), however, the term DEM is used generically for both DTM and (DSM). Both datasets together allow the calculation of a Normalized Digital Surface Model (NDSM), which is the difference between the two DTMs. A NDSM thus helps for example to extract the height of buildings or vegetation species (Notarnicola et al., 2009). DEMs are also a part of regional climate models (RCM) where they serve as reference altitude for the climate variables provided by the RCM itself. A DTM can represent the Earth's surface in two data formats: a triangular irregular network (TIN) or equally spaced raster datasets. Thereby, a TIN is a vector representation of the Earth's surface with the ability to provide a much higher point density in regions of complex or steep terrain than a raster DEM (Fowler and Little, 1979). On the other hand, raster DEMs are well suited for raster-based applications and thus easier to combine with other raster datasets such as satellite images (Wasklewicz et al., 2013; Yang et al., 2005) or RCM data (e.g. Machguth et al., 2009) (Figure 2.4).

2.3.1 DEM generation

Terrain elevation can be generated by a range of methods, each of which has its own advantages and disadvantages (e.g. price, spatial resolution, area coverage, accuracy) and thus its specific field of application. It can be created from photogrammetric or interferometric techniques, the interpolation of digitized contour lines from maps (Desmet, 1997; Racoviteanu et al., 2007), field measurements, or via GPS. The techniques for DEM generation related to this thesis are presented in the following.

One often applied approach for DEM creation is stereo imagery. Several satellite missions (e.g. ASTER and SPOT) acquire images from two different viewing positions (either along-track or across-track) which allow the generation of a stereo image pair (Bolch et al., 2008; Crespi et al., 2008; Jacobsen et al., 2008; Kääb et al., 2002; Kamp et al., 2005; Miller et al., 2009; Pieczonka et al., 2011). Specific software generates elevation values by stereo-correlation techniques (Hirano et al., 2003), from the shift of the corresponding pixels in the stereo pair (Colvocoresses, 1982; Fujisada and Ono, 1994; Toutin, 1995, 2004), showing the same area from at least two different viewing positions. The different viewing angles are either obtained by a different sensor position (across-track sensor) or from the same overflight with nadir- and back or forward looking sensors (along-track stereo). The latter is advantageous because of the short time lapse between the two acquisitions (e.g. one minute for ASTER) which can be used to track objects with rapid changes (Kääb and Prowse, 2011). Across-track sensors like SPOT-HRS can have repetition times of up to 26 days where conditions (snow accumulation, melt, glacier flow) might have

already changed. All optical stereo correlation techniques, however, suffer from the problem of artefacts and data voids, if contrast is low, as over homogeneous snow surfaces or in shadow (Frey and Paul, 2011; Kääb et al., 2002; Rastner et al., 2012).

Another way to create DEMs is based on active radar sensors. Their advantage in comparison to stereo image matching techniques with optical sensors is that they are independent of weather and illumination conditions. Microwaves have the ability to penetrate through clouds and work also during night. This is especially convenient in Polar Regions where for several months in the year polar night is prevails. In creating a DEM from SAR techniques, however, there is the problem of dielectric surface (ice and snow) conditions dependency (Gens and Genderen, 1996) as well as geometric constraints due to the side-looking characteristic of the sensor causing radar shadows, layover and foreshortening effects (Richards and Jia, 2006). The calculation of a DEM is performed using interfereometric techniques (Crosetto and Pérez Aragues, 2000; Li et al., 2013b; Nitti et al., 2013) using phase differences resulting from slightly different viewing angles. A prominent example of a DEM derived from InSAR is the SRTM DEM in a 90 m resolution from February 2000 (Farr et al., 2007; Jordan et al., 1996; Rabus et al., 2003) and the current TanDEM-X/TerraSAR-X mission (Krieger et al., 2007; Moreira et al., 2004).

The highest DEM accuracy and spatial resolution can be obtained using laser-scanning. These are opto-mechanical scanning assemblies which can be ground-borne, air-borne or space-borne. The primary products of data acquisition are coordinates (x, y, z) of single reflection points on the ground which have to be interpolated by inverse distance weighting (IDW) or kriging (KGG) into raster models to generate the secondary product, a high resolution DEM (Cressie, 1993). With spatial resolutions of less than 1 m they are also of high interest for glaciological studies (Geist et al., 2003; Joerg et al., 2012), partly because they allow generation of DEMs in low-contrast snow/firn and shadow areas where photogrammetric methods often fail (Favey et al., 1999; Janke, 2013).

2.3.2 DEM applications

DEMs are key for a wide range of applications. Several of them are related to this thesis and are briefly described in the following.

A key application of DEMs is the orthorectification of satellite imagery to correct the panoramic distortion resulting for terrain at some height h when seen from space under an angle alpha (Fig. 2.11). With a DEM providing elevation values, the pixels are shifted back to a position where each would be if seen from nadir by using a set of GCPs and a map projection/datum. The orthorectification process also transforms a satellite image into a map with euclidean distances (i.e. orthogonal projection) which allows it to be combined with all other geocoded datasets (Aguilar et al., 2013; Geosystems, 2013; Hidayat and Wiweka, 2013; Richards and Jia, 2006). Errors in the DEMs directly impact on the geometric accuracy of the satellite image. The satellite images used in this thesis (L1T product from USGS), however, are already orthorectified with a DEM (named GLS2000) and a global set of GCPs. The accuracy of the orthorectified product is available for each scene from the provided meta-information in tabular and visual form.

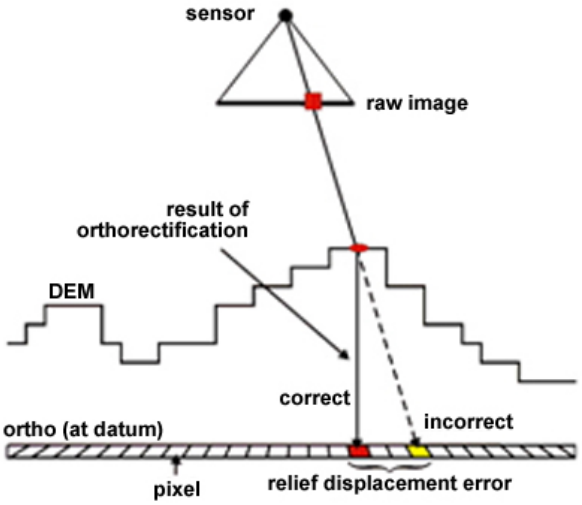

Figure 2.11: Orthorectification of imagery using a sensor geometry model and DEM. The use of a DEM enables the correct relocation (red pixel) of the wrong pixel (yellow pixel). (Hidayat and Wiweka, 2013).

Artificially illuminated DEMs result in a hillshade (Geosystems, 2013) that is extremely useful in quality assessment of the DEM (Van Den Eeckhaut et al., 2005; Janke, 2013). Hillshades allow comparison of the details visible in different DEMs (spatial resolution alone is often a poor indicator for this), recognise artefacts in a DEM (e.g. the presence of holes and bumps), and manual improvement of ice divides, lakes, and debris-covered glacier parts (Le Bris et al., 2011; Frey and Paul, 2011; Rastner et al., 2012) (see Fig. 3.1).

A large number of terrain parameters can be derived from a DEM (e.g. Florinsky, 1998). Of importance in regard to glaciers are minimum/mean/maximum and median elevation that can be directly obtained using a DEM, glacier outlines and zone statistics (Frey and Paul, 2011; Paul et al., 2002). Mean aspect is more difficult to obtain as it is a circular variable which requires to be decomposed aspect into a mean sine and mean cosine grid from which the mean aspect is derived (Paul et al., 2009b). Glacier hypsography (area-elevation distribution) can be derived from reclassifying a DEM in, for example, 100 m elevation bins. Slope is defined by a plane tangent to the surface at any point of the DEM and its value is the maximum rate of change in altitude (from 0 to 100% or 0 to 90°)(Geosystems, 2013). Finally the mean slope for a glacier can also be retrieved by zonal statistics.

A further important application is watershed analysis that helps by identifying drainage divides and thus to separate glacier complexes into individual glaciers. Thereby, geomorphometric properties of the terrain (routing of water) describe where these divides need to be. The most important set of morphometric characteristics consists of pits, peaks, channels, ridges, passes and planes (Fig. 2.12). Thereby the slope of the surface determines the morphometric feature. For example, a sloping surface that is concave in the cross-sectional direction is a channel whereas a sloping surface that is convex in the cross-sectional direction is a ridge. In such a case, the automatic creation of drainage basins is straight forward. The same is also true of passes (convex curvature and one concave curvature). Peaks (like icebergs) have a convex cross-section and convex longitudinal curvature while pits have concave curvatures. The derivation of drainage divides for a terrain with these morphological features is more complex. It gets even more problematical once regions with flat terrain are present. Morphometric features also influence the creation and definition of the ice caps rules in Paper I. Long ranging mountain flanks can be seen as ridges, ice caps as peaks and a confluent flow of ice is triggered by a channel, pass or pit (see section 3.3.3).

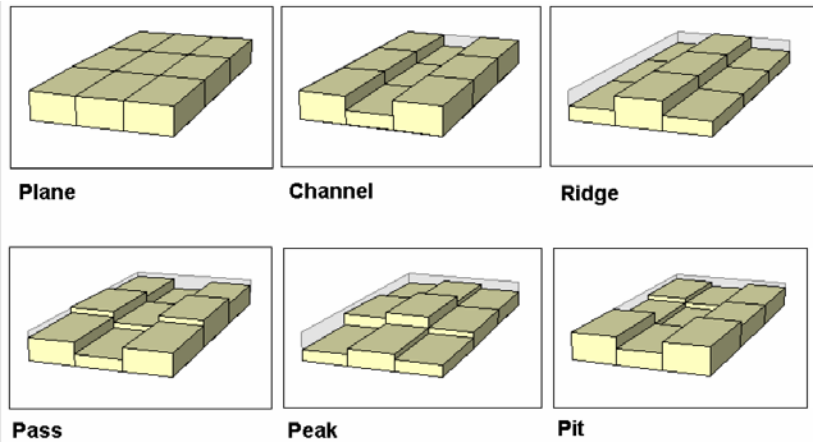

Figure 2.12: Six typical morphometric feature types extractable from a DEM (Wood, 1996). Planes are interesting for the mapping of debris on glaciers as debris accumulates only on flat part of the glacier. Channels and Ridges are interesting for the detection of lateral moraines and consequently also for the distinction of debris covered glacier parts versus other terrain.

Several algorithms are available for calculating drainage divides for glaciers (Bolch et al., 2010; Kienholz et al., 2013; Manley, 2008; Racoviteanu et al., 2009; Schiefer et al., 2008). The DEM quality is crucial in this processing step in particular for flat accumulation regions where small differences in elevation can strongly alter the location (Le Bris et al., 2011). For this reason a test was performed to analyze which of the DEMs available for Greenland are more appropriate (see comparison in ch. 3.1.2). The detailed description of the algorithm applied onto Greenland and its challenges is explained in section 3.3.3.

A DEM is also required to perform a slope correction for ICESat elevation point measurements (plane fitted repeat tracks) (Paper III). This method derives glacier elevation changes from a well-established regression technique that determines surface slope and average elevation change (dh/dt) for planar surfaces that are fitted to 700 m long segments of near-repeat tracks. The applicability is critically dependent on terrain slope, and too steep surface slopes degrade the ICESat performance (Moholdt et al., 2010; Sørensen et al., 2011).

Finally, DEMs are also useful for correcting elevation-dependent atmospheric parameters (e.g. temperature) when values refer to different elevations. Calculating the elevation difference and multiplying it by a lapse rate allows the correction of temperature data referring to different elevations (cf. section 3.6.3).

2.4 Climate models and climate data

Climate models are used to determine past or future climatic conditions from regional to global scales. In general, climatic conditions are determined against a reference or control run that provides statistical mean values of several atmospheric parameters for a control period (mostly the last 20-30 years). In other words, climate change is a statistical comparison of modelled mean values from two periods of about equal length. In the model, the Earth is divided into a three-dimensional grid where information on the respective parameters (e.g. temperature, precipitation, cloud cover) is provided at a high temporal resolution (e.g. every 6 hours). For the calculation of future climate scenarios, climate models are forced by emission scenarios of greenhouse gases, whereas for reconstruction of past climates so-called re-analysis data are used. Climate models have a wide range of spatial resolutions, vertical layers, and complexities. While Global Climate Models (GCMs) cover the entire globe at a rough resolution of 200-500 km (McGuffie and Henderson-Sellers, 2001), Regional Climate Models (RCMs) are applied on a regional scale at a much higher spatial resolution (see section 2.4.3).

2.4.1 Weather station data

Synoptic weather stations (WS) are standardized facilities equipped with instruments for measuring atmospheric conditions, for example temperature, barometric pressure, humidity, wind speed, wind direction, and precipitation in at 3-hour interval. The length of the time series varies significantly within and between stations, partly depending on the location and type of the station (Boas and Wang, 2011). The distribution of WS is biased to accessible regions and thus less dense towards higher altitudes (e.g. Auer et al., 2007). This is unfortunate for glaciological studies, as glaciers are mostly located in remote regions at high elevations. As WS only provide point measurements representing the local conditions, spatial extrapolation to other regions is a general challenge (e.g. Machguth et al., 2009). At a more regional to local scale, WS data are used for a number of other applications, for example the calculation of the surface-energy and mass balance of glaciers (e.g. Oerlemans, 2001) and the downscaling and validation of the climate model output.

2.4.2 Re-analysis data

Re-analysis data are spatially distributed gridded datasets of meteorological variables representing past climatic conditions. The datasets are created via data assimilation schemes which ingest all available observations from synoptic WS, satellites, radiosonde ascents, aircrafts, ships and buoys every 6-12 hours and spatially extrapolate them using an atmospheric model (Kalnay et al., 1996; Uppala et al., 2005). Well-known re-analysis data are the ERA-40 (covering a time span from 1958-2002 in 40 km resolution) (Uppala et al., 2005) the ERA-Interim (from 1 Jan 1979 until near present) from the European Centre for Medium-Range Weather Forecasts (ECMWF) (Dee et al., 2011), the Japanese Reanalysis (JRA-55) from 1958 to 2012 (Ebita et al., 2011; Onogi et al., 2007) and the NCEP/NCAR (1948 near present) (Kalnay et al., 1996; Saha et al., 2010). Re-analysis data are also available for variables that are difficult to measure, such as energy fluxes, evaporation and atmospheric water vapour. They are directly comparable to observations and have also been used in this thesis (Paper IV). Re-analysis data should not be seen as "reality" as the biases in the spatio-temporal coverage of the observations are still large and spatial variability of atmospheric conditions is high (Fig. 2.13) (Uppala et al., 2005). However, the datasets are steadily improved and extended, and provide a key input for large to global scale studies (e.g. Radić and Hock, 2011).

2.4.3 Regional Climate Models (RCMs)

RCMs are models providing climate information on a regional scale. Based on general physical laws, atmospheric conditions are calculated on a three-dimensional grid. RCMs were steadily improved in the last decades, not only regarding their spatial resolution but also by the inclusion of more explicit (i.e. less parameterized) models representing the key processes in all spheres (atmosphere, lithosphere, hydrosphere, cryosphere and biosphere) with their complex exchanges of mass and energy. The horizontal resolution is between 10-50 km, whereas the vertical resolution is unevenly distributed with more layers near the surface as at high altitude or in the deep ocean. RCMs thus provide a higher spatial resolution than GCMs and can better represent regional scale processes, but the model domain is restricted to a typically continent-size scale. This requires forcing the RCMs at their lateral boundaries with other gridded climate data, either using re-analysis data (for the past) or GCMs (for future scenarios).

All grid boxes in an RCM are coupled to each other, allowing energy and mass fluxes to be conservative and consistent throughout the model domain (Wang et al., 2004). The input forcing at the boundary of the RCM can cause artefacts in these regions (Giorgi and Mearns, 1999; Wang et al., 2004) and the region of interest should therefore always be in the centre of the domain (McGregor, 1997). It has also to be noted that RCMs inherit the errors of the input forcing

datasets. Currently three RCMs are available for the region of Greenland: the Modèle Atmosphérique Régional (MAR) (Fettweis, 2007), the HIRHAM model (Aðalgeirsdóttir et al., 2009) and the Regional Atmospheric Climate Model version 2.1 (RACMO2) (Van Meijgaard et al., 2008).

Climate variables derived from an RCM have to be adjusted to local conditions, in particular differences in the underlying topography (which is in general much lower and smoother in RCMs). While this is relatively easy for temperature (due to its strong dependence on altitude), it is very challenging for precipitation due to its high spatial variability (e.g. Schuler et al., 2008; Sevruk et al., 2009). The general way for adjusting temperature to local topography is the use of a lapse rate multiplied by the elevation difference (Glickman, 2000) (cf. section 3.6). In many studies a standard adiabatic lapse rate of 6° to 7 °C km^{-1} is used (Bassford et al., 2006; Otto-Bliesner, 2006; Raper and Braithwaite, 2006). However, the latter lapse rate can, on or close to glacier surfaces, differ substantially from this value (Hanna, 2005; Marshall et al., 2007). Moreover, atmospheric lapse rates vary on diurnal and seasonal time scales and exhibit a strong spatial-regional covariance (Gardner et al., 2009) as they depend on both the aspect of the slope and its location relative to valleys (Minder et al., 2010). After correcting the RCMs temperature value, it can be compared with observations from WS (Fig. 2.13). This latter step is also an important component of model evaluation (Evans et al., 2012; Kotlarski et al., 2010; Wang et al., 2004).

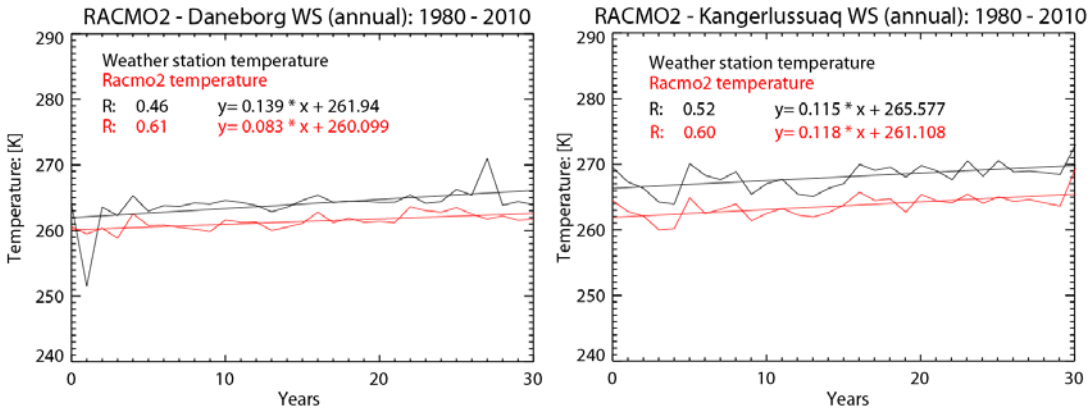

Figure 2.13: Re-analysis data (RACMO2) compared with Daneborg (north-east) and Kangerlussuaq (west-central) in-situ weather station data. RACMO2 reproduces well the temperature of the past (1980-2010), even if a small bias is visible between them.

2.5 Greenland

Greenland is the largest island in the world. It extends from 59°N to 83°N (2600 km) and from 11°W to 74°W (1200 km) covering 2.2 million km^2. The Atlantic Ocean borders Greenland's southeast, the Greenland Sea is to the east, the Arctic Ocean is to the north and Baffin Bay is to the west. Greenland is characterized by a huge ice sheet, which is covers about 80% of Greenland's surface. Its highest point is about 3200 m a.s.l. and its mean ice thickness is about 2000 m, exceeding locally 3000 m (Dahl-Jensen et al., 2009). But the ice sheet is not the only ice mass of Greenland – a large number of glaciers and ice caps can be found in the periphery (Weidick and Morris, 1998).

Greenland's climate is polar to sub-polar. Surface air temperatures in Greenland are dominated by the seasonal cycle because for several months of the year the most northern parts of Greenland have either polar night or continuous daylight. Consequently, mean summer air temperatures are in the northernmost part only 2 °C colder than in the south. In the winter

(September to May), however, mean temperatures in the north can decrease to around -36 °C whereas in the south to only -4 °C (see Paper IV). The temperatures are also strongly influenced by the ocean currents and sea-ice concentration, as inland temperatures in ice-free regions can be 5°C warmer than at the coast. Temperatures in Greenland have been monitored since the 1870s, showing a warming trend from 1885 to 1947 and from 1984 to 2001, predominantly on the western coast (Box, 2002). This warming trend locally exceeds 10 °C along the west coast during winter (Hanna et al., 2012) (Fig. 2.14). The year 2010 was the warmest year on record across Greenland (except for the northeast) since the start of meteorological observations (Tedesco et al., 2013).

Higher temperatures in the region have generally brought increased precipitation to Greenland (Fettweis et al., 2013). This was confirmed by Sørensen et al. (2011) who found a small increase in precipitation in the interior parts of the ice sheet by indirect measurements so that a part of the lost mass has been offset by increased snowfall (Abdalati et al., 2001; Thomas et al., 2008). However, an exact determination of such a trend is difficult due to the small number of weather stations available (Bales et al., 2009; Burgess et al., 2010). According to Ohmura and Reeh (1991), the lowest amounts of precipitations were found in the north-eastern interior (100 mm a^{-1}) and locally around Søndre Strømfjord on the western coast and Narssarssuaq in southern Greenland. The highest annual precipitation amounts occur south of 65° N on the western side (400 – 1000 mm a^{-1}) and south of 70° N on the eastern side (400 – 2500 mm a^{-1}) of Greenland. These amounts are caused by North Atlantic cyclones which often pass south of Greenland. Cyclones are also accompanied by strong winds which often blow directly toward the coast leading to precipitation due to topographic uplifting (e.g. Schuler et al., 2008). During periods with no cyclone activity, wind regimes are driven by local conditions such as the katabatic flow (Dahl-Jensen et al., 2009).

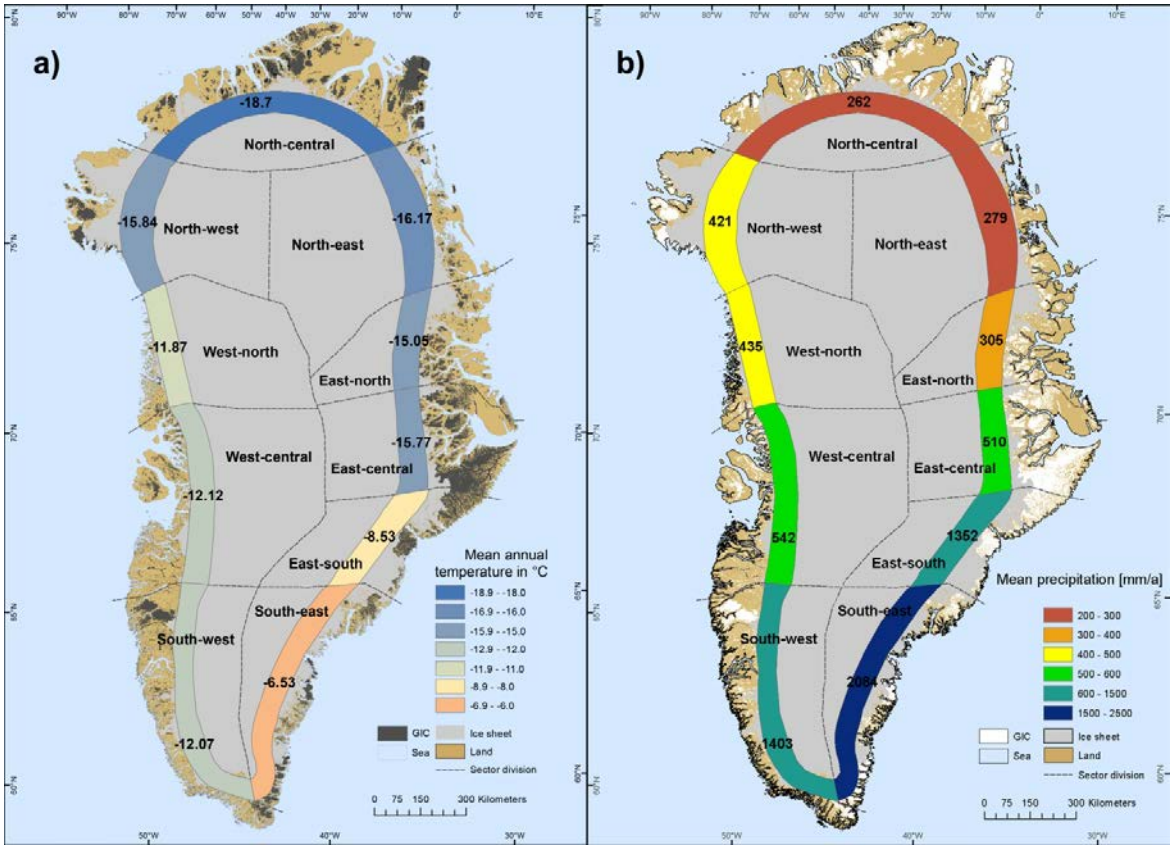

Figure 2.14: Mean annual temperature (left) in °C and precipitation sum in mm per sector (right) from 1980 – 2011 obtained by RACMO2.

2.5.1 Glaciers and ice caps of Greenland

The local glaciers and ice caps (GIC) in Greenland can easily be overlooked in the presence of the Greenland Ice Sheet (GrIS). Local GIC in Greenland occur not just in coastal regions away from the ice sheet, but also on mountain ridges within and adjacent to the ice sheet (Weidick and Morris, 1998). The definition of a local GIC is thereby not consistent. Local GIC can on the one hand merge with the outlet glaciers from the ice sheet in the ablation region, but they could also be well connected in the accumulation region only. Thus, the influence of the ice sheet on a local GIC from a dynamical point of view varies strongly. According to Weidick and Morries (1998) three types of local GIC can be identified: (1) independent from the GrIs, (2) as local fringing glaciers which merge with the GrIS, and (3) local glaciers within the ice sheet zone. Type 1 glaciers are considered as true local GIC whereas the other two are formed as a consequence of local thinning and deglaciation along the ice sheet margin. A first attempt to separate these local GIC from the ice sheet was presented by Weidick and Morris (1998), however, just in a rough graphical manner and not digitally. The resulting number and size of local GIC was therefore very uncertain.

Local GIC occur in all morphological types of the UNESCO primary classification and in all regions surrounding the GrIS. This includes ice fields, ice caps, outlet-, valley- and mountain glacier and glacierets (UNESCO, 1972) (see below for definitions). South and southwest Greenland (Fig. 2.15) has alpine terrain and constitutes many islands and cross-cutting fjords. A high amount of ice caps, valley glaciers and cirque glaciers exist in this region. Glacierized regions in southern West Greenland are the alpine region between Frederikshab Isblink and Godthabsfjorden, the high plateau region close to Kangamiut and the coastal region near the fjord Nordre Isortoq. In central West Greenland local GIC can be found on Disko Island, on Nuussuaq Peninsula, Upernavis and Svartenhuk Peninsula. Small ice caps, valley glaciers and cirque glaciers occur on the largest islands and peninsulas in Northwest Greenland, whereas in North Greenland many ice caps are present with a more alpine type of valley- and cirque glaciers in the northernmost area. The North-eastern coastal plains are mainly ice-free whereas in East Greenland this changes abruptly. Liverpool Land and Stauning Alper are characterized by abundant valley glaciers, cirques and small ice caps. Closer to the GrIS some larger ice caps are present which often merge with the outlet glaciers of the GrIS. Local GIC on the Geikie plateau are mainly located at its margin (Jiskoot and Juhlin, 2010; Jiskoot et al., 2012) often having a close connection with the GrIs in the accumulation region. In Southeast Greenland ice-filled valleys separated by mountain ridges with tributary cirque glaciers can be found in the Sermilik Fjord region. In Ammassalik island small ice caps and cirque glaciers dominate whereas further south intervening glacierized peninsulas and islands follow (Yde, 2011).

Due to the large latitudinal extent, different thermal regimes can be expected for the local GIC. Whereas in the north most GIC are cold, they are polythermal in the central part and in the south temperate GIC are also found (Bull, 1963; Hammer, 2001). Moreover, several surge type local GIC were identified in previous studies. Surge activity is characterized by some of the longest frontal advances ever recorded (about 10 km) and in some cases relatively long surge periodicities (at least 100 years) (Yde, 2011). Glaciers with surge-type characteristics can be found in the Stauning Alper and Geikie Plateau region (Jiskoot et al., 2003, 2012; Weidick, 1988) but also in the Disko/Nuussuaq region (Yde and Knudsen, 2005).

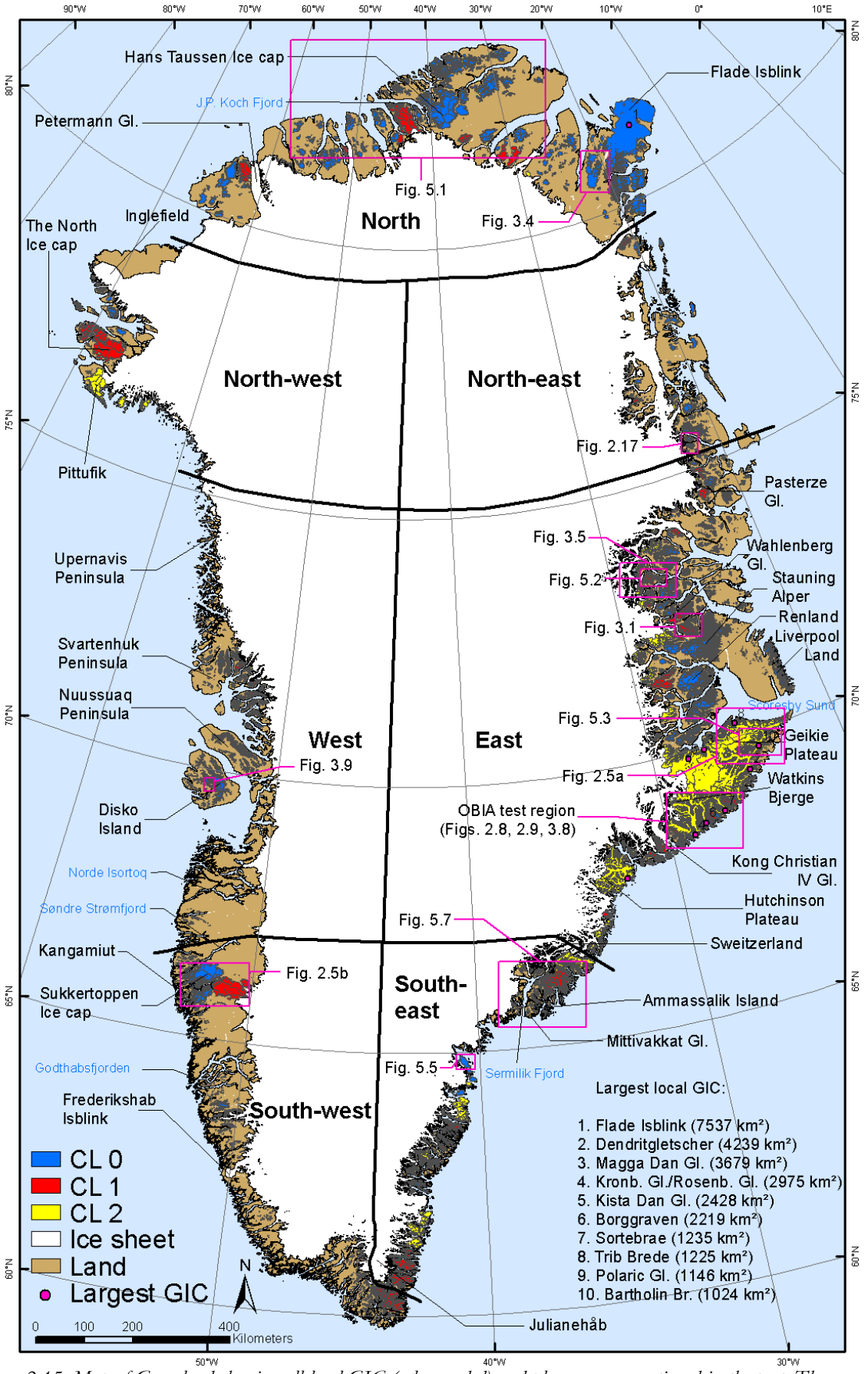

Figure 2.15: Map of Greenland showing all local GIC (colour coded) and place names mentioned in the text. The magenta boxes indicate the location of eight figures depicted in this thesis.

In Fig. 2.16 some examples of the local GIC in Greenland are shown. Fig 2.16 a) and b) illustrate two marine terminating glaciers with a clear medial moraine. Fig 2.16 a) as well as h) belongs to an outlet glacier of the ice sheet, whereas in b) a local glacier is depicted. In most cases as shown in b) these glaciers flow down a valley that is partly or completely filled with ice. Such glaciers have well-defined catchment areas so that a clear separation is feasible. Where the glacier meets the sea, a clear calving front has developed with large icebergs floating in the water in front of it. The shape of the latter glacier type and that of cirques is largely controlled by the terrain, whereas for ice caps and ice fields this is not necessarily the case because they cover the terrain completely. An ice cap (Fig. 2.16c & f) is defined as a dome-shaped ice body with radial flow covering topography, whereas an ice field is defined as a horizontal mass of ice insufficient to obscure the topography completely (Weidick et al., 1992). In many cases the ice caps have outlet glaciers flowing through dips to lower areas where the ice finally melts (Fig. 2.16d). Sometimes, if the terrain is flat enough below the ice cap, piedmont glaciers like the Elephant glacier shown in Fig 2.16d) develops. It has to be noted that it is sometimes difficult to discern between an ice cap and an ice field. For example the Flade Isblink is both an ice cap in the north and an ice field in the south. Figure 2.16e) shows a picture of mountain glaciers and glacierets from the Geikie Plateau in Eastern Greenland. Glacierets are small ice masses of indefinite shape in hollows or on protected slopes developed from snow drifting, avalanching or heavily accumulation in certain years with no marked flow patterns (Fig. 2.16 e & g). Such types of glaciers are the most widespread in Greenland. In detail, a clear distinction between mountain glaciers, glacierets and valley glaciers is often difficult (Weidick et al., 1992).

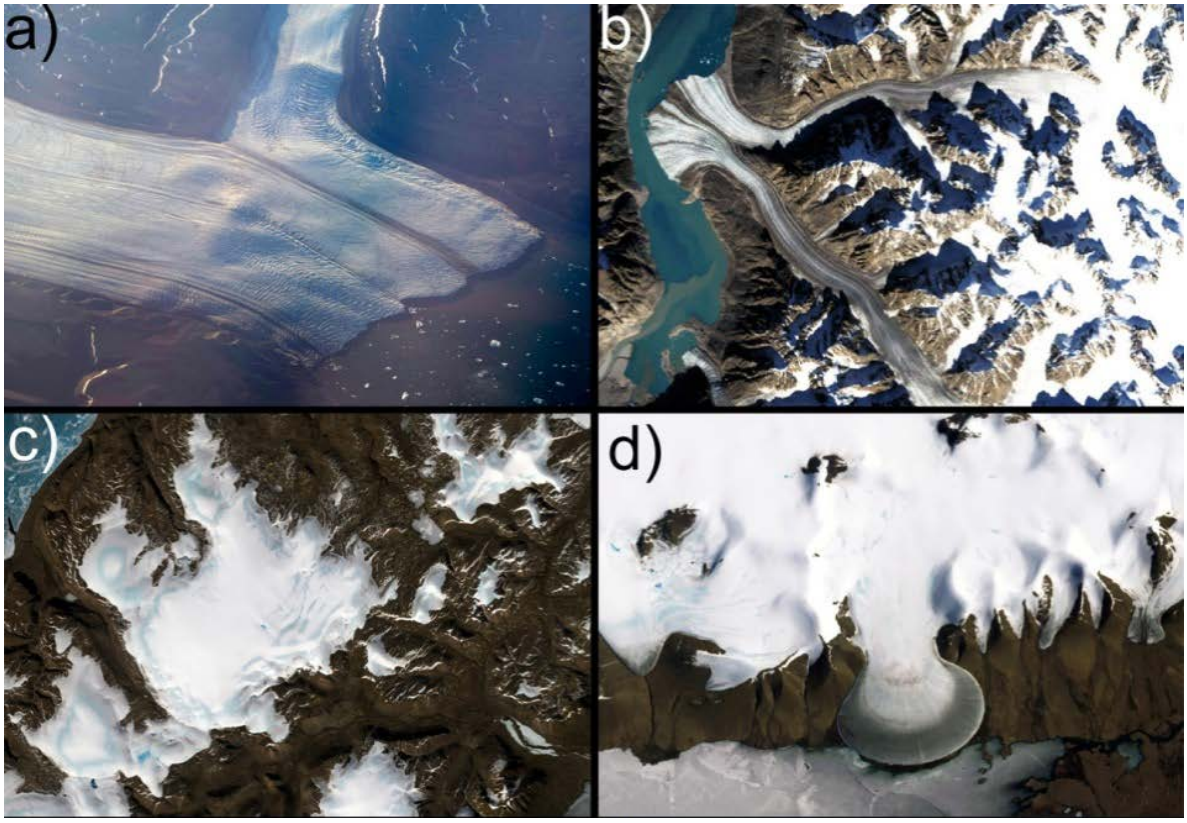

Figure 2.16. For figure caption see next page.

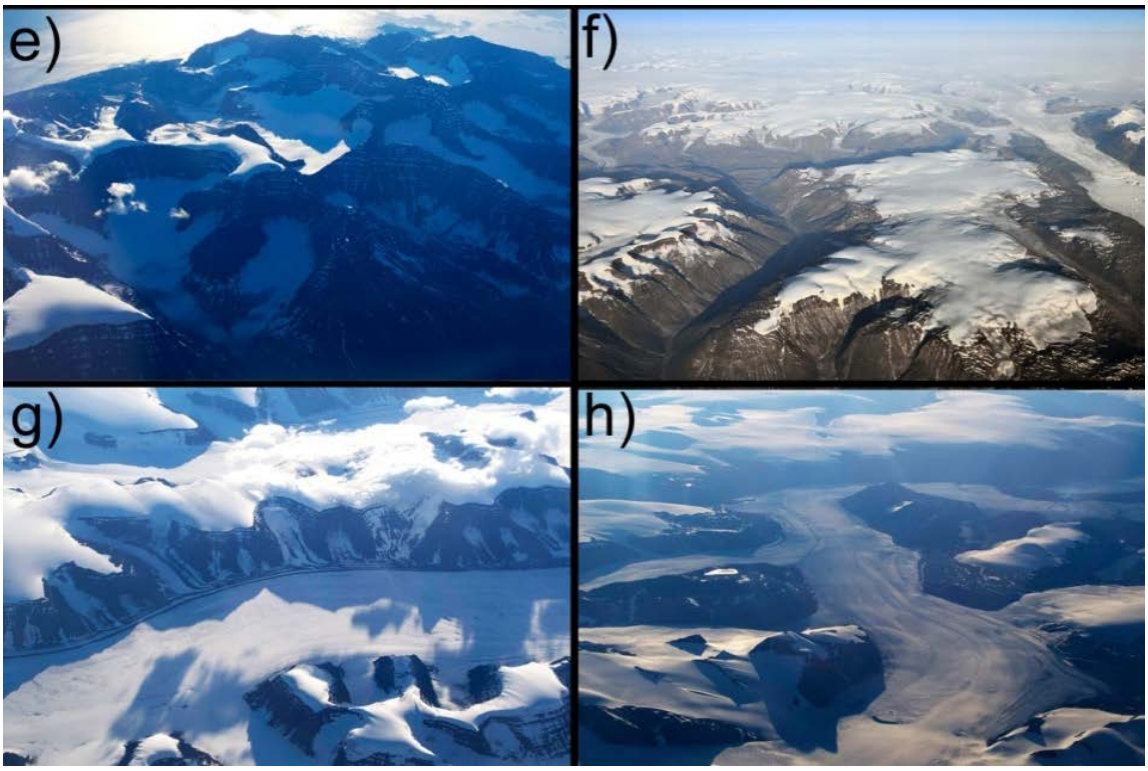

Figure 2.16: A few examples of Greenland's local GIC. Two outlet glaciers are represented in a) and b), ice caps in c) and f), circues and mountain glaciers in e). Elephant foot glacier is a piedmont glacier in d). The images g) and h) highlight the complex situation of local GIC versus the ice sheet. A, e, g, h are aerial photos by P. Rastner; f is taken by F. Paul; b, c, and d are Landsat images processed by T. Bolch.

2.5.2 Vector dataset for glaciers in Greenland

Details of the local GIC on Greenland were limited before the creation of the Greenland Glacier Inventory (GGI). Area estimation ranged from 48599 km² (Weng, 1995) to 49000 km² (Ohmura, 2009; Weidick and Morris, 1998) up to 76200 km² (Dowdeswell and Hambrey, 2002; Weidick and Morris, 1998) mainly due to differences in mapping accuracy, the scale and the variable consideration of GIC attached to the ice sheet.

The first detailed and large-scale inventory was performed by Weidick et al. (1992) for West Greenland with 5000 glaciers (14574 km²) being mapped. Other local inventories were created for the Geikie Plateau and Scoresby Sund region (Jiskoot et al., 2003, 2012) and for the Disko Island and the Nuussuaq – Svartenhuk peninsulas (Citterio et al., 2009). The two available Greenland-wide vector datasets of the total ice-covered area are the GIMP ice mask (Greenland Ice sheet Mapping Project dataset (available at: http://bprc.osu.edu/GDG /icemask.php) (Howat et al., 2014)and the rather coarse outlines from the Digital Chart of the World (DCW, Danko, 1992). The glacier outlines from the DCW are obtained from digitized 1:1000000 scale topographic maps (Danko, 1992) and are thus less accurate and don't include most of the smaller glaciers (Raup et al., 2000). The GIMP ice mask mostly excludes debris-covered glacier parts and includes ice shelves in the northernmost regions (more details on that in the next section). Another dataset, however, not available for scientific research, is the aerophotographic map of Greenland held by GEUS. It is the first high-resolution dataset of the Greenlandic ice masses from the mid 1980s. This dataset has potential for change assessment studies but it suffers from three restrictions due to a lack of suitable reference data for quality assessment: a) quality of ground control points for the orthorectification of the aerial photographs, b) inherent tracing of the ice margin by the stereoplotter operator, and c) operators, bias toward mapping, e.g. seasonal

snow is often mapped as glacierized area, or debris-covered ice as land (Citterio and Ahlstrøm, 2013).

Besides the vector dataset mentioned here, there is also the GGHYDRO raster dataset with 1 degree spatial resolution (Cogley, 2003) available for all of Greenland. This dataset is shown in Fig. 2.5 and described in section 2.1.5.

All datasets described above suffer from the fact that they do not separate the local GIC from the ice sheet or from each other, i.e. they only show continuous ice masses (or glacier complexes) without drainage divides. Moreover, datasets vary in their degree of generalization, temporal frame, and consideration of details (e.g. debris cover or ice shelves). A detailed comparison of all three datasets mentioned above is shown in Fig. 2.17 and listed in Table 2.2.

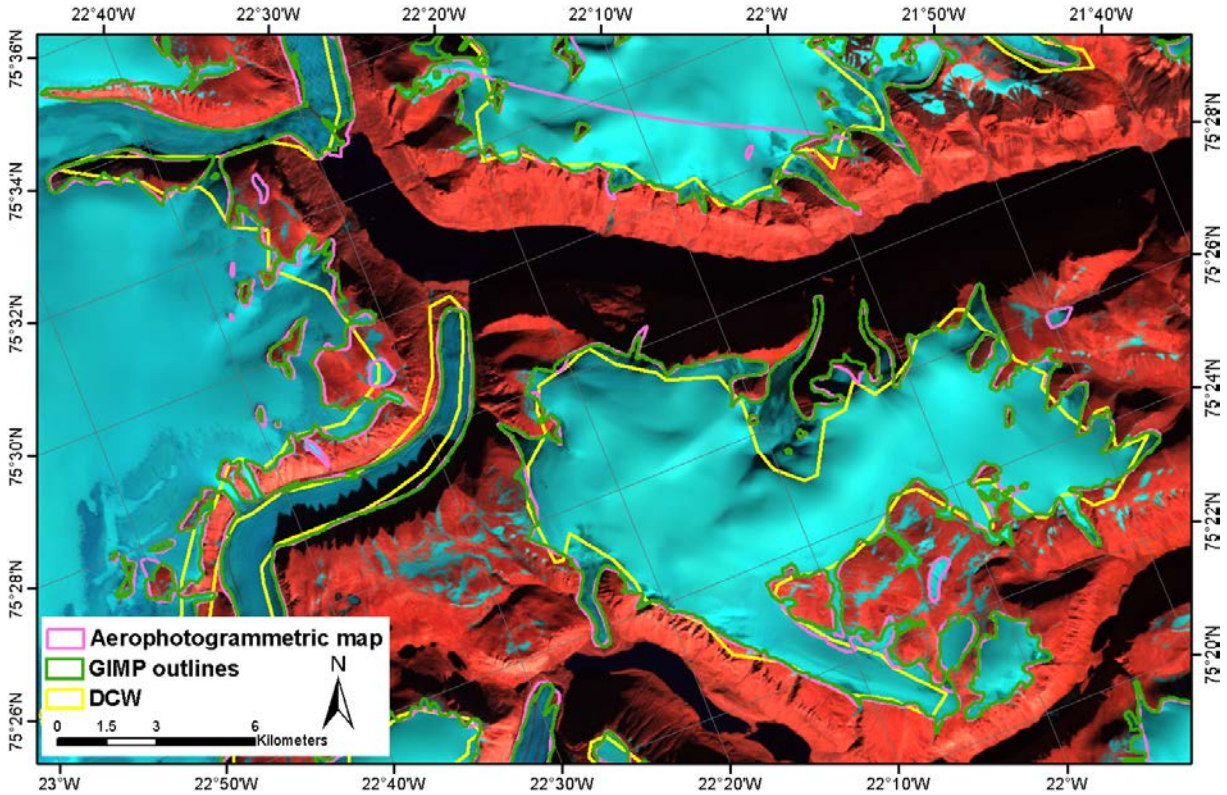

Figure 2.17: Overlaid glacier outlines from different datasets. The most accurate one is the GIMP ice mask. DCW outlines (yellow) are very rough. The aerophotogrammetric map (magenta) is more detailed, however sometimes also not mapped correctly (central top ice cap).

Table 2.2: Available vector data sets of local GIC on Greenland and their differences. The 'area covered (GIC)' row refers to connectivity levels CL0 (see section: 3.3.4). The entire dataset of this study includes the improved GIMP dataset (covering 14068 km²) in the northern-most part of Greenland.

	DCW	GIMP	Aerophotogrammetric map	GGI
Source	Maps 1:1000000	optical/radar	optical	Landsat+GIMP
Period	1950s-1980s	1999-2001	mid 1980	1999-2004
Generalization	high	none	none	none
Drainage divides	no	no	no	yes
Spatial resolution	approx. 2 km	15 m	0.5-1.5 km	30 m
Smallest unit mapped	0.1 km²	0.05 km²	0.01 km²	0.05 km²
Debris cover included?	yes	no	no	yes
Northern-most region incl.	yes	yes	yes	yes, (GIMP ice mask)
Availability	free	free	no	free
Area covered (GIC)	57715 km²	61610 km²	67143 ±1957 km²	65474 ±2029 km²
Area covered (total)	1825030 km²	1798960 km²	1804638 km²	1808575 km²

3 Methods applied to Greenland

This chapter describes the specific methods applied to Greenland in detail. At first, the input data are described (glacier outlines, DEMs and the climate model) and the division of Greenland into sectors is explained. The following four sections give further details on the methods applied for the individual research papers.

3.1 Data

3.1.1 Satellite imagery and data

All satellite data used in Paper I came from Landsat 7 ETM+ and Landsat 5 TM (73 scenes in total). Landsat scenes were downloaded at the already orthorectified format level 1T from the glovis.usgs.gov archive. Details of the sensors are provided in sections 2.2 and 2.2.1. Though each scene has a size of 185 x 185 km, it was required to mosaic scenes to get all GIC included. Mosaiking was also required for scenes that were partly covered by clouds or seasonal snow. The striping of ETM+ scenes after failure of the scan line corrector (SLC) in May 2003 also required combination of several scenes to cover one region completely. In consequence, the outlines of several glaciers and in particular of ice caps in the north of Greenland refer to different dates (years). The selected scenes strongly differ in acquisition date (time of year) and do thus have variable illumination conditions. These are compensated for by using scene-specific thresholds for glacier mapping.

The GIMP ice mask was used in Paper I. The mask is a raster binary land classification mask using 1 for glacier ice and 0 for all other terrain or water. The ice mask data is provided in a 15 m resolution and subdivided into 36 tiles (Howat et al., 2014).

MODIS satellite imagery was used for the region north of 81.2° N for visually crosschecking the GIMP ice mask (Paper I). For this purpose MODIS band 1 in 250 m spatial and 8-bit radiometric resolution (620–670 nm) with level 1A processing was applied.

The ASTER sensor was only used for the mapping of glaciers in Paper II. The increased spatial resolution in the VNIR (15 m) was a particular benefit for the identification of debris cover. All data had 8-bit radiometric resolution and level-1B processing.

3.1.2 DEMs and elevation data

The major DEM source of this thesis was the Greenland Mapping Project - Digital Elevation Model (GIMP DEM). The GIMP DEM has been compiled from different sources, mostly the SPOT SPIRIT DEM and the ASTER GDEM II. They are described in the following (cf. also Howat et al., 2014b) along with some other DEMs in more detail.

The ASTER GDEM II is a follow up dataset for the GDEM I released in October 2011 by NASA and Japan's Ministry of Economy, Trade and Industry (METI) (Hengl and Reuter, 2011; Li et al., 2013a). The GDEM mission is the most complete topographic mapping of the Earth's land surface ever made, covering the planet from 83° North to 83° South (~99% of its surface) and thus an interesting dataset for polar regions. The ASTER GDEM II was compiled

photogrammetrically by automated digital matching of stereo pairs from images acquired between 2000-2009 at a horizontal resolution of 30 m (ASTER GDEM Validation Team, 2009; Hayakawa et al., 2008). The root mean square error RMSE for the GDEM II is given as 8.68 meters, and the absolute vertical accuracy, expressed as a linear error at the 95% confidence level, is 17.01 meters (Tachikawa et al., 2011). The GDEM II benefits from the inclusion of 260000 additional scenes to improve coverage, a smaller correlation kernel (5x5) yielding higher quality, and improved water masking (Li et al., 2012). The DEM is since 2009 freely accessible and can be downloaded from the http://reverb.echo.nasa.gov/reverb/ and other websites.

The Satellite Pour l'Observation de la Terre (SPOT) SPIRIT DEM product was released during the International Polar Year (IPY) in 2009 (Bouillon et al., 2006). For the SPIRIT project, an archive of SPOT 5 HRS images was compiled from 2007 to 2009 over Polar Regions to produce DEMs. The reported absolute horizontal accuracy is 30 m, whereas the vertical one is between -5.5 and 3.5 m (compared to ICESat data) (Korona et al., 2009). The SPIRIT DEM has overall a good quality, although artefacts like bumps and holes were observed in flat accumulation areas. Unfortunately, not the whole of Greenland is covered by the SPIRIT DEM. It covers only patches around the ice sheet margin ranging from 75° N in the west and 72° N in the east southwards.

The GIMP DEM from the University of Ohio has a resolution of 90 m and a reported vertical accuracy of 10 m (Howat et al., 2014). It was merged from several datasets acquired between the years 2000 and 2009. The DEM is constructed from a combination of ASTER and SPOT-5 DEMs for the ice sheet periphery and margin (i.e. below the equilibrium line elevation) south of approximately 82.5°N. As high-resolution photogrammetric DEM extraction only provides accurate results in regions with good optical contrast and is therefore less accurate above the snowline, coarser resolution data (500 m Advanced Very High Resolution Radiometer, AVHRR) was used to improve an earlier 1 km DEM by photoclinometry (Scambos and Haran, 2002) for the ice sheet interior and far north. All tiles of the DEM are horizontally and vertically registered to average ICESat elevations for the 2003-2009 time period, and therefore the ice surfaces in the DEM have a nominal date of 2007. One drawback of the GIMP DEM is that the very far north of Greenland is not covered. Due to the fact that several GIC are present in this region another DEM (see next section) was used to cover this gap. The raw GIMP DEM can be freely downloaded from the GIMP website (http://bprc.osu.edu/GDG/gimpdem.php) in Geo Tiff format with ESPG 3413 projection above the WGS84 ellipsoid (Howat et al., 2014).

The viewfinder panorama – Greenland first edition - (VFP) DEM is created from 1:250000 and 1:500000 scale topographic maps with locally variable quality for the whole of Greenland. The spatial resolution of this DEM is 3" (~ 90 m), however, the topographic resolution is lower in most areas. The accuracy in mountain areas is in general good, but poor in areas with low relief. Substantial errors can be found on coastal ice caps and some local horizontal displacements are present in the west (Ferranti, 2009). This DEM is available for free download from: http://www.viewfinderpanoramas.org/dem3/GL-ReadMe.html.

Also RCMs have a DEM integrated to define elevations of the land surface. The RACMO2 DEM (see next section for details on RACMO2 RCM) has a resolution of 11 km although it is derived from data with 1 km resolution. This original DEM was compiled above the ice sheet from ERS-1 and Geosat radar altimetry. Where gaps in the satellite coverage existed, stereophotogrammetric datasets, synthetic aperture radar interferometry and digitized cartographic maps have been considered. The mean accuracy above the ice sheet is -0.33 ±6.97 m whereas over bare rock areas the accuracy ranges from 20 to 200 m (Bamber et al., 2001). Due to the resampling from 1 to 11 km the original DEM is considerably smoothed and flattened, resulting in much lower elevations in the RACMO2 DEM than in the 1 km version. Accordingly, elevation-dependent variables such as temperature require correction.

Surface elevation change data as used in Paper III (Bolch et al., 2013) are derived from the ICESat GLA12 product (release 531) acquired from October 2003 to March 2008 (downloadable from NSIDC). The laser system has footprints of about 70 m and a sampling frequency of about 170 m along track (Zwally et al., 2002), i.e. the data are spatially limited to profiles of points rather than a continuous DEM (Schutz et al., 2005). The tracks are separated horizontally by ~30 km in southern and ~10 km in northern Greenland. The GLA12 product is a level-2 altimetry product which provides geolocation and time-tagged surface elevation estimates with respect to the Topex/POSEIDON reference ellipsoid (Sørensen et al., 2011). ICESat has a 91 day repeat cycle (release 31) and achieves a single shot elevation accuracy of 0.15 m over gentle sloping terrain. Performance degrades over sloping terrain and under conditions favourable to atmospheric forward scattering and detector saturation (Moholdt et al., 2010). The fact that the ICESat measurements are not exactly repeated complicates the methods for deriving surface elevation changes and a wide range of methods for spatial averaging of the parallel tracks has been developed (Moholdt et al., 2010).

In Fig. 3.1 and in Table 3.1 a comparison of the DEMs discussed above is shown for a region in the north of the Stauning Alper. Prior to calculation of hillshades, all DEMs were reprojected but not resampled to a common spatial resolution. The GIMP DEM (a) reveals good quality in accumulation regions, but data gaps are present in steep north-facing slopes. The viewfinder DEM (b) has no data voids, but the surface is strongly smoothed so that details like lateral moraines are not traceable (right arrow in Fig. 3.4b). The SPIRIT DEM (c) has elsewhere a probably better quality than shown in this example. It lies on the margin of the SPIRIT DEM and has massive artefacts at the borders (arrow 5 and 6), whereas towards the inner part of the DEM the quality is better. The ASTER GDEM II (d) is in general of good quality showing many details. However, in accumulation regions of glaciers or surfaces with low contrast, large artefacts are apparent. In consequence, all calculations (drainage divides, topographic parameters) were performed with the GIMP DEM.

Table 3.1: Available elevation data for Greenland

DEM	Type	Resolution	Date	Sources
ASTER GDEM II	Optical	30 m	2000-2009	http://reverb.echo.nasa.gov
SPOT Spirit	Optical	40 m	2007-2009	http://sirius.spotimage.com
GIMP DEM	InSAR & Optical	90/30 m	2000-2009	http://bprc.osu.edu/GDG/gimpdem.php
Viewfinder DEM	Map based	30 m	-	http://www.viewfinderpanoramas.org
RACMO2 DEM	InSAR, Optical & Map based	11 km	1991-2000	RACMO2 RCM (internal)
ICESat	Laser altimetry	Point measurements	2003-2009	http://reverb.echo.nasa.gov

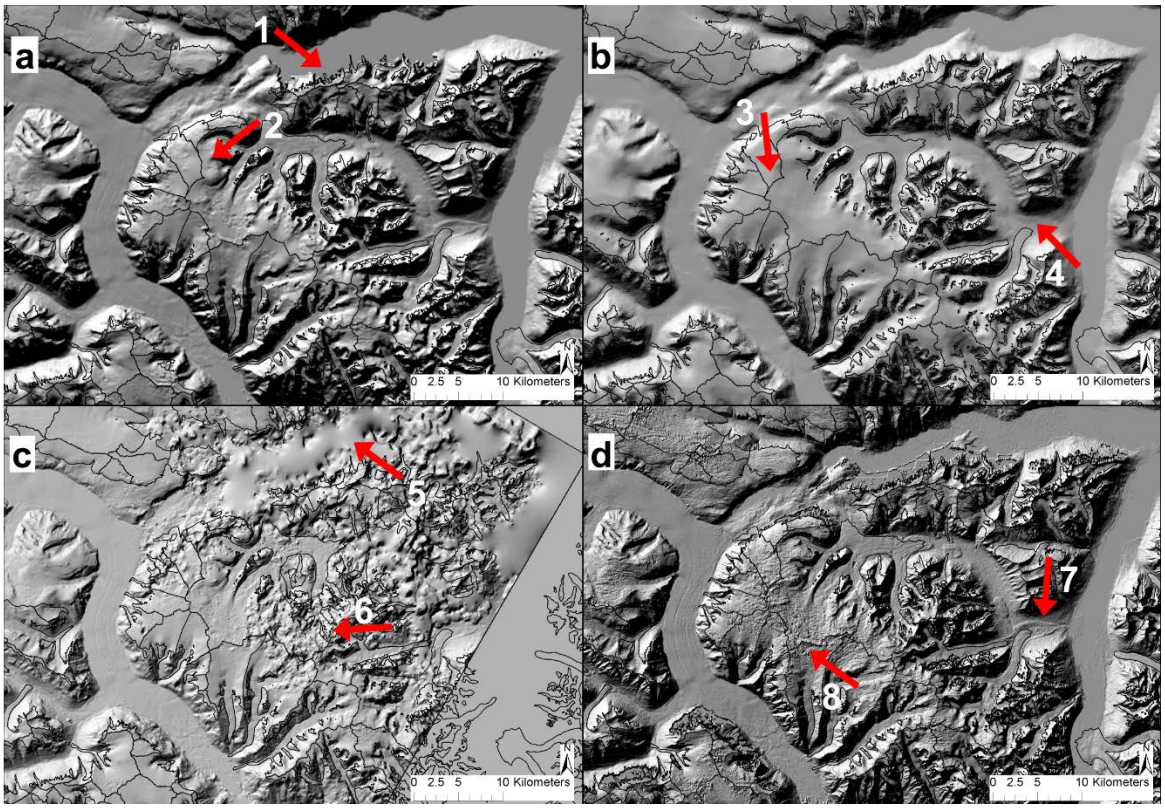

Figure 3.1: Comparison of hillshades for four different DEMs in the Stauning Alper region. In a) the GIMP DEM in 90 m res., in b) the viewfinder in 90 m res, in c) the SPOT SPIRIT in 40 m res and in d) the ASTER GDEMII in 30 m res. is depicted. Arrows indicate particular features explained in the text.

3.1.3 RACMO2 - regional climate model

The RACMO2 RCM produced by the Royal Netherlands Meteorological Institute (KNMI) is currently one of the best regional climate models for Greenland. The RACMO2 RCM was also used in Paper IV to retrieve spatially distributed information about temperature and precipitation in Greenland. RACMO2 consists of two numerical weather prediction models: a) the High Resolution Limited Area Model (HIRLAM) which the atmospheric dynamics originate from, and b) the European Centre for Medium-Range Weather Forecasts (ECMWF) model which the physical processes are derived from.

Over the last decade, RACMO2 has been further adjusted to realistically simulate ice sheet surface mass balance by implementing a multilayer snow model (Ettema et al., 2010), a drifting snow scheme (Lenaerts et al., 2010) and a physical albedo scheme (Kuipers Munneke et al., 2011). Moreover, it has been used as input for the total mass budget of the GrIS (van den Broeke et al., 2009), to describe the momentum budget of the katabatic atmospheric boundary layer (van Angelen et al., 2011). The model is forced every 6 h at the lateral boundaries and at the sea surface by ECMWF ERA-interim re-analysis (Simmons et al., 2007). RACMO2 has 40 vertical atmospheric hybrid-levels, of which the lowest is about 10 m above the surface. Hybrid levels follow the topography close to the surface and pressure levels at higher altitudes. The model domain of RACMO2 encompasses Greenland and its surrounding seas, including the Canadian Arctic Archipelago, Iceland and Svalbard. The domain includes 312×256 model grid points at a horizontal resolution of about 11 km. For accurate topographic representation of the GrIS, elevation data and an ice mask from the DEM of Bamber et al. (2001) are used. The underlying vegetation map is based on the ECOCLIMAP dataset (Masson et al., 2003) and has been manually corrected, because the original dataset had too little tundra and too much bare soil along the east coast of Greenland (Ettema et al., 2010).

A source of uncertainty regarding the analysis in Paper IV is that RACMO2 has been developed for the GrIS rather than for the local GIC surrounding it. A study performed by Ettema et al. (2010) revealed a high correlation between observations of temperature and values modelled with RACMO2 (R= 0.97). An average bias of -0.8 °C was found in that study for the ice sheet and deviations of more than 4°C could be found along the coastline. The largest model bias of -9.8°C is found for the DMI station Timmiarmiut, located in the south-eastern sector. The temperature bias can, according to the study of Ettema et al. (2010), also be attributed to land surface type as persistent warm/cold bias is found over the ice sheet/tundra of 0.9°C / -1.5°C, respectively.

3.1.4 In-situ weather station data

The Danish Meteorological Institute (DMI) maintains a network of Greenlandic weather stations. To validate/quality check the RACMO2 temperature data, 25 long-term (covering at least more than 20 years) coastal synoptic weather stations from all around Greenland were selected. Overall, 23 out of 25 coastal stations used for calibration are all located within 126 m of sea level and are typically surrounded by rough topography. Precipitation data have not been validated as large uncertainties in the measurements are univocal (Sevruk et al., 2009). Unfortunately, most stations are located in the more populated southern, coastal Greenland and only two (Dye 1 and Renland) were available for mountainous regions with short time measurement periods (9 years and 1 year, respectively).

3.2 Greenland sectors

To provide a more regionalized assessment in Papers I, III and IV, Greenland was divided into sectors (Fig. 3.2). The sectors are created large enough to represent regional-scale patterns as one mountain range alone would not provide this information.

A similar glaciological division was made by Weidick et al. (1995) from the Geological Survey of Greenland (GEUS) and consists of three main units: West, North, and East Greenland. Each of these three divisions follows ice sheet divides with diverse flow directions and an ice-free coastal strip. For Paper I four additional sectors were defined (in total seven). The northern zone from Weidick et al (1995) was additionally divided into three zones and the southern zone into two (see Fig. 3.2, green line). For this subdivision, sectors defined by Rignot and Mouginot (2012) from ice velocity mapping, were partly considered. This was necessary to catch the statistical patterns of the local GIC for the particular regions of Greenland (Paper I).

For Papers III and IV, ten sectors were defined to derive a differentiated picture of the regional volume/mass changes and glacier-climate sensitivities (Fig. 3.2, brown line). Five regions were assigned to the east side, four to the western side and one region to the most northern tip of Greenland. Meaningful sectors in latitude direction are crucial, as the influence of temperature and precipitation on the local GIC is strong.

Sector division lines were adjusted manually at Greenland's margin. It was important to avoid a cut through a glacier polygon. In the end, two polygon shapefiles with seven/ten sectors were created to allow spatial queries and sector-averaged calculations in a GIS environment.

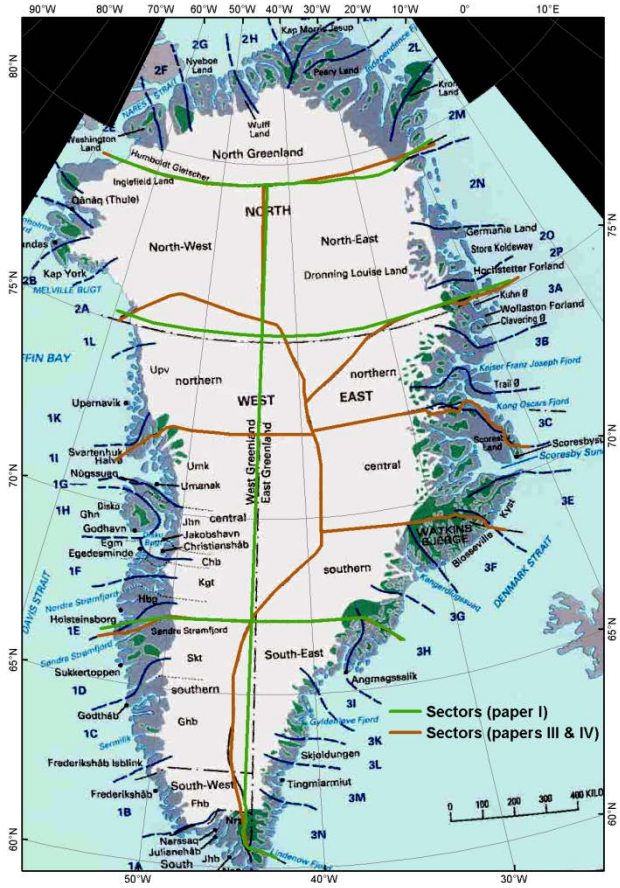

Figure 3.2: Sector divisions for Paper I (green) and Paper III and IV (brown) overlaid with the zones proposed by (Weidick et al., 1995). Inner ice sheet divisions have no influence on the result obtained in this thesis; therefore they are only shown for graphical reasons.

3.3 Compiling the glacier inventory for Greenland

The methods for the mapping of the GIC on Greenland are based on robust and widely tested algorithms (e.g. Paul et al., 2013b). Nevertheless, the GGI is particular, as it introduces ice cap rules (which basically define if an ice cap can be separated into entities or not) and connectivity levels (CL), which are assigned to the local GIC according to their ice sheet connectivity. In order to achieve this, it was necessary to develop rule sets which are on the one hand clear and easy to understand and on the other hand automatically applicable. In this section the steps required to produce the GGI are summarized (see Fig. 3.3) and extended for processing steps that are not described in detail in the paper itself. A comprehensive overview regarding the compilation of glacier inventories is also given in Paul et al. (2009b) and Racoviteanu et al. (2009).

3.3.1 Preprocessing and mapping

Creating a glacier inventory requires satellite imagery and DEMs as baseline datasets. The selection of the appropriate satellite scenes with as little cloud coverage as possible and scenes acquired at the end of the ablation season with as little seasonal snow around the glaciers as possible is of the highest importance. The latter is important because seasonal snow fields can easily be confused with small glaciers and thus introduce errors. Seasonal snow was a severe problem in the north-eastern part of Greenland and consequently several SLC-off scenes from the years 2003 to 2008 with much better snow conditions were mosaiked/filled to get an

appropriate coverage. In the mosaicking process all available images are stitched together so that one large, cohesive image without the scan line corrector errors can be created. Cloud coverage impedes the mapping of glaciers with optical satellite imagery. In maritime regions like the South-east of Greenland it was sometimes difficult to find cloud-free images, which required merging of several scenes to cover a region. In other regions of Greenland clouds were not a major problem.

The mapping was performed on each single Landsat scene in its original UTM WGS-84 projection and using the robust band ratio method with TM3/TM5 to map clean ice and snow (cf. 2.2.2). Problematic in this context was the missing coverage of Landsat north of 80° N. For this region, the GIMP ice cover map (Howat et al., 2014) was used instead and locally improved by visual interpretation of a MODIS 250 m image. As a final step the raw-mapping results were converted into a binary image to convert them into a vector file format (shapefile) to facilitate further processing (manual correction).

Elevation data was derived from the GIMP DEM. The GIMP DEM is broken into 36 tiles with a polar stereographic projection and WGS-84 datum. Hence the 36 tiles were mosaiked together and afterwards reprojected into the Greenland Lambert Azimuthal Equal Area projection with D WGS 1984 datum in order to have an area preserving projection. Unfortunately, the extreme north of Greenland is not covered by the GIMP DEM. Therefore a viewfinder panorama supplement tile "Gl-north" was downloaded. The tiles were mosaiked, reprojected into the Greenland Lambert Azimuthal Equal Area projection with D WGS 1984 datum for the final merging with the GIMP DEM (hereafter referred to as *extended* GIMP DEM). The usage of the GIMP DEM also increased the calculation speed for the creation of drainage divides over large regions.

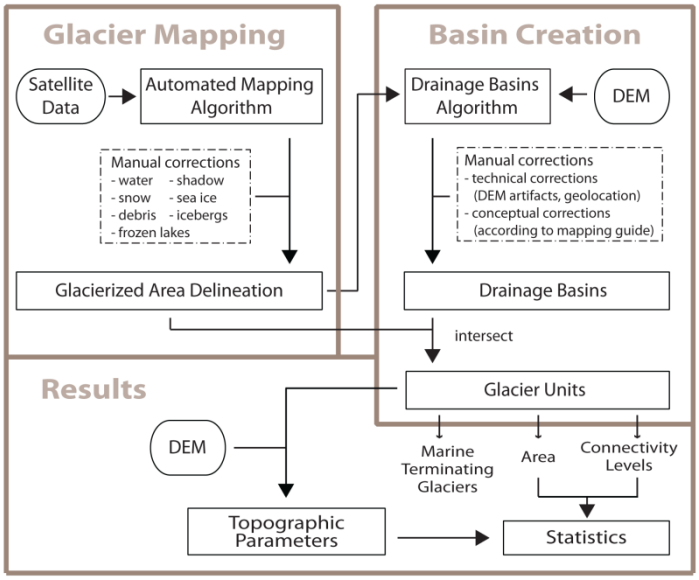

Figure 3.3: Processing steps flow chart for the GGI.

3.3.2 Manual correction

The manual correction of glacier outlines is a crucial step (cf. 2.2.2) where inaccuracies in glacier classification from automatic mapping are corrected. Approximately 80% of the total processing time was spent on the manual correction of glacier outlines of the GGI. Special FCC images in the background of a GIS were used to correct commission and omission errors. Omission errors due to cast shadows in rough topography, lakes, or debris on glaciers had to be included in the class glacier, and commission errors like lakes in the glacier forefield and sea ice, icebergs, perennial snow, were excluded. Multitemporal satellite scenes from different seasons and Google

Earth images helped in the detection of seasonal snow. Hillshades improved the identification of frozen lakes which appear in shaded reliefs as flat and smooth.

3.3.3 Creation of drainage basins

After the manual correction of glacier outlines, drainage basins were obtained from the *extended* GIMP DEM according to the method of (Bolch et al., 2010). This is needed to separate the glacier polygons into single glacier entities so that glacier-specific parameters can be calculated (Racoviteanu et al., 2009) as well as for the assignment of connectivity levels (c.f. 3.3.4). The approach of Bolch et al. (2010) is based on flowshed analysis of a DEM in a GIS. It creates a buffer around the corrected glacier outlines, clips the DEM with this buffer and calculates the basins with hydrologic tools. The method is probably faster than completely manual delineation. However, also here manual editing in a post-processing step is necessary, in particular for ice caps and glaciers close to the sea margin (Fig. 5.4). Manual correction was performed by the utilization of a flow direction grid and by the visualization of hillshades/contour lines or satellite imagery in the background. Moreover, to serve the requirements of the different scientific communities, GIC separation rules have been developed which describe whether an ice cap can be separated into entities or not. This is an important consideration as different research communities are interested in different masks. For instance glaciologists are interested in single glaciers and whole ice caps whereas hydrologists prefer to work with glacier polygons separated by drainage divides (Racoviteanu et al., 2009). According to these rules, an ice cap should only be divided into glacier entities if prominent outlet glaciers and some topographical variability are present in the accumulation area. Secondly, if one outlet glacier of an ice cap is separated, the rest of the ice cap also has to be divided into entities. And thirdly, the smallest number of glaciers for large glacierized mountain flanks and ice caps should be applied (Rastner et al., 2012). Based on our set of rules, some ice caps of the GGI are separated while others are not (Fig. 3.4).

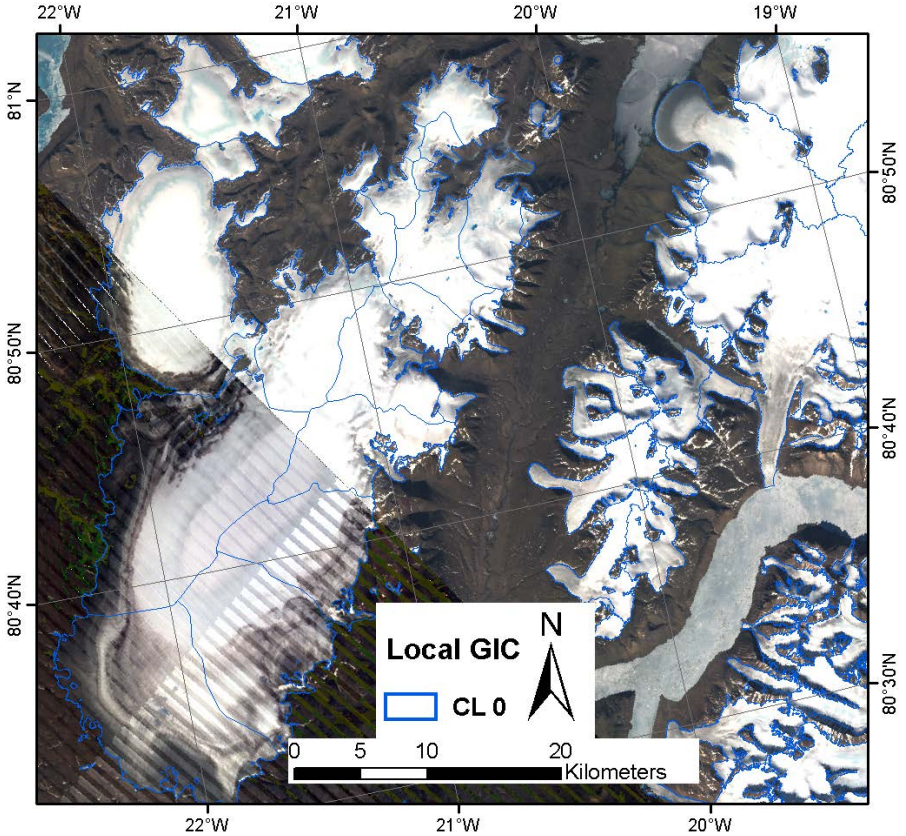

Figure 3.4: Separation of ice caps into glacier entities and from each other. The ice cap upper left has no distinct outlet glaciers and thus is not separated. The large ice cap lower left is separated as two distinct outlet glaciers are present. It is also separated by confluent flow from the ice cap in the north.

3.3.4 Assignment of connectivity levels

A challenging issue in the compilation of the GGI was to define a consistent strategy for separating the GIC from the ice sheet, as the local GIC occur not just in coastal regions away from the ice sheet, but also on mountain ridges within and adjacent to the ice sheet (Weidick and Morris, 1998). Considering the varying requirements of the different scientific communities (e.g. sea-level change or hydrological and glaciological modelling), a classification method had to be found which clearly separates the local GIC from the ice sheet and which can be automated to a high degree and thus consistently applied. This distinction is also required to avoid double counting of their contribution to sea-level rise, as the normally used masks for the GrIS also include (at least partly) local GIC (Paul, 2011).

The development of a consistent strategy was tedious. At conferences, meetings and workshops colleagues were asked to give feedback on the proposed connectivity rules, with the primary result that it is easier to make suggestions based on a selection of possibilities. So we created a set of rules based on already existing deliberations of Weidick and Morris (1998) and considering the different wishes of ice sheet and glacier modellers, and presented them at conferences and workshops. It was finally decided stick to three set of rules: a) ice cap rules (see section 3.3.3), b) specific rules for GIC separation, and c) a topographical heritage rule. This helped to keep the assignment as simple and transparent as possible.

Based on the above mentioned considerations, three connectivity levels (CL) of the GIC with the ice sheet were finally defined. Connectivity level 0 is for GIC's with no connection to the ice sheet, CL1 defines glaciers with a weak connection (clearly separable by drainage divides in the accumulation region, not connected, or only in contact in the ablation region), and CL2 GIC have a strong connection (difficult to separate in the accumulation region and/or confluent flow in the ablation region) to the ice sheet. A visual example of how glaciers were classified is shown in Fig. 3.5.

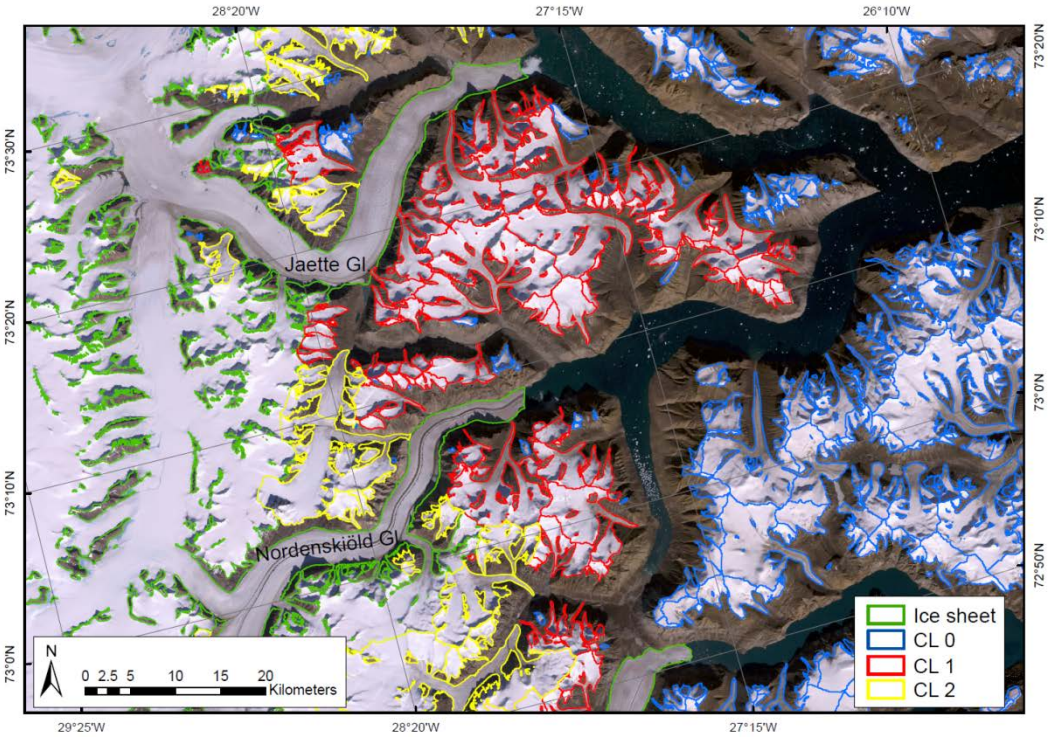

Figure 3.5: Visual example of the assigned CL to the local GIC around Greenland. Glaciers with blue outlines have no connection to the ice sheet, glaciers with red outlines have a moderate connection and glaciers with yellow outlines have strong connection to the ice sheet.

The assignment of connectivity levels was performed largely automatically within a GIS. The process started from the polygons of contiguous ice masses (or glacier complexes) and was based on neighbourhood rules (see flow chart in Fig. 3.6).

At first, the highly discussed regions were analysed. By their common characteristics of connection to the ice sheet they were manually defined as CL2 (CL2_Poly). In order to define CL0, the ice sheet polygon was merged with all connected glacier entities surrounding it. This resulted in one large independent polygon. In a further step, the CL0 attribute information was assigned to all polygons which were not merged, Finally, all glaciers without a CL assignment were classified as CL1.

To ensure a high quality and consistency of the assigned CL, they were finally manually cross checked. Doubtful cases were marked and discussed by all authors of Paper I to finally assign it to one of the connectivity levels.

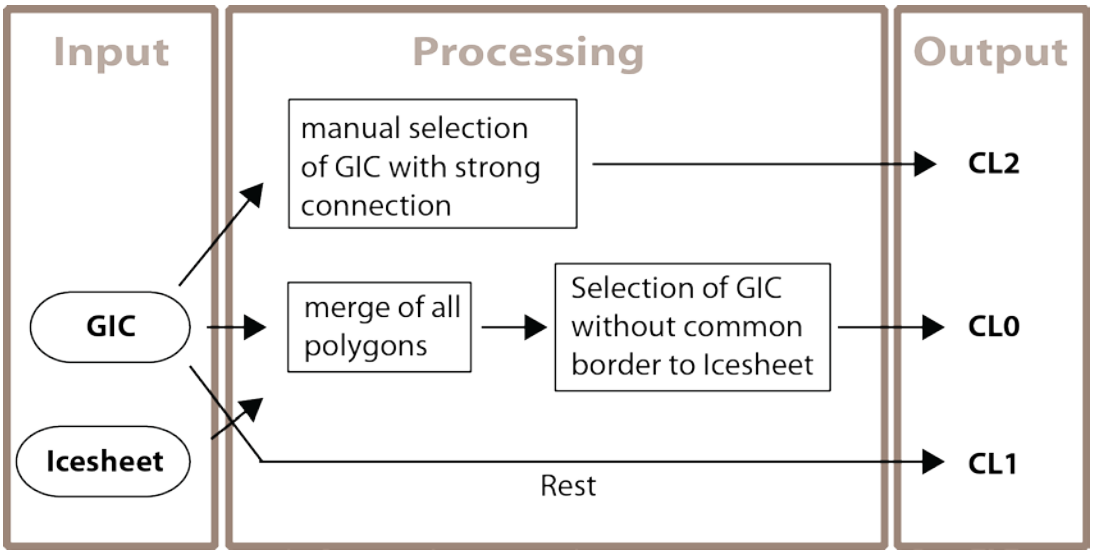

Figure 3.6: Flow chart illustrating the processing steps for the assignment of connectivity levels to glacier entities.

3.3.5 Inventory statistics

After glacier mapping and correction, the creation of drainage divides and the allocation of connectivity levels, glacier specific topographic parameters were calculated using the *extended* GIMP DEM and the seven regions defined in section 3.2 (cf. Fig. 3.2). Based on zonal statistic tools from the GIS software, the size distribution by aspect, the area-elevation distribution and the median altitude of all glaciers were calculated. In addition, nine plots were created where the number of glaciers and glacier-covered area per size class and for each sector, the whole of Greenland and marine terminating glaciers are visualized (see Paper I and supplementary material).

3.4 Glacier mapping with OBIA

Inaccuracies in the automated mapping of glaciers result in time-consuming manual correction. Several methods to improve the mapping of glaciers were proposed in the past (e.g. for debris-cover see (Shukla et al., 2010), however, none of them investigated the potential of OBIA for glacier mapping. This section describes the OBIA methods as applied to Greenland and subsequently also in other regions of the world with challenging mapping conditions (see Paper II).

3.4.1 Pre-processing

Temperature and slope information improves the mapping for debris-covered glacier parts, as several studies have shown (Bhambri et al., 2011; Bolch et al., 2007; Racoviteanu and Williams, 2012). Using this information with OBIA requires some pre-processing of this kind of input data.

Satellite imagery as from Landsat TM / ETM+ and Terra ASTER provides one or more thermal bands, though with different spatial resolution (120, 60 and 90 m, respectively). These thermal bands are helpful for detecting thin debris coverage due to the cooling of the rocks from the ice underneath (Foster et al., 2012; Mihalcea et al., 2008). For this purpose thermal bands have to be converted to physical values (Kelvin), as a threshold in Kelvin is easier to find and more conceivable than a DN. To convert the original DN into physical values, a band-specific radiometric calibration is required. Sometimes satellite providers offer different processing stages of calibrated products like the at-satellite radiance [W/(m² sr μm)] or brightness temperature [K] produced for instance by the ASTER science team (http://asterweb.jpl.nasa.gov /data_products.asp). Other data, like the one from the Landsat sensors are not atmospherically pre-processed and thus offer calibration constants in the metadata or in the online user guides (http://landsathandbook.gsfc.nasa.gov/handbook/handbook_toc.html).

The retrieval of degrees Kelvin or "Top of atmosphere reflectance" (TOAR) follows a two-step process. First, the at-satellite radiance [W/(m² sr μm)] has to be calculated based on the solar zenith angle at the time of satellite overpass. In a second step, the satellite radiance either has to be converted into Kelvin or into TOAR reflectance (Landsat Project Science Office, 2006; Schmugge et al., 2002). A TOAR reflectance map, however, is influenced by topography altering the local incidence angle of solar radiation and thus causing a variable reflectance between otherwise similar soil cover types on a pixel-by-pixel basis. Due to the fact that glaciers are located in high mountain regions, with often steep topography (also causing shadow), a topographic correction is required. Several methods have been developed such as the "Cosine correction", and the "C-factor correction" by Teillet et al. (1982), the Minnaert (1941) and the correction by Ekstrand (1996). A study by Bippus (2011) concluded that the Minnaert correction is a suitable method for correcting large areas, but especially in steep terrain the Ekstrand correction provides better results.

Temperature information must be combined with slope information to retrieve debris coverage on a glacier (e.g. Bhambri et al., 2011; Bolch et al., 2007; Racoviteanu and Williams, 2012). The idea behind using slope information is that debris only accumulates on flat parts of a glacier. DEMs have to be downloaded for the region of interest and subsequently reprojected to the same coordinate system as the satellite imagery. Often DEMs are merged as they have other coverages or tiles from the imagery itself. Finally the slope is calculated using a GIS.

3.4.2 Segmentation

In Greenland an MRS, with a scale factor of 10, a shape factor of 0.1 and a compactness factor of 0.5, was applied (standard settings). This led to the creation of a base segmentation level (level 0) for the later classification of clean snow and ice. This segmentation level was subsequently copied for the creation of two other levels with the same objects resulting from it. The two new segmentation levels served afterwards for the classification of the slope (level 1) and temperature information (level 2) (see next section). Slope and thermal information are besides the VIS and SWIR bands important input parameters for the image segmentation in OBIA. The slope difference between the rather flat glacier surface, and the often steep lateral moraines, calculates image objects which follow the break from flat to steep slopes on the surface topography. The segmentation is even more reliable if temperature information of cooled ice surface is included.

3.4.3 Classification

OBIA allows the creation of a rule-set in which all classification steps follow each other. In Fig. 3.7 the individual steps are visualized. In the case of Greenland, objects were assigned to the class "snow and ice" in level 0 when the mean value of the objects representing the VIS/SWIR ratio (based on the raw DN) exceeded a threshold value of 2.0. Thereafter objects were classified as "gentle slope" for slope values smaller than 14° in level 1 (Fig. 3.7b) and as "positive temperature" if the calculated values were between 273 and 283 K in level 2 (Fig. 3.7c). The starting values for the thresholds of each condition are based on already published values for the selected input data sets, but they were adjusted to the current scene to improve the results. After this step, the classified objects of "gentle slope" in level 1 and "positive temperature" in level 2 were combined if they overlapped, and assigned to the class "debris on ice" (Fig. 3.7d). Finally, "debris on ice" was assigned to the class "glacier" (Fig. 3.7e).

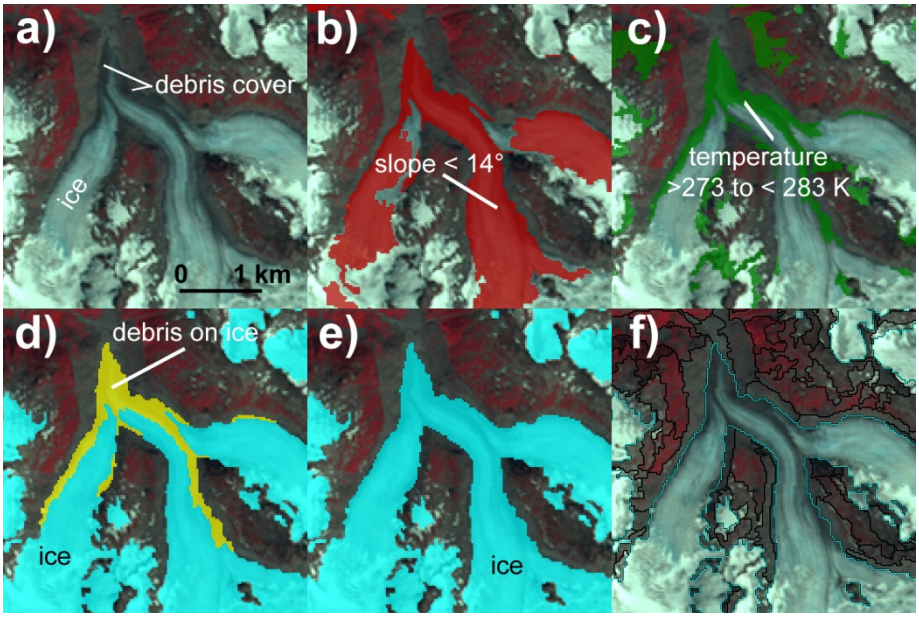

Figure 3.7: Visual example of how slope and thermal information in OBIA can help to incorporate debris-covered parts of a glacier. In a) the raw image is visible, b) shows the classification obtained by the thermal channel of Landsat and c) the classification obtained from the slope. In d) "ice" is classified according to the ratio and "debris on ice" if slope and temperature overlap in yellow. e) Afterwards "debris on ice" is assigned to the class "ice" and f) finally converted into an outline.

3.4.4 Post-processing

The automatic mapping of glaciers always results in wrongly classified pixels and/or objects. In PBIA automatically created outlines must be corrected manually, which is rather time consuming. In OBIA some of this manual correction is performed automatically using neighbourhood relationships. This increases the accuracy of the final automatic mapping, however, manual correction at the end is nevertheless necessary.

The largest initial classification inaccuracies arise from the wrong mapping of debris-covered ice. Even if temperature and slope information is used as an additional input in the mapping, single objects on a glacier surface might still be unclassified. In such a case the implementation of a loop in OBIA, which decreases the threshold for temperature and at the same time increases the threshold for slope, is helpful. With this procedure unclassified objects are selected and assigned to the class "ice" (cf. 3.4.3). Other remaining unclassified objects on a glacier surface can additionally be classified according to neighbourhood relationships. These relationships are based on a calculation of the ratio of the shared border length of an object with a neighbouring object to the total border length. Such an example is shown in Fig. 3.8, where neighbourhood

relationships have successfully been used for the removal of commission errors such as "icebergs", "sea ice" and "sea-border artefacts". In this case an MRS with scale 10, shape 0.1 and compactness 0.5 was performed. The class "ice" is classified by a ratio image (> 2) and "sea" by the NDWI (threshold range: -0.6 - -0.85) in Fig. 3.8b. The classification is shown in c) with filled objects and in b) with object outlines. Thermal and slope information includes more debris coverage but introduces also some "sea-border artefacts" in d). In e) the class "icebergs" (shown in yellow) is introduced according to neighbourhood relationships (relative border to "sea" > 0.85) and assigned to a temporary class which is subsequently assigned to the class "sea" (Fig. 3.8f). The remaining "sea-border artefacts" were selected again with the relative border tool (Fig. 3.8g). This time, however, two (relative border to "unclassified" > 0.35 & relative border to "sea" > 0.35) as two classes ("sea" and "unclassified") border this class.

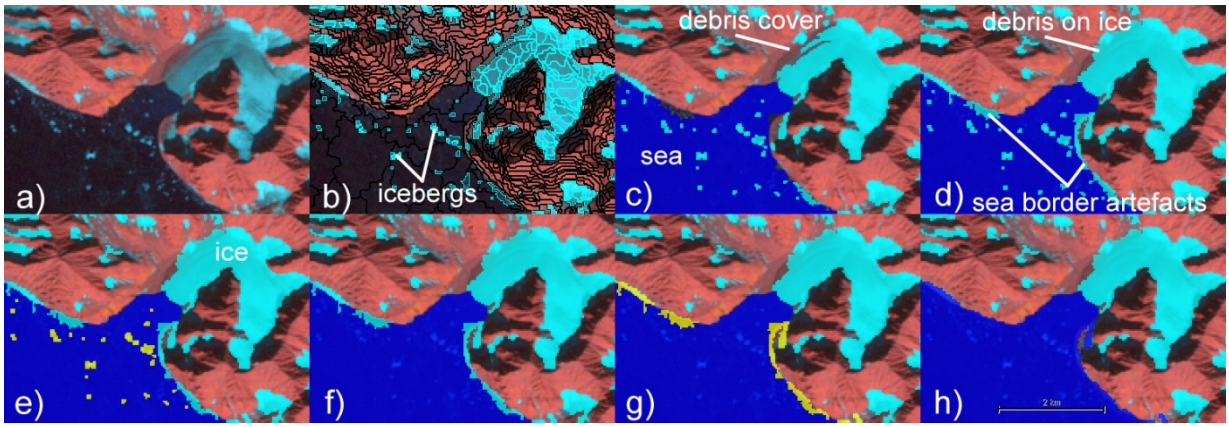

Figure 3.8: Visual example of how OBIA can be used to exclude icebergs from a glacier mask by neighbourhood relationships. In a) a coastal region in the Watkins range in Greenland is visible. A multiresolution segmentation with scale 10, shape 0.1 and compactness 0.5 was performed and b) "ice" classified by ratio image and c) "sea" in this case by the NDWI. The application of neighbourhood relationships allows the e) automatic selection of "icebergs" and g) "sea border artefacts". This helps to clean automatically h) the final class "ice".

Water surfaces can also introduce mapping errors. In many cases a turbid lake on a glacier is not mapped (spectrally correct) but actually belongs to the class glacier, and a clear lake is mapped near a glacier (spectrally wrong) but does not belong to a glacier. By applying post-processing methods including a 'lake surrounded by ice' in the glacier class and excluding a 'lake surrounded by other terrain' OBIA identifies these objects and assigns them to the appropriate class. Moreover, OBIA allows for the treatment of a lake as a whole, whereas the PBIA often just maps only parts of a lake (often in a rather noisy fashion).

Another way to assign correct membership to the class "glacier" is to additionally select objects according to their shape. In particular, medial moraines are often represented as elongated objects after the initial segmentation of the image. This specific shape can be used to distinguish them from other objects and assign them correctly to the class "glacier" (cf. Paper II).

3.5 Glacier and ice cap elevation changes

Altimetry data increases the capacity to quantify glacier elevation changes in remote areas compared to the traditional field measurements of glacier mass balance. The laser altimetry data from NASA's Ice, Cloud and land Elevation Satellite mission (ICESat), in combination with the outlines from the Greenland Glacier Inventory (GGI) allows elevation changes over Greenland's local GIC only to be obtained. This section summarizes the most important processing steps.

3.5.1 Pre-processing

The pre-processing requires the definition of meaningful sectors for spatial averaging (cf. 3.2) and removing problematic measurements from ICESat. This included a correction of saturation thresholds of the so-called IceSvar parameter. The correction is needed as the wave form can induce errors in surface elevation estimates (Smith et al., 2009). Data with multiple peaks caused by reflection of clouds and topography have also been removed. Further filtering of data points was applied by using the outlines of the GGI and selecting only data points lying at more than 250 m from the glacier margin. This procedure helped to reject implausible height change values (>10 m/a) and points with a high variance as derived from a linear regression procedure (> 1.0). These filtering procedures reduced the number of ICESat data points from 40475 to 27799.

3.5.2 Deriving surface elevation changes

ICESat data coverage increases towards the north of Greenland due to the polar orbit of the satellite. For this reason most GIC in the northern sectors were well covered (> 20000 ICESat point measurements), whereas in the southern sectors only 1750 point measurements on local GIC could be used. Elevation changes were thus analyzed in regard to the elevation distribution of the glaciers per sector using the *extended* GIMP DEM. For the sectors with a low regression coefficient elevation changes were retrieved based on dh/dt for all points below and above the ELA. The standard deviation of ICESat points in most elevation bins is within 10% of the measurement value. In particular the lowest elevations, where most surface lowering occurs, are well covered by ICESat data points. Volume loss is derived by multiplying the elevation change values per elevation bin and sector by the respective glacier area.

As the individual ICESat tracks are not precisely repeated by each overflight, particular methods have to be applied for deriving elevation changes (Moholdt et al., 2010; Schutz et al., 2005). In Paper III they were estimated by a well established regression technique. This method determines surface slope and averages elevation change for planar surfaces that are fitted to 500 m along-track resolution of near–repeated tracks (Sørensen et al., 2011).

3.5.3 Mass changes

Firn compaction and material densities must be taken into account to convert the ICESat-derived volume change to mass change. This conversion is also a critical issue when deriving mass changes from geodetically derived volume changes (e.g. Huss, 2013; Zemp et al., 2013). For Greenland, firn density was calculated by an empirical relationship between snow density and mean temperature at 10 m depth based on mean annual air temperature (MAAT) (Reeh et al., 2005). The MAAT is calculated as a function of surface elevation and geographical position for each sector (Fausto et al., 2009). The elevation change values above the ELA were multiplied with regional firn density values (e.g. north-west sectors 528 kg/m³, east-south 796 kg/m³) and below the ELA with the density of ice (900 kg/m³). The ELA is approximated by the median elevation of each glacier as derived from the *extended* GIMP DEM (Braithwaite and Raper, 2009).

Changes of firn properties influence mass changes and must therefore be considered in such calculations. This is achieved by applying a time-dependent snow densification model (Sørensen et al., 2011). This model is forced by the output of the RCM HIRHAM5 at a 5x5 km resolution and calculates the change in air space of the uppermost 15 firn layers also considering the retention of melt water. The resolution of the model is too low to address each glacier individually, but it provides reasonable results for each sector. According to this model, a higher compaction for the wetter east-south sector (-0.05 ±0.01 m/a) and a slight extension of firn pore space in the cold, dry north (+0.09 ±0.01 m/a) are found.

3.6 Determining mass balance and climate sensitivities

A key concept for understanding the connection between glacier changes and climate is the sensitivity of a glacier's mass balance to a change in climatic elements such as temperature (*T*) or precipitation (*P*), the so-called mass balance sensitivity. But also the climate sensitivity is of interest, as glaciers in a wetter and warmer climate tend to have a higher mass turnover and thus react more sensitively to climate change. In Paper IV both sensitivities are analysed by correlating the mass balance derived from ICESat with trends and mean values of *T* and *P* derived from the RACMO2 RCM.

3.6.1 Pre-processing

The first processing step was to assign a sector number to each glacier based on the sectors defined in Paper III (cf. 3.2). This was achieved by digital intersection of the sectors with the glaciers. Finally, all CL0 and CL1 glaciers were selected and exported to a new file.

The glacier vector outlines were subsequently converted into a gridded mask. This was performed with the ENVI software package using the "Export layers to ROI" function. Regions of interest (ROIs) are subsets of images, either selected graphically or by other means such as thresholding. This step resulted in a 1 km gridded glacier mask. Each glacier was tagged with a sector number (1-10), which served as a mask for the retrieval of *T* and *P* from RCM data.

In addition, RACMO2 gridded climate data was resampled to 1 km resolution, to represent the local climate conditions for the GIC around Greenland.

3.6.2 Temperature correction with lapse rates

Gridded climate data cannot be considered as perfectly accurate. For this reason a specific lapse rate was calculated to customize *T* for each sector. Fig. 3.9a shows a glacier on Disco Island (West-Greenland) with its outlines. In 3.9b the *extended* GIMP DEM and 3.9c the RACMO2 DEM is depicted for the corresponding area. Based on the *extended* GIMP DEM and the RACMO2 DEM, grid cells were selected where the elevation difference between the two DEMs was less than 80 m (Fig. 3.9d) above glacierized areas. This assures a higher reliability as only temperature values above glaciated area and close to the "real" altitude are taken in consideration. Subsequently corresponding T values were selected per elevation bin (Fig. 3.9e) and mean *T* retrieved for each elevation band (green contour lines) (Fig. 3.9f). Finally, a linear regression function of the mean *T* values in the different elevation bands was calculated to retrieve the slope value "m" of the regression function $y = m * x + b$. This linear regression function was performed for all seasons and for each sector. The value of m served afterwards as the lapse rate (Fig. 3.9g) (Gardner et al., 2009; Minder et al., 2010).

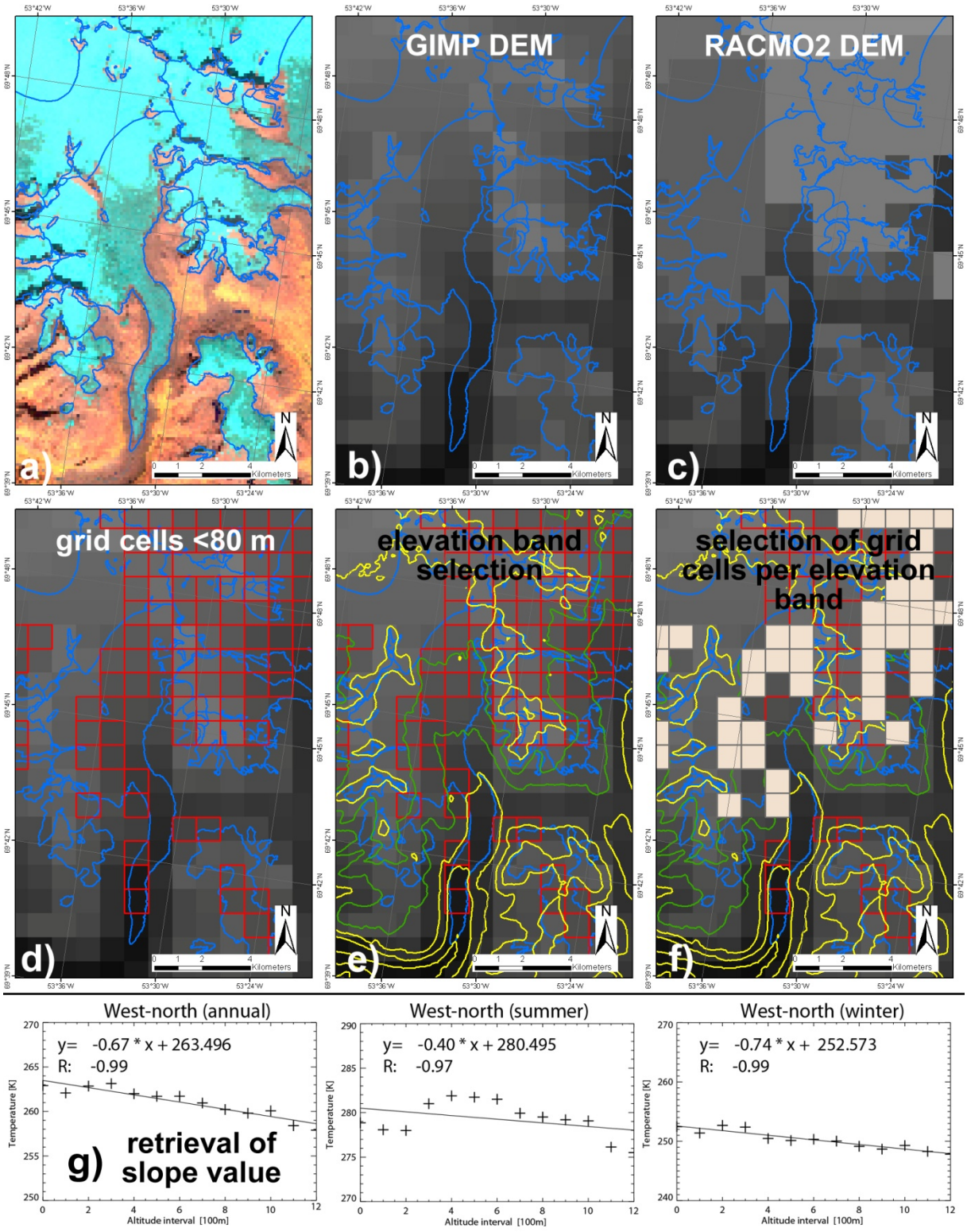

Figure 3.9: A schematic illustration of how the elevation differences (ΔH) between the GIMP DEM and the RACMO2 DEM influenced the calculation of the lapse rate. Blue outlines represent glacier outlines, red boxes represent pixels and yellow lines elevation contours and green lines show selected elevation contours. Filled squares in f) represent a selection of pixels according to one elevation bin (green lines). The description of the retrieval of the lapse rate is given in the text above.

3.6.3 RACMO2 temperature correction and glacier-climate sensitivity assessment

After the retrieval of specific lapse rates per sector and season, *T* values of the RACMO2 were corrected. Before a correction of a gridded *T* with a lapse rate can be performed, the elevation difference of the internal RACMO2 DEM and the *extended* GIMP DEM must be known. This correction was, however, only performed to *T* values where the elevation difference was less than ±200 m. This threshold made it possible to select and then correct only RACMO2 T values where there was a high *T* reliability due to appropriate elevation provided by the RACMO2 DEM. Once the elevation difference was retrieved between the RACMO2 DEM and the GIMP DEM the *T* values were adjusted according to a specific lapse rate obtained before (Fig. 3.10).

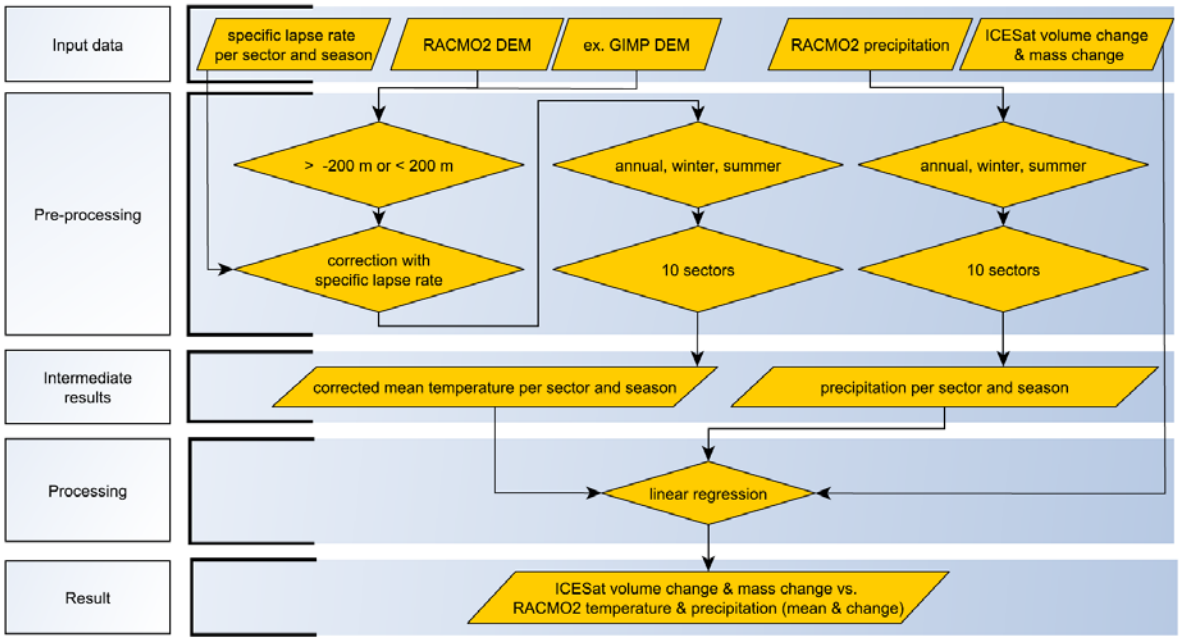

Figure 3.10: Overview of the processing steps performed to assess glacier-climate and mass balance sensitivity

Precipitation data from RACMO2 have not been corrected due to their high spatial and temporal variability and large uncertainties in the measurements (Braithwaite and Raper, 2002; Sevruk et al., 2009). This is in particular true in regions with rough topography and where climate stations are only located at low altitudes as is the case for Greenland. Much of the precipitation further inland is forced by topography and hence underestimated by the meteorological stations near sea level (Ettema et al., 2010). Moreover, in rough topography snow is often redistributed by wind and avalanches, altering the accumulation pattern (Machguth et al., 2006; Plattner et al., 2004).

The corrected RCM *T* values and uncorrected RACMO2 precipitation were compared for each season and sector to the ICESat volume and mass changes derived in Paper III. Correlation values were obtained using a linear regression. In addition to this assessment of climate sensitivity, the mass balance sensitivity was derived by directly dividing the ICESat-derived volume and mass changes by the governing changes in *T* and *P*, analogous to the study by Braithwaite et al. (2013). The changes in *T* and *P* were calculated for each sector by differencing their mean values over two time periods (1980-1995 and 1996-2011).

4 Summary of research papers

The main work of this thesis was the creation of the first complete glacier inventory for all the local GIC on Greenland (the GGI) using optical satellite data and a DEM (Paper I). Due to the required high manual workload for post-processing of the automatically created glacier outlines, one part of this thesis was the investigation of the performance and additional possibilities of object- compared to pixel-based image analysis for glacier mapping (Paper II). The GGI also served as a mask to derive surface elevation changes from ICESat altimetry data over the local GIC only (Paper III). This study resulted in the first estimate of their contribution to sea-level rise. Finally, the elevation changes obtained in Paper III, the glacier outlines from Paper I, and temperature and precipitation data from a regional climate model were used to investigate the climate and mass balance sensitivities of the glaciers on a regionally averaged scale (Paper IV). While Papers I to III are already published in peer-reviewed scientific journals, Paper IV is as yet only submitted. In Chapter 4 of this thesis, a brief summary of each paper is given including a Figure illustrating a key result. Full versions of all papers can be found in Part B of this thesis.

4.1 Paper I: The first complete inventory of the local glaciers and ice caps on Greenland

Rastner, P., Bolch, T., Mölg, N., Machguth, H., Le Bris, R., and Paul, F. (2012). The first complete inventory of the local glaciers and ice caps on Greenland. The Cryosphere 6, 1483–1495.

This paper describes the background, working steps and results of the first glacier inventory for the whole of Greenland. Until 2012, only rough and incomplete inventories existed for the local GIC on Greenland, so that their size and spatial distribution were determined by a range of "estimates". The difficulties related to modelling their future sea-level contribution was a main motivation for this work as well the EU FP7 ice2sea project and the ESA project Glaciers_cci which provided the funding for this thesis. A special challenge for the GIC in Greenland was the development of a consistent strategy for separating the GIC from the ice sheet, i.e. just mapping the glaciers was not sufficient.

More than 70 Landsat scenes (mostly acquired between 1999 and 2002) were processed to map the GIC on Greenland from a ratio image (RED/SWIR). For regions north of 80° N (not covered by Landsat) the GIMP ice mask was used and manually improved in some regions with MODIS data. More than 80% of the processing time was used to manually correct classification inaccuracies like debris cover, seasonal/perennial snow and to find the exact separation of marine terminating glaciers from sea ice or icebergs. Drainage basins were obtained by automated flowshed analysis using the GIMP DEM and the viewfinderpanorama.org DEM and corrected by hand afterwards. Ice cap rules were developed to define where ice caps and glacierized mountain flanks should be separated. Finally, glacier outlines and the drainage basin outlines were digitally intersected to obtain individual glacier entities. All glaciers were classified into three connectivity levels (CL0, CL1, CL2; i.e. no, weak, and strong connection to the ice sheet), to serve the needs of different user communities and to clearly, but still flexibly, distinguish the local GIC from the ice sheet and its outlet glaciers.

In total about 20300 local GIC were mapped, of which about 900 are marine terminating. Considering all glaciers, an ice-covered area of 130076 ±4032 km^2, without the CL2 GIC 89720 ±2781 km^2 was mapped. Glaciers smaller than 0.5 km^2 contribute only 1.5% to the total area but more than 50% (11000) to the total number. In contrast, the 25 largest GIC (> 500 km^2) contribute 28% to the total area but only 0.1% to the total number. There is only a weak dependence of median elevation and of mean glacier aspect, but a clear relationship of the median elevation and the distance to the coast. The mean elevation of the GIC in Eastern Greenland is 1700 m and around 1000 m in the remainder of Greenland.

<u>The major lessons learned from this study are:</u>

- The derived ice-covered area (89720 ±2781 km^2 for CL0 and CL1, 130076 ±4032 km^2 incl. CL2) is about 50% (100% incl. CL2 GIC) larger than the mean value (62600 km^2) assumed in most previous studies.
- Finding clear separation rules was time-consuming and a constant matter for discussion.

- The number of GIC is not well constrained as the separation of ice caps into small entities is often subjective.
- Manual correction of ice in cast shadows of rough topography was challenging due to Greenland's high latitude and steep terrain causing extensive shadows.
- High-resolution satellite scenes in Google Maps helped to determine glacier outlines in some of the problematical areas.
- Greenland's sub-polar to polar climate favours the existence of perennial snow patches. Consequently a higher glacier size threshold (0.01 km² if perfect scenes are available) of 0.05 km² was used to exclude most perennial snow fields from the inventory.
- The quality of the manual correction of glacier outlines depends on the experience of the analyst and its internal quality in the mapping of debris-covered glaciers.

Author's contribution to the paper:

The author contributed to the mapping and the creation of drainage divides in the south east and east central regions of Greenland. After all regions were mapped, vector outlines were reprojected and digitally merged by the author for the corresponding regions. He contributed to the development and implemented the rules for the assignment of connectivity levels and the manual correction of drainage divides. He performed all statistical analyses and led the writing and publication of the paper.

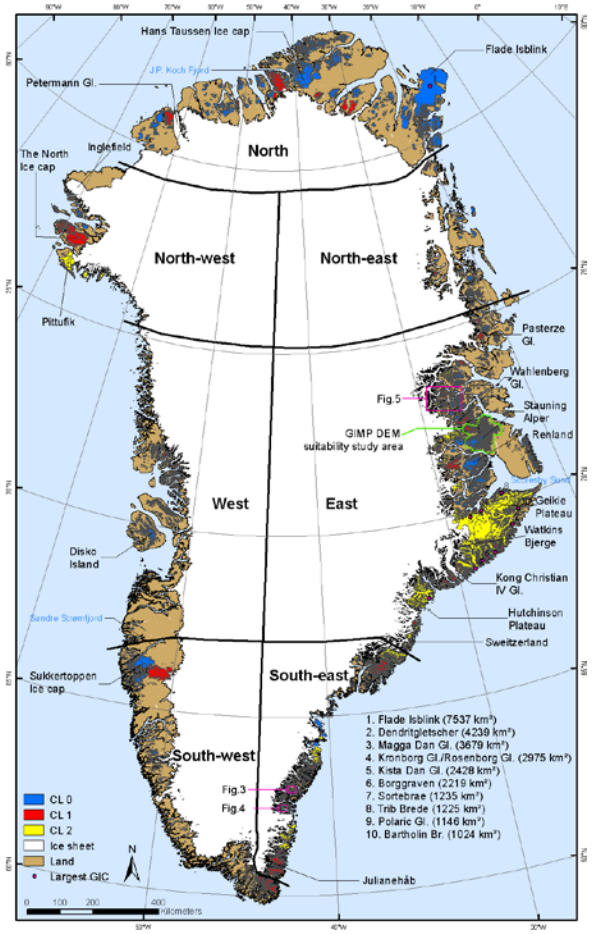

Figure 4.1: Map of Greenland showing all local GIC (colour coded) and place names mentioned in the Paper I. The green box indicates the area selected for the investigation of DEMs and the magenta ones the location of some figures in that paper.

4.2 Paper II: A comparison of pixel- and object-based glacier classification with optical satellite images

Rastner, P., Bolch, T., Notarnicola, C., and Paul, F. (2014). A comparison of pixel- and object-based glacier classification with optical satellite images. IEEE Journal of Selected Topics in Applied Earth Observations and Remote Sensing 7, 853–862.

Mapping glacier outlines is challenging even under optimal conditions and time consuming manual corrections of wrongly classified pixels always remains. Within the last decade, object-based image analysis (OBIA) has emerged as an alternative classification method. This approach adds a semantic dimension to the spectral information, and has here for the first time been applied to the issue of glacier mapping. The aim of this study was first of all to compare the performance of OBIA and the classical pixel-based image approach (PBIA) and secondly to analyse to what degree manual corrections can be reduced.

Three regions (Watkins range/Greenland, Everest region/Nepal and Coast mountains/Canada) with challenging mapping conditions and reliable reference data were selected to investigate the advantages and disadvantages of the two approaches. In both approaches, a ratio image was created to map clean snow and ice while thermal and slope information was used to assist in the identification of debris-covered ice. Thresholds were chosen based on literature results and adjusted to the scene conditions. Two comparison levels were defined to investigate, whether a) OBIA performs better with or b) without its post-processing capabilities. In addition, the PBIA approach was compared twice to the OBIA: once by using the same thresholds as OBIA and once by selecting the best thresholds for PBIA. Finally, the automatic outlines were compared to reference data (manually corrected vector outlines from different glacier inventories) to evaluate the mapping accuracy. During the evaluation both correctly and wrongly classified pixels were investigated. The latter are responsible for most of the workload in post-processing.

Overall, the analysis revealed that OBIA performs slightly better than PBIA. OBIA has a greater than 3% better classification accuracy in comparison to PBIA. When debris cover is present in a region, OBIA has a 12% higher accuracy. Commission errors (wrongly classified pixels) were about half (3.6%) of those in the PBIA approach (6.9%). The post-processing possibilities in OBIA (e.g. the application of a processing loop and neighbourhood analysis) are especially helpful in improving the final classification. Such post-processing allows the removal of objects that do not belong to a glacier from a semantic point of view, but are correctly classified from a spectral point of view (e.g., icebergs). The OBIA approach thus helped considerably in reducing the workload for manual corrections. Overall, the application of OBIA can be recommended for glacier classification in regions where spectrally ambivalent mapping conditions are dominant.

<u>The major lessons learned from this study are:</u>

- OBIA is recommendable for the mapping of glaciers, especially in regions with challenging mapping conditions.
- Clean ice and snow is mapped accurately by both approaches.
- Speckled pixels (wrongly classified pixels) are significantly reduced in the OBIA approach.

- The usage of thermal and slope information greatly improves the mapping result, in particular in the case of debris-covered glaciers.
- Post-processing possibilities in OBIA enable effective cleaning of wrongly classified pixels/objects and at the same time help to improve the final classification for the glacier class.
- As satellite imagery and DEMs are more and more available worldwide, a high transferability of the OBIA rule-set was envisaged.

Author's contribution to the paper:

The author designed the study, performed the mapping of the OBIA and PBIA for all three regions and carried out all statistical analysis and interpretation. He wrote the entire manuscript, designed all graphics and was in charge of the publication of the paper.

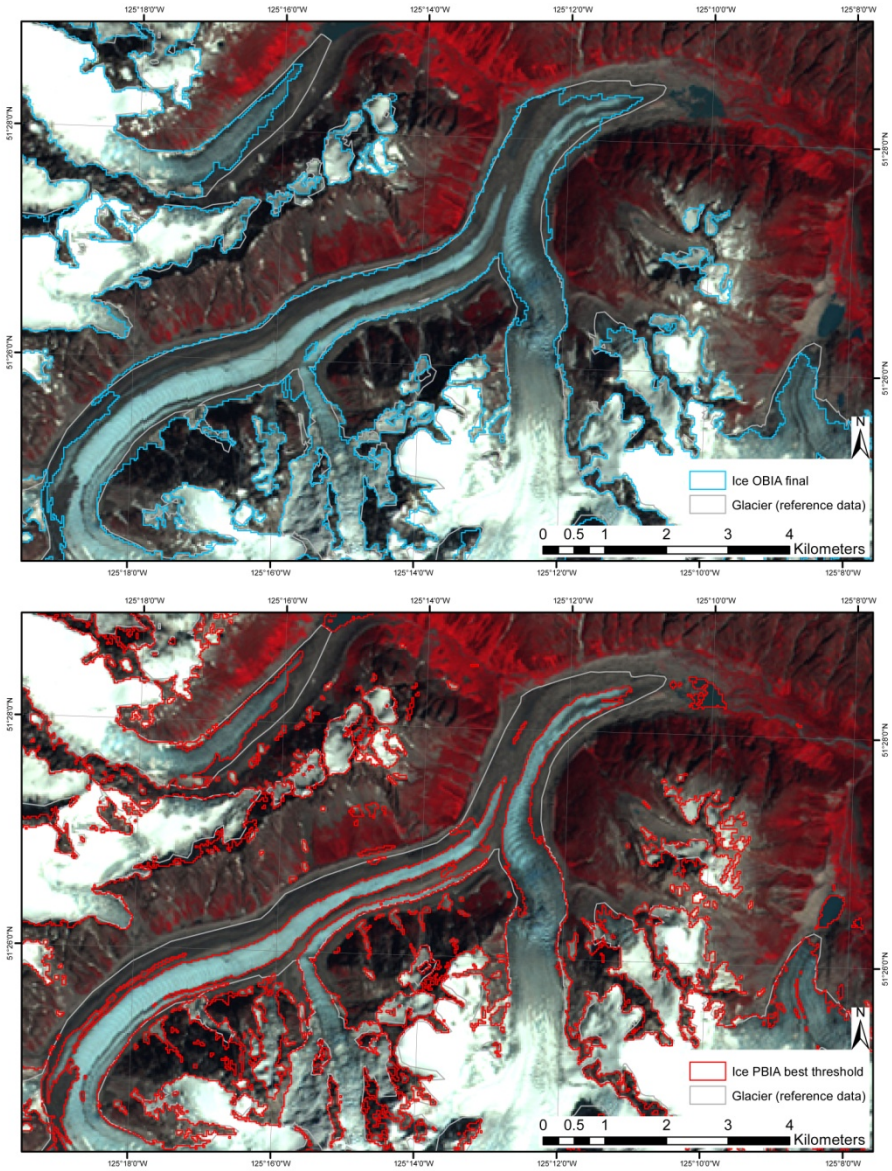

Figure 4.2: Visual example of the performance of OBIA and PBIA for the Coast-mountains test region in Canada

4.3 Paper III: Mass loss of Greenland's glaciers and ice caps 2003–2008 revealed from ICESat laser altimetry data

Bolch, T., Sandberg Sørensen, L., Simonsen, S.B., Mölg, N., Machguth, H., Rastner, P., and Paul, F. (2013). Mass loss of Greenland's glaciers and ice caps 2003-2008 revealed from ICESat laser altimetry data. Geophysical Research Letters 40, 875–881.

This paper investigates the volume and mass losses of the local GIC on Greenland from 2003-2008. It highlights the importance of the new GGI to study the GIC. The glacier mask made it possible for the first time to determine the volume and mass changes of the GIC separately from the ice sheet.

Elevation change values were obtained from the ICESat Geoscience Laser Altimeter System (GLAS). The tracks of GLAS are separated horizontally by ~30 km in southern Greenland and ~10 km in northern Greenland with footprints of about 70 m and a sampling frequency of about 170 m along track. Correction procedures of the ICESat signal include: (a) saturation correction of the waveform to reduce elevation estimation errors, (b) the identification of thresholds to reject data with a large misfit, and (c) the identification and elimination of data with multiple peaks. Mean surface elevation changes were estimated at 500 m along track resolution and associated with the variance from the regression procedure. Further filtering of the data was applied by rejecting implausible surface elevation changes of >10 m a^{-1} and by selecting only data points located at >250 m from the glacier margins. Volume losses for all GIC were obtained by calculating along track dh/dt-curves using an area-elevation distribution function. Density was taken into account by applying a specific firn density (based on the mean annual air temperature) for regions above the ELA and an ice density of 900 kg/m³ below the ELA. Moreover, firn compaction was derived and considered using a densification model forced by the RCM HIRHAM5.

The GIC in Greenland showed a mean surface lowering of around 0.45 m a^{-1} for the period October 2003-March 2008, resulting in an overall volume loss of about 40 km^3 a^{-1} for the CL0 and CL1 glaciers and about 60 km^3 a^{-1} for all local GIC. The resulting mass loss for the CL0 and CL1 glaciers is 27.9 ±10.7 Gt a^{-1}, corresponding to 0.08 ±0.03 mm a^{-1} SLE and 18.5 ±7.2 Gt a^{-1}, when excluding marine-terminating glaciers. The overall ice loss of all Greenland GIC was 40.9 ±16.5 Gt a^{-1} (0.12 ±0.05 mm a^{-1} SLE). The mass loss is not homogeneously distributed. Highest average specific mass losses were observed in the south-eastern (1.0 ±0.3 m w.e. a^{-1}) sector while the lowest were measured in the north-central sector (0.1 ±0.05 m w.e. a^{-1}).

<u>The major lessons learned from this study are:</u>

- The GGI is an important base dataset (mask) for investigating changes of the GIC and the ice sheet separately.
- The largest uncertainties are related to snow, firn and ice densities and the up-scaling of the ICESat data.
- The mass loss per area unit of the GIC is about 2.5 times higher than for the ice sheet.
- The regional melt pattern seems to be similar for the ice sheet and the local GIC.

- The highest mass losses take place in regions which receive most precipitation and vice versa.
- In an Arctic context, the mass loss of Greenland's local GIC is higher than in Svalbard and the Russian Arctic but lower than in the Canadian Arctic.
- The contribution to SLR of the local GIC is statistically significant (0.12 ±0.05 mm a^{-1}).

Author's contribution to the paper:

The author provided the GGI, the sectors and the glacier parameters (connectivity levels). He contributed to the final draft of the paper and designed and produced most of the figures.

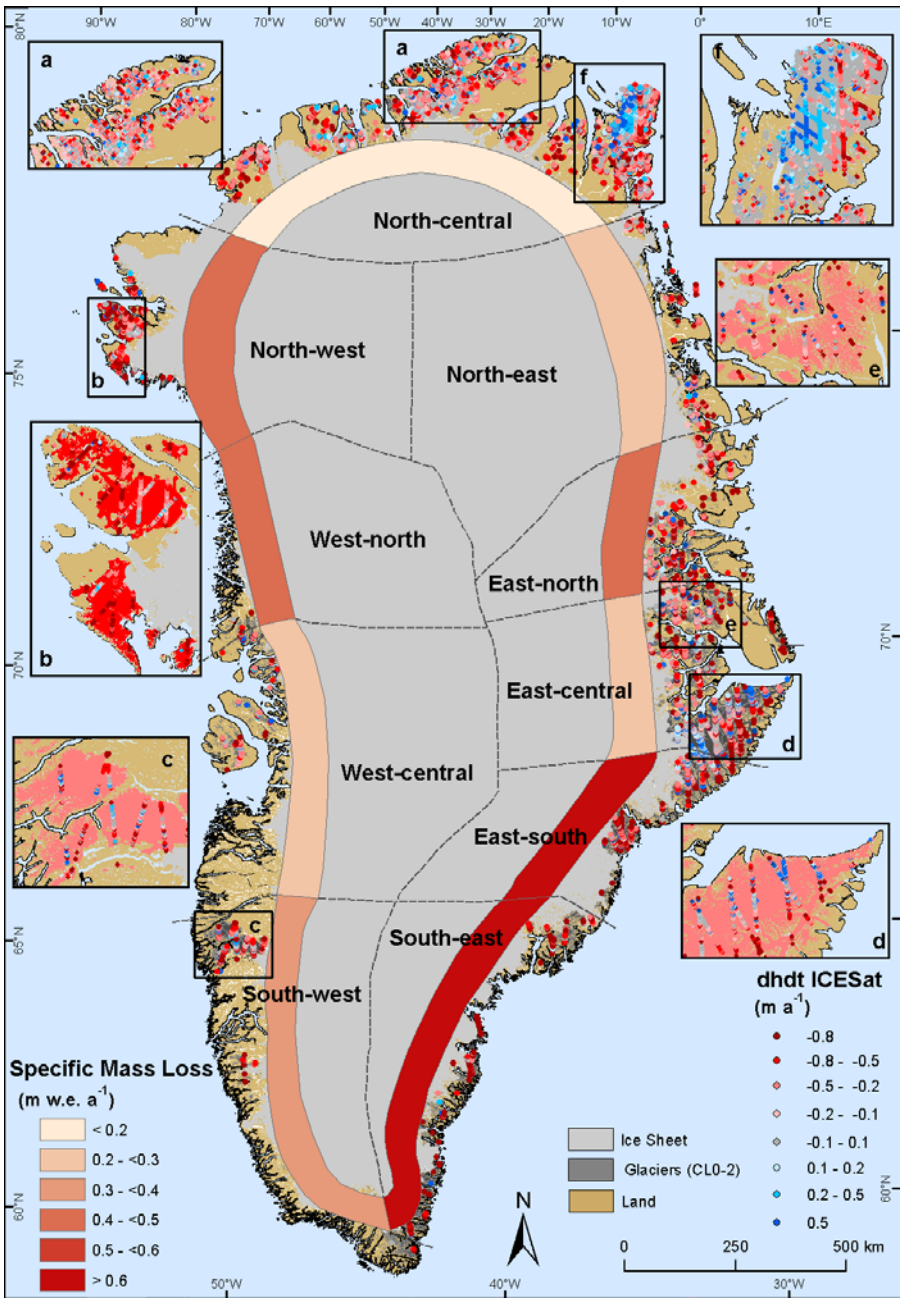

Figure 4.3: Mean specific mass changes for the ten sectors and elevation changes for the GIC derived from ICESat points. The background colour in the insets a-f represents mean elevation changes according to the legend for dh/dt ICESat.

4.4 Paper IV: Climate sensitivity of Greenland's local glaciers and ice caps

Rastner, P., Machguth, H., Bolch, T. and Paul, F. (subm). Climate sensitivity of Greenland's local glaciers and ice caps. Journal of Glaciology.

This study investigated whether there is a relationship between the spatial variability of the mass losses observed in Paper III and climatic elements. This was achieved by analysing the climate and mass balance sensitivity of the local GIC in Greenland, using the mass changes obtained from ICESat and temperature (*T*) and precipitation (*P*) data obtained from downscaled reanalysis data. As a working hypothesis it was assumed that glaciers in a maritime climate have larger mass turnovers, are thus more sensitive to climate changes, and show larger mass changes than glaciers in sub-polar or continental regions. Mass changes in each of the ten sectors were thus compared to (a) long-term mean values of temperature and precipitation sums (as an expression of their climate sensitivity), and (b) changes in *T* and *P* (as a measure of mass balance sensitivity).

Temperature and precipitation values above local GICs (CL0 and CL1 only) for winter, summer and annual time periods were derived from re-analysis data that were physically downscaled with the regional climate model (RCM) RACMO2. Specific lapse rates per season and sector were calculated to compensate for elevation differences between the RCM DEM and the *extended* GIMP DEM (both resampled to 1 km resolution). Ground observations of *T* and *P* around Greenland are sparse and restricted to low elevations near the coast. So they were not used for spatial extrapolation but for model validation.

The study revealed high correlations with mean annual *T* (R=0.82) and somewhat lower ones with mean annual precipitation sums (R=0.74). The mean annual mass balance sensitivity to a 1 K temperature increase gives high sensitivities for the South-east (-1.23 m w.e./a K) and East-south (-0.77 m w.e./a K) sectors. The rest of Greenland has much smaller sensitivities (< -0.28 m w.e./a K). In addition, higher correlations were found for the volume changes than for the mass changes, possibly related to the uncertainty of the conversion from volume to mass. Some uncertainties remain due to the large-scale averaging of climate and mass balance data in ten sectors, but the assumed relations between them could basically be confirmed.

<u>The major lessons learned from this study are:</u>

- The climate and mass balance sensitivity can be obtained from observational data.
- Mean temperature and precipitation can largely explain the observed pattern of glacier mass changes in Greenland.
- Regional differences of trends in *T* and *P* are not reflected in the observed regional differences in mass balance.
- The mass balance sensitivity is high in the South-east (-1.23 m w.e./a K) and East-south (-0.77 m w.e./a K) sectors. Other sectors show lower sensitivities (< -0.28 m w.e./a K).
- The spatial resolution of RACMO2 is too coarse for analysing individual GIC.

Author's contribution to the paper:

The author performed all data processing, including pre-processing and the combination with all RCM data. Monthly climate data were extracted from RACMO2 RCM and all statistical calculations were performed using scripts written by the author. The analysis of the results, the design of the figures and the writing of the paper was performed by the author with support of all co-authors.

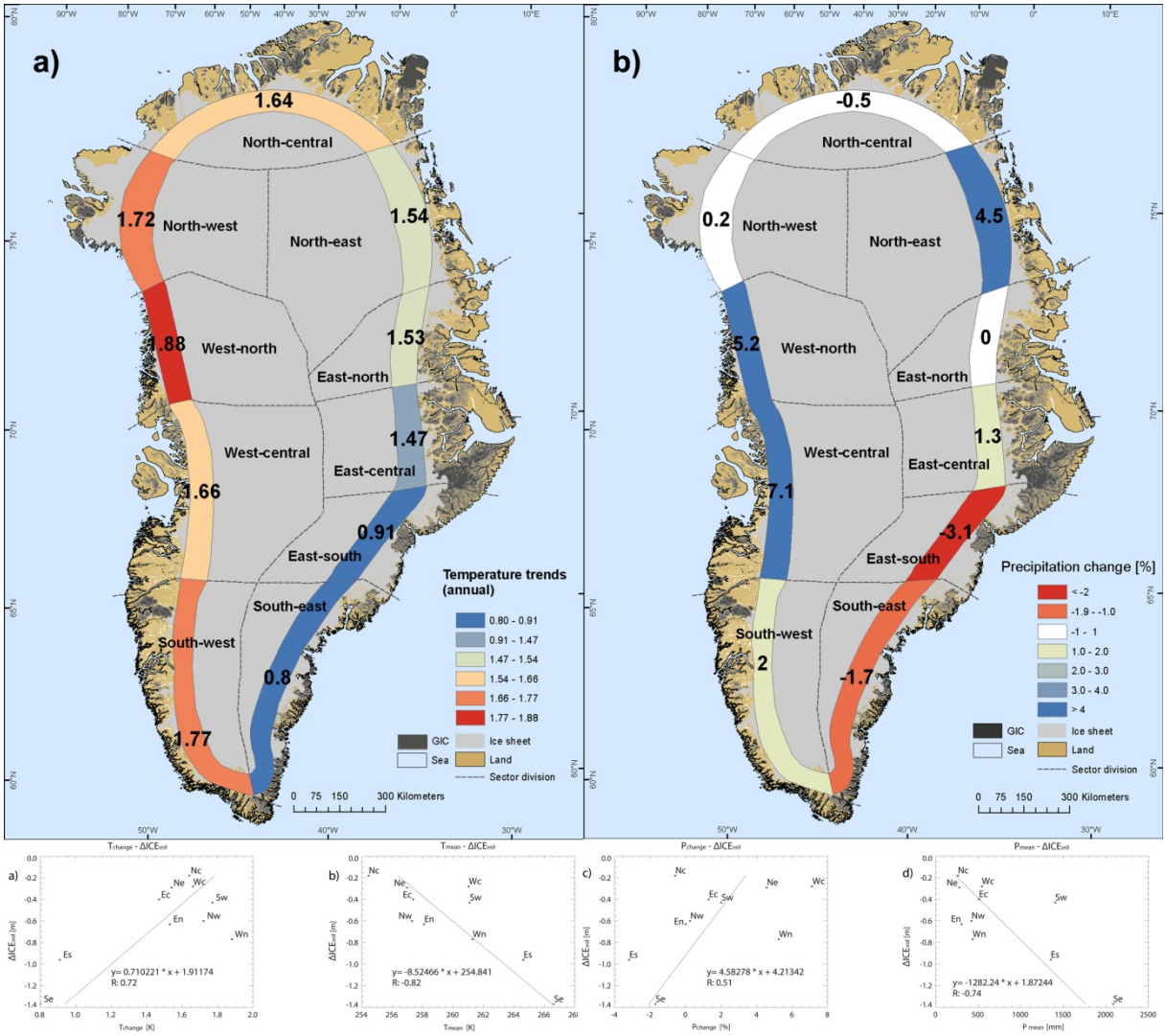

Figure 4.4: Mean annual temperature (a) and precipitation change (b) for ten sectors in Greenland from 1980-2011 (above). In the bottom panel a linear regression analysis of the different parameter combinations is shown. An illustration of the mean annual temperature and precipitation is given in Fig. 2.14 of this thesis.

5 Discussion

In this section the results of the research papers are evaluated and discussed in the context of the overall aim of this PhD thesis. At first, general aspects regarding the new glacier inventory of Greenland (Paper I) and the OBIA approach (Paper II) are presented. As the GGI is an important baseline dataset for further studies, investigations using the GGI as an input are discussed afterwards.

5.1 The Greenland glacier inventory

In this section, scene quality, the accuracy of glacier outlines, connectivity levels and the impact of DEMs are discussed.

5.1.1 Accuracy of glacier outlines and manual correction

The uncertainty of the GGI was assessed by a buffer method developed by Bolch et al. (2010). This method uses a buffer with a width of half a pixel of the original satellite data to account for the wrong placement of the outline during automatic and manual digitalization. A buffer of 15 m applied to all glacier complexes, resulted in a ca. 3% larger total area. This is in line with estimations of other studies (Bolch et al., 2010; Le Bris et al., 2011; Falaschi et al., 2013; Howat et al., 2014; Paul et al., 2011a).

Another source of uncertainty concerning the total area is related to the missing coverage of Landsat above 81.2° N i.e. the very north of Greenland is not covered by Landsat data and outlines from the GIMP ice mask had to be considered (Fig. 5.1). The outlines of the GIMP ice mask of this northern part of Greenland stem from synthetic aperture radar amplitude imagery mosaics acquired between October and December 2000 by the RADARSAT-1 satellite. This is due to the fact that also in the study of Howat et al. (2014b) they suffered from this missing part not being covered by Landsat. The RADARSAT-1 data are distributed at 20 m resolution and were up-sampled through bilinear interpolation to 15 m to match the panchromatic resolution of Landsat. Manual corrections of glacier outlines in the GIMP ice mask for these regions were limited. In fact, during the processing of the GGI, inaccuracies in the GIMP ice mask such as the exclusion of debris-covered glacier parts were found. Moreover, sea ice and ice shelves were partly included in the northernmost region. For these reasons the GIMP ice mask was manually improved by visual interpretation of a MODIS 250 m image of the same region. Even though some mapping inaccuracies in the GIMP ice mask were visible, the absolute geo-location errors were small due to the high geometric precision of the RADARSAT imagery, relative to those of Landsat which are in the order of meters (Howat et al., 2014). As ASTER data were also not available for this region, it is hoped that the future Sentinel 2 satellite (coverage latitudes 56° south and 83° north) will help in further improving the outlines.

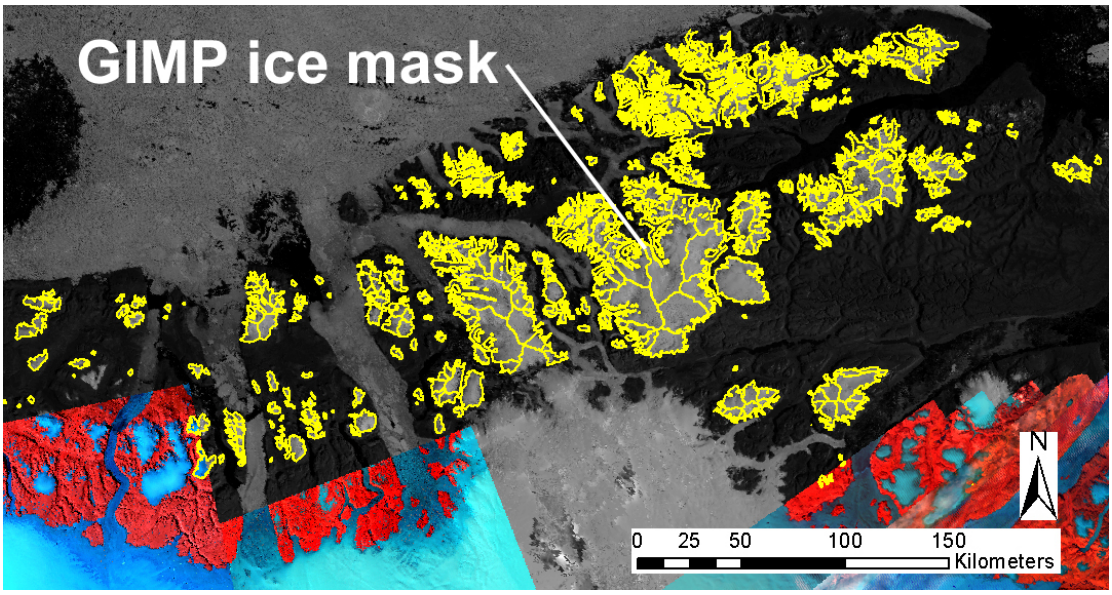

Figure 5.1: Visualization of the northernmost region of Greenland, where glacier outlines from the GIMP ice mask (shown in yellow) were used. Landsat imagery is shown in FCC (5,4,3), whereas the MODIS image is shown in panchromatic mode.

Glacier outlines that are created by automated methods have the advantage of providing fast, robust and reproducible results. However, if a satellite sensor does not have a band in the SWIR part of the electromagnetic spectrum, automatic calculation with the band ratio is not possible. For example, Svoboda and Paul (2009) applied a decision tree classifier using multiple thresholds on various Landsat Multispectral Scanner (MSS) bands. Instead of the SWIR band, an NIR band was used for the band ratio. Manual corrections were more difficult due to the coarse spatial resolution of the MSS sensor. Manual digitization of glacier outlines has to be applied when only black and white images are available or when glaciers are debris covered. This part of the workflow is very time consuming, in particular for large-scale application in regions with many debris-covered glaciers, and the source of the largest uncertainties. Although manual digitization of glacier outlines results in higher product accuracy when glaciers are debris covered, it is hampered by the large workload for large-scale application. To assess the accuracy of manual and automatically-created outlines, a round robin experiment was performed within the ESA Glaciers_cci (http://www.esa-glaciers-cci.org/) project (Paul et al., 2013b). Participants performed a multiple digitizing experiment of a few glaciers from different regions with challenging mapping conditions, such as debris cover, perennial snow and cast shadows. The results confirm that automated mapping of clean ice is as accurate as manual digitization. Moreover, a high spatial resolution does not necessarily result in a more accurate delineation of glacier outlines as the difficulties in interpretation also increase. Outlines digitized for debris-covered parts show large differences from one analyst to another (Paul et al., 2013b). The results confirm earlier studies that identified debris-cover as a major error source (Racoviteanu et al., 2008; Shukla et al., 2010).

One of the regions with large debris-covered glaciers in Greenland is the zone between the Dendritgletscher and the Bartholin Brae on Geikie Plateau (Fig. 5.2). In this region large amounts of manual corrections were necessary, as visible from the overlay of the raw classification (black outlines) and manually corrected (blue, red and yellow outlines) ones in Fig. 5.2a. Problematic are in particular the manual corrections for debris-covered glacier tongues with confluent flow as no clear break in surface slope is traceable. Medial moraines are, however, easier to map as ice borders medial moraines on both sides. Additionally, it is visible from Fig. 5.2a that a large number of speckled pixels are present on debris cover, in shadowed regions and in the sea.

Unfortunately no multiple digitizing experiments were performed for this region so that an accuracy assessment of glacier outlines is also not feasible for the zone. The outlines derived here are thus prone to higher uncertainties. To get a qualitative impression of the performance of the GGI outlines, an overlay in Google Earth is additionally provided in Fig. 5.2 b) and c). Even though the DEM and the satellite image are from a different point in time, the outlines are consistent.

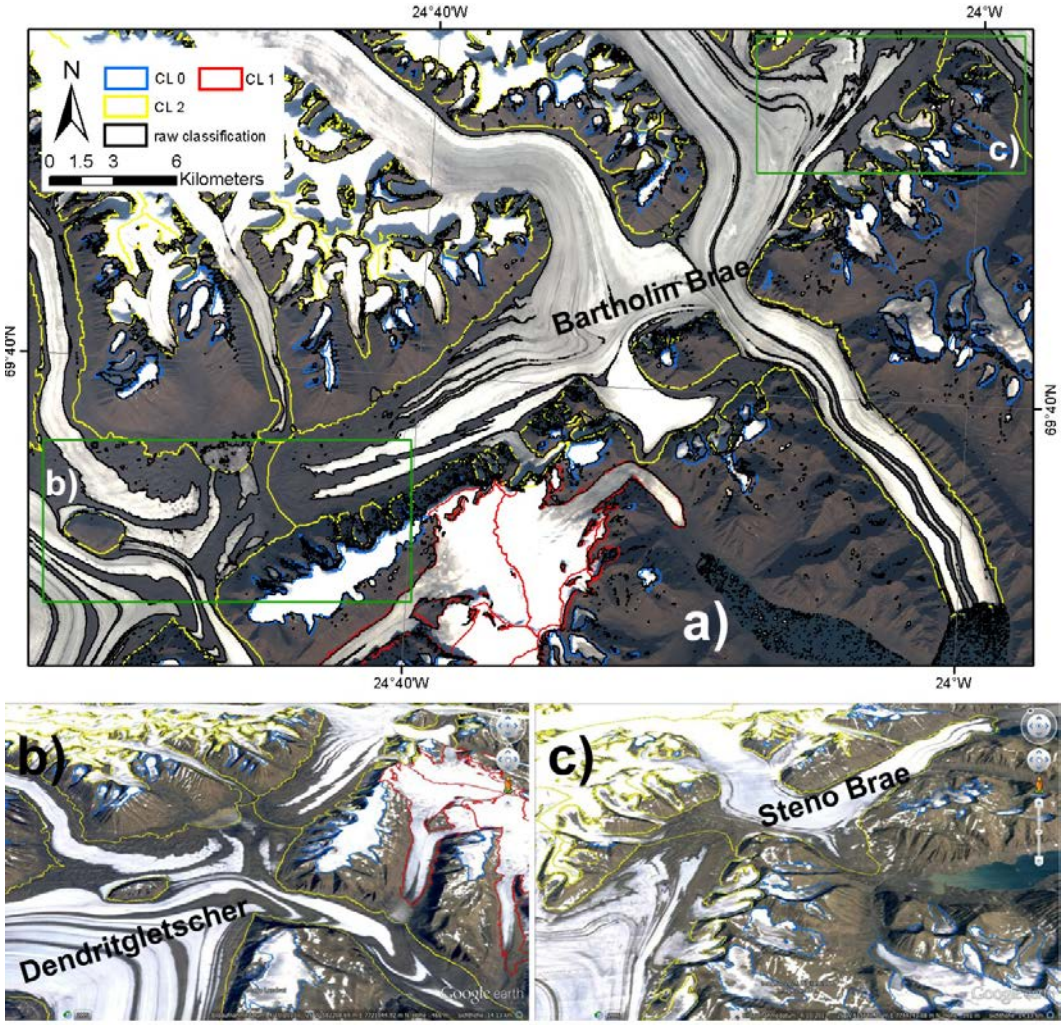

Figure 5.2: The upper image shows an area with glaciers with different connectivity (blue, red and yellow outlines) from the Geikie Plateau in East Greenland. It is overlaid with the raw classification (black outline) to illustrate the high workload of the manual corrections in this area. Fig. 5.2 b) and c) show enlarged subsets of a) (inlets) in a perspective view in Google Earth to highlight the accuracy but also, the difficulty in deriving glacier outlines above debris-covered regions.

5.1.2 Connectivity levels and ice cap rules

The implementation of connectivity levels (CL) in a glacier inventory has not been performed previously, and thus also warrants discussion here. The definition of CL0 glaciers (no connection) is unambiguous, however, for CL1 (moderate connection) and CL2 (strong connection) there is considerable room for interpretation, in particular regarding the heritage rule.

Discussion on this topic in the scientific community reflects the wide range of possibilities which are summarized by Jiskoot in her review of Paper I (http://www.the-cryosphere-discuss.net/6/C1848/2012/tcd-6-C1848-2012-supplement.pdf – page 3): "it could be for instance based on physical processes: these could include shared ice dynamics (e.g. confluence), shared accumulation (divergence), or a connected hydrological system (e.g. sub glacial lakes).

Physically, it also matters whether units are confluent or divergent, even though when either separate both configurations may change from fully- connected to unconnected".

According to this suggestion, it would not be reasonable to have glacier units connected to other units that have been assigned CL1 (or CL2) automatically. The proposed classification scheme would assign GIC a higher number the greater the distance from the ice sheet or outlet glacier is. Glaciers marked with '0' in Fig. 5.3 are tributaries of the ice sheet outlet and glaciers with '1' discharge in the same fjord but do not touch the outlet glacier, and must thus have a different connectivity from the others. Glaciers with a '2' touch glaciers classified as '0' and '1' in the accumulation region and drain into another basin. Further away from the ice sheet, glaciers are classified as '3' because they do not touch glaciers of the classes '0' and '1'. Glaciers with numbering '4' do not touch glaciers of the class '2' because glaciers classified as '3' are in-between, and so forth. This scheme can be extended further, thus giving a gradual classification of glaciers with decreasing numbers towards the ice sheet. This categorization system would lead to the same classification of GIC for CL0 as in the GGI, but glaciers with CL1 connectivity would have another classification. Generally speaking, such a classification is feasible but is very difficult to assign automatically, as mountain ranges would have to be summarized into single sub-regions to always have unique numbers allocated to one glacier. Moreover, in the particular case of long mountain ranges rather high numbers would be required. Though such a scheme might have some practical advantages, it would likely lead to some confusion which we tried to avoid by implementing a simple approach.

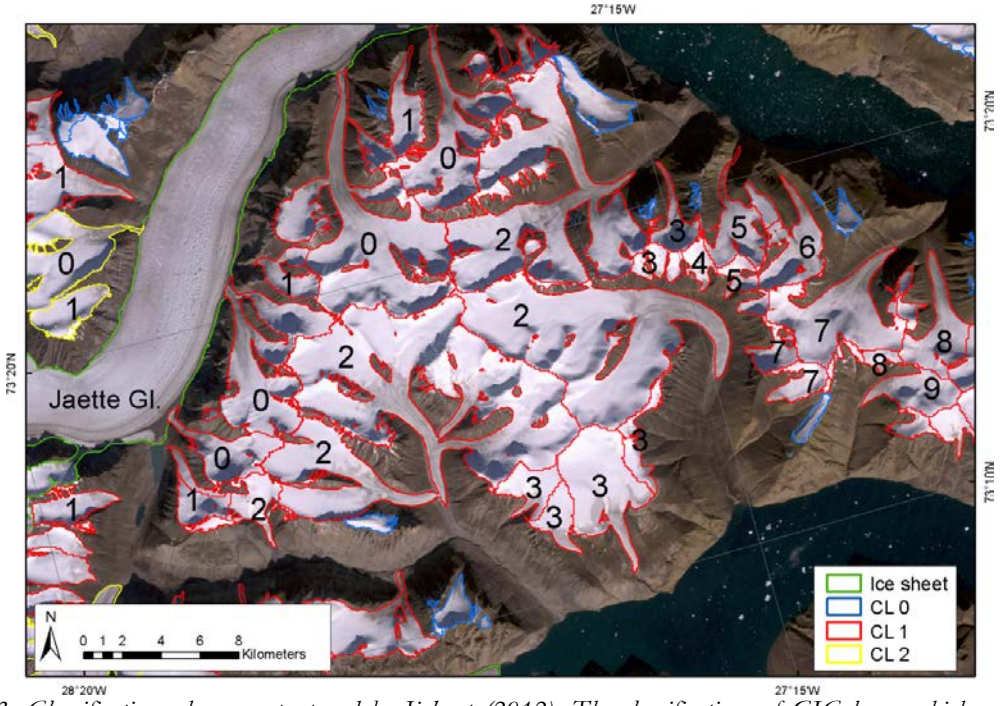

Figure 5.3: Classification scheme as proposed by Jiskoot (2012). The classifications of GIC have a higher number of connectivity the greater the distance from the ice sheet or outlet glacier is. For comparison, local GIC are highlighted by different colours according to the classification in the GGI in the background.

The connectivity levels introduced in the GGI are, however, sometimes also a matter for discussion. This is particularly true for glaciers with CL2 connection. There is, for example, no threshold defining how long an ice divide has to be or how uncertain the ice divides in the accumulation region need to be so that a glacier is classified as CL1 or CL2. This was particularly challenging for the Geikie Plateau region. Most of the glaciers on this plateau were assigned a CL2 connectivity as the location of the drainage divide is highly uncertain owing to the very flat topography in this region, and secondly, the entire region of hydrologically separate ice domes is

strongly connected with the ice sheet in the accumulation region. Furthermore, the plateau is considered by ice sheet modellers as part of the ice sheet (e.g. Fettweis et al., 2013).

The developed ice cap separation rules are a matter for discussion, as other ways of separating can be developed (e.g. Kienholz et al., 2013). However, there is currently no definition of how wide, long or distinct an outlet glacier has to be, or what is seen as topographic variability. This decision is essentially left to the judgement of the analyst, and thus has a high degree of subjectivity. The same is true for the ice cap rule III for the separation of glaciers on mountain flanks into entities. The allocation of CL and the separation of glacier complexes into entities are thus also subjective.

Assessing the impacts of the CL assignment is difficult as no similar dataset in digital form is available. We have thus compared our CL with a manually georeferenced map (see Fig. 5.4) from Weidick and Morris (1998). Their aim was also to propose a classification scheme for the local GIC on Greenland. Interestingly, they classified many more glaciers as being local than in this thesis. For example, they included the Inglefield Ice Cap in the North and Julianehåb Ice Cap in the South, and classified a larger area of the Blosseville and Ammassalik ice caps (central east) as local. Their estimate of the area of all Greenland GIC (70000 km^2), however, is much smaller than our two values for CL0/1 (90000 km^2) and CL0/1/2 (130000 km^2). This confirms that the former estimates of the area of Greenland's GIC were not very accurate.

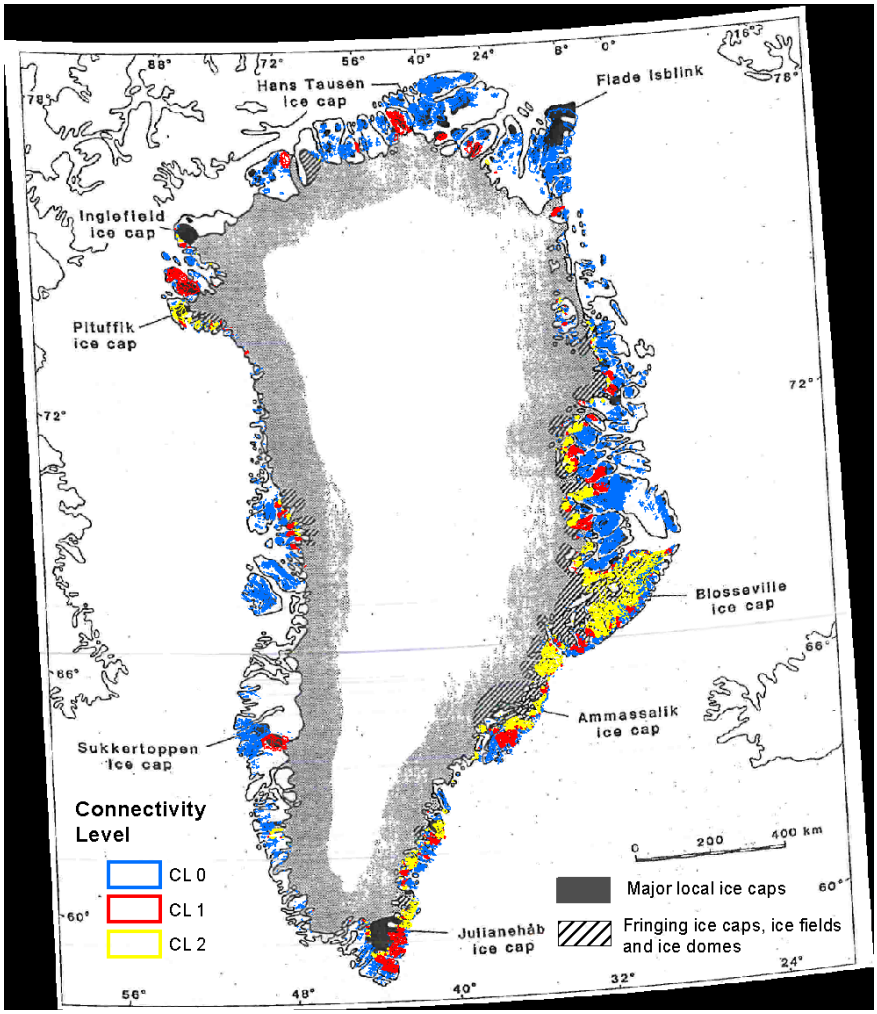

Figure 5.4: Comparison of local GIC from Weidick and Morris (1998) in the background with the outlines by Rastner et al. (2012) in blue, red and yellow. The image shows that Weidick and Morries (1998) classified many more GICs as being local but their area of 70000 km² is much lower than the one published by Rastner et al. (2012).

5.1.3 Ice divides and glacier inventory parameters

In Fig. 5.5 an ice cap in south-eastern Greenland is visualized. The Landsat image is overlaid with raw drainage divides obtained from the GIMP DEM, the ASTER GDEMII and the SPIRIT DEM. Of course, some uncertainty is ubiquitous for all the derived drainage divides. The example shows that the typical variability of the divides on top of the ice cap differ in location by about 1 km (Fig. 5.5; arrow 4). On the other hand, the main ice divides are captured by all DEMs. The only dataset producing realistic basins in the ablation region is the SPIRIT DEM. The latter DEM was, however, not available for the whole of Greenland which is why the GGI has used the GIMP DEM. The GIMP DEM provided good quality basins (Fig. 5.5; arrow 1) and it accelerated the processing speed, as otherwise single ASTER GDEM II data had to be downloaded, mosaiked and reprojected. Moreover, a higher DEM resolution also results in a greater processing time.

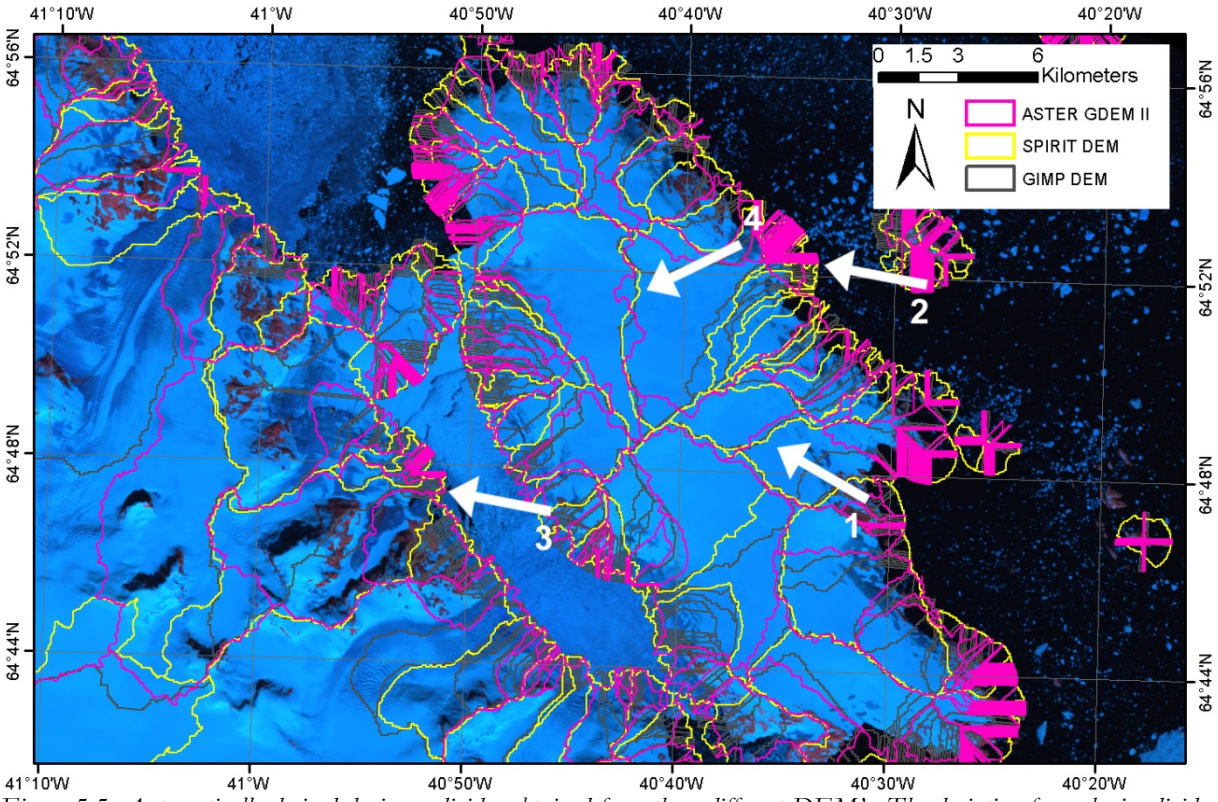

Figure 5.5: Automatically derived drainage divides obtained from three different DEM's. The deviation from the ice divides obtained from the GIMP DEM is quite low (arrow 1) when compared to ice divides derived from higher resolution DEMs. Nevertheless, deviations of about 1km can occur (arrow 4). The lower area of the ice cap contains unrealistic drainage divides (arrows 2, 3). As a result, the processing speed is accelerated, which is a great advantage for large scale inventories.

Apart from the herein applied method of Bolch et al. (2010), other approaches to defining ice divides were presented in the past. The Manley (2008) procedure starts with the median elevation of each glacier and every grid cell below it is considered as a pour point. This approach would lead to wrong assignments when pour points above the median elevation are missed. Moreover, as the median elevation of glaciers varies strongly (see Paper I), neighbouring glaciers would be treated differently. Schiefer et al. (2008) identifies pour points along the outlines of glacier complexes. If the relief between the pour points exceeds a predefined elevation threshold, they are considered to belong to separate glaciers. Their threshold represents a compromise between a lower threshold that identifies multiple termini along undulating glacier tongues, and a higher threshold that fails to detect smaller glaciers. One of the latest approaches was presented by Kienholz et al. (2013). They applied various hydrological modelling tools and a distance-based approach to summarize unrealistic basins like those shown in Fig 5.5 (arrows 2 and 3) based on

neighbourhood analysis.

In general, the accuracy of automatically generated ice divides is heavily dependent on the quality of the DEM used to create them and much less on the algorithm used. The latter has some influence on the remaining workload for manual corrections. Ice divides are accurate in rough topography with steep ridges (if represented well in the DEM), however, in smooth terrain as in the accumulation region of ice caps, they can be rather arbitrary (Fig 5.5, arrow 4). DEM inaccuracies in these regions can be particularly large when optical stereo photogrammetry was used to create them (ASTER GDEM II, SPOT SPIRIT), essentially due to the missing contrast over snow. Inaccuracies are also visible in the flat parts of ablation regions or close to the sea. In such regions the algorithm developed by Bolch et al. (2010) produces large amounts of unrealistic basins which have to be corrected manually (Fig 5.4; arrows 2 and 3).

The accuracy of topographic glacier parameters is an implicit one. They are calculated automatically in a GIS environment, with no interaction of the user (Paul et al., 2009b). The accuracy is thus dependent on the quality of the glacier outlines, which is in particular related to how well the outlines match the DEM with regard to the time of acquisition. Of course, they also vary with the spatial resolution of the DEM and the location of the drainage divides. A more detailed investigation regarding the influence of DEM source and resolution on the derived topographic parameters can be found in Frey and Paul (2011). The latter study revealed that large differences in the values can occur on individual glaciers, but that they average out for larger glacier samples. Parameters that depend on a single DEM value (e.g. minimum or maximum elevation) show a larger variability than parameters that are averaged over the entire glacier area (e.g. mean elevation or mean slope). Moreover, changes due to different acquisition dates and techniques (radar, optical) also have an influence on the inventory parameters. An investigation of these different error sources has, however, not been analysed for the GIMP DEM. But as mentioned above (section 3.1.2), the GIMP DEM has been compiled from data that were acquired in roughly the same period as the glacier outlines (Howat et al., 2014). The 90 m resolution of the GIMP DEM should still provide useful results for the minimum glacier size of the GGI (0.05 km^2).

The area–elevation distribution of the GIC for the seven sectors with 100 m binning reveals a mean elevation of about 1700 m in the eastern sector and around 1000 m elsewhere. This is also the elevation where most of the ice is located. It is significantly lower than, for instance, the glaciers in Alaska where 84% of the ice is located between 600 and 2000 m a.s.l. (Le Bris et al., 2011). The hypsometries of the North and East sector show a more biased distribution of the area, with a sharper peak in a few elevation intervals near the maximum elevation. This is typical for ice caps and rather different from mountain or valley glaciers, which often have large parts of their area at lower elevations (e.g. Manley, 2008; Paul and Andreassen, 2009; Paul et al., 2011b; Svoboda and Paul, 2009). On a global scale (see Pfeffer et al., 2014) the typical ice cap hypsometry is also visible in three regions from the RGI: Arctic Canada North, Arctic Canada South and the Russian Arctic. However, in a worldwide perspective, most glaciers have the main part of their area in the middle of their elevation ranges (Pfeffer et al., 2014).

Mean elevation of a glacier can be seen as a proxy for the equilibrium-line altitude (ELA) that represents balanced budget conditions (e.g. Braithwaite and Raper, 2009). The GICs, with large and high accumulation regions, are those in which a given change in ELA causes the smallest mass balance changes and vice versa. The latter type is also the most sensitive and vulnerable when volume changes of glaciers are considered (De Angelis, 2014), as large parts of the glacier volume are located in the comparably flat and low-lying ablation areas (Linsbauer et al., 2013). In the North-west and South-east of Greenland a large amount of ice is found at low elevations (600 and 800 m, respectively), which indicates that they have a high sensitivity to changes in the ELA (e.g. Nesje et al., 2008).

When the median elevation of the GICs is used as a proxy for the ELA, climatic conditions (e.g. precipitation amounts) can be derived (Ohmura et al., 1992; Oerlemans, 2005). A strong increase in median elevation from the coast to the interior can be seen all around Greenland, with lowest values closest to the coast (0–500 m) and increasingly higher values (up to ~3000 m) towards the interior. Such a strong increase has also been derived for glaciers in Alaska (Le Bris et al., 2011) and Norway (Paul et al., 2011b).

5.2 OBIA for glacier mapping

OBIA is a classification approach for remote sensing images which can be seen as a tool between GIS and image processing. The application of OBIA for glacier mapping has not been tested before, as OBIA is mostly used for land cover classifications on very high resolution imagery (Blaschke et al., 2014). Landsat or ASTER imagery in contrast, have comparably coarse spatial resolutions with a reduced possibility of homogenous objects and often blurred boundaries (mixed pixels). Glaciers, however, are larger features with a generally homogenous and spectrally distinct surface that is represented by a large amount of pixels within these images. An identification of glaciers as objects based on Landsat or ASTER imagery with OBIA seems thus to be feasible and was tested in three regions of the world in Paper II.

OBIA is a kind of a push button methodology enabling further atomization in the mapping, which is a long-standing request of the glacier mapping community (Paul et al., 2013b). The method is based not only on spectral but also on spatial information, thus guaranteeing a high transferability. Moreover, the approach allows quicker creation of glacier outlines, which also became an urgent demand in recent years as glacier changes are accelerating and occurring on faster time scales than estimated. Drawbacks are, for example, related to slightly longer processing times and high initial software costs.

5.2.1 Comparison of OBIA with PBIA

The OBIA approach provided results with statistically higher accuracies for commission (3%) and omission (3%/12%) errors than the PBIA. This is consistent with other studies related to land cover mapping (Castillejo-González et al., 2009; Moosavi et al., 2014; Myint et al., 2011; Whiteside et al., 2011). The main advantages of OBIA compared to PBIA can be attributed to the possibility of considering contextual information (neighbourhood relations) on multiple scales (Blaschke et al., 2014) and of including ancillary data, such as data sets from other sensors, DEMs, or GIS layers, for the classification. This has to be contrasted with the higher workload in establishing the processing line and the cost of the software. The usefulness of glacier classification with OBIA thus critically depends on the specific challenges in the region of interest.

5.2.2 Input bands

Temperature and slope information are important input layers for the initial segmentation. They were particularly useful for the delineation of outlines of debris-covered glaciers that are frequent in the Himalaya (Bolch et al., 2008; Racoviteanu and Williams, 2012; Rastner et al., 2014). Temperature and slope information are not mandatory for the segmentation process in general, but satellite imagery and DEMs are freely available worldwide in a reasonable spatial resolution and can thus be considered. Though the segmentation time is slightly higher in this case, it does not cause more work for the analyst, as the segmentation, classification and post-processing in eCognition is summarized in one processing tree. In a future study it would be interesting to analyze how the segmentation performs with/without the inclusion of the thermal band in regions of bright sunshine (having a small temperature difference from the surrounding area) or in regions with steep shadowed slopes (being cooler than the debris on the glacier). This would

increase the speed of the pre-processing as well as the segmentation process due to fewer input bands being considered. Moreover, it would be interesting to see how the segmentation performs if there are no distinct breaks in slope present.

5.2.3 Mapping glaciers with OBIA

Generally speaking, OBIA shares the key problems of PBIA during glacier mapping. When an object class has a unique spectral 'signature', classification is straight-forward, like the band ratio for mapping of clean ice and snow. As soon as an object class shares spectral signatures with other classes (mixed pixel in PBIA), classification becomes more difficult. But the post-processing possibilities of OBIA are also extremely powerful for classifying objects with a mixed spectral signature. This is promising in particular when shape or neighbourhood relations are distinct. For example, seasonal snow or icebergs can be removed when they are surrounded by specific other objects (other or water in this case) or with a size threshold. In addition, much less noise (the so-called salt and pepper effect) is visible in the final thematic map as OBIA only considers mean pixel values within an object as opposed to individual pixel values (Blaschke, 2010). On the other hand, this means that the classification is not pixel sharp but only object-sharp. If an object is spectrally blurred because some pixels in it belong to another class, its mean value can change in such a way that the entire object is wrongly classified. This can be seen as a serious disadvantage and thus has to be already avoided in the segmentation process.

The mapping of ice and snow in cast shadows and under (optically) thin clouds also causes problems as the spectral information is blurred. The inclusion of a blue band promises to be helpful in such cases (Paul and Kääb, 2005) as already shown in previous studies (Le Bris et al., 2011; Paul et al., 2011b; Racoviteanu et al., 2009). This problem is also a result of the poor radiometric resolution of Landsat and ASTER imagery (8 bit quantization). Current (Landsat 8) and future satellite missions (e.g. Sentinel 2) provide a higher radiometric resolution which may improve the mapping of ice and snow in these regions.

5.2.4 Potential applications for glacier inventories

Several future satellite missions will provide higher spatial resolution than the Landsat data used here. This will result in new details on the glacier surface becoming visible, which may require a different interpretation. In this regard, higher resolution data must not necessarily result in a more accurate delineation of glacier outlines, as the general problems (shadow, debris) are just extended over a larger area (Paul et al., 2013b). In such cases, the application of OBIA might be useful as the approach groups single pixels in larger spectrally homogeneous objects. This means that the large amount of detail visible in high-resolution imagery will be dissolved and after segmentation the imagery can be classified more easily.

A further potential application is the classification of glaciers with OBIA on Landsat 7 SLC-off scenes. The application of a ratio image classifies ice and snow, which results in intersected "ice parts" in SLC-off scenes. They have to be merged manually in a GIS environment afterwards to create one glacier polygon. The latter step could probably be automated with OBIA. Empty stripes of the SLC-off scene normally result in distinct objects, which could be included in the class glacier, based on the relationship to neighbouring objects (i.e. "glacier"). It might also be possible to include slope information to determine the glacier tongue or its lateral boundary. Such morphometric parameters can generally help to determine boundaries of land surface types and thus also glacier borders (Mashimbye et al., 2014).

One of the biggest uncertainties in the creation of glacier inventories and thus also in the GGI are perennial snow patches. Most of these snow patches were deleted by applying a size threshold of 0.05 km^2. Of course, some of the excluded features might indeed be small glaciers so that the calculated number of glaciers is a lower bound. The manual removal of snow patches would

circumvent this problem (Nagai et al., 2014), but this is not really applicable for large-scale inventories. There might be a possibility of detecting them automatically with OBIA by including more selection parameters, such as shape, altitude and slope of the potential snow field and a relation to neighbouring objects. With a related rule-set, objects on steep northern flanks can be classified as glaciers while those which are flat or have a mean aspect facing south are regarded as snow patches.

The possibility of considering the individual shape of features in OBIA could also be interesting for the classification of individual GIC into different glacier types in the GGI (ice cap, valley glacier, circue). The knowledge of the glacier type is important as it determines to some extent the elevation distribution of the area and would support ice volume calculations that have to be performed differently for glaciers than for ice caps (Grinsted, 2013). In general, ice caps and ice fields have most of their volume stored at higher elevations (here they are flat and thus thick) while it is vice versa for valley glaciers (most volume is in the flat and thus thick tongues at low elevations). Such a distinction would also help improve estimates of future ice volume change that are currently assessed by much simpler schemes (Marzeion et al., 2014). Such a classification is not yet implemented in the GGI, as it would have to be done by a manual classification of the more than 20000 glaciers.

5.3 Applications of the Greenland Glacier Inventory

5.3.1 The Randolph Glacier Inventory (RGI)

A glacier inventory for the entire world was already requested during the international hydrological decade (1965-1974) and endorsed by international organizations such as the World Meteorological Organization (2004) and in the IPCC AR4 (Lemke et al., 2007). The GGI and some other recently published inventories, such as the one from Svalbard (Nuth et al., 2013) and Norway (Andreassen and Winsvold, 2012), closed major gaps in unmapped glacierized regions around the world (e.g. Ohmura, 2009). Combined with the already existing glacier outlines in the GLIMS glacier database, this new data situation led to the compilation of a new globally complete glacier inventory, named the "Randolph Glacier Inventory" (RGI), after a small village in the USA where a coordinating group met to plan the work (Pfeffer et al., 2014). The GGI contributed 12% of the total area of the RGI. The worldwide comparison based on the RGI reveals that 45% of the GIC area is located in Arctic regions (Arctic Canada North, Arctic Canada South, Greenland, Svalbard, and Russian Arctic) and 18% in the Antarctic and Subantarctic. High Mountain Asia (Central Asia, South Asia West, South Asia East) accounts for 16% and Alaska for 12% (Pfeffer et al., 2014).

All outlines were assembled over a 2-year period at the University of Alaska in Fairbanks. Most of the glacier outlines in the RGI were derived from Landsat satellite imagery (Landsat 5 TM and Landsat 7 ETM+) acquired in 1999 or later. However, for some regions such as the Chinese glacier inventory, outlines refer to the 1970s or even earlier. While glacier outlines derived from satellite data were mostly mapped by automatic or semi-automatic routines (like for instance the inventory of the Alps and Norway), glaciers were digitized by hand when outlines were taken from maps (e.g. the Chinese and northern Eurasia glacier inventory; cf. Khromova et al., 2014; Shi et al., 2010). Glacier complexes were subdivided into glaciers either by visual identification or flow divides obtained with semi-automated algorithms from Bolch et al. (2010) or Kienholz et al. (2013). The RGI is divided into 19 first-order regions, and 89 second-order regions, derived from

the regions suggested by Radić and Hock (2010). Most of the regional boundaries follow parallels and meridians, but some regions are separated along major drainage divides, for example in the Himalaya (Fig. 5.6) Priority in the RGI was given to complete coverage rather than to extensive documentation, meta-data compilation and quality improvement. Based on this dataset, the total area covered by GIC could be calculated as 727310 ±35685 km^2 for a total number of 195214 glaciers (Pfeffer et al., 2014). The total ice-covered area of the RGI is similar to earlier estimates (Dyurgerov and Meier, 2005; Hock et al., 2009; Radić and Hock, 2010), although these are often not exactly comparable. When the Greenland and Antarctic glaciers are included, earlier estimates differ from the RGI by as much as –6% and +8%. The differences mainly reflect substantial improvement in the sources of information. Rastner et al. (2012) identified considerably more peripheral ice in Greenland than any previous investigation, and Bliss et al. (2013) relied mainly on the Antarctic Digital Database (ADD Consortium, 2000), a more accurate source than those of earlier estimates. The RGI is distributed through the GLIMS/NSIDC website (http://www.glims.org/RGI/randolph.html), and is accompanied by technical documentation showing who has contributed the outlines (Arendt et al., 2013).

The dataset with complete global glacier coverage was specially requested for several global-scale investigations. These include the calculation of global glacier volume (Bahr et al., 1997; Grinsted, 2013), the determination and global up-scaling of mass balance measurements from a range of techniques (DEM differencing, altimetry, gravimetry, field measurements) (Berthier et al., 2010; Bolch et al., 2013; Gardner et al., 2013), and the determination of past and future changes in glacier mass (Bahr et al., 2009; Machguth et al., 2013; Marzeion et al., 2012; Radić and Hock, 2011). All of these studies were cited in the last IPCC report (Vaughan et al., 2013), underlining the importance of such global assessment. The GGI compiled within the framework of this thesis and provided to the RGI could thus also make an important contribution to the IPCC report.

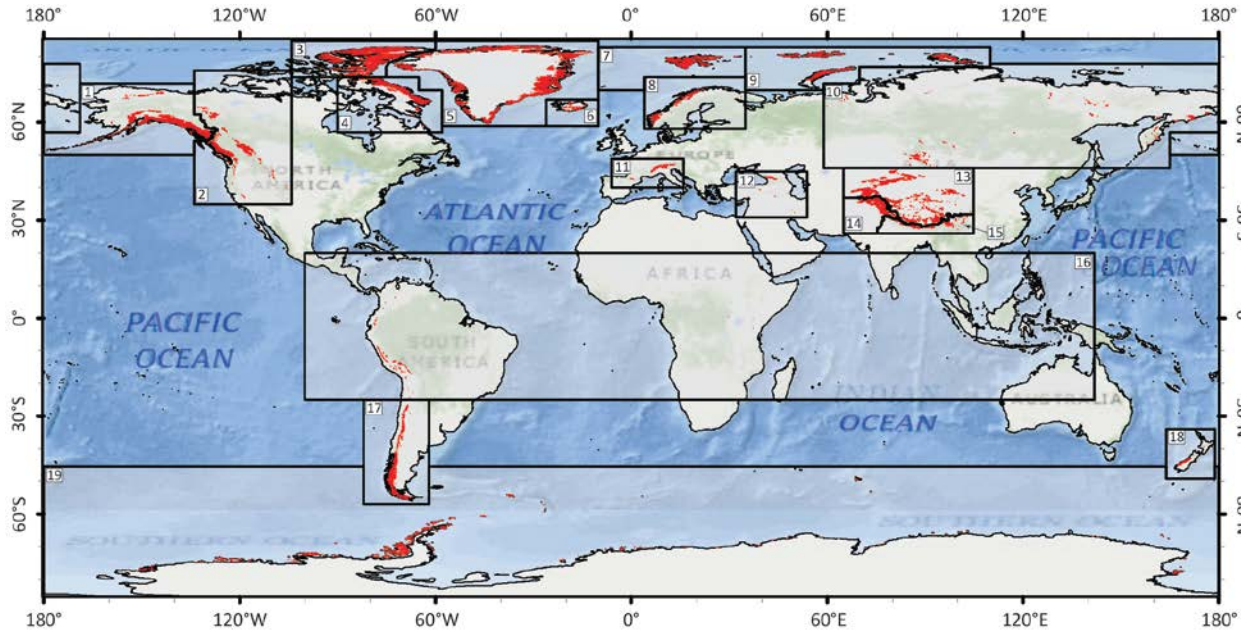

Figure 5.6: First-order regions of the RGI, with glaciers shown in red. Region numbers are those of table 2 in Pfeffer et al. (2014).

5.3.2 Elevation changes

The GGI was applied in Paper III as a glacier mask to a) constrain the ICESat elevation measurements to the local GIC, and b) for determination of elevation, volume and mass changes of marine- and land-terminating glaciers in Greenland (Bolch et al., 2013).

The analysis revealed significantly higher mass loss rates in the wet south east than in the dryer west and even dryer north and north-east of Greenland (Bolch et al., 2013; Gardner et al., 2013). This spatial variability might thus be related to the climatic sensitivity of the glaciers that is largely governed by annual precipitation amounts (see Paper IV). Comparing the results to field measurements is difficult as only few exist. For example, in the Ammassalik region it has been reported that five glaciers completely melted away during the period 1986-2011. All of those glaciers were located at different mean elevations ranging from 460 to 1110 m a.s.l. and with different aspects (Mernild et al., 2012). In the same region, this trend was also recorded by in-situ measurements on Mittivakkat glacier. Between 1986 and 2011 the mean annual net balance was -0.97 ±0.75 m w.e. a^{-1} (Mernild et al., 2013). On Flade Isblink in the far north, the mean surface elevation change was close to zero (0.03 ±0.03 m a^{-1}) between fall 2002 and 2009, which is in line with other altimetry-derived measurements (Bolch et al., 2013; Gardner et al., 2013; Rinne et al., 2011).

Interpreting the median elevation as a proxy for the equilibrium line altitude (ELA) under balanced-budget conditions is a convenient approach for large scale studies (Braithwaite and Raper, 2009). This approximation allows a distinction to be made between the accumulation- and ablation region of a glacier using its median elevation, which can be easily derived from the glacier inventory. This distinction allows a more realistic conversion of surface elevation into mass changes as different density assumptions for the various zones can be applied. For example, values of 410-610 kg/m^3 and 680-790 kg/m^3 are used for the conversion of surface elevation changes to mass changes in the accumulation and ablation region, respectively (Li and Zwally, 2011). Moreover, the assumed densities might also change with the observation period. Huss (2013) recommends a value of 850 ±60 kg/m^3 for analyses of more than five years. For periods shorter than three years he reports that density values may show erratic behaviour with values between 0-2000 kg m^{-3}. The empirical relationship applied in Paper III is derived from a model using mean annual air temperature averaged over larger regions. It provides values within the above ranges that might be seen as being more realistic than prescribed (constant) values for all glaciers, but in the end they are modelled rather than measured and thus also rather uncertain.

These uncertainties are evident when comparing the volume and mass changes obtained from the two independent studies by Bolch et al. (2013) and Gardner et al. (2013). Both studies used the same glacier outlines and ICESat measurement, but the methods applied for deriving volume and mass changes differed. In Paper III a mass loss of CL0 and CL1 glaciers of -27.9 ±10.7 Gt a^{-1} and a volume loss of about ~40 km^3/a have been calculated whereas in Gardner et al. (2013) a mass loss of -38 ±7 Gt a^{-1} and a volume loss of ~42 km^3/a were determined. While their estimate of volume loss is approximately the same, their mass loss estimate differs greatly (+27%), but still falls within their uncertainty bars. The study by Gardner et al. (2013) uses an average density of 700 ±200 kg m^3 in the accumulation and 900 ±17 kg m^3 in the ablation area. In contrast, in Paper III a regionally variable firn density for the accumulation regions (north-west 528 kg/m^3, east-south 796 kg/m^3) was used, and below the median elevation the standard density of ice (900 kg/m^3) was applied. Moreover, the size of the accumulation region is only 1/3 of the total area in the study by Gardner et al. (2013) while Bolch et al. (2013) uses 1/2.

An additional source of uncertainty for the mass change rates derived in Paper III is the large horizontal distance between neighbouring ICESat tracks in the South of Greenland. The observed strong surface elevation changes in the South might be biased by ICESat due to low point density and hence a low number of measurement values. Though mass change results from GRACE confirm the general pattern of mass loss trends derived here for GIC only, GRACE results are too coarse to resolve individual mountain ranges (Velicogna, 2009). The determination of surface elevation changes from the GIMP DEM and the ASTER GDEM II would be possible from a technical point of view, however, acquisition times of both DEMs are unknown and mean annual changes can thus not be calculated. Another possibility for retrieving elevation

changes from the local GIC is the creation of DEMs from stereoscopic image matching techniques using aerial images acquired in the past, in comparison with current DEMs (e.g. Kjaer et al., 2012). However, this is difficult as historical imagery around Greenland is often lacking, hard to access, and a high manual workload has to be taken into account for the generation of orthorectified mosaics and DEMs.

The specific mass changes calculated for all GIC of Greenland (-0.31 ±0.12 m w.e. a^{-1}) are comparable to other arctic regions. For instance, glaciers on Svalbard lost about −0.12 ±0.04 m w.e. a^{-1} for the period 2003-2008 (Moholdt et al., 2010), and for the glaciers on the Canadian Arctic Archipelago the loss was -0.41 ±0.05 m w.e. a^{-1} from 2004-2009 (Gardner et al., 2011). When focusing on the same region (all local GIC on Greenland), absolute changes for SLE can also be compared. A contribution of 0.12 ±0.05 mm a^{-1} for all GIC and 0.08 ±0.04 mm a^{-1} for CL0 and CL1 GIC for the period 2003-2008 could be retrieved. For the period 2005-2009, Cogley (2009b) and Marzeion et al. (2012) derived values of 0.15 ±0.03 mm SLE a^{-1}, whereas the study by Gardner et al. (2013) revealed 0.10 ±0.02 mm SLE a^{-1} for 2003-2009. This is about 10% of the estimated contribution from the world's GIC to sea level. Values estimated for the future depend on the climate scenario used but are in the same order of magnitude. Machguth et al. (2013) obtained up-scaled contributions between 0.05 and 0.11 mm a^{-1} for the period 2000 to 2098, while Radić et al. (2014) obtained annual mean values from 0.13 to 0.21 mm a^{-1} for the period 2006-2100, and Giesen and Oerlemans (2013) established 0.15 a^{-1} mm as a mean over the 2000-2099 period.

5.3.3 Glacier sensitivity to climate

In Paper IV climatic and mass-balance sensitivities have been calculated for ten sectors based on observed mass changes and time series of temperature and precipitation from downscaled reanalysis and weather station data for all GIC on Greenland.

The term climate sensitivity is not used consistently in glaciology. Therefore, a key issue in Paper IV was to discriminate between climate sensitivity and mass balance sensitivity. The climate sensitivity is related to mean climatic conditions (e.g. annual precipitation amounts governing mass balance gradients) and to geometric glacier characteristics (e.g. mean slope influencing the response time). The climatic sensitivity describes in a generalized way how glaciers in a maritime climate, characterized by high amounts of precipitation (P) and relatively high temperatures (T) react more sensitively to a given change in climate than glaciers in continental regions (e.g. Braithwaite and Zhang, 1999). This is mainly a result of the required higher mass turnover and hence mass-balance gradients in a maritime environment, both also implies a strong feedback of temperature on (solid) precipitation (Oerlemans and Fortuin, 1992; Oerlemans and Reichert, 2000). The climate sensitivity is of interest for studies where mass balance gradients are derived from precipitation amounts, for example to reconstruct temperatures of the past from glacier length fluctuations and response times (Leclercq and Oerlemans, 2011; Oerlemans, 2005).

The mass balance sensitivity (MBS) on the other hand is a more mathematical term that describes how the mass balance of a glacier changes with a given change in temperature (in general +1°C) and precipitation (+10%). The MBS also depends on the mass balance gradient (and is thus closely related to climate sensitivity), as well as on glacier hypsometry (Furbish and Andrews, 1984), i.e. its value changes when the geometry of a glacier changes (Paul, 2010). This sensitivity is generally derived from modelling studies, for example using a distributed mass-balance model (Anderson et al., 2010; Braithwaite et al., 2013; Klok and Oerlemans, 2002; Oerlemans, 1981; Vincent, 2002), but analytical approaches have been applied as well (e.g. Kuhn, 1985). The advantage of models is that temperature and precipitation can be changed either uniformly or for selected time periods, such as for individual months or seasons. Thus, the impact of seasonal changes in climate can also be investigated using so-called seasonal sensitivity characteristics

(Oerlemans and Reichert, 2000). Mass-balance modelling has shown that approximately a 30% increase in annual precipitation is typically needed to compensate for the mass loss due to a uniform 1 K warming (Braithwaite and Zhang, 2000; Oerlemans, 2001). Of course, there are local differences, as several studies suggest that precipitation has to increase by 27-38% in Norway (Laumann and Reeh, 1993), around 20% for glaciers in Switzerland (Braithwaite and Zhang, 2000), by 30-40% for the whole Alps (Braithwaite et al., 2013) and about 50% for instance for glaciers lying in very maritime areas like New Zealand (Anderson et al., 2010).

The MBS can also be derived from long term field observations, as shown in the study of Braithwaite et al. (2013), by using long-term field observations of mass balance performed on eight glaciers in the Alps in combination with 13 long-term temperature time-series obtained from weather stations (WS). In Paper IV of this thesis, the MBS was also computed from observed mass balance data (derived from satellite altimetry) and temperature and precipitation data as derived from gridded reanalysis data. However, the MBS was calculated only for temperature but not for precipitation as no clear change in precipitation could be found for the last 30 years in Greenland and large uncertainties in the measurement and modelling of precipitation have to be considered (Sevruk et al., 2009). The study shows a temperature increase of 1 K for the South-east and more than 1.5 K in other regions of Greenland. The precipitation trends show a slight decrease of about 2% and an increase of >7% in the sector West-central Greenland. This is probably too small to compensate for the temperature increase in this region.

Due to the size of the study area and the datasets available, both types of sensitivities were analyzed using sector mean values instead of individual glacier sensitivities. This also permits a better comparison of the large-scale variability. If median elevation is interpreted as a proxy for precipitation, a strong decrease in climatic sensitivity can be expected from the coast into the ice sheet, as median elevations strongly increase (and precipitation thus decreases) with distance from the coast (Burgess et al., 2010; Rastner et al., 2012). This change in sensitivity is erased by sector-wise averaging. This also applies to the calculated sector averages of the MBS. Though these are in line with values reported from other Arctic regions (e.g. De Woul and Hock, 2005), the wide range of individual glacier sensitivities is averaged out. Moreover, their determination is based on a calculation of a continuous temperature time-series from sparse input data and its increase is interpreted as the driver behind the measured mass changes. However, the approach worked well for the European Alps (Braithwaite et al., 2013), where glaciers reacted to a quasi step-change in temperature increase in the mid 1980ies, but cause and effect are not necessarily the same in Greenland.

Both glacier sensitivities are not only different in various geographic locations but also different at various altitudes on a glacier. The sensitivities related to altitude were not analysed in Paper IV, because they were investigated over large sectors. The fact that sensitivity differs with altitude was highlighted by Vallon et al. (1998), during a study performed on glacier d'Argentière in the Mont Blanc region. The study shows that (a) the annual mass-balance fluctuations are dependent on elevation and (b) the MBS to temperature decreases with altitude. This is also underlined by Marzeion et al. (2014) who quantified equilibrium sensitivities of global glacier mass to climate change. In this study they rely on the RGI glacier outlines and include the adjustment of changes in the glacier hypsometry as a consequence of long-term mass changes. They state that the adjustment in a glacier's geometry (retreat to higher elevations) reduces the rates of global glacier-mass loss with time. This is also confirmed by other authors (Braithwaite and Raper, 2002; Braithwaite and Zhang, 2000; Paul, 2010; De Woul and Hock, 2005).

Changes in the slope of a glacier also influence its climate-sensitivity. If a relatively flat valley glacier experiences a small increase of the ELA, a comparably large part of the glacier turns into ablation zone and is thus prone to increased melt (Jiskoot et al., 2010). In contrast this effect is small for steep glaciers (Oerlemans, 2005). These geometry changes over time also motivate one

to consider dynamic instead of static sensitivities (e.g. Marzeion et al., 2014; Radić and Hock, 2013). Static sensitivities, as used in Paper IV, neglect changes in glacier size and geometry, mass-balance elevation feedback and dynamic imbalance. They only refer to the change in area-weighted average mass balances (Braithwaite and Zhang, 1999; De Woul and Hock, 2005) and have thus limited applicability for future scenarios, i.e. they are valid only for a few decades.

A problematic issue in the method of retrieving the MBS in Paper IV is the length of the compared periods in a climatological context and the lack of a reference point for temperature in the interval A in Paper IV. On the one hand, a time period from 2003-08 is used for mass balance changes, which is rather short and subject to climate variability, and on the other hand, a time period of more than 30 years (1980-2011) for climatological parameters is used which is long enough and influenced by trends and variability. In these 30 years a continuous positive trend in temperature is visible, however, no distinctive or sudden change is visible. This limits the definition of a reference point for temperature and thus the derivation of a temperature change. This is different for the Alps where a natural break in MB is visible, facilitating the definition of two periods for comparison (Braithwaite et al., 2013). Additionally, there is a lack of mass balance data for the 1980-1995 period and MB can only be assumed to be zero for the different sectors in Greenland before the observation period. Linking thus such a short period of MB data with a normal climatic period can be problematic due to different adjustment times of the heterogeneous GIC in the study area.

The MBS of a glacier is variable throughout the year as the contribution of solid precipitation and temperature to mass gain and loss is also variable. Oerlemans and Reichert (2000) proposed therefore to analyse the dependence of the mass-balance on monthly anomalies in temperature and precipitation. For instance it has been shown that GIC in maritime climates (e.g. south-east Greenland) are more sensitive to winter than summer precipitation, as the latter falls as rain for most of the glaciers and does not contribute to mass gain. With an extended melt season at the lower part of a glacier, a future temperature increase in the winter months can lead to continuous melt and a more negative mass balance (De Angelis, 2014). This is because of year round melt on the tongue and the reduction in the fraction of precipitation falling as snow.

The GIC in the sectors East-central and East-north are found between the wet climate in the South and the dry North. The topography in these areas is more mountainous and higher so that accumulation areas cover a larger altitudinal range. As a result, the slight increase in summer precipitation (East-central +2%, East-north +4%) still can make a contribution to the annual balance. The effect of temperature on GIC in the very far north of Greenland is restricted to a few summer months. Mean temperatures in the summer range from about 4 °C in the North-east to 3.7 °C (North-west) and 2.3 °C in the North-central part. For the GIC in the north of Greenland it doesn't matter in what month an increase in precipitation takes places as apparently all precipitation is likely to fall as snow. Summer temperature is thus an important factor for glaciers in a cold and dry climate (Oerlemans and Reichert, 2000). For glaciers in a wetter climate, spring and fall temperature can also make a significant contribution to the overall sensitivity as it governs the percentage of snow being part of the total precipitation (Oerlemans and Reichert, 2000).

Besides the conceptual limitations of this work, the coarse spatial resolution (e.g. 11 km in RACMO2) is also simply too rough to work on a glacier by glacier basis (Fig. 5.7). In particular precipitation patterns in regions of complex topography or of heterogeneous land cover are variable and might even be enhanced by the topography. The uncertainty in reproducing temperature and precipitation values is probably also related to the internal deficits of the RACMO2 physics and an underestimation of topography in the RACMO2 DEM (Fig. 5.8). While the elevation differences per sector could be corrected with a specific lapse rate, precipitation values have not been touched and could be erroneous, i.e. MBS as derived here

should not be overinterpreted, it is only a first guess.

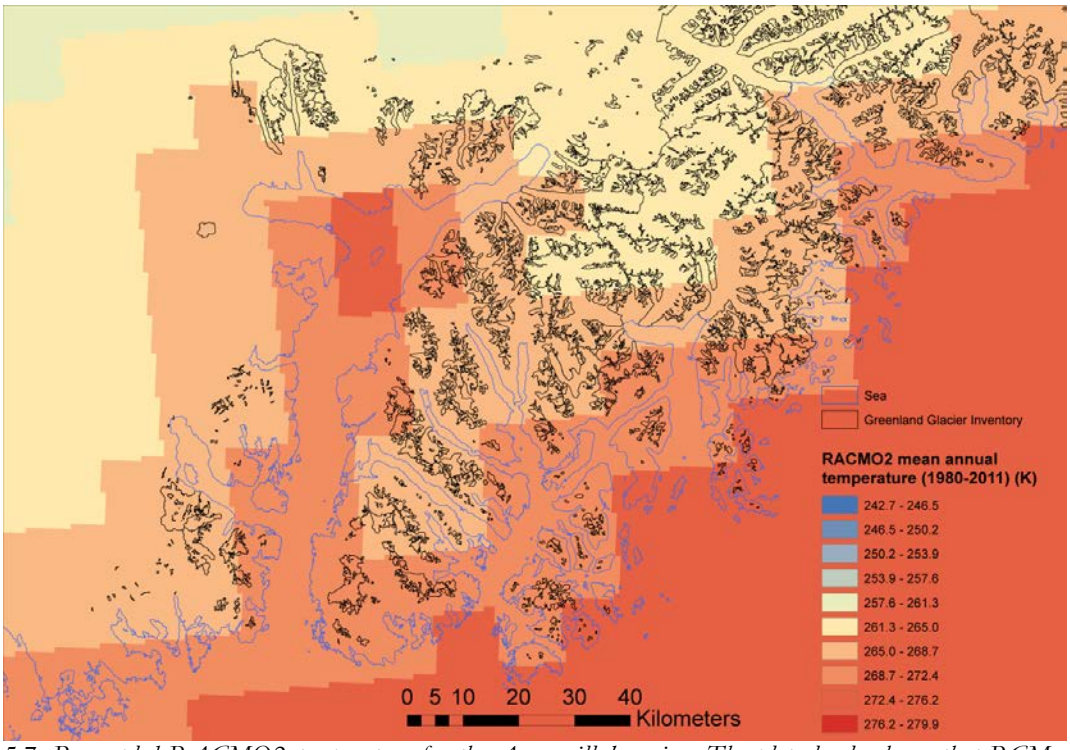

Figure 5.7: Resampled RACMO2 temperature for the Ammasillak region. The plot clearly shows that RCM grids in RACMO2 are still too coarse for local GIC, thus giving too high T values.

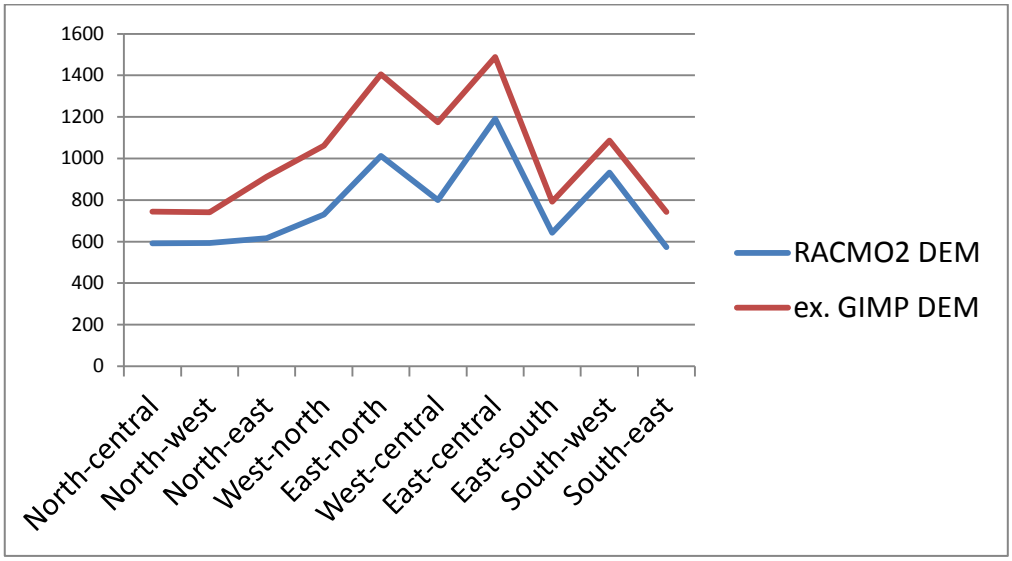

Figure 5.8: Mean elevation difference per sector between the extended RACMO2 DEM and the ex. GIMP DEM (both resampled to 1000 m)

Together with the rough DEM it might also be possible that the internal land cover map in RACMO2 is erroneous and thus influences temperature values by calculating wrong heat fluxes. Using a relatively coarse dataset representing soil types, GICs are too small to be resolved and treated as land surface, leading to higher *temperature* values over glaciers. Ettema (2010) confirms that the model surface includes the ice sheet but excludes most peripheral ice caps. In Fig. 5.9 the

mean ice concentration per sector has been calculated by zonal statistics based on the RACMO2 internal soil cover map and compared with the area of CL0 and CL1 GIC from the GGI in each sector. It is clear that the ice concentration is severely underestimated in each sector, in particular in the West-north sector (covering only 13%).

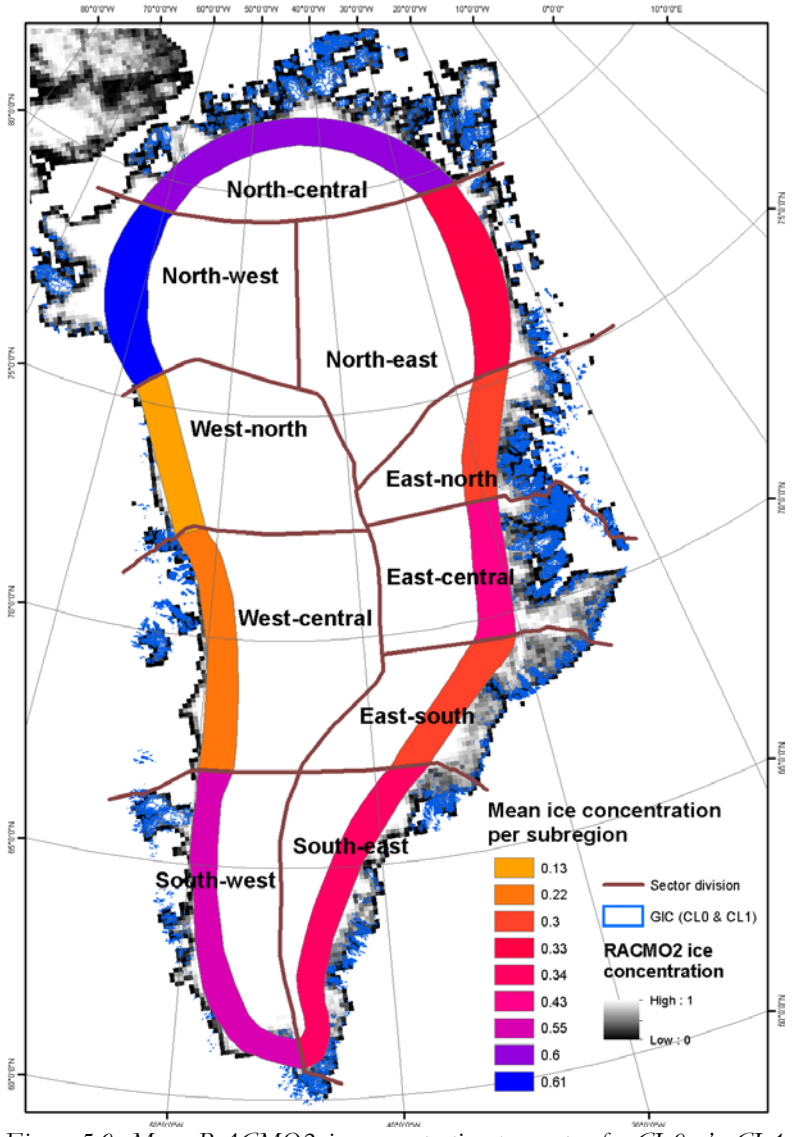

Figure 5.9: Mean RACMO2 ice concentration per sector for CL0 & CL1 GIC. The plot shows that GIC are clearly underrepresented in the RACMO2 ice concentration mask in each sector

However, considering the limitations of the available climatic input data (spatial resolution, correctness of the values) one can argue that the sector-averaging performed in Paper IV might be the only useful way of working with the climate data. Calculating the mass balance as well as the climatic sensitivity on a glacier-by-glacier basis can be seen as a far stretch of the input data that might lead to arbitrary results.

5.4 Results achieved in the context of ongoing studies and research

During this thesis many research questions could be addressed and answered. Some of them enabled a better insight into the initial research questions of this thesis but others generated new questions. Some of these new issues are discussed in the following.

The GGI was an important dataset for answering many open research questions, such as the spatial extent of the GIC and their separation from the ice sheet. Nevertheless, the GGI has still some issues requiring attention. Starting from the data input, the most northern part of Greenland (north of 80°N) was not mapped by Landsat satellite imagery due to coverage limitations. The same is valid for the extended GIMP DEM. A gap was also observed for the most northern part of Greenland. These data limitations result in less reliable information provided by the GGI in these regions. This drawback of data availability is, however, rather common for studies in the Arctic. Other research activities too, like the retrieval of melt ponds on Arctic sea ice (Rösel and Kaleschke, 2011) or the production of a land cover map for northern Canada suffered from a lack of data in the most northern parts (Olthof et al., 2009). In this regard upcoming satellite data like those from Sentinel 2 (Drusch et al., 2012; Malenovský et al., 2012) or a globally complete DEM (Gruber et al., 2012) are an urgent need for researchers. With the new Landsat 8 and the future Sentinel 2 satellites a higher spatial (−56° to +84°) and temporal (up to 5 days with Sentinel 2a and 2b) coverage with a 12 bit radiometric and a 10 m spatial resolution (from Sentinel) will be available for the most northern parts of Greenland as well as most other regions on the planet. This data can hopefully be used to better determine small perennial snow fields (Fontana et al., 2010) thus distinguishing them from glaciers (Paul and Andreassen, 2009; Paul et al., 2009b). Most likely, they will also facilitate glacier mapping as more acquisitions with good snow and cloud conditions will be available. Consequently, a unique scene covering the entire region at a particular acquisition date might become available, which is currently difficult to find in the northeastern part of Greenland. The same is true for the topographic parameters derived by zonal statistics from the extended GIMP DEM. Currently it is not possible to determine the year of the calculated parameters of any region in Greenland, as the extended GIMP DEM is a composite of several datasets and includes only averaged elevation data over the period 2003–2009 (Howat et al., 2014). Glacier geometry changes through time are also an issue for the assignment of connectivity levels (CL). Most likely, several glaciers will fall into a new CL class in the future. Moreover, it is currently not possible to apply an automatic method for the assignment of CLs, as, for example, the length of an ice divide or a clear definition in terms of topographic variability has to be elaborated. This also limits the transferability of the method to other regions or the performance if it is applied by another analyst.

Regarding image classification, this thesis showed that the OBIA approach can be recommended for glacier mapping, in particular if large debris-covered glaciers are present. This could be of interest in mapping the debris coverage for all glaciers in Greenland, as this influences their energy balance, dynamics and response to climate change (Mihalcea et al., 2006; Scherler et al., 2011; Stokes et al., 2007). These debris-covered parts of a glacier can be mapped comparably accurately with the developed approach, thus helping to reduce workload for manual editing. However, there is still a need to verify whether it is possible to run the process tree with batch processing so that a large amount of data can be analyzed effectively. One solution could be using the eCognition Server software, which enables overlapping tile processing as other studies have shown (Groom et al., 2013; Meneguzzo et al., 2013; Ranson et al., 2011). Moreover, the performance of the developed process tree should be tested with the new Landsat OLI and forthcoming Sentinel 2 MSI sensors. Previous studies have shown that the usage of the blue band

for mapping ice in shadow (e.g. Winsvold et al., 2014) increases the accuracy of the resulting glacier outlines (Paul and Kääb, 2005). Therefore, the new blue band (OLI 1) should be incorporated in the process tree, and the performance of the new band 1 of OLI compared to OLI band 2 (the traditional blue band) needs to be tested. Finally, an investigation of the mapping accuracy could be performed for multi-temporal and multi-scale satellite data (for example the combined use of MODIS with Landsat or other high resolution satellite imagery) as well as the impact on accuracy when considering ancillary soil and topography data as shown in the study of Li and Chen (2005).

One major drawback identified in paper IV and in other studies was the resolution of the RCM used to provide climatic data for an entire region (Boberg and Christensen, 2012; Kapnick et al., 2014). During the processing, it was revealed that the spatial resolution (horizontal), the resolution of the internal DEM (vertical) and the internal land cover map are likely major reasons for the questionable results. A higher DEM resolution would lead to a greater number of high and low elevation grid points in each sector, thus representing topography in more detail. This, together with improved information about land cover (i.e. a realistic percentage of the region covered by ice in each RCM cell), could improve the calculation of energy fluxes (Pielke, 2005; Wilson and Henderson-Sellers, 1985) which may improve the data for temperature and precipitation. Moreover, such RCMs would help to better model glacier facies (Benson, 1962), mainly regarding the modelled surface albedo (governs the amount of absorbed solar energy). RCMs could further help to derive density values for firn and snow, help in the calculation of densification trough time (Reeh, 2008) and facilitate the understanding of the impact on impurities on glacier surfaces (Hörhold et al., 2012).

After all, it is also of major importance to maintain existing and enlarge current field measurements in various glacier zones, altitudes and time periods. This is especially true in Greenland 's percolation zone, where firn density profiles are rare (Brown et al., 2012). Taken together, new datasets like the GGI and the RGI from remote sensing data, improved input data like the forthcoming World DEM from the TanDEM-X mission, advances in theory, improved modeling, and new methods for combining models and observations can be expected to provide improved RCM output in the future (Hawkins and Sutton, 2009), which will also provide more reliable results for several downstream applications like mass balance modeling or determination of the glacier melt contribution to sea level (Ettema et al., 2009; Radić and Hock, 2013).

6 Conclusions and outlook

6.1 Conclusions

This thesis demonstrated that the data, tools and methods available today can considerably improve our knowledge about the glaciers on Greenland and their changes. With the creation of the first complete inventory of the local GIC on Greenland - that was compiled using freely available satellite data and DEMs – the basis for a large amount of further studies was set, within this thesis but also by other researchers. Combining the well-established methods for glacier mapping and drainage divide calculation enabled the creation of an inventory at the level of detail and accuracy requested by the science community. Three connectivity levels with the ice sheet were defined (CL0: no connection, CL 1: weak connection, CL2: moderate connection). The total areas derived here (~89720 ±2781 km^2 for CL0 and CL1, ~130076 ±4032 km^2 incl. CL2) are about 50% and 100% larger than the mean value (~62600 km^2) of the more recent previous estimates that included the two ice domes Julianehåb and Inglefield. Hence, the previous estimates have severely underestimated the area of the local GIC on Greenland.

The new glacier inventory for Greenland closed a prominent gap in the global inventory and made it possible to create the first globally complete inventory (the Randolph Glacier Inventory, RGI) in a given amount of time. It was thus used a lot for modelling studies serving the latest IPCC report (AR5) with the most accurate numbers on global glacier volume or past and future mass changes (Gardner et al., 2013; Giesen and Oerlemans, 2013; Grinsted, 2013; Huss and Farinotti, 2012; Marzeion et al., 2014; Radić and Hock, 2011).

The creation of the glacier inventory for Greenland was time-consuming due to a large amount of manual work related to the manual correction of glacier outlines (e.g. in regions with debris cover, shadow, and seasonal snow). It was thus investigated whether object-based image analysis (OBIA) with its special post-processing capabilities (e.g. consideration of semantic rules and neighbourhood classification) could reduce the workload compared to the traditional pixel-based classification (PBIA). Classification with OBIA clearly outperformed PBIA under challenging mapping conditions and could thus indeed help to reduce workload, though some manual corrections were necessary as well. Unfortunately, the high expert knowledge and licence costs for the software limit its global applicability.

The new inventory was also utilized for further investigations that could not be performed before. Using the freely available data provided by the ICESat laser altimeter in combination with the GGI allowed us for the first time to determine the volume and mass changes for all GIC on Greenland separately from the ice sheet. It was found that the GIC with CL0 and CL1 connectivity lost 27.9 ±10.7 Gt a^{-1} between October 2003 and March 2008 and all GIC lost 40.9 ±16.5 Gt a^{-1} (0.12 ±0.05 mm a^{-1} sea level equivalent). This is about 15% of the total mass loss from Greenland (including the ice sheet) and nearly 10% of the estimated sea level contribution from all glaciers. The loss was highest in the south-eastern and lowest in northern sectors of Greenland. Elevation changes of land- and marine-terminating glaciers were rather similar.

In another study that is part of this thesis climate data derived from an RCM (used for downscaling of re-analysis data) were combined with the volume and mass changes from Paper III to determine the climate and mass balance sensitivity of the GIC on Greenland. A

significantly high correlation with the mean annual temperature (R=0.69) and a still substantial one with mean annual precipitation sums were found (R=0.56). This confirms that the observed pattern of mass changes can indeed be related to the climatic sensitivity of the glaciers in the respective sector. The mass balance sensitivity was only calculated for a temperature change as no trends in precipitation during the analysed time period (1980-2005) were found. The values obtained were high in the South-east and East-south sectors (-1.23/-0.77 m w.e. a^{-1} K), and rather low (< -0.28 m w.e. a^{-1} K) in the other sectors of Greenland.

The work performed during this thesis was funded by application-oriented projects like the EU FP7 project ice2sea (Vaughan, 2013) and the ESA Glaciers_cci project (Paul et al., 2013a). This allowed the generated datasets to be made freely available to the scientific community and their use for several further applications. Despite the requirement to locally further improve the generated dataset (e.g. in regions with seasonal snow or for the GIC in the very north) and seek consistency of drainage divides obtained by other algorithms, several methodological improvements and further data analysis can still be performed (see next section).

6.2 Outlook

In the following, a number of further investigations are listed that could not be accomplished within this thesis, but offer exciting potential for in-depth analysis. An overall summary and outlook is provided at the end.

GGI: There is still considerable room for improvement in the GGI. For instance a distinction between different glacier types should be included, as this is important for modelling the glacier response to climate change. Subsequently some drainage divides, especially near glacier tongues, could be adjusted and increased to facilitate area change assessments. The currently still reduced quality of the outlines in the very North of Greenland (not covered by Landsat) should be improved. Finally, topographic attributes have to be added and the final GGI has to be converted to the GLIMS format and integrated into the GLIMS database.

Area changes of the local GIC: The GGI could be used to study area changes of the local GIC, in particular because vector outlines from the 1980s (aerophotogrammetric map) are available for the whole of Greenland. Also Landsat imagery is available for the mid-1980s, Landsat 8 has just started to create a recent snap shot and trimlines from the little ice age can be digitized in many regions.

Length changes of the local GIC: With the recently developed promising approaches to calculating glacier flow lines automatically and thus to deriving length changes based on the digital intersection with glacier outlines from a different point in time, knowledge about glacier fluctuations in Greenland can be extended in space and time. A comparison of changes from marine- and land-terminating glaciers would also be of interest.

Mapping glacier zones: Landsat 8 has and Sentinel 2 will have an increased radiometric resolution of 12 bit which opens up new perspectives in the mapping of glacier zones, in particular in distinguishing snow from ice. In combination with a distributed mass balance model the maps of snow-covered area might be used for deriving mass balances and precipitation amounts over large glacier samples.

Real-time glacier applications: The Sentinel 2 mission will be a constellation of two optical satellites with a repeat interval of five days. This would enable near real-time applications, like the

derivation of snow lines (e.g. for hydrological modelling) or flow-speed monitoring for fast-flowing glaciers. The shorter repeat interval would also increase the chance of acquiring cloud-free scenes without seasonal snow.

Volume change from DEM differencing: The future global availability of a detailed high-quality DEM from the TanDEM-X mission will improve the accuracy of the derived drainage divides and topographic parameters as well as providing a new way of deriving volume changes and thus mass balance of the GIC on Greenland over a longer time period. Potential DEMs from earlier points in time include specific ASTER-derived DEMs and those from the mid-1980s compiled by the University of Copenhagen.

Firn compaction and densification models: Assumptions about ice density and modelling of firn compaction and densification still have high uncertainties. In view of an intensified measurement program and new glaciers with mass balance measurements (e.g. Freya Glacier on Clavering Island) a better process understanding might help to further improve the related models. This would also be important for converting the satellite-derived volume changes (e.g. ICESat) mentioned before, into mass changes.

The present thesis was a big step forward in the field of Arctic glaciology. The creation of the GGI and the assignment of three different connectivity levels to all GIC made it for the first time ever possible to investigate the local GIC on Greenland separately from the ice sheet. As they are remote and difficult to access in the field, the GGI provides an important baseline for all forthcoming glaciological investigations (area changes, volume estimates, future evolution, upscaling of sparse field data). Moreover, the big picture of the worlds GICs could finally be achieved and a much improved assessment of their number, area, volume and contribution to present and future sea-level changes was possible. This was a huge step forward in the latest IPCC report (AR5).

Of course, after the work is finalized new questions arise and new data and methods constantly emerge (e.g. the automatic calculation of central flowlines). They will further improve our knowledge (more details and better statistics) about the local GIC on Greenland in the future. The quality of the derived data is, however, only assured when a combination of different approaches and datasets (e.g. field data, remote sensing and modelling) is applied.

7 References

Abdalati, W., Krabill, W., Frederick, E., Manizade, S., Martin, C., Sonntag, J., Swift, R., Thomas, R., Wright, W., and Yungel, J. (2001). Outlet glacier and margin elevation changes: Near-coastal thinning of the Greenland ice sheet. Journal of Geophysical Research: Atmospheres *106*, 33729–33741.

Aðalgeirsdóttir, G., Stendel, M., Hesselbjerg Christensen, J., Cappelen, J., Flemming, V., Helle, A.K., Mottram, R., and Lucas-Picher, P. (2009). Assessment of the temperature, precipitation and snow inthe RCM HIRHAM4 at 25 km resolution. Danish Climate Centre Report 09-08, Copenhagen: Danish Meteorological Institute 1–80.

ADD Consortium (2000). Antarctic digital database, version 3.0, database, manual and bibliography (Cambridge, UK: Scientific Committee on Antarctic Research).

Aguilar, M.A., Saldaña, M. del M., and Aguilar, F.J. (2013). Assessing geometric accuracy of the orthorectification process from GeoEye-1 and WorldView-2 panchromatic images. International Journal of Applied Earth Observation and Geoinformation *21*, 427–435.

Ahlstrøm, A.P., Gravesen, P., Bech Andersen, S., van As, D., Citterio, M., Fausto, R.S., Nielsen, S., Jepsen, H.F., Kristensen, S.S., Christensen, E.L., et al. (2008). A new programme for monitoring the mass loss of the Greenland ice sheet. Geological Survey of Denmark and Greenland Bulletin *15*, 61–64.

Anderson, B., Mackintosh, A., Stumm, D., George, L., Kerr, T., Winter-Billington, A., and Fitzsimons, S. (2010). Climate sensitivity of a high-precipitation glacier in New Zealand. Journal of Glaciology *56*, 114–128.

Andreassen, L.M., and Winsvold, S.H. (2012). Inventory of Norwegian glaciers (Oslo: Norwegian Water Resources and Energy Directorate).

Andreassen, L., Paul, F., Kääb, A., and Hausberg, J. (2008). Landsat-derived glacier inventory for Jotunheimen, Norway, and deduced glacier changes since the 1930s. The Cryosphere *2*, 131–145.

Van Angelen, J.H., van den Broeke, M.R., and van de Berg, W.J. (2011). Momentum budget of the atmospheric boundary layer over the Greenland ice sheet and its surrounding seas. Journal of Geophysical Research *116*, D10101.

De Angelis, H. (2014). Hypsometry and sensitivity of the mass balance to changes in equilibrium-line altitude: the case of the Southern Patagonia Icefield. Journal of Glaciology *60*, 14–28.

Aniya, M., Sato, H., Naruse, R., Skvarca, P., and Casassa, G. (1996). The use of satellite and airborne imagery to inventory outlet glaciers of the Southern Patagonia Icefield, South America. Photogrammetric Engineering and Remote Sensing *62*, 1361–1369.

Arendt, A., Bolch, T., Cogley, J.G., Gardner, A.S., Hagen, J.O., Hock, R., Kaser, G., Pfeffer, W.T., Moholdt, G., Paul, F., et al. (2013). Randolph Glacier Inventory [v3.2]: A dataset of global glacier outlines. (Boulder Colorado, USA.).

ASTER GDEM Validation Team (2009). ASTER Global DEM Validation Summary Report.

Auer, I., Böhm, R., Jurkovic, A., Lipa, W., Orlik, A., Potzmann, R., Schöner, W., Ungersböck, M., Matulla, C., Briffa, K., et al. (2007). HISTALP—historical instrumental climatological surface time series of the Greater Alpine Region. International Journal of Climatology *27*, 17–46.

Baatz, M., Benz, U.C., Dehghani, S., Heynen, M., Höltje, A., Hofmann, P., Lingenfelder, I., Mimler, M., Solbach, M., Weber, M., et al. (2005). Definiens Imaging - eCognition User Guide 4 (München: Definiens AG).

Bahr, D.B., Meier, M.F., and Peckham, S.D. (1997). The physical basis of glacier volume-area scaling. Journal of Geophysical Research *102*, 20355–20362.

Bahr, D.B., Dyurgerov, M., and Meier, M.F. (2009). Sea-level rise from glaciers and ice caps: A lower bound. Geophysical Research Letters *36*, L03501.

Bales, R.C., Guo, Q., Shen, D., McConnell, J.R., Du, G., Burkhart, J.F., Spikes, V.B., Hanna, E., and Cappelen, J. (2009). Annual accumulation for Greenland updated using ice core data developed during 2000–2006 and analysis of daily coastal meteorological data. Journal of Geophysical Research *114*, D06116.

Bamber, J.L., and Rivera, A. (2007). A review of remote sensing methods for glacier mass balance determination. Global and Planetary Change *59*, 138–148.

Bamber, J.L., Ekholm, S., and Krabill, W.B. (2001). A new, high resolution digital elevation model of Greenland fully validated with airborne laser data. Journal of Geophysical Research *106*, 6733–6745.

Bassford, R.P., Siegert, M.J., Dowdeswell, J.A., Oerlemans, J., Glazovsky, A.F., and Macheret, Y.Y. (2006). Quantifying the mass balance of ice caps on Severnaya Zemlya, Russian high arctic. I: Climate and mass balance of the Vavilov Ice Cap. Arctic Antarctic and Alpine Research *38*, 1–12.

Bayr, K.J., Hall, D.K., and Kovalick, W.M. (1994). Observations on glaciers in the eastern Austrian Alps using satellite data. International Journal of Remote Sensing *15*, 1733–1742.

Benson, C.S. (1962). Stratigraphic studies in the snow and firn of the Greenland ice sheet. SIPRE-RR-70. Snow Ice and Permafrost Research Establishment. *70*.

Berthier, E., Schiefer, E., Clarke, G.K.C., Menounos, B., and Rémy, F. (2010). Contribution of Alaskan glaciers to sea-level rise derived from satellite imagery. Nature Geoscience *3*, 92–95.

Bhambri, R., Bolch, T., and Chaujar, R.K. (2011). Mapping of debris-covered glaciers in the Garhwal Himalayas using ASTER DEMs and thermal data. International Journal of Remote Sensing *32*, 8095–8119.

Bippus, G. (2011). Characteristics of summer snow areas on glaciers observed by means of Landsat data. Dissertation. University of Innsbruck.

Bishop, M.P., Shroder, J.F., and Hickman, B.L. (1999). SPOT panchromatic imagery and neural networks for information extraction in a complex mountain environment. Geocarto International *14*, 19–28.

Bishop, M.P., Bonk, R., Kamp, U., and Shroder, J.F. (2001). Terrain analysis and data modeling for alpine glacier mapping. Polar Geography *25*, 182–201.

Bishop, M.P., Olsenholler, J.A., Shroder, J.F., Barry, R.G., Raup, B.H., Bush, A.B.G., Copland, L., Dwyer, J.L., Fountain, A.G., Haeberli, W., et al. (2004). Global Land Ice Measurements from Space (GLIMS): remote sensing and GIS investigations of the Earth's cryosphere. Geocarto International *19*, 57–84.

Blaschke, T. (2010). Object based image analysis for remote sensing. ISPRS Journal of Photogrammetry and Remote Sensing *65*, 2–16.

Blaschke, T., and Strobl, J. (2001). What's wrong with pixels? Some recent developments interfacing remote sensing and GIS. Geo-Informations-Systems (GIS) *6*, 12–17.

Blaschke, T., Hay, G.J., Kelly, M., Lang, S., Hofmann, P., Addink, E., Queiroz Feitosa, R., van der Meer, F., van der Werff, H., van Coillie, F., et al. (2014). Geographic Object-Based Image Analysis – towards a new paradigm. ISPRS Journal of Photogrammetry and Remote Sensing *87*, 180–191.

Bliss, A., Hock, R., and Cogley, J.G. (2013). A new inventory of mountain glaciers and ice caps for the Antarctic periphery. Annals of Glaciology *54*, 191–199.

Boas, L., and Wang, P.R. (2011). Weather and climate data from Greenland, 1958-2010, observation data with description (Copenhagen: Danish Meteorological Institute).

Boberg, F., and Christensen, J.H. (2012). Overestimation of mediterranean summer temperature projections due to model deficiencies. Nature Climate Change *2*, 433–436.

Bolch, T., and Kamp, U. (2006). Glacier mapping in high mountains using DEMs, Landsat and ASTER data. Grazer Schriften Der Geographie Und Raumforschung *41*, 37–48.

Bolch, T., Buchroithner, M.F., Kunert, A., and Kamp, U. (2007). Automated delineation of debris-covered glaciers based on ASTER data. In Geoinformation in Europe: Proceedings of 27th EARSel Symposium, 04-07 June 2007, (Bozen, Italy), pp. 403–410.

Bolch, T., Buchroithner, M., Pieczonka, T., and Kunert, A. (2008). Planimetric and volumetric glacier changes in the Khumbu Himalaya, Nepal, since 1962 using Corona, Landsat TM and ASTER data. Journal of Glaciology *54*, 592–600.

Bolch, T., Menounos, B., and Wheate, R. (2010). Landsat-based inventory of glaciers in western Canada, 1985-2005. Remote Sensing of Environment *114*, 127–137.

Bolch, T., Pieczonka, T., and Benn, D.I. (2011). Multi-decadal mass loss of glaciers in the Everest area (Nepal Himalaya) derived from stereo imagery. The Cryosphere *5*, 349–358.

Bolch, T., Sandberg Sørensen, L., Simonsen, S.B., Mölg, N., Machguth, H., Rastner, P., and Paul, F. (2013). Mass loss of Greenland's glaciers and ice caps 2003-2008 revealed from ICESat laser altimetry data. Geophysical Research Letters *40*, 875–881.

Bouillon, A., Bernard, M., Gigord, P., Orsoni, A., Rudowski, V., and Baudoin, A. (2006). SPOT 5 HRS geometric performances: Using block adjustment as a key issue to improve quality of DEM generation. ISPRS Journal of Photogrammetry and Remote Sensing *60*, 134–146.

Box, J.E. (2002). Survey of Greenland instrumental temperature records: 1873-2001. International Journal of Climatology *22*, 1829–1847.

Braithwaite, R.J., and Raper, S.C.B. (2002). Glaciers and their contribution to sea level change. Physics and Chemistry of the Earth, Parts A/B/C *27*, 1445–1454.

Braithwaite, R.J., and Raper, S.C.B. (2009). Estimating equilibrium-line altitude (ELA) from glacier inventory data. Annals of Glaciology *50*, 127–132.

Braithwaite, R.J., and Zhang, Y. (1999). Modelling changes in glacier mass balance that may occur as a result of climate changes. Geogr. Ann. Ser. A-Phys. Geogr. *81A*, 489–496.

Braithwaite, R.J., and Zhang, Y. (2000). Sensitivity of mass balance of five Swiss glaciers to temperature changes assessed by tuning a degree-day model. Journal of Glaciology *46*, 7–14.

Braithwaite, R.J., Raper, S.C.B., and Candela, R. (2013). Recent changes (1991–2010) in glacier mass balance and air temperature in the European Alps. Annals of Glaciology *54*, 139–146.

Le Bris, R., Paul, F., Frey, H., and Bolch, T. (2011). A new satellite-derived glacier inventory for western Alaska. Annals of Glaciology *52*, 135–143.

Van den Broeke, M., Bamber, J., Ettema, J., Rignot, E., Schrama, E., van de Berg, W.J., van Meijgaard, E., Velicogna, I., and Wouters, B. (2009). Partitioning recent Greenland mass loss. Science *326*, 984–986.

Brown, J., Bradford, J., Harper, J., Pfeffer, W.T., Humphrey, N., and Mosley-Thompson, E. (2012). Georadar-derived estimates of firn density in the percolation zone, western Greenland ice sheet. Journal of Geophysical Research *117*, F01011.

Buchroithner, M.F., and Bolch, T. (2007). An automated method to delineate the ice extension of the debris-covered glaciers at Mt. Everest based on ASTER imagery. In 9th International Symposium on High Mountain Remote Sensing Cartography: Proceedings, 14 - 15 September 2006, (Graz, Austria), pp. 71–78.

Bull, C. (1963). Glaciological reconnaissance of the Sukkertoppen ice cap, south-west Greenland. Journal of Glaciology *21*, 813–817.

Burgess, E.W., Forster, R.R., Box, J.E., Mosley-Thompson, E., Bromwich, D.H., Bales, R.C., and Smith, L.C. (2010). A spatially calibrated model of annual accumulation rate on the Greenland ice sheet (1958–2007). Journal of Geophysical Research *115*, F02004.

Burns, P., and Nolin, A. (2013). Using atmospherically-corrected Landsat imagery to measure glacier area change in the Cordillera Blanca, Peru from 1987 to 2010. Remote Sensing of Environment *140*, 165–178.

Burrough, P.A., and McDonnell, R. (1998). Principles of geographical information systems (Oxford: Oxford University Press).

Castillejo-González, I.L., López-Granados, F., García-Ferrer, A., Peña-Barragán, J.M., Jurado-Expósito, M., de la Orden, M.S., and González-Audicana, M. (2009). Object- and pixel-based analysis for mapping crops and their agro-environmental associated measures using QuickBird imagery. Computers and Electronics in Agriculture *68*, 207–215.

Citterio, M., and Ahlstrøm, A.P. (2013). Brief communication "The aerophotogrammetric map of Greenland ice masses." The Cryosphere *7*, 445–449.

Citterio, M., Paul, F., Ahlstrom, A.P., Jepsen, H.F., and Weidick, A. (2009). Remote sensing of glacier change in West Greenland: accounting for the occurrence of surge-type glaciers. Annals of Glaciology *50*, 70–80.

Cogley, J.G. (2003). GGHYDRO – Global Hydrographic Data, Release 2.3.1. Trent University, Department of Geography. - In : Trent Technical Note: 2003-1.

Cogley, J.G. (2009a). Geodetic and direct mass-balance measurements: comparison and joint analysis. Annals of Glaciology *50*, 96–100.

Cogley, J.G. (2009b). A more complete version of the World Glacier Inventory. Annals of Glaciology *50*, 32–38.

Cogley, J.G. (2012). The future of the world's glaciers. In The Future of the World's Climate, (Elsevier), pp. 197–222.

Cogley, J.G., Hock, R., Rasmussen, L., Arendt, A.A., Bauder, A., Braithwaite, R.J., Jansson, P., Kaser, G., Möller, M., and Nicholson, L. (2011). Glossary of glacier mass balance and related terms. IHP-VII Technical Documents in Hydrology *86*, 1–124.

Colvocoresses, A.P. (1982). Automated satellite mapping system (MAPSAT) (Washington).

Crespi, M., Poli, D., de Vendictis, L., Wolff, K., Colosimo, G., Grün, A., and Volpe, F. (2008). Radiometric quality and DSM generation analysis of CARTOSAT-1 stereo imagery. International Archives of Photogrammetry, Remote Sensing and Spatial Information Sciences *37 (Part B1)*, 1349–1356.

Cressie, N. (1993). Statistics for spatial data (Ohio: Wiley-Interscience).

Crosetto, M., and Pérez Aragues, F. (2000). Radargrammetry and SAR interferometry for DEM generation validation and data fusion. ESA-Publication *450*, 367–372.

Cuffey, K.M., and Paterson, W.S.B. (2010). The physics of glaciers (Academic press).

Dahl-Jensen, D., Bamber, J., Boeggild, C.E., Buch, E., Christensen, J.H., Dethloff, K., Fahnestock, M., Marshall, S., Rosing, M., Steffen, K., et al. (2009). The Greenland ice sheet in a changing climate: snow, water, ice and permafrost in the Arctic (SWIPA) 2009 (Oslo: Artic Monitoring and Assessment Programme).

Danko, D.M. (1992). The digital chart of the world project. Photogrammetric Engineering and Remote Sensing *58*, 1125–1128.

Dee, D.P., Uppala, S.M., Simmons, A.J., Berrisford, P., Poli, P., Kobayashi, S., Andrae, U., Balmaseda, M.A., Balsamo, G., Bauer, P., et al. (2011). The ERA-Interim re-analysis: configuration and performance of the data assimilation system. Quarterly Journal of the Royal Meteorological Society *137*, 553–597.

Definiens, A. (2007). Definiens Developer 7 user guide (München: Definiens AG.).

Van Den Eeckhaut, M., Poesen, J., Verstraeten, G., Vanacker, V., Moeyersons, J., Nyssen, J., and van Beek, L.P.H. (2005). The effectiveness of hillshade maps and expert knowledge in mapping old deep-seated landslides. Geomorphology *67*, 351–363.

Desmet, P.J.J. (1997). Effects of interpolation errors on the analysis of DEMs. Earth Surface Processes and Landforms *22*, 563–580.

Dobhal, D.P. (2011). Dead ice. Encyclopedia of Snow, Ice and Glaciers *16*, 186.

Dowdeswell, J., and Hambrey, M.J. (2002). Islands of the Arctic. (Cambridge, UK: Cambridge University Press).

Dozier, J. (1989). Spectral signature of alpine snow cover from the landsat thematic mapper. Remote Sensing of Environment *28*, 9–22.

Drusch, M., Del Bello, U., Carlier, S., Colin, O., Fernandez, V., Gascon, F., Hoersch, B., Isola, C., Laberinti, P., Martimort, P., et al. (2012). Sentinel-2: ESA's optical high-resolution mission for GMES operational services. Remote Sensing of Environment *120*, 25–36.

Dyurgerov, M. (2003). Mountain and subpolar glaciers show an increase in sensitivity to climate warming and intensification of the water cycle. Journal of Hydrology *282*, 164–176.

Dyurgerov, M.B., and Meier, M.F. (2005). Glaciers and the Changing Earth System: A 2004 Snapshot. Institute of Arctic and Alpine Research, Occasional Paper *58*, 1–118.

Ebita, A., Kobayashi, S., Ota, Y., Moriya, M., Kumabe, R., Onogi, K., Harada, Y., Yasui, S., Miyaoka, K., Takahashi, K., et al. (2011). The Japanese 55-year re-analysis "JRA-55": An interim report. SOLA *7*, 149–152.

Ekstrand, S. (1996). Landsat TM-based forest damage assessment: correction for topographic effects. Photogrammetric Engineering and Remote Sensing *62*, 151–162.

Ettema, J. (2010). The present-day climate of Greenland. A study with a regional climate model. Dissertation. University of Utrecht.

Ettema, J., Van Den Broeke, M.R., Van Meijgaard, E., Van De Berg, W.J., Bamber, J.L., Box, J.E., and Bales, R.C. (2009). Higher surface mass balance of the Greenland ice sheet revealed by high-resolution climate modeling. Geophysical Research Letters *36*, L12501.

Ettema, J., van den Broeke, M.R., van Meijgaard, E., van de Berg, W.J., Box, J.E., and Steffen, K. (2010). Climate of the Greenland ice sheet using a high-resolution climate model – Part 1: Evaluation. The Cryosphere *4*, 511–527.

Evans, I.S., and Cox, N.J. (2005). Global variations of local asymmetry in glacier altitude: separation of northsouth and eastwest components. Journal of Glaciology *51*, 469–482.

Evans, J., McGregor, J., and McGuffie, K. (2012). Future regional climates. In The Future of the World's Climate, (Elsevier), pp. 223–250.

Falaschi, D., Bravo, C., Masiokas, M., Villalba, R., and Rivera, A. (2013). First glacier inventory and recent changes in glacier area in the Monte San Lorenzo region (47°S), Southern Patagonian Andes, South America. Arctic, Antarctic, and Alpine Research *45*, 19–28.

Farr, T.G., Rosen, P.A., Caro, E., Crippen, R., Duren, R., Hensley, S., Kobrick, M., Paller, M., Rodriguez, E., and Roth, L. (2007). The shuttle radar topography mission. Reviews of Geophysics *45*, 1–43.

Fausto, R.S., Ahlstrom, A.P., Van As, D., Boggild, C.E., and Johnsen, S.J. (2009). A new present-day temperature parameterization for Greenland. Journal of Glaciology *55*, 95–105.

Favey, E., Geiger, A., Gudmundsson, G.H., and Wehr, A. (1999). Using airborne LiDAR and USGS DEM data for assessing rock glaciers and glaciers. Geografiska Annaler *81 A (4)*, 555–561.

Ferranti, J. (2009). Greenland first edition DEM.

Fettweis, X. (2007). Reconstruction of the 1979-2006 Greenland ice sheet surface mass balance using the regional climate model MAR. The Cryosphere *1*, 123–168.

Fettweis, X., Franco, B., Tedesco, M., van Angelen, J.H., Lenaerts, J.T.M., van den Broeke, M.R., and Gallée, H. (2013). Estimating the Greenland ice sheet surface mass balance contribution to future sea level rise using the regional atmospheric climate model MAR. The Cryosphere *7*, 469–489.

Fisher, P. (1997). The pixel: A snare and a delusion. International Journal of Remote Sensing *18*, 679–685.

Florinsky, I.V. (1998). Combined analysis of digital terrain models and remotely sensed data in landscape investigations. Progress in Physical Geography *22*, 33–60.

Fontana, F.M.A., Trishchenko, A.P., Luo, Y., Khlopenkov, K.V., Nussbaumer, S.U., and Wunderle, S. (2010). Perennial snow and ice variations (2000–2008) in the arctic circumpolar land area from satellite observations. Journal of Geophysical Research *115*, F04020.

Foster, L.A., Brock, B.W., Cutler, M.E.J., and Diotri, F. (2012). A physically based method for estimating supraglacial debris thickness from thermal band remote-sensing data. Journal of Glaciology *58*, 677–691.

Fowler, R.J., and Little, J.J. (1979). Automatic extraction of irregular network digital terrain models. Siggraph Computer Graphics *13*, 199–207.

Frey, H., and Paul, F. (2011). On the suitability of the SRTM DEM and ASTER GDEM for the compilation of topographic parameters in glacier inventories. International Journal of Applied Earth Observation and Geoinformation *18*, 480–490.

Frey, H., Haeberli, W., Linsbauer, A., Huggel, C., and Paul, F. (2010). A multi-level strategy for anticipating future glacier lake formation and associated hazard potentials. Natural Hazards Earth System Sciences *10*, 339–352.

Frey, H., Paul, F., and Strozzi, T. (2012). Compilation of a glacier inventory for the western Himalayas from satellite data: methods, challenges, and results. Remote Sensing of Environment *124*, 832–843.

Fujisada, H., and Ono, A. (1994). Observational performance of ASTER instrument on EOS-AM1 spacecraft. Advances in Space Research *14*, 147–150.

Furbish, D.J., and Andrews, J.T. (1984). The use of hypsometry to indicate long term stability and response of valley glaciers to changes in mass transfer. Journal of Glaciology *30*, 199–211.

Gao, J., and Liu, Y. (2001). Applications of remote sensing, GIS and GPS in glaciology: a review. Progress in Physical Geography *25*, 520–540.

Gardelle, J., Berthier, E., and Arnaud, Y. (2012). Slight mass gain of Karakoram glaciers in the early twenty-first century. Nature Geoscience *5*, 322–325.

Gardelle, J., Berthier, E., Arnaud, Y., and Kääb, A. (2013). Region-wide glacier mass balances over the Pamir-Karakoram-Himalaya during 1999-2011. The Cryosphere *7*, 1263–1286.

Gardner, A.S., Sharp, M.J., Koerner, R.M., Labine, C., Boon, S., Marshall, S.J., Burgess, D.O., and Lewis, D. (2009). Near-surface temperature lapse rates over arctic glaciers and their implications for temperature downscaling. Journal of Climate *22*, 4281–4298.

Gardner, A.S., Moholdt, G., Wouters, B., Wolken, G.J., Burgess, D.O., Sharp, M.J., Cogley, J.G., Braun, C., and Labine, C. (2011). Sharply increased mass loss from glaciers and ice caps in the Canadian Arctic Archipelago. Nature *473*, 357–360.

Gardner, A.S., Moholdt, G., Cogley, J.G., Wouters, B., Arendt, A.A., Wahr, J., Berthier, E., Hock, R., Pfeffer, W.T., Kaser, G., et al. (2013). A reconciled estimate of glacier contributions to sea level rise: 2003 to 2009. Science *340*, 852–857.

GCOS (2003). The second report on the adequacy of the global observing systems for climate in support of the UNFCCC (GCOS).

Geist, T., Lutz, E., and Stötter, J. (2003). Airborne laser scanning technology and its potential for applications in glaciology. International Archives of Photogrammetry, Remote Sensing and Spatial Information Science *34*, 101–106.

Gens, R., and Genderen, J.L. (1996). Analysis of the geometric parameters of SAR interferometry for spaceborn systems. International Archives of Photogrammetry and Remote Sensing *31*, 107–110.

Geosystems, L. (2013). ERDAS field guide (Huntsville: Intergraph Corporation).

Giesen, R.H., and Oerlemans, J. (2013). Climate-model induced differences in the 21st century global and regional glacier contributions to sea-level rise. Climate Dynamics *7*, 3283–3300.

Giorgi, F., and Mearns, L.O. (1999). Introduction to special section: Regional climate modeling revisited. Journal of Geophysical Research *104*, 6335–6352.

Glickman, T. (2000). Glossary of meteorology (Boston: American Meteorological Society).

Grinsted, A. (2013). An estimate of global glacier volume. The Cryosphere *7*, 141–151.

Groom, G., Stjernholm, M., Nielsen, R.D., Fleetwood, A., and Petersen, I.K. (2013). Remote sensing image data and automated analysis to describe marine bird distributions and abundances. Ecological Informatics *14*, 2–8.

Gross, G., Kerschner, H., and Patzelt, G. (1977). Methodische Untersuchungen über die Schneegrenze in alpinen Gletschergebieten. Zeitschrift Für Gletscherkunde Und Glazialgeologie *12*, 223–251.

Gruber, A., Wessel, B., Huber, M., and Roth, A. (2012). Operational TanDEM-X DEM calibration and first validation results. ISPRS Journal of Photogrammetry and Remote Sensing *73*, 39–49.

Haeberli, W. (2005). Changing views of changing glaciers. In Darkening Peaks: Glacier Retreat, Science, and Society., (Berkeley: University of California Press), pp. 23–32.

Haeberli, W., and Alean, J. (1985). Temperature and accumulation of high altitude firn in the Alps. Annals of Glaciology *6*, 161–163.

Haeberli, W., and Hoelzle, M. (1995). Application of inventory data for estimating characteristics of and regional clirnate-change effects on mountain glaciers: a pilot study with the European Alps. Annals of Glaciology *21*, 206–212.

Haeberli, W., Bösch, H., Scherler, K., Ostrem, K., and Wallén, C.C. (1989). World Glacier Inventory - Status 1988. IAHS (ICSI)/UNEP/UNESCO, World Glacier Monitoring Service, Zurich, Switzerland.

Haeberli, W., Maisch, M., and Paul, F. (2002). Mountain glaciers in global climate-related observation networks. WMO-Bulletin *51*, 18–25.

Haeberli, W., Hoelzle, M., Paul, F., and Zemp, M. (2007). Integrated monitoring of mountain glaciers as key indicators of global climate change: the European Alps. Annals of Glaciology *46*, 150–160.

Hall, D.K., and Martinec, J. (1985). Remote sensing of ice and snow (New York: Chapman and Hall).

Hall, D.K., Ormsby, J.P., Bindschadler, R.A., and Siddalingaiah, H. (1987). Characterization of snow and ice reflectance zones on glaciers using Landsat Thematic Mapper data. Annals of Glaciology *9*, 104–108.

Hall, D.K., Riggs, G.A., and Salomonson, V.V. (1995). Development of methods for mapping global snow cover using moderate resolution imaging spectroradiometer data. Remote Sensing of Environment *54*, 127–140.

Hammer, C.U. (2001). The Hans Tausen Ice Cap. Glacialogy and glacial geology. (Copenhagen: Meddelelser om Grønland).

Hanna, E. (2005). Runoff and mass balance of the Greenland ice sheet: 1958–2003. Journal of Geophysical Research *110*, D13108.

Hanna, E., Huybrechts, P., Steffen, K., Cappelen, J., Huff, R., Shuman, C., Irvine-Fynn, T., Wise, S., and Griffiths, M. (2008). Increased runoff from melt from the Greenland Ice Sheet: A response to global warming. Journal of Climate *21*, 331–341.

Hanna, E., Mernild, S.H., Cappelen, J., and Steffen, K. (2012). Recent warming in Greenland in a long-term instrumental (1881–2012) climatic context: I. Evaluation of surface air temperature records. Environmental Research Letters *7*, 045404.

Hawkins, E., and Sutton, R. (2009). The potential to narrow uncertainty in regional climate predictions. American Meteorological Society *90*, 1095–1107.

Hayakawa, Y.S., Oguchi, T., and Lin, Z. (2008). Comparison of new and existing global digital elevation models: ASTER G-DEM and SRTM-3. Geophysical Research Letters *35*, L17404.

Hengl, T., and Reuter, H. (2011). How accurate and usable is GDEM? A statistical assessment of GDEM using LiDAR data. Geomorphometry *2*, 45–48.

Hidayat, S.A., and Wiweka (2013). Accuracy evaluation orthorectification of SPOT image. International Conference on ICT for Smart Society (ICISS) 1–10.

Hirano, A., Welch, R., and Lang, H. (2003). Mapping from ASTER stereo image data: DEM validation and accuracy assessment. ISPRS Journal of Photogrammetry and Remote Sensing *57*, 356–370.

Hock, R., de Woul, M., Radić, V., and Dyurgerov, M. (2009). Mountain glaciers and ice caps around Antarctica make a large sea-level rise contribution. Geophysical Research Letters *36*, L07501.

Hörhold, M.W., Laepple, T., Freitag, J., Bigler, M., Fischer, H., and Kipfstuhl, S. (2012). On the impact of impurities on the densification of polar firn. Earth and Planetary Science Letters *325-326*, 93–99.

Howat, I.M., Negrete, A., and Smith, B.E. (2014). The Greenland Ice Mapping Project (GIMP) land classification and surface elevation data sets. The Cryosphere *8*, 1509–1518.

Huggel, C., Kääb, A., Haeberli, W., Teysseire, P., and Paul, F. (2002). Remote sensing based assessment of hazards from glacier lake outbursts: a case study in the Swiss Alps. Canadian Geotechnical Journal *39*, 316–330.

Huggel, C., Haeberli, W., Kääb, A., Bieri, D., and Richardson, S. (2004). An assessment procedure for glacial hazards in the Swiss Alps. Canadian Geotechnical Journal *41*, 1068–1083.

Huss, M. (2011). Present and future contribution of glacier storage change to runoff from macroscale drainage basins in Europe. Water Resources Research *47*, 1–14.

Huss, M. (2013). Density assumptions for converting geodetic glacier volume change to mass change. The Cryosphere *7*, 877–887.

Huss, M., and Farinotti, D. (2012). Distributed ice thickness and volume of all glaciers around the globe. Journal of Geophysical Research *117*, F04010.

Jacob, T., Wahr, J., Pfeffer, W.T., and Swenson, S. (2012). Recent contributions of glaciers and ice caps to sea level rise. Nature *482*, 514–518.

Jacobs, J.D., Simms, E.L., and Simms, A. (1997). Recession of the southern part of Barnes Ice Cap, Baffin Island, Canada, between 1961 and 1993, determined from digital mapping of Landsat TM. Journal of Glaciology *43*, 98–102.

Jacobsen, K., Crespi, M., Fratarcangeli, F., and Giannone, F. (2008). DEM generation with CARTOSAT-1 stereo imagery. In EARSeL Joint Workshop, (Bochum (Germany)), pp. 5–7.

Janke, J.R. (2013). Using airborne LiDAR and USGS DEM data for assessing rock glaciers and glaciers. Geomorphology *195*, 118–130.

Jiskoot, H., and Juhlin, D.T. (2010). Changes in central East Greenland glaciers from a new glacier inventory and GDEM. In The Dynamics and Mass Budget of Arctic Glaciers, (Obergurgl, Austria), pp. 1–72.

Jiskoot, H., Murray, T., and Luckman, A. (2003). Surge potential and drainage-basin characteristics in East Greenland. Annals of Glaciology *36*, 142–148.

Jiskoot, H., Curran, C.J., Tessler, D.L., and Shenton, L.R. (2010). Changes in Clemenceau Icefield and Chaba Group glaciers, Canada, related to hypsometry, tributary detachment, length–slope and area–aspect relations. Annals of Glaciology *50*, 133–143.

Jiskoot, H., Juhlin, D., St Pierre, H., and Citterio, M. (2012). Tidewater glacier fluctuations in central East Greenland coastal and fjord regions (1980s–2005). Annals of Glaciology *53*, 35–44.

Joerg, P.C., Morsdorf, F., and Zemp, M. (2012). Uncertainty assessment of multi-temporal airborne laser scanning data: A case study on an Alpine glacier. Remote Sensing of Environment *127*, 118–129.

Jordan, R.L., Caro, E.R., Kim, Y., Kobrick, M., Shen, Y., Stuhr, F.V., and Werner, M.U. (1996). Shuttle radar topography mapper (SRTM). Microwave Sensing and Synthetic Aperture Radar *412*, 1–43.

Kääb, A. (2008). Glacier volume changes using ASTER satellite stereo and ICESat GLAS laser altimetry. A test study on Edgeøya, Eastern Svalbard. IEEE Transactions on Geoscience and Remote Sensing *46*, 2823–2830.

Kääb, A., and Prowse, T. (2011). Cold-regions river flow observed from space. Geophysical Research Letters *38*, L08403.

Kääb, A., Huggel, C., Paul, F., Wessels, R., Raup, B., Kieffer, H., and Kargel, J. (2002). Glacier monitoring from ASTER imagery: accuracy and applications. In Observing Our Cryosphere from Space: Proceedings of EARSeL LISSIG Workshop, 11-13 March 2002, (Bern, Switzerland), pp. 43–53.

Kääb, A., Berthier, E., Nuth, C., Gardelle, J., and Arnaud, Y. (2012). Contrasting patterns of early twenty-first-century glacier mass change in the Himalayas. Nature *488*, 495–498.

Kalnay, E., Kanamitsu, M., Kistler, R., Collins, W., Deaven, D., Gandin, L., Iredell, M., Saha, S., White, G., and Woollen, J. (1996). The NCEP/NCAR 40-year re-analysis project. Bulletin of the American Meteorological Society *77*, 437–471.

Kamp, U., Bolch, T., and Olsenholler, J. (2005). Geomorphometry of Cerro Sillajhuay (Andes, Chile/Bolivia): Comparison of Digital Elevation Models (DEMs) from ASTER remote sensing data and contour maps. Geocarto International *20*, 23–33.

Kapnick, S.B., Delworth, T.L., Ashfaq, M., Malyshev, S., and Milly, P.C.D. (2014). Snowfall less sensitive to warming in Karakoram than in Himalayas due to a unique seasonal cycle. Nature Geoscience *1*, 1–7.

Kargel, J.S., Abrams, M.J., Bishop, M.P., Bush, A., Hamilton, G., Jiskoot, H., Kääb, A., Kieffer, H.H., Lee, E.M., Paul, F., et al. (2005). Multispectral imaging contributions to global land ice measurements from space. Remote Sensing of Environment *99*, 187–219.

Kaser, G., and Osmaston, H. (2002). Tropical glaciers. UNESCO International Hydrological Series 207.

Kaser, G., Fountain, A., and Jansson, P. (2003). A manual for monitoring the mass balance of mountain glaciers (Paris: UNESCO).

Khromova, T., Nosenko, G., Kutuzov, S., Muraviev, A., and Chernova, L. (2014). Glacier area changes in Northern Eurasia. Environmental Research Letters *9*, 015003.

Kienholz, C., Hock, R., and Arendt, A.A. (2013). A new semi-automatic approach for dividing glacier complexes into individual glaciers. Journal of Glaciology *59*, 913–925.

Kjaer, K.H., Khan, S.A., Korsgaard, N.J., Wahr, J., Bamber, J.L., Hurkmans, R., van den Broeke, M., Timm, L.H., Kjeldsen, K.K., Bjork, A.A., et al. (2012). Aerial photographs reveal late 20th century dynamic ice loss in northwestern Greenland. Science *337*, 569–573.

Klok, E.J., and Oerlemans, J. (2002). Model study of the spatial distribution of the energy and mass balance of Morteratschgletscher, Switzerland. Journal of Glaciology *48*, 505–518.

König, M., Winther, J.-G., and Isaksson, E. (2001). Measuring snow and glacier ice properties from satellite. Reviews of Geophysics *39*, 1–27.

Korona, J., Berthier, E., Bernard, M., Rémy, F., and Thouvenot, E. (2009). SPIRIT. SPOT 5 stereoscopic survey of Polar Ice: Reference images and topographies during the fourth International Polar Year (2007–2009). ISPRS Journal of Photogrammetry and Remote Sensing *64*, 204–212.

Kotlarski, S., Paul, F., and Jacob, D. (2010). Forcing a distributed glacier mass balance model with the regional climate model REMO. Part I: Climate model evaluation. Journal of Climate *23*, 1589–1606.

Kressler, F.P., Steinnocher, K., and Franzen, M. (2005). Object-oriented classification of orthophotos to support update of spatial databases. In Geoscience and Remote Sensing Symposium, (Melbourne (Australia)), pp. 253–256.

Krieger, G., Moreira, A., Fiedler, H., Hajnsek, I., Werner, M., Younis, M., and Zink, M. (2007). TanDEM-X: A Satellite formation for high-resolution SAR interferometry. IEEE Transactions on Geoscience and Remote Sensing *45*, 3317–3341.

Kropáček, J., Neckel, N., and Bauder, A. (2013). Estimation of volume changes of mountain glaciers from ICESat data: an example from the Aletsch Glacier, Swiss Alps. The Cryosphere Discussions *7*, 3261–3291.

Kuhn, M. (1985). Fluctuations of climate and mass balance: different responses of two adjacent glaciers. Zeitschrift Für Gletscherkunde Und Glazialgeologie *21*, 409–416.

Kuipers Munneke, P., van den Broeke, M.R., Lenaerts, J.T.M., Flanner, M.G., Gardner, A.S., and van de Berg, W.J. (2011). A new albedo parameterization for use in climate models over the Antarctic ice sheet. Journal of Geophysical Research *116*, D05114.

Landsat Project Science Office (2006). Landsat 7 science data users handbook (Greenbelt, MD: Landsat Project Science Office).

Laprise, R. (2008). Regional climate modelling. Journal of Computational Physics *227*, 3641–3666.

Laumann, T., and Reeh, N. (1993). Sensitivity to climate change of the mass balance of glaciers in southern Norway. Journal of Glaciology *39*, 656–665.

Leclercq, P.W., and Oerlemans, J. (2011). Global and hemispheric temperature reconstruction from glacier length fluctuations. Climate Dynamics *38*, 1065–1079.

Lemke, P., Ren, J., Alley, R.B., Allison, J., Carrasco, J., Flato, G., Fujii, Y., Kaser, G., Mote, P., Thomas, R.H., et al. (2007). Climate change 2007: the physical science basis: contribution of Working Group I to the Fourth Assessment Report of the Intergovernmental Panel on Climate Change (Cambridge University Press).

Lenaerts, J.T.M., van den Broeke, M.R., Déry, S.J., König-Langlo, G., Ettema, J., and Munneke, P.K. (2010). Modelling snowdrift sublimation on an Antarctic ice shelf. The Cryosphere *4*, 179–190.

Li, J., and Chen, W. (2005). A rule-based method for mapping Canada's wetlands using optical, radar and DEM data. International Journal of Remote Sensing *26*, 5051–5069.

Li, J., and Zwally, H.J. (2011). Modeling of firn compaction for estimating ice-sheet mass change from observed ice-sheet elevation change. Annals of Glaciology *52*, 1–7.

Li, P., Shi, C., Li, Z., Muller, J.-P., Drummond, J., Li, X., Li, T., Li, Y., and Liu, J. (2012). Evaluation of ASTER GDEM version 2 using GPS measurements and SRTM version 4. 1 in China. ISPRS Annals of Photogrammetry, Remote Sensing and Spatial Information Sciences *I-4*, 181–186.

Li, P., Shi, C., Li, Z., Muller, J.-P., Drummond, J., Li, X., Li, T., Li, Y., and Liu, J. (2013a). Evaluation of ASTER GDEM using GPS benchmarks and SRTM in China. International Journal of Remote Sensing *34*, 1744–1771.

Li, Y., Hu, C., Long, T., and Zhu, M. (2013b). DEM generation of TerraSAR-X spotlight data. In Radar Conference, (Ottawa), pp. 1–5.

Li, Z., Zhu, Q., and Gold, C. (2005). Digital terrain modeling: principles and methodology (New York: CRC Press).

Lillesand, T.M. (2006). Remote sensing and image interpretation (New York: John Wiley & Sons).

Linsbauer, A., Paul, F., and Haeberli, W. (2012). Modeling glacier thickness distribution and bed topography over entire mountain ranges with GlabTop: Application of a fast and robust approach. Journal of Geophysical Research *117*, F03007.

Linsbauer, A., Paul, F., Machguth, H., and Haeberli, W. (2013). Comparing three different methods to model scenarios of future glacier change in the Swiss Alps. Annals of Glaciology *54*, 241–253.

Liu, D., and Xia, F. (2010). Assessing object-based classification: advantages and limitations. Remote Sensing Letters *1*, 187–194.

Liu, T., Kinouchi, T., and Ledezma, F. (2013). Characterization of recent glacier decline in the Cordillera Real by LANDSAT, ALOS, and ASTER data. Remote Sensing of Environment *137*, 158–172.

Machguth, H., Eisen, O., Paul, F., and Hoelzle, M. (2006). Strong spatial variability of snow accumulation observed with helicopter-borne GPR on two adjacent Alpine glaciers. Geophysical Research Letters *33*, L13503.

Machguth, H., Paul, F., Kotlarski, S., and Hoelzle, M. (2009). Calculating distributed glacier mass balance for the Swiss Alps from regional climate model output: A methodical description and interpretation of the results. Journal of Geophysical Research *114*, D19106.

Machguth, H., Rastner, P., Bolch, T., Mölg, N., Sørensen, L.S., Aðalgeirsdottir, G., van Angelen, J.H., van den Broeke, M.R., and Fettweis, X. (2013). The future sea-level rise contribution of Greenland's glaciers and ice caps. Environmental Research Letters *8*, 025005.

Malenovský, Z., Rott, H., Cihlar, J., Schaepman, M.E., García-Santos, G., Fernandes, R., and Berger, M. (2012). Sentinels for science: Potential of Sentinel-1, -2, and -3 missions for scientific observations of ocean, cryosphere, and land. Remote Sensing of Environment *120*, 91–101.

Manley, W.F. (2008). Geospatial inventory and analysis of glaciers: a case study for the eastern Alaska Range. In Satellite Image Atlas of Glaciers of the World., (Denver, CO), pp. 424–439.

Mark, D.M. (1975). Computer analysis of topography: A comparison of terrain storage methods. Geografiska Annaler. Series A, Physical Geography *57*, 179–188.

Marshall, S.J., Sharp, M.J., Burgess, D.O., and Anslow, F.S. (2007). Near-surface-temperature lapse rates on the Prince of Wales Icefield, Ellesmere Island, Canada: implications for regional downscaling of temperature. International Journal of Climatology *27*, 385–398.

Marzeion, B., Jarosch, A.H., and Hofer, M. (2012). Past and future sea-level change from the surface mass balance of glaciers. The Cryosphere *6*, 1295–1322.

Marzeion, B., Jarosch, A.H., and Gregory, J.M. (2014). Feedbacks and mechanisms affecting the global sensitivity of glaciers to climate change. The Cryosphere *8*, 59–71.

Mashimbye, Z.E., de Clercq, W.P., and Van Niekerk, A. (2014). An evaluation of digital elevation models (DEMs) for delineating land components. Geoderma *213*, 312–319.

Masson, V., Champeaux, J.-L., Chauvin, F., Meriguet, C., and Lacaze, R. (2003). A global database of land surface parameters at 1-km resolution in meteorological and climate models. Journal of Climate *16*, 1261–1282.

McGregor, J.L. (1997). Regional climate modelling. Meteorology and Atmospheric Physics *63*, 105–117.

McGuffie, K., and Henderson-Sellers, A. (2001). Forty years of numerical climate modelling. International Journal of Climatology *21*, 1067–1109.

Meier, M.F., Dyurgerov, M.B., Rick, U.K., O'Neel, S., Pfeffer, W.T., Anderson, R.S., Anderson, S.P., and Glazovsky, A.F. (2007). Glaciers dominate eustatic sea-level rise in the 21st century. Science *317*, 1064–1067.

Van Meijgaard, E., Van Ulft, L.H., Van de Berg, W.J., Bosveld, F.C., Van den Hurk, B., Lenderink, G., and Siebesma, A.P. (2008). The KNMI regional atmospheric climate model RACMO version 2.1 (Koninklijk Nederlands Meteorologisch Instituut).

Meneguzzo, D.M., Liknes, G.C., and Nelson, M.D. (2013). Mapping trees outside forests using high-resolution aerial imagery: a comparison of pixel- and object-based classification approaches. Environmental Monitoring and Assessment *185*, 6261–6275.

Mernild, S., Knudsen, N., Lipscomb, W., Yde, J., Malmros, J., Hasholt, B., and Jakobsen, B. (2011). Increasing mass loss from Greenland's Mittivakkat Gletscher. The Cryosphere *5*, 341–348.

Mernild, S.H., Malmros, J.K., Yde, J.C., and Knudsen, N.T. (2012). Multi-decadal marine- and land-terminating glacier recession in the Ammassalik region, southeast Greenland. The Cryosphere *6*, 625–639.

Mernild, S.H., Knudsen, N.T., Hoffman, M.J., Yde, J.C., Hanna, E., Lipscomb, W.H., Malmros, J.K., and Fausto, R.S. (2013). Volume and velocity changes at Mittivakkat Gletscher, southeast Greenland. Journal of Glaciology *59*, 660–670.

Mihalcea, C., Mayer, C., Diolaiuti, G., Lambrecht, A., Smiraglia, C., and Tartari, G. (2006). Ice ablation and meteorological conditions on the debris-covered area of Baltoro glacier, Karakoram, Pakistan. Annals of Glaciology *43*, 292–300.

Mihalcea, C., Brock, B.W., Diolaiuti, G., D'Agata, C., Citterio, M., Kirkbride, M.P., Cutler, M.E.J., and Smiraglia, C. (2008). Using ASTER satellite and ground-based surface temperature measurements to derive supraglacial debris cover and thickness patterns on Miage Glacier (Mont Blanc Massif, Italy). Cold Regions Science and Technology *52*, 341–354.

Miller, P.E., Kunz, M., Mills, J.P., King, M.A., Murray, T., James, T.D., and Marsh, S.H. (2009). Assessment of glacier volume change using ASTER-based surface matching of historical photography. IEEE Transactions on Geoscience and Remote Sensing *47*, 1971–1979.

Minder, J.R., Mote, P.W., and Lundquist, J.D. (2010). Surface temperature lapse rates over complex terrain: Lessons from the Cascade Mountains. Journal of Geophysical Research *115*, D14122.

Minnaert, M. (1941). The reciprocity principle in lunar photometry. Astrophysical Journal *93*, 403–410.

Moholdt, G., Nuth, C., Hagen, J.O., and Kohler, J. (2010). Recent elevation changes of Svalbard glaciers derived from ICESat laser altimetry. Remote Sensing of Environment *114*, 2756–2767.

Moosavi, V., Talebi, A., and Shirmohammadi, B. (2014). Producing a landslide inventory map using pixel-based and object-oriented approaches optimized by Taguchi method. Geomorphology *204*, 646–656.

Moreira, A., Krieger, G., Hajnsek, I., Hounam, D., Werner, M., Riegger, S., and Settelmeyer, E. (2004). TanDEM-X: a TerraSAR-X add-on satellite for single-pass SAR interferometry. In Geoscience and Remote Sensing Symposium: Proceedings of IGARSS, 20-24 September 2004, (Anchorage, Alaska), pp. 1000–1003.

Myint, S.W., Gober, P., Brazel, A., Grossman-Clarke, S., and Weng, Q. (2011). Per-pixel vs. object-based classification of urban land cover extraction using high spatial resolution imagery. Remote Sensing of Environment *115*, 1145–1161.

Nagai, H., Fujita, K., Sakai, A., Nuimura, T., and Tadono, T. (2014). Climatic and topographic influences on glacier distribution in the Bhutan Himalaya. The Cryosphere Discussions *8*, 1305–1336.

Nakawo, M., Morohoshi, T., and Uehara, S. (1993). Satellite data utilization for estimating ablation of debris covered glaciers. In Kathmandu Symposium on Snow and Glacier Hydrology: Proceedings, 16–21 November 1992, (Kathmandu, Nepal), pp. 75–83.

Narumalani, S., Zhou, Y., and Jelinski, D.E. (1998). Utilizing geometric attributes of spatial information to improve digital image classification. Remote Sensing Reviews *16*, 233–253.

Neckel, N., Kropáček, J., Bolch, T., and Hochschild, V. (2014). Glacier mass changes on the Tibetan Plateau 2003–2009 derived from ICESat laser altimetry measurements. Environmental Research Letters *9*, 014009.

Nesje, A., Bakke, J., Dahl, S.O., Lie, Ø., and Matthews, J.A. (2008). Norwegian mountain glaciers in the past, present and future. Global and Planetary Change *60*, 10–27.

Nitti, D.O., Bovenga, F., Nutricato, R., Intini, F., and Chiaradia, M.T. (2013). On the use of COSMO/SkyMed data and weather models for interferometric DEM generation. European Journal of Remote Sensing *46*, 250–271.

Notarnicola, C., Frick, A., Kass, S., Rastner, P., Pulighe, G., and Zebisch, M. (2009). Semiautomatic classification procedure for updating landuse maps with high resolution optical images. In Geoscience and Remote Sensing Symposium, (Cape Town (South Africa)), pp. 975–978.

Nuth, C., Kohler, J., König, M., von Deschwanden, A., Hagen, J.O., Kääb, A., Moholdt, G., and Pettersson, R. (2013). Decadal changes from a multi-temporal glacier inventory of Svalbard. The Cryosphere *7*, 1603–1621.

Oerlemans, J. (1981). Some basic experiments with a vertically-integrated ice sheet model. Tellus *33*, 1–11.

Oerlemans, J. (1994). Quantifying global warming from the retreat of glaciers. Science *264*, 243–245.

Oerlemans, J. (2001). Glaciers and climate change (Rotterdam, Netherlands: Taylor & Francis).

Oerlemans, J. (2005). Extracting a climate signal from 169 glacier records. Science *308*, 675–677.

Oerlemans, J., and Fortuin, J.P.F. (1992). Sensitivity of glaciers and small ice caps to greenhouse warming. Science *258*, 115–117.

Oerlemans, J., and Reichert, B.K. (2000). Relating glacier mass balance to meteorological data by using a seasonal sensitivity characteristic. Journal of Glaciology *152*, 1–6.

Ohmura, A. (2009). Completing the world glacier inventory. Annals of Glaciology *50*, 144–148.

Ohmura, A., and Reeh, N. (1991). New precipitation and accumulation maps for Greenland. Journal of Glaciology *37*, 140–148.

Ohmura, A., Kasser, P., and Funk, M. (1992). Climate at the equilibrium line of glaciers. Journal of Glaciology *38*, 397–411.

Olthof, I., Latifovic, R., and Pouliot, D. (2009). Development of a circa 2000 land cover map of northern Canada at 30 m resolution from Landsat. Canadian Journal of Remote Sensing *35*, 152–165.

Onogi, K., Tsutsui, J., Koide, H., Sakamoto, M., and Kobayashi, S. (2007). The JRA-25 re-analysis. Journal of the Meteorological Society of Japan *85*, 369–432.

Otto-Bliesner, B.L. (2006). Simulating arctic climate warmth and icefield retreat in the last interglaciation. Science *311*, 1751–1753.

Paul, F. (2010). The influence of changes in glacier extent and surface elevation on modeled mass balance. The Cryosphere *4*, 569–581.

Paul, F. (2011). Melting glaciers and ice caps. Nature Geoscience *4*, 71–72.

Paul, F., and Andreassen, L.M. (2009). A new glacier inventory for the Svartisen region, Norway, from Landsat ETM+ data: challenges and change assessment. Journal of Glaciology *55*, 607–618.

Paul, F., and Haeberli, W. (2008). Spatial variability of glacier elevation changes in the Swiss Alps obtained from two digital elevation models. Geophysical Research Letters *35*, L21502.

Paul, F., and Kääb, A. (2005). Perspectives on the production of a glacier inventory from multispectral satellite data in Arctic Canada: Cumberland Peninsula, Baffin Island. Annals of Glaciology *42*, 59–66.

Paul, F., Kääb, A., Maisch, M., Kellenberger, T., and Haeberli, W. (2002). The new remote-sensing-derived Swiss glacier inventory: I. Methods. Annals of Glaciology *34*, 355–361.

Paul, F., Huggel, C., and Kääb, A. (2004). Combining satellite multispectral image data and a digital elevation model for mapping debris-covered glaciers. Remote Sensing of Environment *89*, 510–518.

Paul, F., Machguth, H., and Kääb, A. (2005). On the impact of glacier albedo under conditions of extreme glacier melt: the summer of 2003 in the Alps. EARSeL eProceedings *4*, 139–149.

Paul, F., Maisch, M., Rothenbühler, C., Hoelzle, M., and Haeberli, W. (2007). Calculation and visualisation of future glacier extent in the Swiss Alps by means of hypsographic modelling. Global and Planetary Change *55*, 343–357.

Paul, F., Kääb, A., Rott, H., Shepherd, A., Strozzi, T., and Volden, E. (2009a). Globglacier: A new ESA project to map the world's glaciers and ice caps from space. EARSeL eProceedings *8*, 11–25.

Paul, F., Barry, R.G., Cogley, J.G., Frey, H., Haeberli, W., Ohmura, A., Ommanney, C.S.L., Raup, B., Rivera, A., and Zemp, M. (2009b). Recommendations for the compilation of glacier inventory data from digital sources. Annals of Glaciology *50*, 119–126.

Paul, F., Frey, H., and Le Bris, R. (2011a). A new glacier inventory for the European Alps from Landsat TM scenes of 2003: challenges and results. Annals of Glaciology *52*, 144–152.

Paul, F., Andreassen, L.M., and Winsvold, S.H. (2011b). A new glacier inventory for the Jostedalsbreen region, Norway, from Landsat TM scenes of 2006 and changes since 1966. Annals of Glaciology *52*, 153–162.

Paul, F., Bolch, T., Kääb, A., Nagler, T., Shepherd, A., and Strozzi, T. (2012). Satellite-based glacier monitoring in the ESA project Glaciers_cci. In Geoscience and Remote Sensing Symposium (IGARSS), 2012 IEEE International, pp. 3222–3225.

Paul, F., Bolch, T., Kääb, A., Nagler, T., Nuth, C., Scharrer, K., Shepherd, A., Strozzi, T., Ticconi, F., Bhambri, R., et al. (2013a). The glaciers climate change initiative: Methods for creating glacier area, elevation change and velocity products. Remote Sensing of Environment *113*, 1–19.

Paul, F., Barrand, N.E., Baumann, S., Berthier, E., Bolch, T., Casey, K., Frey, H., Joshi, S.P., Konovalov, V., Bris, R.L., et al. (2013b). On the accuracy of glacier outlines derived from remote-sensing data. Annals of Glaciology *54*, 171–182.

Pellikka, P., and Rees, W.G. (2009). Remote Sensing of glaciers: Techniques for topographic, spatial and thematic mapping of glaciers (Taylor & Francis).

Pfeffer, W.T., Bliss, A., Bolch, T., Cogley, J.G., Gardner, A.S., Hagen, J.-O., Hock, R., Kaser, G., Kienholz, C., Miles, E.S., et al. (2014). The Randolph Glacier Inventory: a globally complete inventory of glaciers. Journal of Glaciology *60*, 537–552.

Pieczonka, T., Bolch, T., and Buchroithner, M. (2011). Generation and evaluation of multitemporal digital terrain models of the Mt. Everest area from different optical sensors. ISPRS Journal of Photogrammetry and Remote Sensing *66*, 927–940.

Pieczonka, T., Bolch, T., Junfeng, W., and Shiyin, L. (2013). Heterogeneous mass loss of glaciers in the Aksu-Tarim catchment (Central Tien Shan) revealed by 1976 KH-9 Hexagon and 2009 SPOT-5 stereo imagery. Remote Sensing of Environment *130*, 233–244.

Pielke, R.A. (2005). Land use and climate change. Science *310*, 1625–1626.

Plattner, C., Braun, L.N., and Brenning, A. (2004). Spatial variability of snow accumulation on Vernagtferner, Austrian Alps, in winter 2003/2004. Zeitschrift Für Gletscherkunde Und Glazialgeologie *39*, 43–57.

Quincey, D.J., Richardson, S.D., Luckman, A., Lucas, R.M., Reynolds, J.M., Hambrey, M.J., and Glasser, N.F. (2007). Early recognition of glacial lake hazards in the Himalaya using remote sensing datasets. Global and Planetary Change *56*, 137–152.

Rabatel, A., Dedieu, J.-P., Thibert, E., Letreguilly, A., and Vincent, C. (2008). 25 years (1981-2005) of equilibrium-line altitude and mass-balance reconstruction on Glacier Blanc, French Alps, using remote-sensing methods and meteorological data. Journal of Glaciology *54*, 307–314.

Rabus, B., Eineder, M., Roth, A., and Bamler, R. (2003). The shuttle radar topography mission—a new class of digital elevation models acquired by spaceborne radar. ISPRS Journal of Photogrammetry and Remote Sensing *57*, 241–262.

Racoviteanu, A., and Williams, M.W. (2012). Decision tree and texture analysis for mapping debris-covered glaciers in the Kangchenjunga area, eastern Himalaya. Remote Sensing *4*, 3078–3109.

Racoviteanu, A.E., Manley, W.F., Arnaud, Y., and Williams, M.W. (2007). Evaluating digital elevation models for glaciologic applications: An example from Nevado Coropuna, Peruvian Andes. Global and Planetary Change *59*, 110–125.

Racoviteanu, A.E., Williams, M.W., and Barry, R.G. (2008). Optical remote sensing of glacier characteristics: A review with focus on the Himalaya. Sensors *8*, 3355–3383.

Racoviteanu, A.E., Paul, F., Raup, B., Khalsa, S.J.., and Armstrong, R. (2009). Challenges and recommendations in mapping of glacier parameters from space: results of the 2008 Global Land Ice Measurements from Space (GLIMS) workshop, Boulder, Colorado, USA. Annals of Glaciology *50*, 53–69.

Radić, V., and Hock, R. (2010). Regional and global volumes of glaciers derived from statistical upscaling of glacier inventory data. Journal of Geophysical Research *115*, F01010.

Radić, V., and Hock, R. (2011). Regionally differentiated contribution of mountain glaciers and ice caps to future sea-level rise. Nature Geoscience *4*, 91–94.

Radić, V., and Hock, R. (2013). Glaciers in the Earth's hydrological cycle: Assessments of glacier mass and runoff changes on global and regional scales. Surveys in Geophysics *35*, 813–837.

Radić, V., Bliss, A., Beedlow, A.C., Hock, R., Miles, E., and Cogley, J.G. (2014). Regional and global projections of twenty-first century glacier mass changes in response to climate scenarios from global climate models. Climate Dynamics *42*, 37–58.

Ranson, K.J., Montesano, P.M., and Nelson, R. (2011). Object-based mapping of the circumpolar taiga–tundra ecotone with MODIS tree cover. Remote Sensing of Environment *115*, 3670–3680.

Raper, S.C.B., and Braithwaite, R.J. (2006). Low sea level rise projections from mountain glaciers and icecaps under global warming. Nature *439*, 311–313.

Rastner, P., Bolch, T., Mölg, N., Machguth, H., Le Bris, R., and Paul, F. (2012). The first complete inventory of the local glaciers and ice caps on Greenland. The Cryosphere *6*, 1483–1495.

Rastner, P., Bolch, T., Notarnicola, C., and Paul, F. (2014). A comparison of pixel- and object-based glacier classification with optical satellite images. IEEE Journal of Selected Topics in Applied Earth Observations and Remote Sensing *7*, 853–862.

Raup, B., and Khalsa, S.J.S. (2010). GLIMS analysis tutorial.

Raup, B., Kääb, A., Kargel, J.S., Bishop, M.P., Hamilton, G., Lee, E., Paul, F., Rau, F., Soltesz, D., Khalsa, S.J.., et al. (2007). Remote sensing and GIS technology in the Global Land Ice Measurements from Space (GLIMS) project. Computers & Geosciences *33*, 104–125.

Raup, B.H., Kieffer, H.H., Hare, T.M., and Kargel, J.S. (2000). Generation of data acquisition requests for the ASTER satellite instrument for monitoring a globally distributed target: glaciers. IEEE Transactions on Geoscience and Remote Sensing *38*, 1105–1112.

Reeh, N. (2008). A nonsteady-state firn-densification model for the percolation zone of a glacier. Journal of Geophysical Research *113*, F03023.

Reeh, N., Fisher, D.A., Koerner, R.M., and Clausen, H.B. (2005). An empirical firn-densification model comprising ice lenses. Annals of Glaciology *42*, 101–106.

Richards, J.A., and Jia, X. (2006). Remote sensing digital image analysis (New York: Springer-Verlag Berlin Heidelberg).

Rignot, E., and Mouginot, J. (2012). Ice flow in Greenland for the International Polar Year 2008–2009. Geophysical Research Letters *39*, L11501.

Rignot, E., Rivera, A., and Casassa, G. (2003). Contribution of the Patagonia Icefields of South America to Sea Level Rise. Science *302*, 434–437.

Rinne, E.J., Shepherd, A., Palmer, S., van den Broeke, M.R., Muir, A., Ettema, J., and Wingham, D. (2011). On the recent elevation changes at the Flade Isblink Ice Cap, northern Greenland. Journal of Geophysical Research *116*, F03024.

Rösel, A., and Kaleschke, L. (2011). Comparison of different retrieval techniques for melt ponds on Arctic sea ice from Landsat and MODIS satellite data. Annals of Glaciology *52*, 185–191.

Rott, H. (1994). Thematic studies in alpine areas by means of polarimetric SAR and optical imagery. Advances in Space Research *14*, 217–226.

Saha, S., Moorthi, S., Pan, H.-L., Wu, X., Wang, J., Nadiga, S., Tripp, P., Kistler, R., Woollen, J., Behringer, D., et al. (2010). The NCEP climate forecast system re-analysis. Bulletin of the American Meteorological Society *91*, 1015–1057.

Scambos, T.A., and Haran, T. (2002). An image-enhanced DEM of the Greenland Ice Sheet. Annals of Glaciology *34*, 291–298.

Scherler, D., Bookhagen, B., and Strecker, M.R. (2011). Spatially variable response of Himalayan glaciers to climate change affected by debris cover. Nature Geoscience *4*, 156–159.

Schiefer, E., Menounos, B., and Wheate, R. (2007). Recent volume loss of British Columbian glaciers, Canada. Geophysical Research Letters *34*, L16503.

Schiefer, E., Menounos, B., and Wheate, R. (2008). An inventory and morphometric analysis of British Columbia glaciers, Canada. Journal of Glaciology *54*, 551–560.

Schmugge, T., French, A., Ritchie, J.C., Rango, A., and Pelgrum, H. (2002). Temperature and emissivity separation from multispectral thermal infrared observations. Remote Sensing of Environment *79*, 189–198.

Schowengerdt, R.A. (2006). Remote Sensing: Models and Methods for Image Processing (Academic press).

Schrama, E., Wouters, B., and Vermeersen, B. (2011). Present day regional mass loss of Greenland observed with satellite gravimetry. Surveys in Geophysics *32*, 377–385.

Schuler, T.V., Crochet, P., Hock, R., Jackson, M., Barstad, I., and Jóhannesson, T. (2008). Distribution of snow accumulation on the Svartisen ice cap, Norway, assessed by a model of orographic precipitation. Hydrological Processes *22*, 3998–4008.

Schutz, B.E., Zwally, H.J., Shuman, C.A., Hancock, D., and DiMarzio, J.P. (2005). Overview of the ICESat mission. Geophysical Research Letters *32*, L21S01.

Sevruk, B., Ondrás, M., and Chvíla, B. (2009). The WMO precipitation measurement intercomparisons. Atmospheric Research *92*, 376–380.

Shepherd, A., Ivins, E.R., A, G., Barletta, V.R., Bentley, M.J., Bettadpur, S., Briggs, K.H., Bromwich, D.H., Forsberg, R., Galin, N., et al. (2012). A reconciled estimate of ice-sheet mass balance. Science *338*, 1183–1189.

Shi, Y., Liu, C., and Kang, E. (2010). The glacier inventory of China. Annals of Glaciology *50*, 1–4.

Shukla, A., Gupta, R.P., and Arora, M.K. (2010). Delineation of debris-covered glacier boundaries using optical and thermal remote sensing data. Remote Sensing Letters *1*, 11–17.

Sidjak, R., and Wheate, R. (1999). Glacier mapping of the Illecillewaet icefield, British Columbia, Canada, using Landsat TM and digital elevation data. International Journal of Remote Sensing *20*, 273–284.

Simmons, A., Uppala, S.M., Dee, D.P., and Kobayashi, S. (2007). ERA Interim: new ECMWF re-analysis products from 1989 onwards. ECMWF Newsletter *110*, 29–35.

Smith, B.E., Fricker, H.A., Joughin, I.R., and Tulaczyk, S. (2009). An inventory of active subglacial lakes in Antarctica detected by ICESat (2003-2008). Journal of Glaciology *55*, 573–595.

Sørensen, L.S., Simonsen, S.B., Nielsen, K., Lucas-Picher, P., Spada, G., Adalgeirsdottir, G., Forsberg, R., and Hvidberg, C.S. (2011). Mass balance of the Greenland ice sheet (2003–2008) from ICESat data – the impact of interpolation, sampling and firn density. The Cryosphere *5*, 173–186.

Steffen, K., and Box, J. (2001). Surface climatology of the Greenland ice sheet: Greenland climate network 1995-1999. Journal of Geophysical Research - Atmospheres *106*, 33951–33964.

Stocker, T., Dahe, Q., and Kasper Plattner, G. (2013). Working group I contribution to the IPCC fifth assessment report climate change 2013: The physical science basis.

Stokes, C.R., Popovnin, V., Aleynikov, A., Gurney, S.D., and Shahgedanova, M. (2007). Recent glacier retreat in the Caucasus mountains, Russia, and associated increase in supraglacial debris cover and supra-/proglacial lake development. Annals of Glaciology *46*, 195–203.

Svoboda, F., and Paul, F. (2009). A new glacier inventory on southern Baffin Island, Canada, from ASTER data: I. Applied methods, challenges and solutions. Annals of Glaciology *50*, 11–21.

Tachikawa, T., Kaku, M., Iwasaki, A., Gesch, D., Oimoen, M., Zhang, Z., Danielson, J., Krieger, T., Curtis, B., and Haase, J. (2011). ASTER Global Digital Elevation Model version 2–summary of validation results. ASTER GDEM Validation Team 1–27.

Tangborn, W., and Rana, B. (2000). Mass balance and runoff of the partially debris-covered Langtang Glacier, Nepal. IAHS Publication *264*, 99–108.

Taschner, S., and Ranzi, R. (2002). Comparing the opportunities of Landsat-TM and Aster data for monitoring a debris covered glacier in the Italian Alps within the GLIMS project. In Geoscience and Remote Sensing Symposium, pp. 1044–1046.

Tedesco, M., Fettweis, X., Mote, T., Wahr, J., Alexander, P., Box, J.E., and Wouters, B. (2013). Evidence and analysis of 2012 Greenland records from spaceborne observations, a regional climate model and reanalysis data. The Cryosphere *7*, 615–630.

Teillet, P.M., Guindon, B., and Goodenough, D.G. (1982). On the slope-aspect correction of multispectral scanner data. Canadian Journal of Remote Sensing *8*, 84–106.

Thomas, R., Davis, C., Frederick, E., Krabill, W., Li, Y., Manizade, S., and Martin, C. (2008). A comparison of Greenland ice-sheet volume changes derived from altimetry measurements. Journal of Glaciology *54*, 203–212.

Toutin, T. (1995). Creating DEM from stereo images with a photogrammetric approach: Examples with VIR and SAR data. EARSeL *4*, 110–117.

Toutin, T. (2004). Comparison of stereo-extracted DTM from different high-resolution sensors: SPOT-5, EROS-a, IKONOS-II, and QuickBird. IEEE Transactions on Geoscience and Remote Sensing *42*, 2121–2129.

Toutin, T. (2008). ASTER DEMs for geomatic and geoscientific applications: a review. International Journal of Remote Sensing *29*, 1855–1875.

Trimble (2011). eCognition Developer 8.64.1 - user guide (München: Trimble Germany GmbH).

UNEP (2011). UNEP climate change strategy, for the UNEP programme of work 2010-2011 (Kenya).

UNESCO (1972). Perennial ice and snow masses. A guide for compilation and assemblage of data for a World Glacier Inventory. In IAHS Technical Papers in Hydrology, (Zürich), pp. 1–56.

Uppala, S.M., K\aallberg, P.W., Simmons, A.J., Andrae, U., Bechtold, V., Fiorino, M., Gibson, J.K., Haseler, J., Hernandez, A., and Kelly, G.A. (2005). The ERA-40 re-analysis. Quarterly Journal of the Royal Meteorological Society *131*, 2961–3012.

Vallon, M., Vincent, C., and Reynaud, L. (1998). Altitudinal gradient of mass-balance sensitivity to climatic change from 18 years of observations on glacier d'Argentière, France. Journal of Glaciology *44*, 93–96.

Vaughan, D.G. (2013). From ice to high seas (Cambridge, UK: British Antarctic Survey).

Vaughan, D.G., Comiso, J.C., Allison, J., Carrasco, J., Kaser, G., Kwok, R., Mote, P., Murray, T., Paul, F., Ren, J., et al. (2013). Observations: Cryosphere. In Climate Change 2013: The Physical Science Basis. Contribution of Working Group I to the Fifth Assessment Report of the Intergovernmental Panel on Climate Change [Stocker, T.F., D. Qin, G.-K. Plattner, M. Tignor, S.K. Allen, J. Boschung, A. Nauels, Y. Xia, V. Bex and P.M. Midgley (eds.)], (Cambridge, United Kingdom and New York, USA: Cambridge University Press), pp. 317–382.

Velicogna, I. (2009). Increasing rates of ice mass loss from the Greenland and Antarctic ice sheets revealed by GRACE. Geophysical Research Letters *36*, L19503.

Vincent, C. (2002). Influence of climate change over the 20th century on four french glacier mass balances. Journal of Geophysical Research *107*, 4375–4387.

Wang, Y., Leung, L.R., McGregor, J.L., Lee, D.-K., Wang, W.-C., Ding, Y., and Kimura, F. (2004). Regional climate modeling: progress, challenges, and prospects. Journal of the Meteorological Society of Japan *82*, 1599–1628.

Wasklewicz, T., Staley, D.M., Reavis, K., and Oguchi, T. (2013). Digital terrain modeling. In Treatise on Geomorphology, (Elsevier), pp. 130–161.

Weidick, A. (1984). Studies of glacier behaviour and glacier mass balance in Greenland: a review. Geografiska Annaler. Series A. Physical Geography *66A*, 183–195.

Weidick, A. (1988). Surging glaciers in Greenland - a status. Rapp. Grønl. Geol. Unders. *140*, 106–110.

Weidick, A., and Morris, E. (1998). Local glaciers surrounding the continental ice sheets. In: Haeberli, W, Hoelzle, M., and Suter, S. (eds.), Into the Second Century of World Glacier Monitoring- Prospects and Strategies. A Contribution to the IHP and the GEMS. Prepared by the World Glacier Monitoring Service UNESCO (Chapter 12) *1*, 197–207.

Weidick, A., Bøggild, C.E., and Knudsen, N.T. (1992). Glacier inventory and atlas of west Greenland (Boulder: National Snow and Ice Data Center).

Weidick, A., Williams, R.S., and Ferrigno, J.G. (1995). Satellite image atlas of glaciers of the world: Greenland (Denver: United States government printing office).

Weng, W.L. (1995). The area of Greenland and the ice cap. Letter to the editor. Arctic *48(2)*, 206–206.

Wenlu Qi, and Braun, A. (2013). Accelerated elevation change of Greenland's Jakobshavn glacier observed by ICESat and IceBridge. IEEE Geoscience and Remote Sensing Letters *10*, 1133–1137.

WGMS (2012). Fluctuations of Glaciers 2005–2010, Volume X - with addenda from earlier years. ICSU(WDS)/IUGG(IACS)/UNEP/UNESCO/WMO *10*, 1–336.

Whiteside, T.G., Boggs, G.S., and Maier, S.W. (2011). Comparing object-based and pixel-based classifications for mapping savannas. International Journal of Applied Earth Observation and Geoinformation *13*, 884–893.

Williams, R.S., Hall, D., and Benson, C.S. (1991). Analysis of glacier facies using satellite techniques. Journal of Glaciology *37*, 120–128.

Wilson, M.F., and Henderson-Sellers, A. (1985). A global archive of land cover and soils data for use in general circulation climate models. Journal of Climatology *5*, 119–143.

Winsvold, S.H., Andreassen, L.M., and Kienholz, C. (2014). Glacier area and length changes in Norway from repeat inventories. The Cryosphere *8*, 1885–1903.

Wood, J.D. (1996). The geomorphological characterisation of digital elevation models. Dissertation. University of Leicester.

World Meteorological Organization (1997). GHOST: Global Hierarchical Observing Strategy. (Geneva, Switzerland: World Meteorological Organization).

World Meteorological Organization (2004). Implementation plan for the Global Observing System for climate in support of the UNFCCC. *WMO/TD 1219*.

De Woul, M., and Hock, R. (2005). Static mass-balance sensitivity of Arctic glaciers and ice caps using a degree-day approach. Annals of Glaciology *42*, 217–224.

Wouters, B., Chambers, D., and Schrama, E.J.O. (2008). GRACE observes small-scale mass loss in Greenland. Geophysical Research Letters *35*, L20501.

Wulder, M.A., Masek, J.G., Cohen, W.B., Loveland, T.R., and Woodcock, C.E. (2012). Opening the archive: How free data has enabled the science and monitoring promise of Landsat. Remote Sensing of Environment *122*, 2–10.

Yang, B., Shi, W., and Li, Q. (2005). An integrated TIN and Grid method for constructing multi-resolution digital terrain models. International Journal of Geographical Information Science *19*, 1019–1038.

Yde, J. (2011). Greenland glaciers outside the ice sheet. In Encyclopedia of Snow, Ice and Glaciers, (Springer).

Yde, J.C., and Knudsen, N.T. (2005). Observations of debris-rich naled associated with a major glacier surge event, Disko Island, West Greenland. Permafrost and Periglacial Processes *16*, 319–325.

Zemp, M., Hoelzle, M., and Haeberli, W. (2009). Six decades of glacier mass-balance observations: a review of the worldwide monitoring network. Annals of Glaciology *50*, 101–111.

Zemp, M., Thibert, E., Huss, M., Stumm, D., Rolstad Denby, C., Nuth, C., Nussbaumer, S.U., Moholdt, G., Mercer, A., Mayer, C., et al. (2013). Reanalysing glacier mass balance measurement series. The Cryosphere *7*, 1227–1245.

Zeng, Q., Cao, M., Feng, X., Liang, F.X.C., and Sheng, W. (1984). A study of spectral reflection characteristics for snow, ice and water in the north of China. Scientia Sinica (Series B) *46*, 647–656.

Zwally, H.J., Schutz, B., Abdalati, W., Abshire, J., Bentley, C., Brenner, A., Bufton, J., Dezio, J., Hancock, D., and Harding, D. (2002). ICESat's laser measurements of polar ice, atmosphere, ocean, and land. Journal of Geodynamics *34*, 405–445.

Part II

Research papers

Paper I

Rastner, P., Bolch, T., Mölg, N., Machguth, H., Le Bris, R., and Paul, F. (2012). The first complete inventory of the local glaciers and ice caps on Greenland. The Cryosphere 6, 1483–1495.

The Cryosphere, 6, 1483–1495, 2012
www.the-cryosphere.net/6/1483/2012/
doi:10.5194/tc-6-1483-2012

The Cryosphere

The first complete inventory of the local glaciers and ice caps on Greenland

P. Rastner[1], **T. Bolch**[1,2], **N. Mölg**[1], **H. Machguth**[1,3], **R. Le Bris**[1], **and F. Paul**[1]

[1]Department of Geography, University of Zurich, Zurich, Switzerland
[2]Institute for Cartography, Technische Universität Dresden, Dresden, Germany
[3]Marine Geology and Glaciology, Geological Survey of Denmark and Greenland – GEUS, København, Denmark

Correspondence to: P. Rastner (philipp.rastner@geo.uzh.ch)

Received: 11 June 2012 – Published in The Cryosphere Discuss.: 16 July 2012
Revised: 8 November 2012 – Accepted: 13 November 2012 – Published: 10 December 2012

Abstract. Glacier inventories provide essential baseline information for the determination of water resources, glacier-specific changes in area and volume, climate change impacts as well as past, potential and future contribution of glaciers to sea-level rise. Although Greenland is heavily glacierised and thus highly relevant for all of the above points, a complete inventory of its glaciers was not available so far. Here we present the results and details of a new and complete inventory that has been compiled from more than 70 Landsat scenes (mostly acquired between 1999 and 2002) using semi-automated glacier mapping techniques. A digital elevation model (DEM) was used to derive drainage divides from watershed analysis and topographic attributes for each glacier entity. To serve the needs of different user communities, we assigned to each glacier one of three connectivity levels with the ice sheet (CL0, CL1, CL2; i.e. no, weak, and strong connection) to clearly, but still flexibly, distinguish the local glaciers and ice caps (GIC) from the ice sheet and its outlet glaciers. In total, we mapped $\sim 20\,300$ glaciers larger than $0.05\,km^2$ (of which ~ 900 are marine terminating), covering an area of $130\,076 \pm 4032\,km^2$, or $89\,720 \pm 2781\,km^2$ without the CL2 GIC. The latter value is about 50 % higher than the mean value of more recent previous estimates. Glaciers smaller than $0.5\,km^2$ contribute only 1.5 % to the total area but more than 50 % (11 000) to the total number. In contrast, the 25 largest GIC ($> 500\,km^2$) contribute 28 % to the total area, but only 0.1 % to the total number. The mean elevation of the GIC is 1700 m in the eastern sector and around 1000 m otherwise. The median elevation increases with distance from the coast, but has only a weak dependence on mean glacier aspect.

1 Introduction

Glaciers and ice caps (GIC in the following) are key indicators of climate change (e.g. Lemke et al., 2007), important water resources and their melt water could potentially make a substantial contribution to sea-level rise during this century (e.g. Meier et al., 2007; Hock et al., 2009; Radić and Hock, 2010). Related assessments require accurate knowledge about their location and extent as available in glacier inventories. The periphery of the Greenland Ice Sheet is one of the regions with a potentially large contribution to sea-level rise, but inventory information is incomplete and digital outlines are missing (Kargel et al., 2012). Moreover, the situation in Greenland is special due to the highly complex boundary between the ice sheet and its outlet glaciers and the local GIC (Paul, 2011). To overcome this problem and to provide a sound database for global-scale modelling applications (e.g. Huss and Farinotti, 2012; Radić and Hock, 2010), a complete dataset (vector outlines) of all GIC on Greenland is an urgent demand.

So far, only parts of Greenland's GIC have been inventoried in detail: the inventory of west Greenland (Weidick et al., 1992), the Geikie Plateau and Scoresby Sund region inventory (Jiskoot et al., 2003, 2012) and the inventory of Disko Island and the Nuussuaq – Svartenhuk peninsulas (Citterio et al., 2009). Only two datasets (Geikie plateau and South Kronprins Christian Land) are downloadable from the Global Land Ice Measurements from Space (GLIMS, www.glims.org) database. The two currently available Greenland-wide vector datasets of the total ice-covered area are the GIMP (Greenland Ice sheet Mapping Project)

dataset (available at: http://bprc.osu.edu/GDG/icemask.php) (Howat and Negrete, 2012) and the rather coarse outlines from the Digital Chart of the World (DCW, Danko, 1992). However, both datasets do not separate the local GIC from the ice sheet or from each other, i.e. they only show contiguous ice masses (or glacier complexes) without drainage divides. A similarly comprehensive dataset with vector outlines of all GIC and the ice sheet is held by GEUS based on map data from the 1980s, but not (yet) available for scientific research (Citterio and Ahlstrøm, 2012). All of the above datasets vary in their degree of generalisation, temporal frame, and consideration of details (e.g. debris cover or ice shelves).

Due to the lack of complete inventory data (the DCW was never used for that purpose) the total area covered by local GIC on Greenland has been assessed by a range of (not always fully documented) techniques. The more recently reported values range from about 49 000 km^2 (Ohmura, 2009; Weidick and Morris, 1998) up to 76 200 km^2 (Dowdeswell and Hambrey, 2002; Weidick and Morris, 1998). Despite the large area covered (approximately 7 % of all GIC worldwide, cf. Hock et al., 2009), the calculation of the sea-level rise contribution of Greenland's GIC has received only limited attention. The absence of a consistent and complete inventory required the application of rough extrapolation schemes (Radić and Hock, 2010), their complete exclusion (Raper and Braithwaite, 2006), or a separate treatment (Lemke et al., 2007).

For the above reasons we have compiled the first glacier inventory of all GIC in Greenland by applying semi-automated glacier-mapping techniques (e.g. Paul and Kääb, 2005) to more than 70 Landsat scenes. In combination with a digital elevation model (DEM) drainage divides were derived following Bolch et al. (2010) and digitally intersected with the glacier outlines to obtain individual glaciers and to calculate topographic parameters for each entity from the DEM following Paul et al. (2009). A rather challenging issue in this regard was to define a consistent strategy for separating the GIC from the ice sheet, as the local GIC occur not just in coastal regions away from the ice sheet, but also on mountain ridges within and adjacent to the ice sheet (Weidick and Morris, 1998). Considering the varying requirements of the different scientific communities (e.g. sea-level change or hydrological and glaciological modelling), we assigned three connectivity levels (CL) to all GIC describing the strength of connection (no, weak, strong) to the ice sheet. This distinction is required, for instance, to avoid double counting of their contribution to sea-level rise, as the normally used ice masks for the Greenland Ice Sheet also include (at least partly) local GIC (Paul, 2011).

The main purposes of the inventory presented here are thus to close the knowledge gap about the local GIC on Greenland and to provide a sound base for proper change assessment (Kargel et al., 2012). While the full dataset will be made available through the GLIMS database (Bishop et al., 2004; Raup et al., 2007), the outlines along with their connectivity levels have already been made available within the Randolph Glacier Inventory (RGI) documented by Arendt et al. (2012).

2 Study region and datasets

2.1 Study region

Our study region is the whole of Greenland (Fig. 1), extending from 60° to 84° N (2650 km) and from 11° to 74° W (1200 km). More than 80 % of Greenland is covered by ice ranging from sea level to 3200 m a.s.l. at the central dome of the ice sheet and to almost 3700 m a.s.l. on Greenland's highest mountain (Gunnbjørn Fjeld). To provide a more regionalised assessment of the GIC characteristics, we divided Greenland into seven glaciological subregions (Fig. 1) following the suggestion of Weidick (1995), but combining the southern part in two sectors. All place names used in this study are based on Weidick (1995) with missing names being added from Rignot and Mouginot (2012).

Greenland's climate is polar to sub-polar. The island acts climatologically as a centre of cooling, and hydrologically as a large store of freshwater. Temperatures in Greenland have been monitored since the 1870s, showing a warming trend since the 1980s that increased during the 1990s predominantly on the western coast (Cappelen et al., 2007). The year 2010 was the warmest year across Greenland (except for the northeast) since the start of meteorological observations (Box et al., 2006). The present-day accumulation pattern in Greenland is roughly captured by measurements (Bales et al., 2009; Burgess et al., 2010) and regional climate modelling (Box et al., 2006; Ettema et al., 2009; Fettweis et al., 2008), with large uncertainties remaining in regions where measurements are sparse (Helsen et al., 2012). According to Ohmura and Reeh (1991), the highest annual precipitation amounts occur south of 65° N on the western side (400–1000 mm a^{-1}) and south of 70° on the eastern side (400–2500 mm a^{-1}) of Greenland. The lowest amounts are found in the northeastern interior (100 mm a^{-1}) and locally around Søndre Strømfjord on the western coast and Narssarssuaq in southern Greenland.

A large variety of glacier types from ice caps with numerous outlet glaciers, to valley and mountain glaciers of all shapes and cirques are found in Greenland. Due to the large north–south extent, different thermal regimes can be expected for the glaciers. Whereas in the north most GIC are cold, they are polythermal in the central part and in the south also temperate GIC are found (Bull, 1963; Hammer, 2001). Several glaciers on Greenland were identified as being of surge type; for instance in the Stauning Alper and Geikie Plateau region (Jiskoot et al., 2003, 2012; Weidick, 1988) but also in the Disko/Nuussuaq region (Yde and Knudsen, 2005).

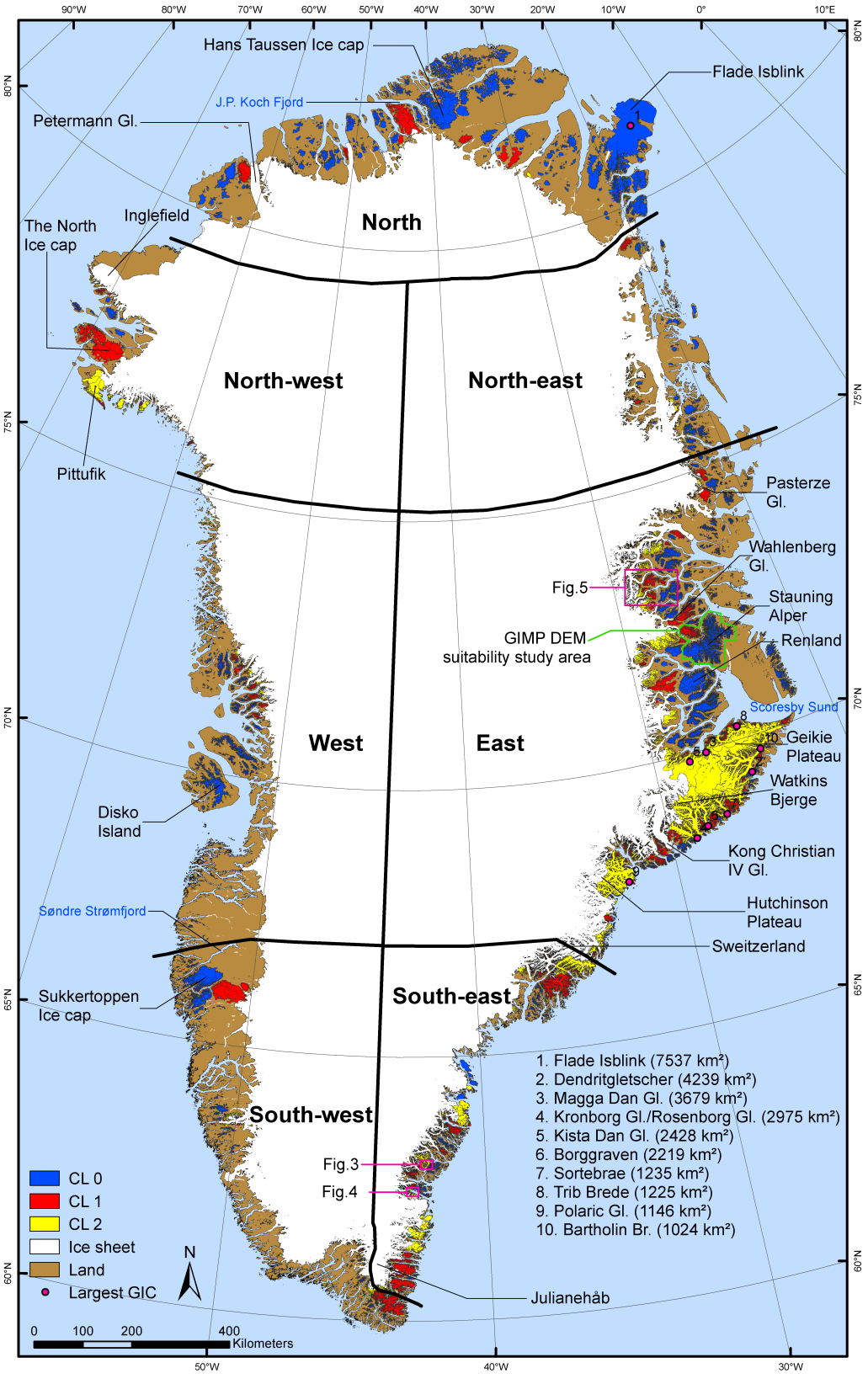

Fig. 1. Map of Greenland showing all local GIC (colour coded) and place names mentioned in the text. The green box indicates the area selected for the investigation of DEMs and the magenta ones the location of Figs. 3, 4 and 5.

2.2 Datasets

We selected 73 of the most suitable (with minimum seasonal snow, and largely cloud free) Landsat scenes available from the glovis.usgs.gov archive, focussing on Landsat 7 ETM+ scenes (1999–2002) dating from before the failure of the scan line corrector (SLC) in 2003 (Table S1 and Fig. S1). Seasonal snow was a severe problem in the north-eastern part of Greenland and we mosaicked several SLC-off scenes from the years 2003 to 2008 with much better snow conditions to get an appropriate coverage. We also used some Landsat TM scenes from the period 1994 to 2008 to fill remaining data gaps. It has to be noted that during this period some glaciers have shown considerable changes in extent (e.g. Yde and Knudsen, 2005). The acquisition date of each scene processed is documented in the attribute table of each glacier polygon, so that a reference for change assessment is available.

To address the missing coverage with Landsat data north of 80° N, we used the outlines of the GIMP ice cover map that is available online at http://bprc.osu.edu/GDG/icemask.php (Howat and Negrete, 2012) as a baseline dataset. The GIMP ice cover map mostly excludes debris-covered glacier parts and glaciers smaller than 0.05 km^2. In the northernmost region, ice shelves were included as the purpose of the GIMP dataset is to consider all ice-covered areas. We improved the GIMP outlines by visual interpretation of a MODIS 250 m image of the same region. This was important as ice shelves and some wrongly classified ice-covered lakes adjacent to outlet glaciers of the Hans Tausen Ice Cap (cf. Hammer, 2001) had to be removed for our purpose.

For our inventory, we decided to stick to the DEM of the Greenland Ice sheet Mapping Project (GIMP, Howat et al., 2012) with the supplement tile "Gl-north" from the website www.viewfinderpanoramas.org (VFP) in the very far north that was not covered by the GIMP DEM. The GIMP DEM has a resolution of 90 m and a reported vertical accuracy of 10 m (Howat et al., 2012). It was merged from several datasets acquired between the years 2000 and 2009. As high-resolution photogrammetric DEM extraction only provides accurate results in regions with good optical contrast and is therefore less accurate above the snow line, coarser resolution DEM data (500 m Advanced Very High Resolution Radiometer, AVHRR) was merged with the GIMP DEM (Howat et al., 2012). The VFP DEMs were mainly created from 1 : 250 000 and 1 : 500 000 scale topographic maps with locally variable quality (Ferranti, 2012). Additionally, the ASTER GDEM II (http://reverb.echo.nasa.gov/reverb/) was used to assess the suitability of the GIMP DEM for extracting topographic parameters in the Stauning Alper region.

3 Methods

The data processing workflow can roughly be subdivided into three steps (Fig. 2): (a) glacier mapping and editing, (b) creation of drainage divides to separate the local GIC from the ice sheet and from each other, and (c) intersection of the edited glacier outlines with the drainage divides, and a subsequent calculation of glacier-specific statistics using again the DEM. These three steps are described in the following in more detail.

3.1 Glacier mapping

For the glacier mapping we applied the well-established semi-automated band ratio method (e.g. Paul and Andreassen, 2009) using the raw digital numbers of Landsat ETM+ bands 3 (red) and 5 (shortwave infrared/SWIR). An optimal threshold for the ratio image was chosen interactively for each scene with pixels being classified as ice when the band 3/band 5 ratio exceeded 1.6 or slightly higher values (scene dependent). For several scenes an additional threshold in band 1 (blue) was applied to improve the mapping in shadow regions where path radiance otherwise introduces misclassification (cf. Paul and Kääb, 2005). In the next step, a median filter (3×3 kernel) was applied to reduce noise and the classified raster image was converted into a vector format (shapefile). Clean ice was accurately mapped by the algorithm and did not require manual correction for scenes with good snow conditions. However, the corrections for clouds, shadow, debris cover, seasonal snow and icebergs were time consuming, and took approximately 80 % of the total processing time (see examples in Figs. 3 and 4). Similar to the experience in other regions (e.g. Paul and Andreassen, 2009; Bolch et al., 2010), one of the most challenging questions was related to the correct consideration of extended snow fields that showed no ice but might be perennial rather than seasonal. As a general rule, we included all polygons showing ice and excluded most of the "snow only" polygons, in particular at low elevations. Moreover, most snow patches were removed by applying a size threshold of < 0.05 km^2. The correct identification of frozen lakes was in some regions also difficult, a well-known problem when working in Arctic regions (e.g. Paul and Kääb, 2005; Racoviteanu et al., 2009). In this study we have additionally used DEM information (hillshades) and multi-temporal satellite images to improve their identification. The mapping and the manual corrections were always performed in the local UTM system of the respective scene (all scenes together spanning UTM zones 18–28). After that, the resulting outlines were mosaicked and reprojected with an area-preserving projection (Greenland Lambert Azimuthal Equal Area projection with D WGS 1984 datum), as the UTM projection is not area preserving.

The accuracy of the glacier outlines is difficult to assess as appropriate reference data are required but were not available for this region. However, a recent round robin experiment has

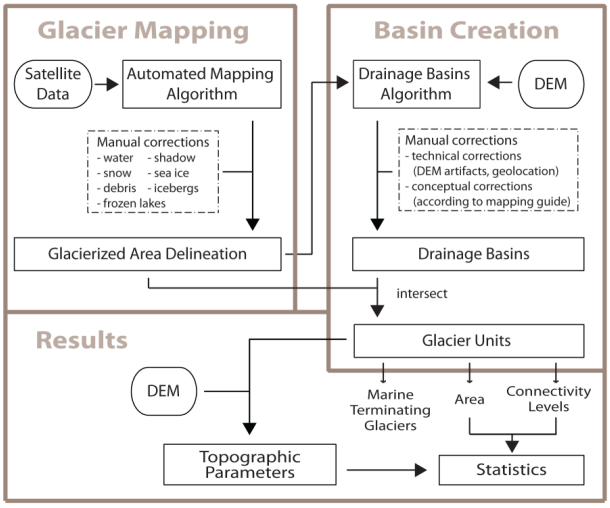

Fig. 2. Schematic flow chart illustrating the connection of the individual processing steps.

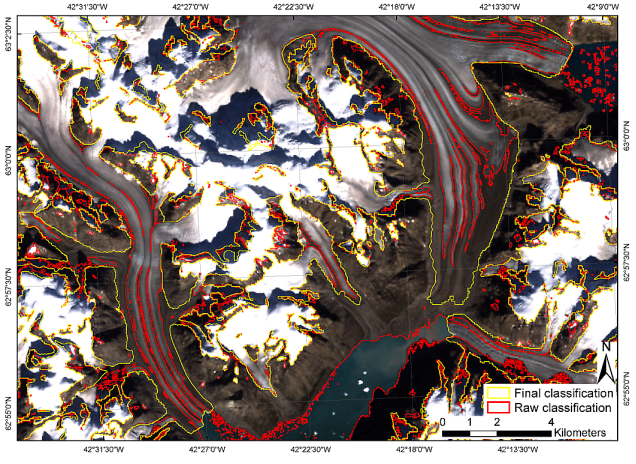

Fig. 3. Close-up of the raw classification (red) and the result after manual correction (yellow) (Landsat ETM+, 233 016, 10 September 2001).

analysed accuracy issues in more detail (Paul et al., 2012) comparing outlines derived automatically and from multiple manual digitisation of the same set of glaciers by the same and different analysts. The study concluded that the two methods (manual and automated) have about the same precision for clean ice (standard deviations between 2 and 5 %) and that results for debris-covered ice were strongly variable, with area differences exceeding 30 %. For clean ice, the locations of manually-digitized outlines were found to vary by about 1 TM pixel or 30 m (Paul et al., 2012). We thus determined the precision of the outlines derived here by applying a +15 m buffer around all glacier complexes (cf. Bolch et al., 2010). Adding this uncertainty gives a 3.1 % larger total area,

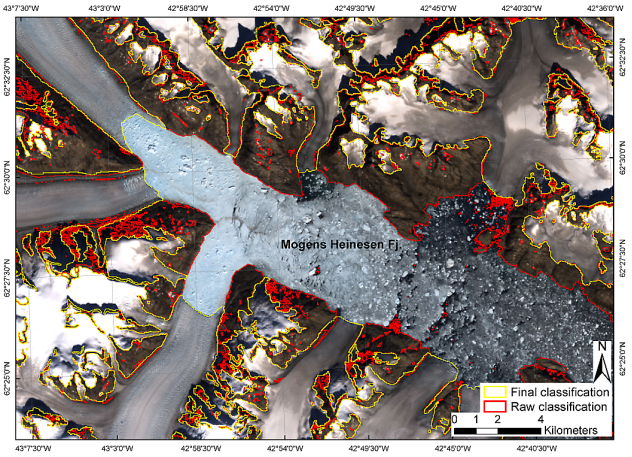

Fig. 4. Sea ice in front of marine terminating glaciers is mapped correctly with the band ratio method and has to be manually removed afterwards (Landsat ETM+, 233 016, 10 September 2001).

which is in the following used as a measure of uncertainty for the derived area values.

3.2 Drainage divides and assignment of connectivity levels

We derived drainage divides to separate the glacier complexes into individual glaciers in a two-step approach: First, drainage divides were automatically calculated by the GIS using watershed analysis following a modified version of an approach developed by Bolch et al. (2010), and in a second step they were manually adjusted using a colour-coded flow direction grid in the background.

The separation of local GIC was actually rather challenging, as outlet glaciers from otherwise disconnected ice caps can join outlets from the ice sheet (and thus contribute to their flow), or glaciers that are connected to the ice sheet in the accumulation region can have completely separated ablation regions. To serve the varying requirements of different communities (e.g. hydrological and glaciological modelling), we defined three connectivity levels (CL) of the GIC with the ice sheet:

- CL0: no connection;
- CL1: weak connection (clearly separable by drainage divides in the accumulation region, not connected or only in contact in the ablation region);
- CL2: strong connection (difficult to separate in the accumulation region and/or confluent flow in the ablation region).

To assign the connectivity level automatically in the GIS, we also applied a "topological heritage" rule. Glacier entities connected to other entities that have been assigned CL1 will adopt the same class. This is also the case for entities

connected to CL2 entities. CL0 entities (either individual or within a group of connected entities) have no connection to the ice sheet or any of the CL1 or CL2 GIC. A colour-coded illustration of the assigned connectivity levels is depicted in Fig. 5.

Indeed, the topological heritage rule could only be applied after the glacier complexes were separated into distinct entities. And here the next set of challenges started: as pointed out by Racoviteanu et al. (2009), separating an ice cap into entities is difficult from a methodological point of view and it can be discussed if an ice cap should be separated into entities at all (glaciological vs. hydrological application). A further issue is that a watershed algorithm can find a very large number of divides for an ice cap with a near symmetric shape that do not make sense even from a hydrological point of view. This changes when an ice cap has prominent outlet glaciers and at least some topographic variability such as the Jostedalsbreen ice cap in Norway (Paul et al., 2011). The further set of rules to separate the glacier-complexes consistently is:

- GIC rule I: divide an ice cap only when it has prominent outlet glaciers and at least some topographic variability in the accumulation area.
- GIC rule II: if one outlet glacier is separated, the entire ice cap has to be divided into entities.
- GIC rule III: for ice caps and glacierised mountain flanks, the fewest number of glaciers should be created, only considering the most prominent topographic divides.

We are aware that rule III is a very subjective one. As an example, we show in Fig. 6 two larger ice caps. Only one of the ice caps is subdivided, as the other one has no topographic variability and no prominent outlet glacier. The correction of the raw drainage divides provided by the automated flowshed algorithm according to the rules above was a tedious and time-consuming work for all local GIC on Greenland. To support interpretation, we additionally used a hillshade and contour lines from the DEM, as well as contrast enhanced versions of the respective Landsat scenes.

3.3 Topographic parameters and DEM accuracy

Finally, the glacier outlines were digitally intersected with the drainage divides to obtain the glacier entities (cf. Bolch et al., 2010; Paul et al., 2002). This dataset is then digitally combined with the DEM and products thereof to derive a set of topographic parameters (area, minimum, maximum, mean and median elevation, mean slope and aspect) from the zonal statistics function in the GIS (calculates statistics on values of a raster dataset within the zones of another dataset) following Paul et al. (2009). As the smallest glacier in the sample (0.05 km^2) covers only about six cells in the GIMP DEM, the quality of the derived parameters is reduced for

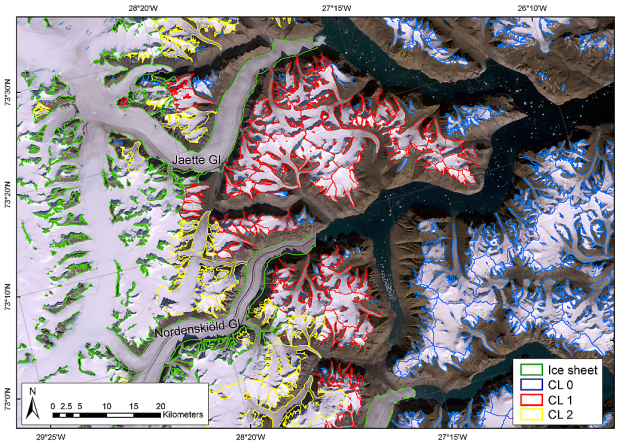

Fig. 5. Close-up of the assigned connectivity levels (colour-coded). Glaciers in contact with the ice sheet get their connectivity level first. Afterwards connected neighbouring polygons adopt the connectivity level, and finally disconnected glaciers are assigned to CL0 (Landsat ETM+, 232 008, 18 August 2001).

such small glaciers. We have thus calculated for a subset of 620 glaciers in the Stauning Alper region (see Fig. 1 for location) the minimum, maximum, mean and median elevation with the GIMP DEM and the ASTER GDEM II. A visual comparison of the hillshades of both DEMs highlights the much more uneven surface (with many artefacts) in the GDEM (Fig. 7). Although the standard deviation of the differences between individual glaciers are rather high (minimum: 636 m, maximum: 609 m, mean: 546 m, and median: 391 m) we found that the differences of these parameters between the two DEMs are rather small in the mean (minimum: 67 m, maximum: −46 m, mean: 1 m, and median: 3 m). On that basis we deemed the GIMP DEM acceptable also for small glaciers.

4 Results

In Fig. 1 we show an overview of all local GIC and their connectivity level. Three large regions, the Pittufik in the north-west, the entire Geikie Plateau with some glaciers of the Watkins Bjerge area and the Hutchinson Plateau in the east, and some smaller regions have CL2 connectivity according to our rules. In the southern sectors, we defined the peninsula in the south-east of Sweitzerland as CL1, together with three further peninsulas in the far south-east and the Sukkertoppen Ice Cap. In the northern sectors, we classified the North Ice Cap, the ice cap touching Petermann Glacier at the western side, and the ice cap south of J. P. Koch Fjord as CL1. The most prominent examples for the CL1 class in the eastern sector are the two ice caps located at the north and south of Pasterze Glacier, the two ice caps south of Wahlenberg Glacier and the ice cap in the east of Renland (see Fig. 1 for location).

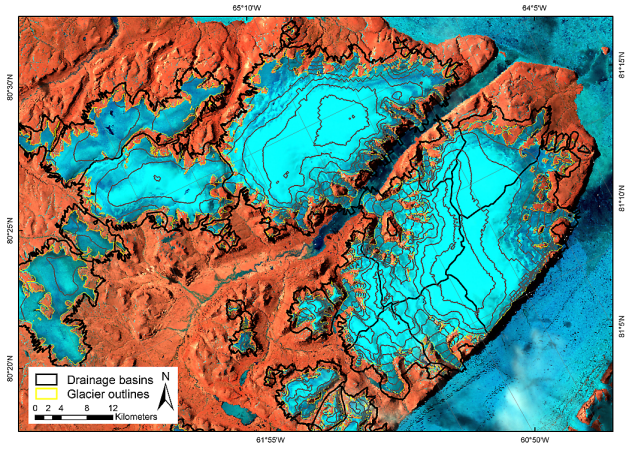

Fig. 6. Separation of ice caps into glacier entities and from each other. Though the large ice cap in the upper centre has several distinct outlet glaciers, it is not separated, as topographic structure is missing in the accumulation area (Landsat ETM+, 045 001, 30 June 2000).

Table 1. Area covered and number of GIC for each connectivity level and the ice sheet.

	Area [km^2]	Number
CL0	65 474 ± 2029	17 508
CL1	24 246 ± 751	1815
CL2	40 355 ± 1251	957
Total GIC	130 076 ± 4032	20 280
Ice sheet	1 678 500 ± 52 033	1
Total ice cover Greenland	1 808 575 ± 56 065	20 281

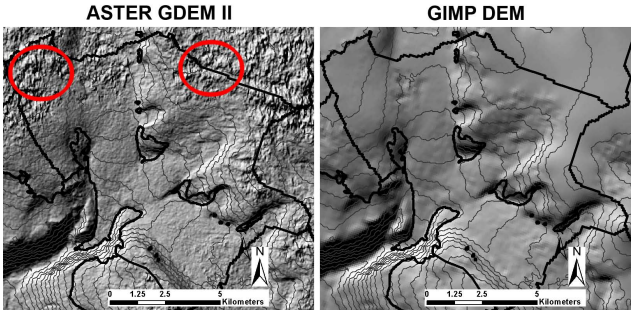

Fig. 7. Comparison of hillshades derived from the GIMP DEM and the ASTER GDEM II for a small sub region in the test area. Red circles indicate artefacts in the ASTER GDEM II that likely result from poor contrast in snow-covered regions.

Considering only entities larger than 0.05 km^2, all CL0 and CL1 GIC have a total area of 89 720 ± 2781 km^2. CL2 glaciers add 40 355 ± 1251 km^2 for a total of 130 076 ± 4032 km^2 and ∼ 20 300 GIC overall. The ice sheet itself has an area of ∼ 1 678 500 ± 52 033 km^2 according to our dataset and the entire ice covered area in Greenland is thus ∼ 1.8 million km^2. Hence, the area covered by the local GIC is ∼ 7.2 % of the total ice-covered area (Table 1). From the entire sample (including CL2), 904 (4.5 %) GIC are identified as marine terminating with an area of 64 975 ± 2014 km^2 (Table S2). They are mostly found in the south-east and east of Greenland (Fig. S2). The area covered by marine terminating glaciers in the Geikie Plateau is 24 494 km^2 in our study and thus considerably lower than in the study by Jiskoot et al. (2012) who found 37 432 km^2. This is because in the latter study Kong Christian IV Glacier is included, while we have excluded this large glacier due to a very long and uncertain divide on shallow ice ridges. Subtracting the area of Kong Christian IV Glacier (11 079 km^2) from the area determined by Jiskoot et al. (2012) yields an area of 26 352 km^2 which is quite close to our result (±750 km^2), considering the error bounds in both inventories.

Plotting the area covered and number of glaciers per size class separately for the seven sectors, all glaciers and the marine terminating glaciers only, reveals interesting differences (Fig. 8). In six subregions and Greenland as a whole the size classes 0.1–0.5 and 1.0–5.0 km^2 have the highest relative contributions by number (about 35 and 20 %, respectively), but together they account for only a small part (10 %) of the total area. In contrast, glaciers larger than 10 km^2 contribute only 8 % to the number but nearly 84 % to the total area in these regions. This is rather different for the marine terminating glaciers where glaciers > 5 km^2 contribute 64.3 % to the total number and 98 % to the total area; i.e. their mean size is much larger (71.8 km^2) compared to the other regions (Table S3). In absolute terms, the largest glaciers are found in the east and northern sectors (Fig. 8; Table S3) followed by the southern and west sectors. The second largest of the size classes (100–500 km^2) is dominant in the north-west where large ice caps are present. Small glaciers are mostly found in the southern and western sectors.

The size distribution by aspect sector for CL0 and CL1 glaciers is listed in Table S4 (absolute values) and illustrated in Fig. 9 (relative values). The distribution is rather uniform for the two south as well as the east and west sectors (Fig. 9a), but concentrated towards SW for the sector north, towards N and S in the north-west sector and again rather uniform for the north-east sector (Fig. 9b). The SW exposition is also dominant for the whole of Greenland.

The area-elevation distributions for each sector and all of Greenland are depicted in Fig. 10 for all classes, and for the sector east and entire Greenland also with CL0 and CL1 separately. The largest ice-covered areas can be found in the north and east sectors, with remarkably different maxima around 1000 m a.s.l. and 1700 m a.s.l., respectively. The lower maximum in the elevation distribution in the northern sector can be ascribed to the predominance of ice caps, and likely also to the lower mean annual air temperature (MAAT) in this region. The special topography of the numerous ice

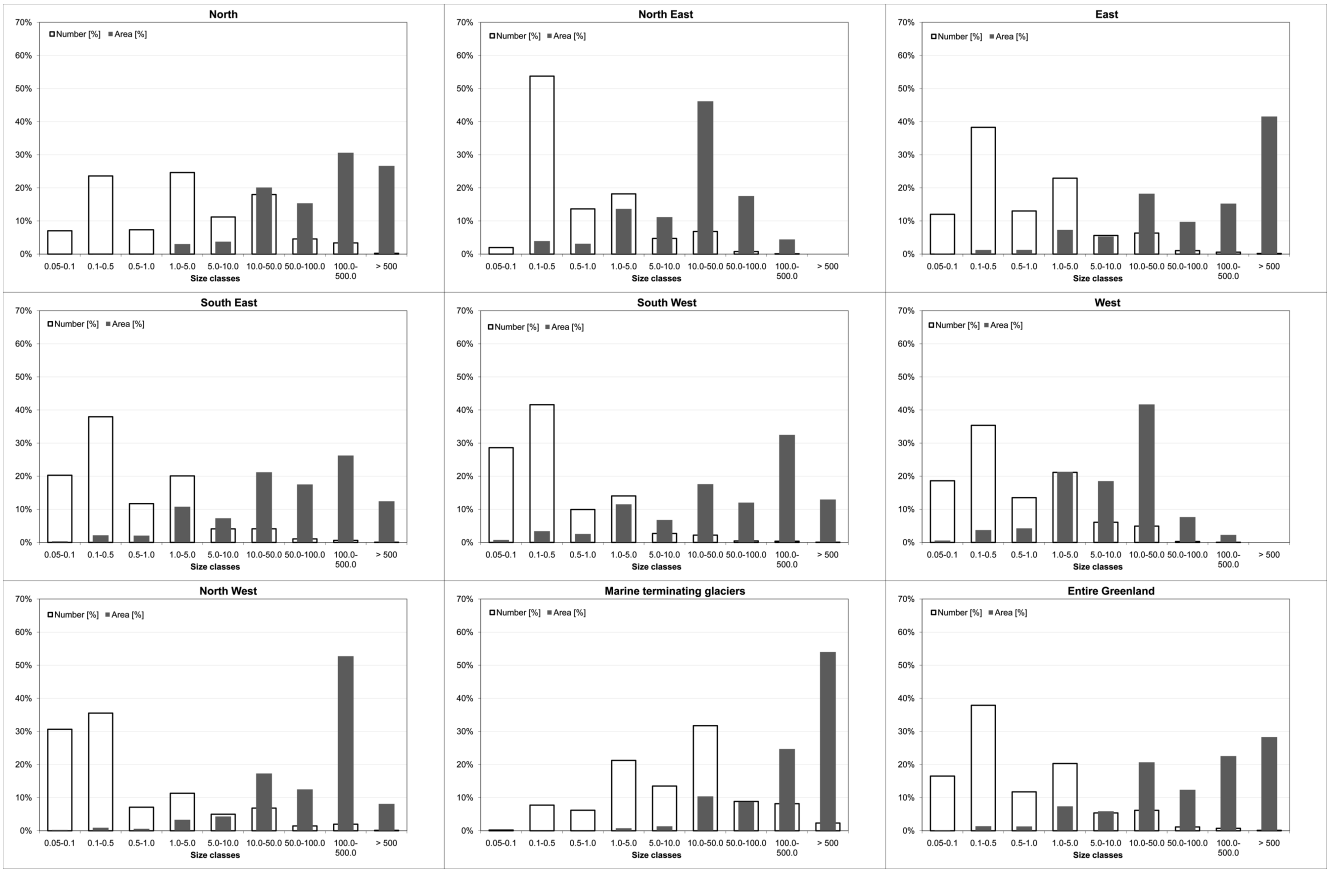

Fig. 8. Number of glaciers and area covered per size class and for each sector, the whole of Greenland and marine terminating glaciers.

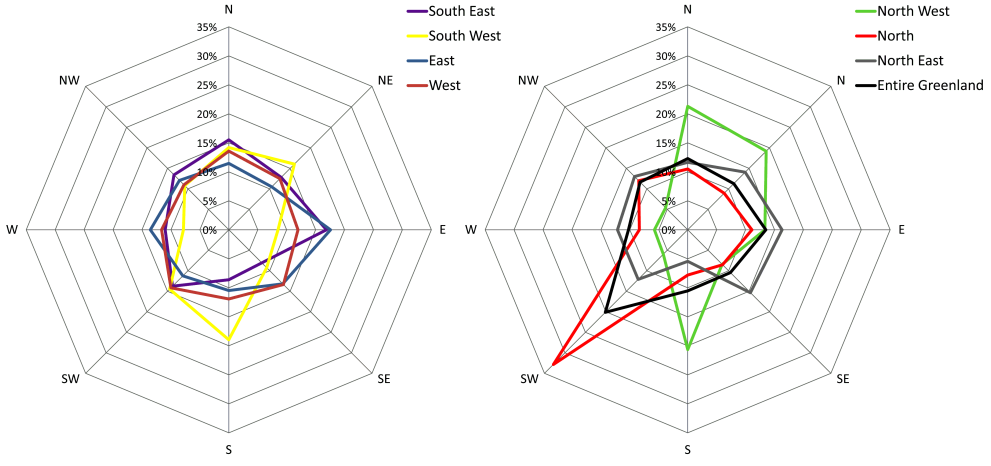

Fig. 9. Area distribution versus aspect per sector for all GIC with CL0 and CL1.

caps also creates a drop in the ice-covered area below 1000 m for all glaciers. In contrast, the other sectors contain much less ice and its distribution with elevation is more homogeneous. Maximum coverage is found around 900 and 1200 m a.s.l. The lower elevation of glacier complexes in the southern sector hints at a generally higher MAAT (or much higher precipitation) than in the north. The CL2 glaciers increase the area covered for the eastern sector considerably, whereas in the north this is not the case as nearly all ice caps are disconnected from the ice sheet. Above 2000 m a.s.l. ice is only found in the eastern sector and the area-elevation distribution is thus the same as for Greenland as a whole. Taken together,

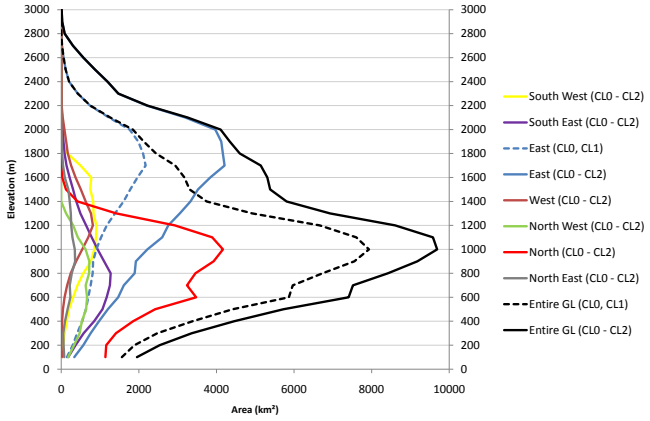

Fig. 10. Area-elevation distribution in 100 m bins for the seven sectors and all GIC. Dotted lines show the hypsometry for GIC with CL0 and CL1 only.

most of the ice (∼ 56 %) is found between 600 and 1400 m with the peak at 1000 m a.s.l.

In Fig. 11 the spatial distribution of median elevation is shown as colour-coded circles for all GIC. A strong increase in median elevation from the coast to the interior can be seen all around Greenland with lowest values closest to the coast (0–500 m) and increasingly higher values (up to ∼ 3000 m) towards the interior.

5 Discussion

5.1 Assignment of connectivity levels

The assignment of connectivity levels and the rules for subdividing glacier complexes into glaciers are certainly a matter for discussion. Weidick et al. (1992) already mentioned the separation of the local GIC from the ice sheet as a major problem for Greenland, but since then no consistent solution for the whole of Greenland was presented. Assigning connectivity levels 0 and 1 (CL0 and CL1) was in most cases straight forward due to clearly identifiable drainage divides. We introduced CL2 to have strongly connected local GIC available for both, ice sheet modellers who traditionally included them in the ice sheet and GIC modellers who see them as separate entities. The hydrologic divides as derived from watershed analysis are obtained objectively, but need some editing and human interpretation to serve both communities. With the interpretation provided here we have provided a useful and sufficiently flexible solution. When better suggestions for a consistent separation come up, e.g. based on a more precise DEM or a more appropriate approach, it is possible to refine the divides in the digital database. The manual correction of the drainage divides was time consuming, but clearly faster than the manual correction of the glacier mapping errors (debris, shadow, seasonal snow). According to our rules, the Julianehåb and Inglefield ice domes have been

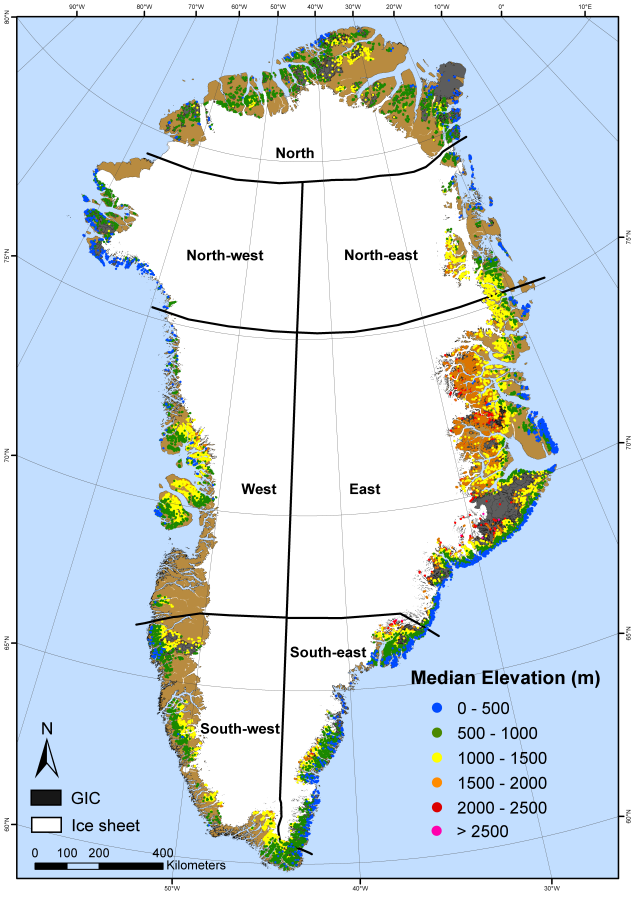

Fig. 11. Colour-coded visualisation of median elevation for all GIC. The mapped local GIC are shown in dark grey in the background. (min median elevation: 12 m, max median elevation: 3100 m).

interpreted as being part of the ice sheet in our inventory. Weidick et al. (1992), however, counted these ice masses as being local, but this is not compliant with the extent used in current ice sheet models (e.g. Fettweis et al., 2008). We have thus decided to exclude them completely from the local GIC.

5.2 Comparison to other datasets

The comparison of the total area for all glaciers > 0.05 km^2 with CL0 connectivity to the other two available Greenland-wide datasets (DCW, GIMP) listed in Table 2 reveals that the area is highest in our dataset (65 474 ± 2029 km^2), second highest in the GIMP dataset (61 610 km^2) and lowest in the DCW dataset (57 715 km^2). This indicates that the generalisation in the DCW and the partly missing debris cover in the GIMP outlines make quite a difference (−12 % and −6 %, respectively) for the total area covered. The glacier outlines from the hydrologic layer of the DCW are obtained from digitized 1 : 1 000 000 scale topographic maps (Danko, 1992) and are thus expected not to include most of the smaller glaciers.

Table 2. Available vector datasets of covering the local GIC on Greenland and their differences. The "area covered (GIC)" row refers to connectivity levels CL0 and CL1. The entire dataset of this study includes the improved GIMP dataset (covering 14 068 km^2) in the northernmost part of Greenland.

	DCW	GIMP	new inventory
Source	Maps 1 : 1 000 000	optical/radar	Landsat + GIMP
Period	1950s–1980s	1999–2001	1999–2004
Generalisation	high	none	none
Drainage divides	no	no	yes
Spatial resolution	approx. 2 km	15 m	30 m
Smallest unit mapped	0.1 km^2	0.05 km^2	0.05 km^2
Debris cover included?	yes	no	yes
Northernmost region included?	yes	yes	Yes, (improved GIMP)
Availability	free	free	free
Area covered (GIC)	57 715 km^2	61 610 km^2	65 474 ± 2029
Area covered (total)	1 825 030 km^2	1 798 960 km^2	1 808 575 km^2

Earlier studies used a wide range of techniques to estimate the total area covered by local GIC (cf. Sect. 1 or Cogley, 2012). The values derived here ($\sim 89\,720 \pm 2781$ km^2 for CL0 and CL1, $\sim 130\,076 \pm 4032$ km^2 incl. CL2) are about 50 % and 100 % larger than the mean value ($\sim 62\,600$ km^2) of the more recent previous estimates (e.g. Ohmura, 2009; Weidick and Morris, 1998; Dowdeswell and Hambrey, 2002). It has to be noted that Weidick and Morris (1998) also include CL2 GIC in their estimate as well as some larger ice domes (e.g. Julianehåb) that are not included in our assessment. The much higher total area found here implies that also the volume of the local GIC (and hence their potential sea-level rise contribution) might be higher than assumed in previous studies.

Comparing the entire ice-covered area in Greenland with the results from Kargel et al. (2012) reveals a difference of only 7480 km^2, which is less than 0.5 %. Other estimates calculated this area as 1.765×10^6 km^2 form the union of all pixels in a MODIS image composite that was acquired over twelve years (http://bprc.osu.edu/wiki/Mapping_Land_Ice) or as 1.756×10^6 km^2 derived from a 1 : 2 500 000 map (Weidick and Morris, 1998).

5.3 Inventory data

The distribution of the area and number of glaciers with the size class is similar to distributions reported for other regions, but has locally also deviations due to the dominant presence of large ice caps. The total number of GIC (20 300) depends on the algorithm used for creating divides. The latter also determine, along with the topography in each sector, the aspect distribution presented here. Hence, using another DEM or other rules to create the divides will also result in a different number of glaciers and aspect distribution. It has also to be noted that the mean aspect of ice caps is rather arbitrary, even when they are divided into entities. The mean or median elevation did not appear to depend on aspect as in other regions (Evans and Cox, 2005), but rather on the distance from the coast. Interpreting the median elevation as a proxy for the equilibrium line altitude (ELA) and hence as an indicator of the precipitation amount (e.g. Braithwaite and Raper, 2009), a decreasing precipitation trend from the coast to the interior of Greenland can be inferred. Such a trend was also found in previous studies and other regions with a maritime climate (Le Bris et al., 2011; Jiskoot et al., 2003, 2012; Paul et al., 2011; Weidick et al., 1995), and is confirmed here from an interpretation of the topographic glacier parameters for the entire perimeter of Greenland. Deriving such a trend from direct measurements is difficult, because weather stations in Greenland are either coastal (Danish Meteorological Institute stations) or located on the ice sheet (GC-Net and PROMICE Network) (Ahlstrøm et al., 2008; Steffen and Box, 2001).

5.4 DEM quality impacts

The quality of the DEM impacts on the inventory. As a DEM with a high spatial resolution (e.g. 30 m) and quality (e.g. no artefacts) is not available so far, we have given preference to the "low resolution with sufficient quality" version of the GIMP DEM. It had clear advantages for delineating the drainage divides in the accumulation areas compared to the higher resolution GDEM, and topographic parameters were not much different from the GDEM. The VFP DEM used for the northernmost part of Greenland was the only dataset available. It is difficult to determine the quality of this DEM, but at least the visual inspection (hillshade) revealed its general suitability. Until a higher resolution and more precise DEM is available for the entire region (e.g. from the TanDEM-X mission), the values calculated here have likely the highest quality possible today.

5.5 Accuracy

Apart from the methodological constraints, for example related to the position of ice divides and the interpretation of

perennial snow fields, we find that the accuracy of the glacier outlines is similar to that reported in other studies having applied automated glacier mapping in combination with manual correction (e.g. Paul et al., 2002, 2012; Bolch, 2007; Bolch et al., 2010). We derived an area uncertainty of about 3 % in the mean over all glaciers with the buffer method, but this value can be much higher for individual glaciers and those with debris cover. The latter could mostly be delineated rather accurately, because solar elevation is low at the latitude of Greenland and thus provides sufficient illumination differences. However, for small glaciers and those located in regions of permafrost, the issue is more challenging. Accurate mapping of ice caps is more straightforward due to the missing debris cover, but attached snow patches (either seasonal or perennial) introduced considerable uncertainty, in particular in the northern sector of the study region.

In the same region, the impact of the missing glacier area in the SLC-off scenes from Landsat ETM+ acquired after 2002 is locally non-negligible, but overall smaller than other uncertainties. Without using these scenes it would have been nearly impossible to determine whether some of the mapped features were glaciers or not. In this regard, the mosaicking of several SLC-off scenes with much less snow cover than in the SLC-on scenes was worth the effort.

We also analysed the error due to re-projection between the UTM and the Greenland Lambert Azimuthal Equal Area projection system with latitude, and found mean area differences of 0.02 % in the south and 0.05 % in the north. Hence, they are two orders of magnitude smaller and negligible.

6 Summary

We presented the first glacier inventory for the whole of Greenland based on the classification of multispectral satellite imagery and manual editing of more than 70 Landsat scenes obtained from http://glovis.usgs.gov/. Additionally, we included data from an ice-cover map (http://bprc.osu.edu/GDG/icemask.php) for the northernmost part of Greenland that is not covered by Landsat. The new inventory revealed a 50 % greater total area ($89\,720 \pm 2781\,km^2$) than in the mean of the more recent previous estimates. Counting also glaciers with a strong connectivity to the ice sheet (CL2) as being local, the total area is $130\,076 \pm 4032\,km^2$ from $\sim 20\,300$ entities (of which about 900 are marine terminating with an area of $64\,975 \pm 2014\,km^2$). The much higher area indicates the importance of assigning connectivity levels to each entity to have samples serving the needs of different user communities. While this assignment could be implemented more or less automatically, the separation of the local GIC into entities was tedious and time consuming work. Though the quality of the inventory differs regionally, the presented inventory is in our opinion the best possible dataset available to date. However, as the location of drainage divides depends on the DEM used and the rules applied for subdividing glacier complexes, differences to other or future assessments can be expected. In any case, the differences between the datasets compared here have nothing to do with real area changes of the local GIC.

The correction of the automatically mapped glacier outlines (e.g. for debris, shadow and snow) took about 80 % of the glacier mapping workload. Excluding glaciers smaller than $0.05\,km^2$ helped to reduce the uncertainty due to seasonal snow. Applying a $1/2$ pixel buffer around all outlines revealed an overall area uncertainty of 3 %. The obtained size-class distributions are in general similar to those found in other regions, but are slightly different in regions dominated by ice caps. The largest number of local GIC is found in the east sector and the smallest in the west sector, largely due to the different topography of the two regions. Most of the ice is found around 1700 m a.s.l. in the East sector and around 1000 m a.s.l. in all other sectors. A dependence of glacier area on aspect was only found in the North and South sectors. The Median elevation strongly increased with the distance from the coast, indicating decreasing precipitation amounts towards the interior of Greenland. In view of current approaches to determine the future evolution of GIC under various scenarios of climate change at a global scale, we recommend using the outlines from the CL0 and CL1 GIC in combination with the GIMP DEM.

Supplementary material related to this article is available online at: http://www.the-cryosphere.net/6/1483/2012/tc-6-1483-2012-supplement.pdf.

Acknowledgements. This work was supported by the ESA project Glaciers_cci (4000101778/10/I-AM) and funding from the ice2sea programme from the European Union 7th Framework Programme, grant number 226375. Ice2sea contribution number 097. H. M. acknowledges funding from the Programme for Monitoring of the Greenland Ice Sheet (PROMICE). Landsat scenes were obtained from USGS (http://glovis.usgs.gov/), and MODIS scenes from the NASA-Reverb website (http://reverb.echo.nasa.gov/reverb/). Glacier outlines in the north of Greenland were downloaded from the Ohio State University – Byrd Polar Research Center webpage (http://bprc.osu.edu/GDG/icemask.php). We gratefully acknowledge Paul Leclercq for his help with the digitizing of some regions in SW Greenland, Ian Howat for providing the GIMP DEM, Michael Phillip Stainsby for proof reading the paper, and H. Jiskoot and G. Cogley for the thorough reviews.

Edited by: C. O'Cofaigh

References

Ahlstrøm, A. P., Gravesen, P., Bech Andersen, S., van As, D., Citterio, M., Fausto, R. S., Nielsen, S., Jepsen, H. F., Kristensen, S. S., Christensen, E. L. Stenseng, L., Forsberg, R., Hanson, S., and Petersen, D.: A new programme for monitoring the mass loss of the Greenland ice sheet, Geological Survey of Denmark and Greenland Bulletin, 15, 61–64, 2008.

Arendt, A., Bolch, T., J.G. Cogley, J.G, Gardner, A., Hagen, J.-O., Hock, R., Kaser, G., Pfeffer, W.T., Moholdt, G., Paul, F., Radić, V., Andreassen, L., Bajracharya, S., Beedle, M., Berthier, E., Bhambri, R., Bliss, A., Brown, I., Burgess, E., Burgess, D., Cawkwell, F., Chinn, T., Copland, L., Davies, B., De Angelis, H., Dolgova, E., Filbert, K., Forester, R., Fountain, A., Frey, H., Giffen, B., Glasser, N., Gurney, S., Hagg, W., Hall, D., Haritashya, U.K., Hartmann, G., Helm, C., Herreid, S., Howat, I., Kapustin, G., Khromova, T., Kienholz, C., Koenig, M., Kohler, J., Kriegel, D., Kutuzov, S., Lavrentiev, I., LeBris, R., Lund, J., Manley, W., Mayer, C., Miles, E., Li, X., Menounos, B., Mercer, A., Moelg, N., Mool, P., Nosenko, G., Negrete, A., Nuth, C., Pettersson, R., Racoviteanu, A., Ranzi, R., Rastner, P., Rau, F., Raup, B.H., Rich, J., Rott, H., Schneider, C., Seliverstov, Y., Sharp, M., Sigurðsson, O., Stokes, C., Wheate, R., Winsvold, S., Wolken, G., Wyatt, F., and Zheltyhina, N.: Randolph Glacier Inventory [v2.0]: A Dataset of Global Glacier Outlines. Global Land Ice Measurements from Space, Boulder Colorado, USA, Digital Media, 2012.

Bales, R. C., Guo, Q., Shen, D., McConnell, J. R., Du, G., Burkhart, J. F., Spikes, V. B., Hanna, E., and Cappelen, J.: Annual accumulation for Greenland updated using ice core data developed during 2000–2006 and analysis of daily coastal meteorological data, J. Geophys. Res, 114, D06116, doi:10.1029/2008JD011208, 2009.

Bishop, M. P., Olsenholler, J. A., Shroder, J. F., Barry, R. G., Raup, B. H., Bush, A. B. G., Copland, L., Dwyer, J. L., Fountain, A. G., Haeberli, W., Kääb, A., Paul, F., Hall, D. K., Kargel, J. S., Molnia, B. F., Trabant, D. C., and Wessels, R.: Global Land Ice Measurements from Space (GLIMS): remote sensing and GIS investigations of the Earth's cryosphere, Geocarto International, 19, 57–84, 2004.

Bolch, T.: Climate change and glacier retreat in northern Tien Shan (Kazakhstan/Kyrgyzstan) using remote sensing data, Global Planet. Change, 56, 1–12, 2007.

Bolch, T., Menounos, B., and Wheate, R.: Landsat-based inventory of glaciers in western Canada, 1985–2005, Remote Sens. Environ., 114, 127–137, 2010.

Box, J. E., Bromwich, D. H., Veenhuis, B. A., Bai, L. S., Stroeve, J. C., Rogers, J. C., Steffen, K., Haran, T., and Wang, S. H.: Greenland Ice Sheet Surface Mass Balance Variability (1988–2004) from Calibrated Polar MM5 Output, J. Climate, 19, 2783–2800, 2006.

Braithwaite, R. J. and Raper, S. C. B.: Estimating equilibrium-line altitude (ELA) from glacier inventory data, Ann. Glaciol., 50, 127–132, 2009.

Bull, C. and Studies, O. S. U. I. of P.: Glaciological reconnaissance of the Sukkertoppen ice cap, south-west Greenland, Ohio State University, Institute of Polar Studies, 813–816, 1963.

Burgess, E. W., Forster, R. R., Box, J. E., Mosley-Thompson, E., Bromwich, D. H., Bales, R. C., and Smith, L. C.: A spatially calibrated model of annual accumulation rate on the Greenland Ice Sheet (1958–2007), J. Geophys. Res, 115, F02004, doi:10.1029/2009JF001293, 2010.

Cappelen, J., Laursen, E. V., Jørgensen, P. V., and Kern-Hansen, C.: DMI monthly Climate Data Collection 1768–2006, Denmark, The Faroe Islands and Greenland, Technical Report 07-06, 2007.

Citterio, M. and Ahlstrøm, A. P.: Brief communication "The aerophotogrammetric map of Greenland ice masses", The Cryosphere Discuss., 6, 3891–3902, doi:10.5194/tcd-6-3891-2012, 2012.

Citterio, M., Paul, F., Ahlstrom, A. P., Jepsen, H. F., and Weidick, A.: Remote sensing of glacier change in West Greenland: accounting for the occurrence of surge-type glaciers, Ann. Glaciol., 50, 70–80, 2009.

Cogley, G.: The Future of the World's Glaciers. In: The Future of the World's Climate, edited by: Henderson-Sellers, A. and McGuffie, K., Elsevier, Amsterdam, 197–222, 2012. 2012.

Danko, D. M.: The digital chart of the world project, Photogrammetric Engineering and Remote Sensing, 58, 1125–1128, 1992.

Dowdeswell, J. and Hambrey, M.: Islands of the Arctic. Cambridge: Cambridge University Press, 280 pp., 2002.

Ettema, J., Van Den Broeke, M. R., Van Meijgaard, E., Van De Berg, W. J., Bamber, J. L., Box, J. E., and Bales, R. C.: Higher surface mass balance of the Greenland ice sheet revealed by high-resolution climate modeling, Geophys. Res. Lett., 36, L12501, doi:10.1029/2009GL038110, 2009.

Evans, I. S. and Cox, N. J.: Global variations of local asymmetry in glacier altitude: separation of northsouth and eastwest components, J. Glaciol., 51, 469–482, 2005.

Ferranti, J.: Greenland first edition DEM, available at: http://www.viewfinderpanoramas.org/dem3.html #greenland, 2012.

Fettweis, X., Hanna, E., Gallée, H., Huybrechts, P., and Erpicum, M.: Estimation of the Greenland ice sheet surface mass balance for the 20th and 21st centuries, The Cryosphere, 2, 117–129, doi:10.5194/tc-2-117-2008, 2008.

Hammer, C. U.: The Hans Tausen Ice Cap, Meddelelser om Grønland, Geoscience, 39, Copenhagen, Danish Polar Center, 2001.

Helsen, M. M., van de Wal, R. S. W., van den Broeke, M. R., van de Berg, W. J., and Oerlemans, J.: Coupling of climate models and ice sheet models by surface mass balance gradients: application to the Greenland Ice Sheet, The Cryosphere, 6, 255–272, doi:10.5194/tc-6-255-2012, 2012.

Hock, R., de Woul, M., Radic, V., and Dyurgerov, M.: Mountain glaciers and ice caps around Antarctica make a large sea-level rise contribution, Geophys. Res. Lett., 36, L07501, doi:10.1029/2008GL037020, 2009.

Howat, I. and Negrete, A.: A high-resolution ice mask for the Greenland Ice Sheet and peripheral glaciers and icecaps, available at: http://bprc.osu.edu/GDG/icemask.php (last access: December 2012), in preparation, 2012.

Howat, I., Negrete, A., Scambos, T., and Haran, T.: A high-resolution elevation model for the Greenland Ice Sheet from combined stereoscopic and photoclinometric data, available at: http://bprc.osu.edu/GDG/gimpdem.php (last access: December 2012), in preparation, 2012.

Huss, M. and Farinotti, D.: Distributed ice thickness and volume of all glaciers around the globe, J. Geophys. Res., 117, F04010, doi:10.1029/2012JF002523, 2012.

Jiskoot, H., Murray, T., and Luckman, A.: Surge potential and drainage-basin characteristics in East Greenland, Ann. Glaciol.,

36, 142–148, 2003.

Jiskoot, H., Juhlin, D., St. Pierre, H., and Citterio, M.: Tidewater glacier fluctuations in central East Greenland coastal and fjord regions (1980s–2005), Ann. Glaciol., 53, 35–44, doi:10.3189/2012AoG60A030, 2012.

Kargel, J. S., Ahlstrøm, A. P., Alley, R. B., Bamber, J. L., Benham, T. J., Box, J. E., Chen, C., Christoffersen, P., Citterio, M., Cogley, J. G., Jiskoot, H., Leonard, G. J., Morin, P., Scambos, T., Sheldon, T., and Willis, I.: Brief communication Greenland's shrinking ice cover: "fast times" but not that fast, The Cryosphere, 6, 533–537, doi:10.5194/tc-6-533-2012, 2012

Le Bris, R., Paul, F., Frey, H., and Bolch, T.: A new satellite-derived glacier inventory for western Alaska, Ann. Glaciol., 52, 135–143, 2011.

Lemke, P.: Climate change 2007: the physical science basis: contribution of Working Group I to the Fourth Assessment Report of the Intergovernmental Panel on Climate Change, Cambridge Univ. Pr., 2007.

Meier, M. F., Dyurgerov, M. B., Rick, U. K., O'Neel, S., Pfeffer, W. T., Anderson, R. S., Anderson, S. P., and Glazovsky, A. F.: Glaciers Dominate Eustatic Sea-Level Rise in the 21st Century, Science, 317, 1064–1067, doi:10.1126/science.1143906, 2007.

Ohmura, A.: Completing the world glacier inventory, Ann. Glaciol., 50, 144–148, 2009.

Ohmura, A. and Reeh, N.: New precipitation and accumulation maps for Greenland, J. Glaciol., 37, 140–148, 1991.

Paul, F.: Melting glaciers and ice caps, Nature Geosci., 4, 71–72, 2011.

Paul, F. and Andreassen, L. M.: A new glacier inventory for the Svartisen region, Norway, from Landsat ETM+ data: challenges and change assessment, J. Glaciol., 55, 607–618, 2009.

Paul, F. and Kaab, A.: Perspectives on the production of a glacier inventory from multispectral satellite data in Arctic Canada: Cumberland Peninsula, Baffin Island, Ann. Glaciol., 42, 59–66, 2005.

Paul, F., Kaab, A., Maisch, M., Kellenberger, T. and Haeberli, W.: The new remote-sensing-derived Swiss glacier inventory: I. Methods, Ann. Glaciol., 34, 355–361, 2002.

Paul, F., Barry, R. G., Cogley, J. G., Frey, H., Haeberli, W., Ohmura, A., Ommanney, C. S. L., Raup, B., Rivera, A., and Zemp, M.: Recommendations for the compilation of glacier inventory data from digital sources, Ann. Glaciol., 50, 119–126, 2009.

Paul, F., Andreassen, L. M., and Winsvold, S. H.: A new glacier inventory for the Jostedalsbreen region, Norway, from Landsat TM scenes of 2006 and changes since 1966, Ann. Glaciol., 52, 153–162, 2011.

Paul, F., Barrand, N., Berthier, E., Bolch, T., Casey, K., Frey, H., Joshi, S. P., Konovalov, V., Le Bris, R., Mölg, N., Nosenko, G., Nuth, C., Pope, A., Racoviteanu, A., Rastner, P., Raup, B., Scharrer, K., Steffen, S., and Winsvold, S.: On the accuracy of glacier outlines derived from remote sensing data, Ann. Glaciol., 54, in press, 2012.

Racoviteanu, A. E., Paul, F., Raup, B., Khalsa, S. J., and Armstrong, R.: Challenges and recommendations in mapping of glacier parameters from space: results of the 2008 Global Land Ice Measurements from Space (GLIMS) workshop, Boulder, Colorado, USA, Ann. Glaciol., 50, 53–69, 2009.

Radić, V. and Hock, R.: Regional and global volumes of glaciers derived from statistical upscaling of glacier inventory data, J. Geophys. Res, 115, F01010, doi:10.1029/2009JF001373, 2010.

Raper, S. C. and Braithwaite, R. J.: Low sea level rise projections from mountain glaciers and icecaps under global warming, Nature, 439, 311–313, 2006.

Raup, B., Kääb, A., Kargel, J. S., Bishop, M. P., Hamilton, G., Lee, E., Paul, F., Rau, F., Soltesz, D., Khalsa, S. J. Beedle, M., and Helm, C.: Remote sensing and GIS technology in the Global Land Ice Measurements from Space (GLIMS) project, Comput. Geosci., 33, 104–125, 2007.

Rignot, E. and Mouginot, J.: Ice flow in Greenland for the International Polar Year 2008–2009, Geophys. Res. Lett., 39, L11501, doi:10.1029/2012GL051634, 2012.

Steffen, K. and Box, J. E.: Surface climatology of the Greenland ice sheet: Greenland Climate Network 1995–1999, J. Geophys. Res., 106, 951–964, 2001.

Weidick, A.: Surging glaciers in Greenland – a status, Rapp. Grønl. Geol. Unders., 140, 106–110, 1988.

Weidick, A. and Morris, E.: Local glaciers surrounding the continental ice sheets, in: Into the Second Century of World Glacier Monitoring- Prospects and Strategies. A contribution to the IHP and the GEMS, edited by: Haeberli, W, Hoelzle, M., and Suter, S., Prepared by the World Glacier Monitoring Service UNESCO (Chapter 12), 197–207, 1998.

Weidick, A., Boeggild, C. E., and Knudsen, N. T.: Glacier inventory and atlas of West Greenland, Rapp. Grønl. Geol. Unders., 158, 194 pp., 1992.

Weidick, A.: Greenland, in: Satellite image atlas of glaciers of the world, edited by: Williams Jr., R. S. and Ferrigno, J. G., US Geological Survey Professional Paper 1386-C, 141 pp., 1995.

Yde, J. C. and Knudsen, N. T.: Observations of debris-rich naled associated with a major glacier surge event, Disko Island, West Greenland, Permafrost and Periglacial Processes, 16, 319–325, doi:10.1002/ppp.533, 2005.

Supplementary Material

of

“The first complete inventory of the local glaciers

and ice caps on Greenland”

Authors: P. Rastner, T. Bolch, N. Mölg, H. Machguth, R. Le Bris, and F. Paul

Table S1. Overview of the Landsat scenes used in this study. The numbers in the column "Label" refer to Fig. S1.

Label	Path	Row	Date	SLC_off	Label	Path	Row	Date	SLC_off
0	228	009	2000-08-19	0	36	231	014	1999-09-07	0
1	035	003	1999-07-24	0	37	005	016	2000-08-25	0
2	033	001	2000-06-26	0	38	021	001	2004-01-01	1
3	031	005	2000-06-28	0	39	012	002	2005-07-23	1
4	029	006	2002-08-23	0	40	012	010	2002-08-16	0
5	018	008	2001-08-07	0	41	229	011	2001-07-12	0
6	023	006	2001-08-26	0	42	003	017	2000-08-27	0
7	039	001	1999-07-20	0	43	019	001	2004-01-01	1
8	039	002	1999-07-20	0	44	010	002	2003-07-20	1
9	019	007	2001-08-30	0	45	010	011	2001-08-15	0
10	035	004	1999-07-24	0	46	227	011	2000-08-28	0
11	026	006	2000-07-27	0	47	001	005	2004-07-01	1
12	013	001	2001-07-03	0	48	008	003	2008-07-01	1
13	230	007	2001-08-20	0	49	008	012	2001-08-01	0
14	230	008	2001-08-20	0	50	024	001	2004-01-01	1
15	230	009	2001-08-20	0	51	225	011	2002-09-05	0
16	230	010	2001-09-21	0	52	015	001	2003-07-01	1
17	004	005	2003-07-26	1	53	015	009	2002-08-21	0
18	020	001	2004-01-01	1	54	232	006	2004-01-01	1
19	228	012	1999-08-11	0	55	006	015	2009-07-31	1
20	002	017	2001-08-23	0	56	022	001	2004-01-01	1
21	226	012	2001-08-08	0	57	231	011	2000-09-09	0
22	016	001	2003-07-01	1	58	232	008	2001-08-18	0
23	233	014	2002-07-27	0	59	224	010	2002-09-14	0
24	233	015	2002-07-27	0	60	228	010	2000-08-19	0
25	233	016	2001-09-10	0	61	009	013	1994-07-12	0
26	233	017	2002-08-12	0	62	008	013	2001-08-01	0
27	233	018	2002-08-12	0	63	008	014	2000-08-14	0
28	007	003	2003-07-01	1	64	045	001	2000-06-30	0
29	007	004	2003-07-31	1	65	027	001	2006-06-02	1
30	007	013	2000-08-23	0	66	228	010	2001-08-06	0
31	007	014	2000-08-23	0	67	012	011	2001-08-29	0
32	023	001	2004-01-01	1	68	035	001	2000-06-24	0
33	231	006	2005-09-07	1	69	035	005	2010-07-06	1
34	231	012	2002-08-14	0	70	227	011	2000-08-28	0
35	231	013	2000-09-09	0	71	040	001	2002-07-03	0
					72	226	010	2003-08-14	1

Table S2. Number and area of marine terminating glaciers per sector for all connectivity levels.

	Number	Area [km^2]
South-west	60	3162 ± 98
South-east	236	8979 ± 278
East	379	$31\,922 \pm 990$
West	18	344 ± 11
North-west	67	3316 ± 103
North	135	$16\,877 \pm 523$
North-east	9	372 ± 12
Total	904	$64\,972 \pm 2014$

Table S3. Absolute numbers for all connectivity levels per sector, the whole of Greenland and the marine terminating glaciers. The ± 3.1 % uncertainty is not shown.

	North Greenland		North-east		East	
	Number	Area [km^2] $\overline{a}$: 21.1 km^2	Number	Area [km^2] $\overline{a}$: 3.0 km^2	Number	Area [km^2] $\overline{a}$: 7.2 km^2
0.05–0.1	117	8	21	1	960	69
0.1–0.5	392	90	567	126	3060	721
0.5–1.0	122	88	144	101	1041	742
1.0–5.0	409	1062	192	442	1832	4263
5.0–10.0	186	1314	50	361	449	3112
10.0–50.0	299	7046	72	1495	507	10 654
50.0–100.0	76	5385	8	568	83	5688
100.0–500.0	56	10 725	1	143	46	8907
> 500	4	9334	0	0	15	24 293
	1661	35 052	1055	3237	7993	58 449
	South-east		South-west		West	
	Number	Area [km^2] $\overline{a}$: 4.0 km^2	Number	Area [km^2] $\overline{a}$: 2.7 km^2	Number	Area [km^2] $\overline{a}$: 2.2 km^2
0.05–0.1	596	42	933	66	483	34
0.1–0.5	1115	258	1356	308	917	222
0.5–1.0	344	243	324	230	351	252
1.0–5.0	590	1286	458	1044	549	1268
5.0–10.0	120	871	88	614	158	1101
10.0–50.0	121	2532	72	1595	128	2478
50.0–100.0	31	2090	15	1088	7	455
100.0–500.0	18	3133	12	2944	1	135
> 500	2	1484	2	1173	0	0
	2937	11 939	3260	9062	2594	5945
	North-west		Marine Terminating		Entire Greenland	
	Number	Area [km^2] $\overline{a}$: 8.3 km^2	Number	Area [km^2] $\overline{a}$: 71.8 km^2	Number	Area [km^2] $\overline{a}$: 6.4 km^2
0.05–0.1	233	16	2	0,2	3343	236
0.1–0.5	270	57	70	19	7677	1782
0.5–1.0	54	37	56	41	2380	1693
1.0–5.0	86	211	192	491	4116	9576
5.0–10.0	38	274	122	873	1089	7647
10.0–50.0	52	1101	287	6741	1251	26 901
50.0–100.0	11	794	80	5676	231	16 068
100.0–500.0	15	3356	74	16 044	149	29 343
> 500	1	515	21	35 086	24	36 799
	760	6361	904	64 971.2	20 260	130 045

Table S4. Absolute area (in km^2) covered by local GIC per aspect sector for all subregions and the whole of Greenland (CL0, CL1). The ±3.1 % uncertainty is not shown.

Sector	South-east	South-west	East	West	North-west	North	North-east	Entire Greenland
N	1196	1234	3209	774	699	4409	312	11 833
NE	906	1393	3132	710	744	3800	340	11 025
E	642	740	3285	679	613	3679	218	9856
SE	567	804	4257	759	797	3206	531	10 921
S	604	1648	3094	678	894	2700	495	10 113
SW	672	1256	3110	805	161	3134	378	9516
W	890	682	2808	662	266	11 241	385	16 934
NW	1428	937	2749	627	162	2815	322	9040
Total/sector	6905	8694	25 644	5694	4336	34 984	2981	89 238

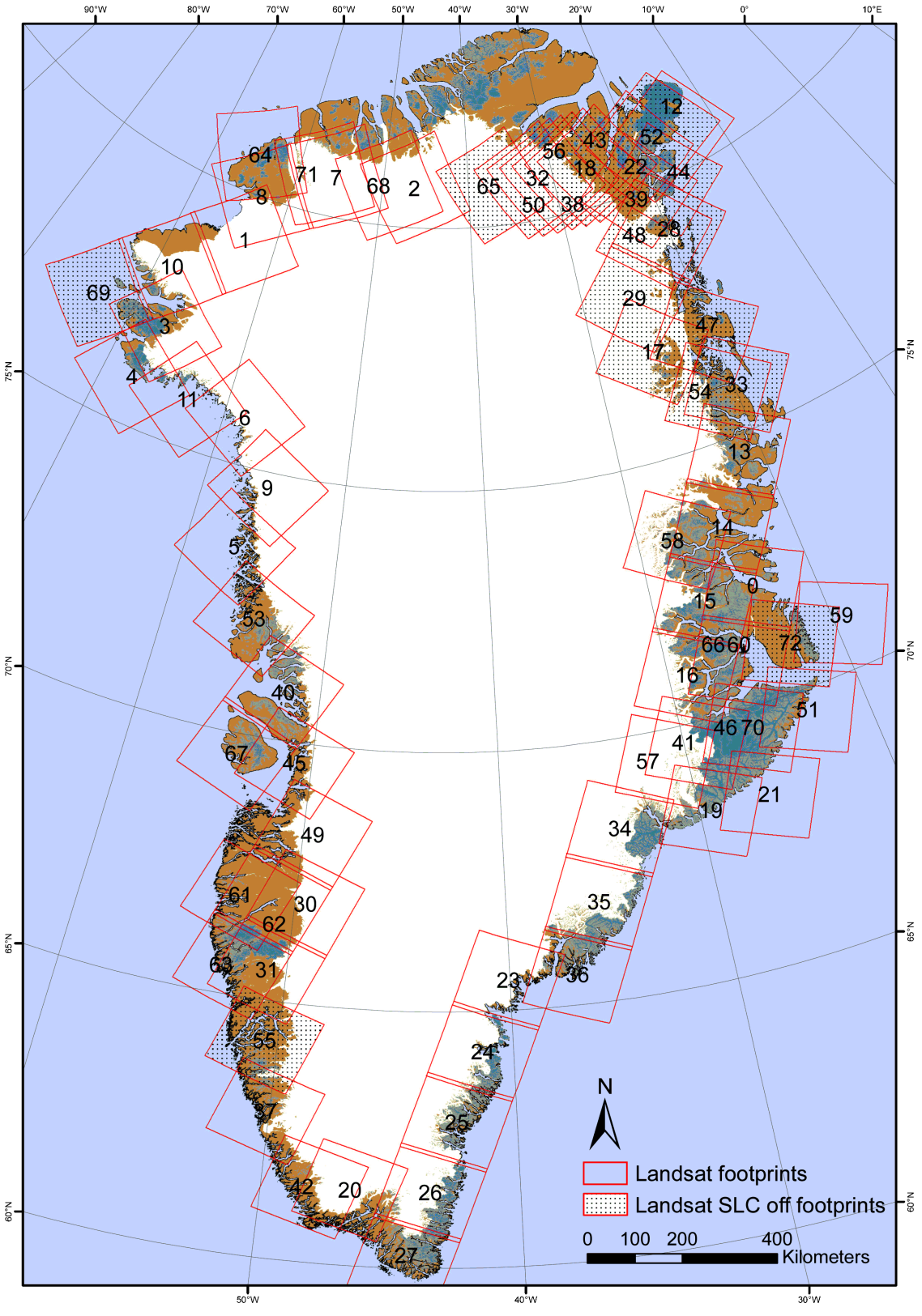

Fig. S1. Scene location (footprint) overview map (see Table S1 for path, row and acquisition date).

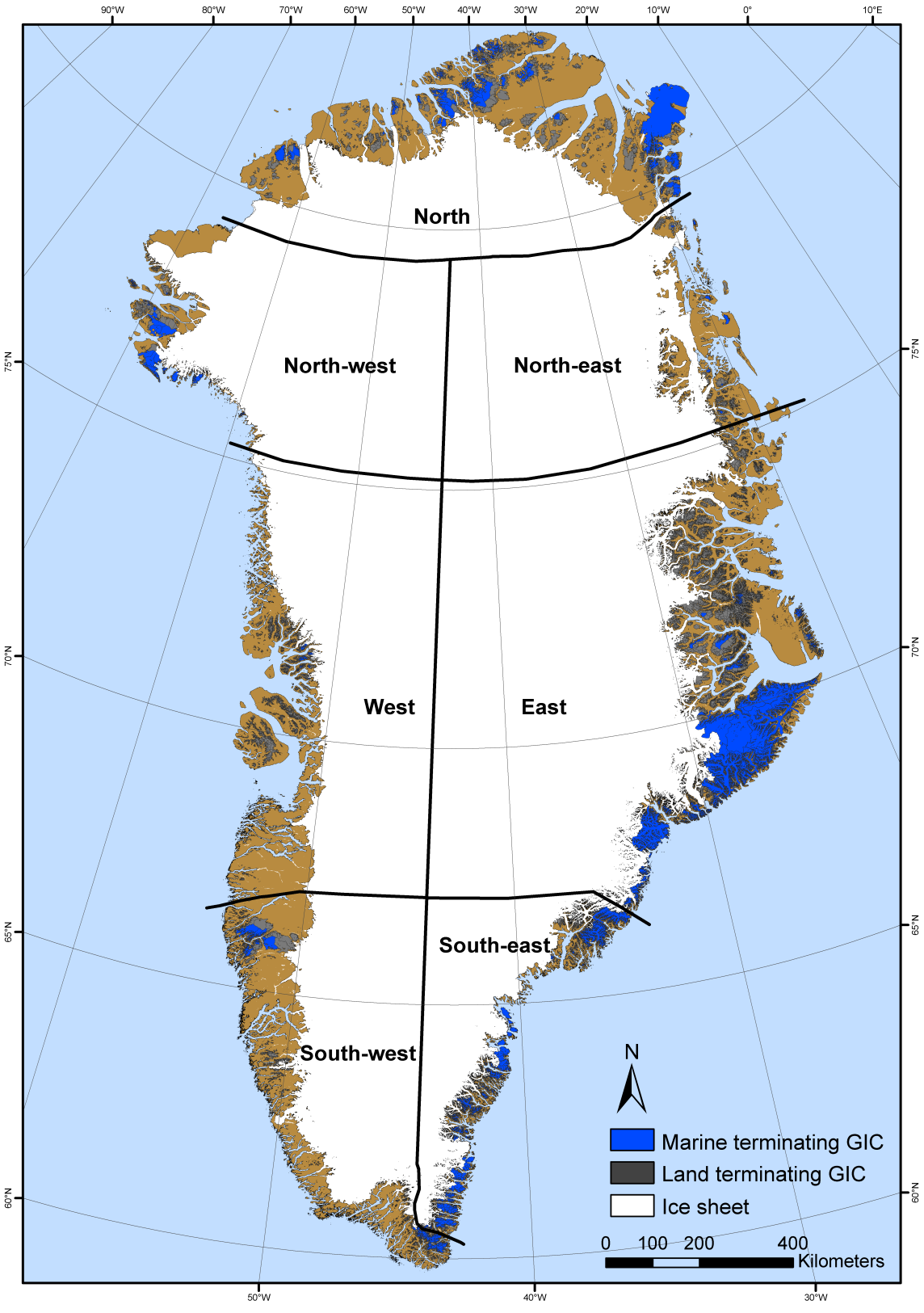

Fig. S2. Location map of all marine (blue) and land (grey) terminating glaciers in Greenland.

Paper II

Rastner, P., Bolch, T., Notarnicola, C., and Paul, F. (2014). A comparison of pixel- and object-based glacier classification with optical satellite images. IEEE Journal of Selected Topics in Applied Earth Observations and Remote Sensing 7, 853–862.

A Comparison of Pixel- and Object-Based Glacier Classification With Optical Satellite Images

Philipp Rastner, Tobias Bolch, Claudia Notarnicola, *Member, IEEE*, and Frank Paul

***Abstract*—Precise information about the size and spatial distribution of glaciers is needed for many research applications, for example water resources evaluation, determination of glacier specific changes in area and volume, and for calculation of the past and future contribution of glaciers to sea-level change. However, mapping glacier outlines is challenging even under optimal conditions due to time consuming manual corrections of wrongly classified pixels. In the last decades, advantages in computer technologies have led to the development of object-based-image analysis (OBIA), an image classification technique that can be seen as an alternative to the common pixel-based image analysis (PBIA). In this study we compare the performance of OBIA with PBIA for glacier mapping in three test regions with challenging mapping conditions. In both approaches, a ratio image was created to map clean snow and ice while thermal and slope information was used to assist in the identification of debris-covered ice. The mapping results of OBIA have overall a ∼3% higher quality than PBIA, in particular in the processing of debris-covered glaciers where OBIA has a 12% higher accuracy. The post-processing possibilities in OBIA (e.g., the application of a processing loop and neighborhood analysis) are especially powerful to improve the final classification. This leads also to a reduction of the workload for the manual corrections, which are still required to achieve a sufficient accuracy.**

***Index Terms*—ASTER, debris-cover, digital elevation model, glacier, Landsat, object-oriented-mapping, pixel-based-mapping, sea-ice.**

I. Introduction

INFORMATION about the spatial extent of glaciers (i.e., a body of ice that originated from compressed snow and flows downwards due to stresses induced by its weight), is crucial for applications such as the modeling of their future evolution in response to climate change or their contribution to sea-level rise [1]. Mapping glaciers automatically from optical satellite images works very well for clean ice, but can be time consuming when it comes to the required manual correction of wrongly classified parts [2]–[6]. The latter includes omission errors (e.g., regions with debris cover that are not mapped but belong to a glacier) and commission errors (e.g., turbid lakes that are mapped but do not physically belong to a glacier). Further surface types are spectrally mapped correctly, but are semantically wrong or vice versa. For example, a turbid lake on a glacier is not mapped (spectrally correct) but actually belongs to the glacier, while other types of ice such as sea ice (frozen seawater) and icebergs (large pieces of ice originating from a calving glacier and freely floating in open water) are mapped (spectrally correct), but are semantically wrong (i.e., they do not belong to a glacier). Hence 'wrongly classified' has two dimensions, spectral and semantic or object-oriented. While pixel-based classification is restricted to the spectral dimension (and pixel-based analysis), object-oriented approaches add the semantic dimension to the classification. This allows including a 'lake surrounded by ice' in the glacier class and excluding a 'lake surrounded by other terrain'. For such distinctions the units mapped have to be treated as objects rather than pixel clusters.

Furthermore, the accurate manual delineation of debris-covered glaciers is demanding and related to a high workload. These glacier parts have to be included by definition and play an important role when interpreting glacier dynamics (e.g., [7]), or glacier mass and energy balance (e.g., [8]). Thick debris cover can impede melting (insulating) whereas a thin layer (<2 cm) of debris, dust or soot can increase melt rates due to the lower albedo of the material. Owing to the cooling effect of the underlying ice, thin supraglacial debris can be several degrees colder than debris without ice underneath (e.g., [9], [10]). However, with increasing thickness of the debris on the glacier surface the thermal differences become smaller (i.e., their temperature is higher and more similar to the surrounding terrain) and the temperature-based mapping more difficult [11], [12]. In consequence, several methods have been developed to map debris-covered parts automatically using supplementary information such as digital elevation models (DEMs) and brightness temperature derived from a thermal band. A study by Paul *et al.* (2004) [13] combined a ratio image using the near-infrared (NIR) and the short-wave infrared (SWIR) bands (for mapping of clean ice) with all cells from a DEM that had slopes $< 24°$, were free of vegetation (derived with a normalized difference vegetation index, NDVI) and were connected to clean glacier ice (using for the first time neighborhood analysis). The idea of using a low slope value for mapping of debris-covered glacier parts is related to debris only accumulating on the

Manuscript received December 19, 2012; revised April 05, 2013 and July 08, 2013; accepted July 19, 2013. Date of publication August 19, 2013; date of current version March 14, 2014. This work was supported by funding from the ice2sea program from the European Union 7th framework program, grant number 226375, Ice2sea contribution number 143. The work of P. Rastner, T. Bolch, and F. Paul was additionally funded by the ESA project Glaciers_cci (4000101778/10/I-AM).

P. Rastner and F. Paul are with the Department of Geography, University of Zurich, Zurich, Switzerland.

T. Bolch is with the Department of Geography, University of Zurich, Zurich, Switzerland. He is also with the Institute of Cartography, Technische Universität Dresden, Dresden, Germany.

C. Notarnicola is with EURAC Research, Institute of Applied Remote Sensing, Bolzano, Italy.

Color versions of one or more of the figures in this paper are available online at http://ieeexplore.ieee.org.

Digital Object Identifier 10.1109/JSTARS.2013.2274668

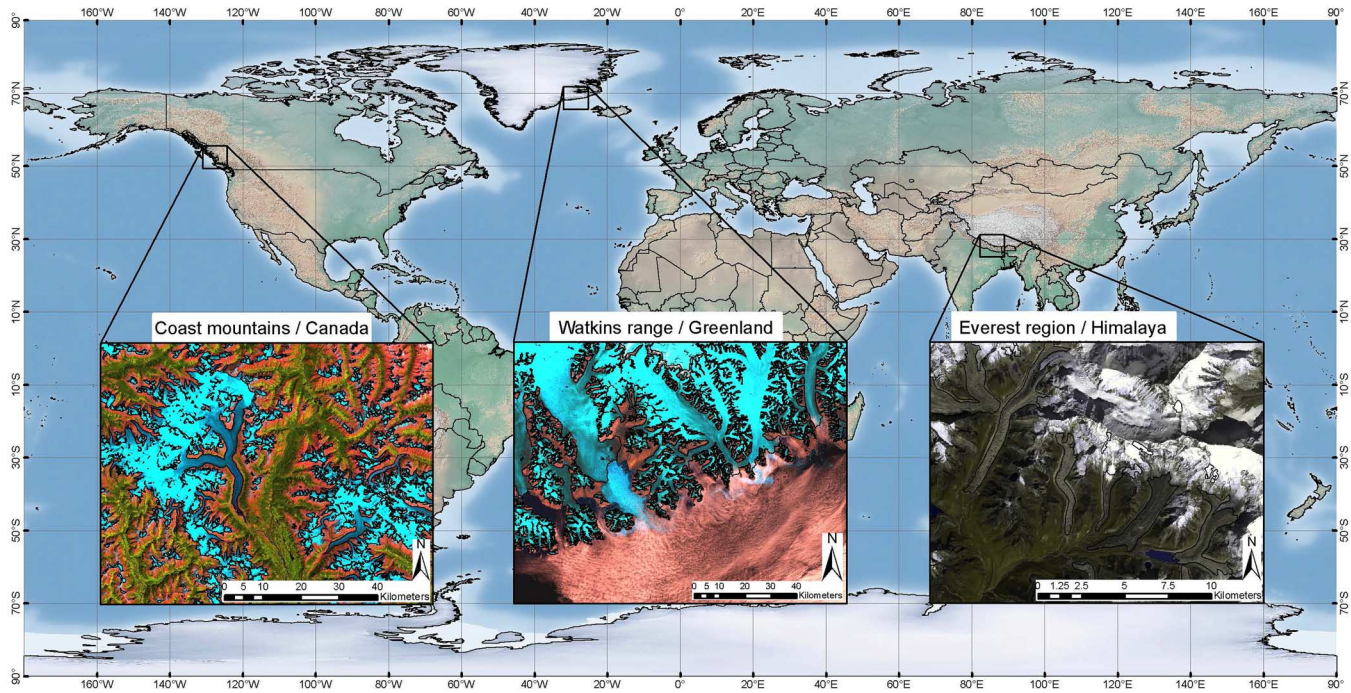

Fig. 1. Location map of the three test regions with close-ups.

surface when it is not too steep. Bolch *et al.* (2007) [14] and Bhambri *et al.* (2011) [15] showed the suitability of a combination of morphometric analysis and thermal information using the Terra ASTER sensor for mapping debris-covered glaciers in Khumbu and Garhwal Himalaya. Racoviteanu and Williams (2012) [16] also presented an approach to map debris on ice by: a) incorporating the slope and thermal information with a decision-tree algorithm combined with multispectral satellite images, and b) using image texture analysis. The accuracy of the results of both approaches differ only slightly and manual editing is still required to achieve results with an accuracy of the derived area better than 5% (as recommended by the Integrated Global Observing Strategy (IGOS) Cryosphere Theme report) [17].

Classification of multispectral images is historically carried out at pixel level. The pixel-based image analysis (PBIA) utilizes the spectral information stored for each pixel in the individual image bands and classifies each pixel based on the variability of reflectance values in each band [18]. Advances in computer technology led to the development of an image classification technique called object-based image analysis (OBIA) [19], [20]. This approach introduces, besides a classification based on spectral characteristics, also spatial contextual information such as shape, texture and relationships between the objects [21]. The classification using OBIA starts with a segmentation of the image [22]. The algorithm is a bottom-up method initiating with individual pixels and merging these pixels into groups (i.e., objects) based on three parameters: scale, shape and compactness [23]. The scale parameter influences the size of individual objects and the shape defines the textural homogeneity of the resulting image object. The criterion "compactness" optimizes the resulting objects in regard to the overall compactness within the shape criterion [24]. Moreover, the input datasets such as the different satellite bands can be weighted in the segmentation process. This allows influencing the creation of objects according to size, shape and number. After the segmentation the image can be classified according to well-established classification procedures such as the band ratio or the combination of slope and thermal information. The major advantage of OBIA compared to the PBIA is, however, the potential of the post-processing possibilities. For our purpose, OBIA can, e.g., be used to automatically remove icebergs, sea ice, and water bodies or include debris-covered glacier tongues or ice in cast shadows in the 'glacier' class. Moreover, OBIA can capture a lake as a whole [25], while PBIA often only maps parts of a lake (depending on the turbidity distribution) [26].

In this study we investigate the potential of the OBIA approach to map glaciers in the following three test regions with challenging mapping conditions such as debris cover, adjacent water bodies or ice in cast shadow: the Watkins Range in eastern Greenland, the Nepalese Mt. Everest region in the Himalaya and the Coast Mountains in western Canada. In these regions we had reliable reference data available to evaluate the mapping accuracy of both approaches in detail.

II. Study Regions and Data Sets

The first study region is located at the south-eastern coast of Greenland (67–69°N, 32–26°W) in the Watkins range close to Gunnbjørn Fjeld, Greenland's highest mountain (Fig. 1). It covers a glacierized area of about ∼9800 km^2 and elevations range from sea level to about 3700 m a.s.l.. Large valley glaciers as well as outlet glaciers from the ice sheet reaching the sea dominate the region. Numerous supraglacial lakes, icebergs and sea ice allow us to test the contextual mapping with OBIA. The second region is located south of Mt. Everest in the Nepalese Himalaya (27.6–28.3°N, 86.6–87.0°W). Glacier coverage is

TABLE I
OVERVIEW OF THE USED DATASETS IN THE THREE TEST REGIONS

	Watkins range/Greenland	Everest region (Himalaya)	Coast mountains/Canada
Imagery	Landsat ETM+ 30 m VIS 30 m SWIR 60 m TIR Date: 01/08/2001	ASTER 15 m VIS 30 m SWIR 90 m TIR Date: 20/12/2001	Landsat TM 30 m VIS 30 m SWIR 120 m TIR Date: 22/07/2004
DEMs	ASTER GDEM II	ASTER DEM	ASTER GDEM II

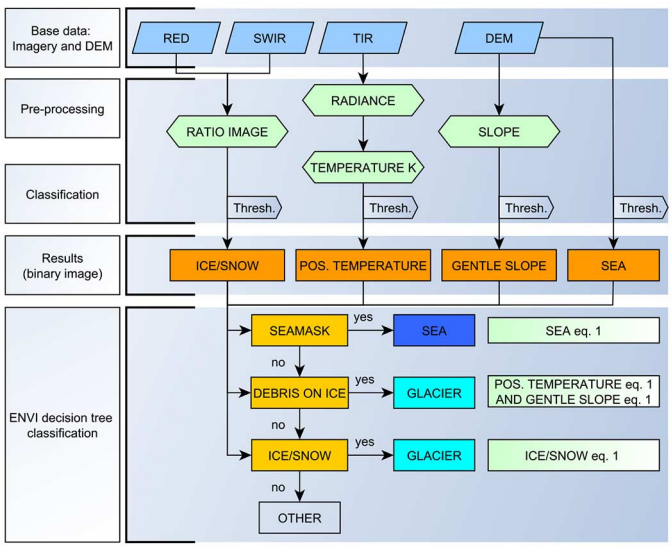

Fig. 2. Flowchart of the PBIA_1a and 1b approach. Thresholds are shown in Table III.

about 87 km^2 with about 40% being extensively debris covered [27] due to the common steep and high relief surrounding the glaciers [15], [28]. Consequently deep shadows and numerous supraglacial lakes with different spectral characteristics (e.g., due to a varying turbidity) are present in this region as well [25], [29]. Glaciers in this test region range in elevation from ~4750 m to ~8250 m a.s.l. The third region is located in the Canadian Coast Mountains (Ha-Iltzuk Icefields and Mount Waddington area (50.4–51.4°N, 124.5–126.2°W)) with an ice-covered area of 1555 km^2 and a minimum/maximum elevation of 130 m and 3950 m a.s.l., respectively [30]. This is a more alpine-type environment with elongated valley glaciers with long medial moraines and pro-glacial lakes and deep shadows covering parts of the glaciers.

For the spectral classification we used a Landsat ETM+ scene for the Watkins range in Greenland, a Landsat TM scene for the Canadian Coast Mountains, and an ASTER scene for the Everest region. Additionally, digital elevation models (DEMs) were used to provide topographic information. For test region one and three the ASTER GDEM II (http://asterweb.jpl.nasa.gov/gdem.asp) is applied, whereas for the Everest region we chose an existing ASTER DEM (cf. [27]). As reference data sets, we used the manually corrected vector outlines from the Greenland glacier inventory [31], the Canadian glacier inventory [3] and manually corrected outlines of an automatic classification for the Himalaya [27]. Before using the reference data sets as validation, they were further improved using hillshades (shaded reliefs derived from a DEM [32]) and multi-temporal satellite images (Table I). Hillshades were especially helpful for visually correcting the outlines of frozen lakes, which appear as flat and smooth areas or debris-covered glaciers which are characterized by a more 'noisy' surface. Multi-temporal satellite images from different seasons helped in the identification of frozen lakes or glacier ice in shadows as the images offer different illumination conditions. All data sets were co-registered with the UTM projection and WGS84 datum before processing.

III. METHODOLOGY

A. Pixel-Based Glacier Mapping

Clean ice and snow were mapped using a band ratio algorithm with the raw digital numbers (DN) of a visible (VIS) and shortwave infrared (SWIR) band [33] (see Fig. 2 for an overall flow chart). This method utilizes the strong differences in spectral reflectance of ice and snow in these bands (high in the VIS and very low in the SWIR) [33]. The thermal bands from Landsat TM and ETM+ were resampled (nearest neighbor) to 30 m and transformed into brightness temperatures (in Kelvin) following the description in the Landsat data user handbook (2006) [34]. This information is used to investigate a potential thermal separation of debris located on ice from other debris. In the Everest region we resampled the thermal band (TIR band 10) and the SWIR band 4 to 15 m and calculated the brightness temperature for the Everest test region according to Schmugge *et al.* (2002) [35]. The DEMs served in all test regions to extract surface slope and in Greenland also as a sea-mask.

The datasets described before were assigned to four classes: "snow/ice", "positive temperature", "gentle slope", and "sea". We defined a class "gentle slope" because the slope needs to be gentle to include the debris-covered parts of a glacier (debris mainly accumulates on flat parts), as well as a class "positive temperature" to consider the sunlit debris-covered parts of a glacier (that has usually temperatures above 273.15 K) [16]. All four classes served as an input to a decision tree classifier performing a multistage classification. Each condition divides pixels into one of two classes using a threshold value (Fig. 2) similar to the study of Racoviteanu and Williams (2012) but with less input bands [16]. Finally, classes were merged (e.g., "gentle slope" and "positive temperature" to "glacier"), a majority filter of 3×3 kernel size was applied and the class "glacier" was converted to vector format (shapefile).

B. The OBIA Approach

1) Segmentation and Classification: In the OBIA approach, the images have to be segmented into objects (step 1) before

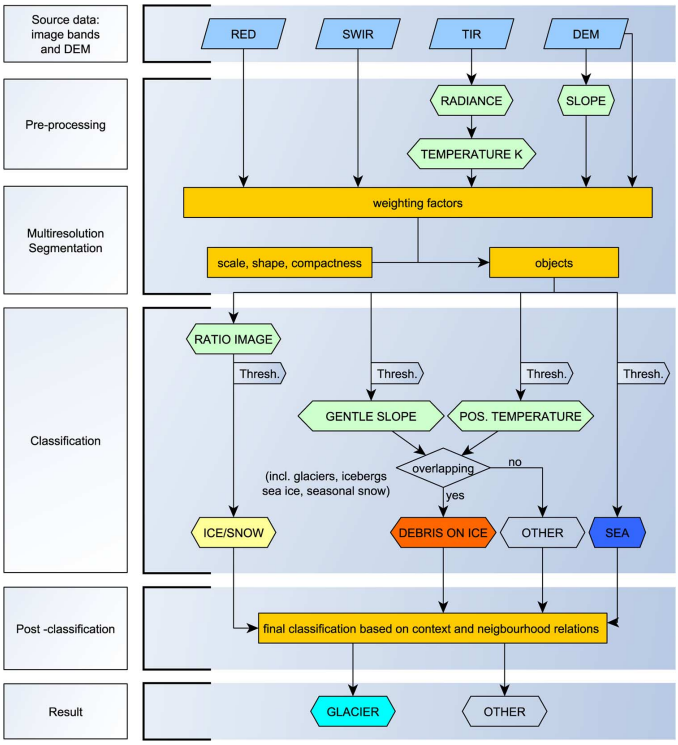

Fig. 3. Flowchart of the OBIA approach. Thresholds are shown in Table III.

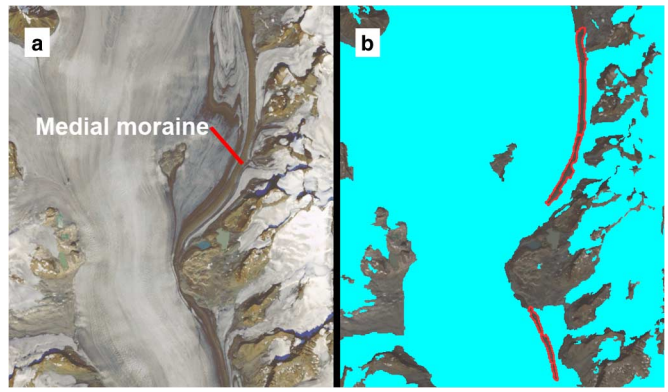

Fig. 4. Close-up of the result of OBIA segmentation-classification process. Medial moraines are clearly selectable as elongated objects that can be assigned afterwards to the class glacier.

the classification can start (step 2). In Fig. 3 these two principle steps are illustrated along with their corresponding criteria and the final post-classification. For this study we applied a multiresolution segmentation algorithm with different weighting of the four input datasets (red, SWIR, TIR, slope). We defined the scale, shape and compactness (see Table II for values) and run the segmentation to create the objects for the classification procedure. For the test region Greenland a scale factor of 10 was selected and for the other regions 20 is used as more debris cover is present in these regions.

In the classification step of the OBIA rule-set, objects representing the VIS/SWIR ratio (based on DN) were assigned to the class "snow and ice" when the mean value of each object exceeded the threshold of 2.0 [31]. The starting values for the thresholds of each condition are based on already published values for the selected input data sets, but they were adjusted to the current scene to improve the results. Thereafter objects were classified as "gentle slope" for slope values smaller than 14° and as "positive temperature" if 273 K was exceeded. After this step, the classified objects of "gentle slope" and "positive temperature" were combined if they overlapped, and assigned to the class "debris on ice". Finally, this class was assigned to the class "glacier".

2) Post-Processing in OBIA: The application of a ratio image for the mapping of clean ice and snow is fairly robust (e.g., [5]). It maps all ice and snow-covered surfaces not considering whether the snow is located on a glacier (and thus belonging to the class "glacier") or outside. On the other hand, medial moraines, debris-covered glacier parts or supraglacial lakes are not mapped with this method, but have to be included in the class "glacier" as well.

For this kind of distinction, the post-processing capabilities of OBIA can be applied. It is possible to reconsider omission and commission errors of the class assignment based on their context and include them in the correct class. For post-processing of the classification results we created a loop in the rule-set that increased or decreased the thresholds for the related input dataset. With this procedure it was possible to select still unclassified objects, such as gaps in the glacier map due to debris cover (including medial moraines) and assign them to the class "glacier". To include the remaining unclassified objects, we used more specific OBIA tools which assigned objects to the class "glacier", for example by using neighborhood rules. Such a rule might relate the ratio of the shared border length of an object with a neighboring object assigned to a defined class, to the total border length [24]. This allowed for instance to select objects representing icebergs and exclude them from the class "glacier", as icebergs are usually surrounded by objects with the class "sea". Another possibility to assign correct membership to the class "glacier" is to additionally select objects according to their shape. In particular, medial moraines are often represented as elongated objects after the initial segmentation of the image (Fig. 4). This specific shape can be used to distinguish them from other objects and assign them correctly to the class "glacier".

In the following we summarize step by step the developed rule-set for glacier mapping with OBIA (based on eCognition). The entire workflow has four major parts (pre-processing, segmentation, classification, and post-processing) with each part subdivided in distinct processing steps (see Fig. 3). The thresholds values given below vary for the individual test regions.

— Preprocessing

- import and format conversion of image bands and DEM calculation of band ratio (red/SWIR)
- calculation of radiance and temperature from the thermal band (TIR)
- calculation of slope from the DEM
- creation of contrast enhanced (false-color) composite images for visual analyses of results

TABLE II
PRODUCED LEVELS, SCALE FACTOR, INPUT BANDS, WEIGHT, SHAPE AND COMPACTNESS USED FOR THE OBIA PROCESSING IN EACH OF THE THREE TEST REGIONS

Region	Levels	Scale factor	Input Bands/Files	Weight	Shape	Compactness
Watkins range/Greenland	3	10	red/swir/tir/slope	1/1/2/3	0.1	0.5
Everest region (Himalaya)	3	20	red/swir/tir/slope	1/1/2/3	0.1	0.5
Coast mountains/Canada	3	20	red/swir/tir/slope	1/1/2/3	0.1	0.5

— Segmentation:
- selection of scale factor (10 if few regions are debris covered; 20 if extensive debris cover is present)
- shape and compactness: fixed to 0.1 and 0.5; respectively
- assignment of input data weights: 1 for VIS, 2 or 3 for thermal infrared or slope information
- creation of objects by running the segmentation

— Classification:
- application of threshold values (TV) to create intermediate classifications (binary data) from all input datasets resulting in the classes "ice and snow" $(\mathrm{TV} > 2)$, "gentle slopes" $(\mathrm{TV} < 12°)$, "positive temperature" $(\mathrm{TV} > 273\ \mathrm{K})$, and "sea" $(\mathrm{TV} < 10\ \mathrm{m})$
- iterative adjustment of threshold values to obtain optimal results (based on visual analysis)
- combination of intermediate classes to new classes (e.g., "debris cover" on ice for regions where "gentle slope" overlaps with "positive temperature")

— Post-processing:
- neighborhood relationships: relative length of a border to another class (e.g., to exclude icebergs) and shape related analysis (elongated features) to identify medial moraines
- merging of all relevant classes to the class "glacier"
- Export of the result as a vector layer

C. Implementation and Accuracy Assessment

We defined two comparison levels (CL) to compare the OBIA with the PBIA approach (Fig. 5). To investigate whether OBIA performed better already without its post-processing capabilities, we compared the raw processing of OBIA (OBIA_1) to the PBIA results (CL_1). In addition, PBIA was tested and compared to OBIA twice, once by using the same thresholds as in the OBIA approach (PBIA_1a) and once by selecting the best thresholds for PBIA (PBIA_1b). At the second level (CL_2), the classification results of OBIA were post-processed (OBIA_2) for all three test regions and compared to the PBIA results (without further post-processing steps). Classification accuracy was defined as the minimum standardized accepted value of 85% which indicates the overall success of correctly classified pixels to the total of all considered pixels [36]. In addition, we also investigated the wrongly classified pixels as they are responsible for most of the workload of the post-processing.

IV. RESULTS

Overall, OBIA performed better in all test regions. Despite slightly longer processing time of several minutes for OBIA due to its initial segmentation process, the approach showed much less isolated pixels than PBIA (Figs. 6, 7, and 8). For the test region Greenland OBIA included more of the dark ice and glacier ice in shadow than PBIA, i.e., the workload to remove misclassification was much reduced. Sea-ice artifacts are visible in both approaches but were successfully removed in the post-processing of OBIA in stage CL_2 (Fig. 6). At CL_1 (raw processing) OBIA achieved a slightly higher overall accuracy (98.5%) than PBIA (95.5%) (Table III). The application of post-processing tools in CL_2 for the OBIA interestingly only provided a minor improvement in the classification accuracy (98.6%). However, a stronger improvement resulted for commission errors: from 4.1% wrongly classified pixels at CL_1 to 3.6% at CL_2, whereas PBIA had 6.9% (Table III). Adjusting the thresholds in PBIA_1b increased the overall accuracy to 98.3% without a change in the commission errors (Fig. 6).

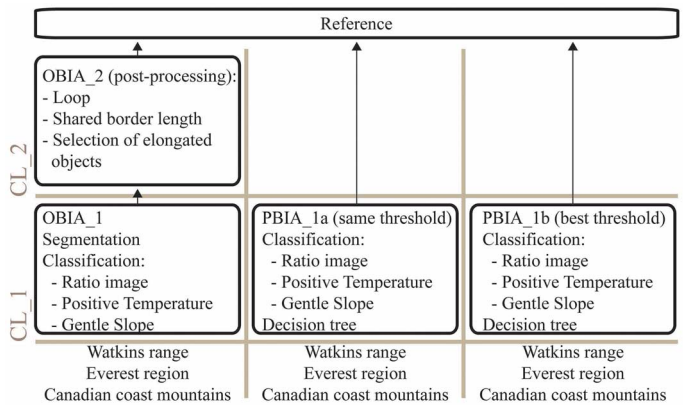

Fig. 5. Schematic overview of the four processing methods applied for the three test regions.

In the Mt. Everest test region, the OBIA_2 approach showed good results for the mapping of debris-covered glacier tongues with a classification accuracy of 88.5%. The limits of PBIA become clearly visible here with a high amount of isolated pixels. The usage of the same thresholds for OBIA and PBIA_1a provided poor results while the selection of individual thresholds for PBIA_1b gave better results (Table IV). Nevertheless, the workload for manual corrections remained high for PBIA. While PBIA_1a only reached an overall accuracy of 55.5%, PBIA_1b reached 76.6% (Fig. 7, Table III). Hence, PBIA did not reach the 85% accuracy minimum. The better performance of OBIA resulted from the high weighting of the slope at the initial segmentation and the enhanced post-processing capabilities of OBIA.

In the Canadian Coast Mountains, the overall accuracies of the PBIA_1a and the PBIA_1b approaches were about two percent higher (96.2% and 96.6%, respectively) than the accuracy

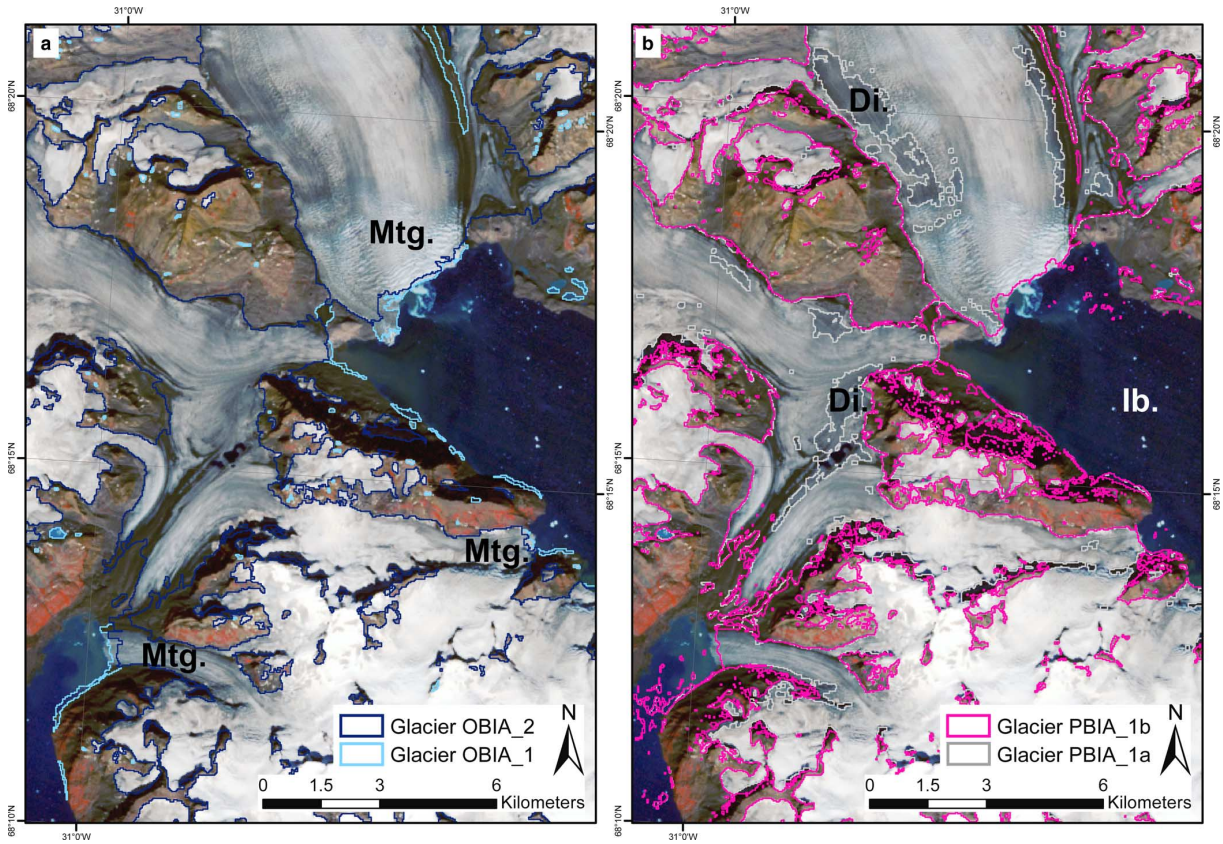

Fig. 6. Comparison of (a) the OBIA_1 and OBIA_2 and (b) the PBIA_1a and PBIA_1b method for the Watkins range/Greenland. Icebergs (Ib.) are visible in the sea due to marine terminating glaciers (Mtg.). Dark ice (Di.) patches also poses a problem if the same thresholds as OBIA are used (PBIA_1a).

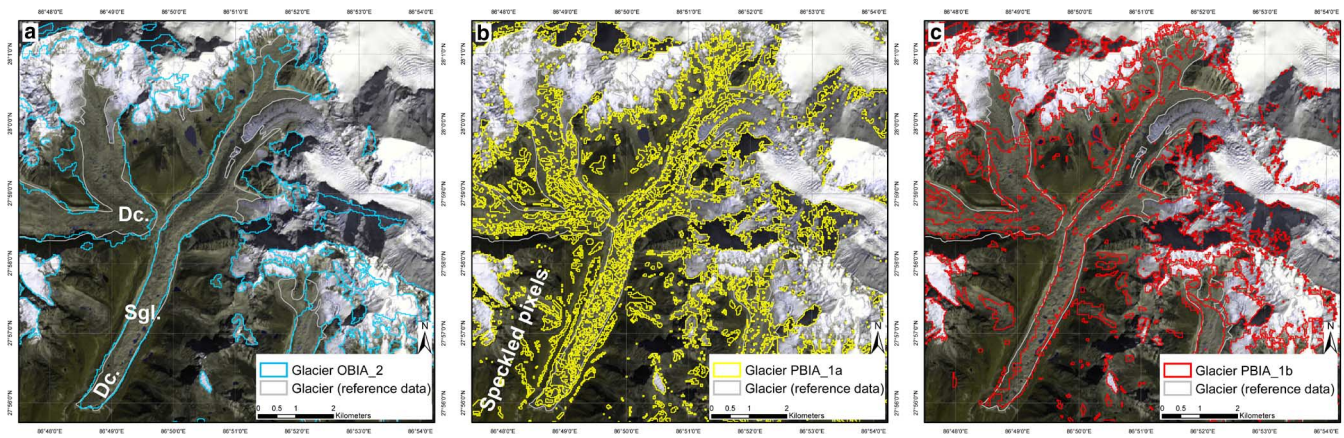

Fig. 7. Comparison of all three processing methods for mapping of heavily debris covered tongues in the Everest region (Himalaya). Debris cover (Dc.) and supraglacial lakes (Sgl.) impede effective glacier mapping massively however in a) a promising result could be achieved.

of the OBIA_2 approach (94.5%). This can probably be attributed to large areas of clean ice which can easily be mapped with the band ratio TM3/TM5. However, PBIA again had more commission and omission errors. The OBIA_2 approach had only 3.8%, while PBIA_1b had 5.9% and PBIA_1a had 8.6%, which is about twice as much as with OBIA_2 (Fig. 8, Table III). Scattered wrongly classified pixels are especially visible in the PBIA approaches in south-exposed slopes due to a high threshold of the brightness temperature. These settings did not allow mapping the thick medial moraines on the glaciers, as they had higher surface temperatures than the threshold, while in the OBIA approach it was possible to integrate them with the shape parameter.

We also investigated the impact of the empirically selected thresholds for the band ratio, the slope and the thermal bands on classification accuracy (Table IV). While the thresholds for the band ratio and slope are similar in both approaches, the thresholds for temperature are more widely spread. The thresholds range from 273 K to 287 K with OBIA and 268 K–282 K with PBIA. The PBIA approach is more sensitive at the lower temperature range (268 K–273 K) whereas OBIA is relatively stable ~273 K.

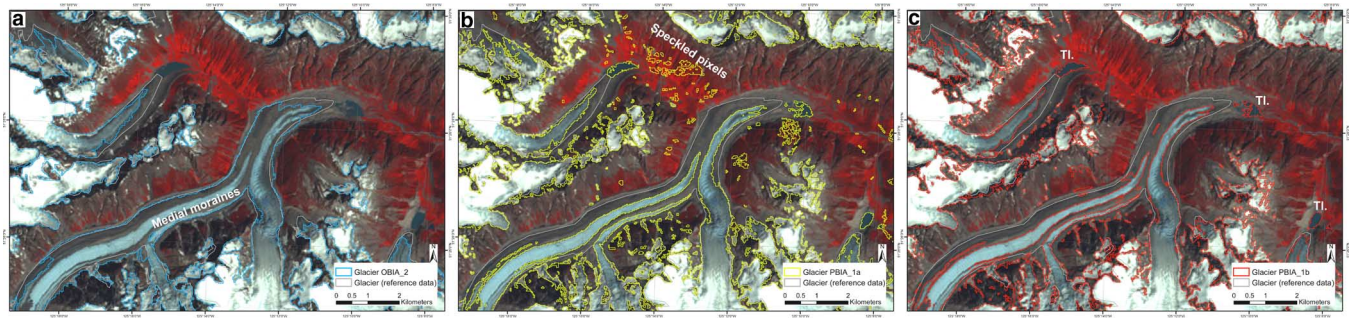

Fig. 8. Comparison of all three processing methods for the mapping of glaciers with some debris cover in Coast mountains/Canada. Medial moraines are (a) successfully included in the glacier mask whereas in the PBIA approaches (b) and c) they are only to a certain degree. Turbid lakes (Tl.) in the glacier forefields are always included in the glacier mask in (b) and (c).

TABLE III
MAPPING RESULTS OF THE FOUR DIFFERENT APPROACHES FOR THE THREE TEST REGIONS IN PERCENT

	Classification accuracy in % (correctly classified)				Classification accuracy in % (wrongly classified)			
Region	OBIA_1	OBIA_2	PBIA_1a	PBIA_1b	OBIA_1	OBIA_2	PBIA_1a	PBIA_1b
Watkins range/Greenland	98.5	98.6	95.5	98.3	4.1	3.6	6.9	6.9
Everest region (Himalaya)	-	88.5	55.5	76.6	-	-	-	-
Coast mountains /Canada	-	94.5	96.2	96.6	-	3.8	8.6	5.9

V. DISCUSSION

Our investigation revealed that OBIA achieved in two of three cases a higher overall accuracy than PBIA for glacier mapping under the selected challenging conditions. Similar results were found in previous studies for other landform classifications [37]–[40]. The particular strengths of OBIA are the handling of image information in the object space and the post-processing capabilities that consider neighborhood relationships and thus context-based information (Table V). The raw mapping in CL_1 (ratio image with slope and thermal information) revealed similar results for both approaches (OBIA and PBIA) (Table III). However, the mapping errors (commission) were always larger with the PBIA approach (∼3%). The post-processing in CL_2 with OBIA showed minor improvements regarding omission errors (0.1%), but was capable of automatically removing many of the commission errors, hence reducing the workload for manual correction. All ratio algorithms or the NDSI fail to identify debris cover on ice from spectral properties [6]. We found that high weighting of the slope and the thermal band at the initial segmentation process along with the post-processing possibilities of OBIA, helped in mapping also debris-covered glacier parts. The crucial point is the slope difference of the rather flat glacier surface compared to the often steep lateral moraines as well as the glacier forefield (cf. Bolch and Kamp 2006) [37]. Weighting the slope at the initial segmentation calculates image objects which follow this break in surface topography. This was also emphasized by other morphometric glacier mapping studies [13], [14], [16], [38], [39], who found that slope information was a key factor for the delineation of debris-covered glaciers. Interestingly, Bolch *et al.* 2007 [9] and Racovitenau and Williams (2012) found a lower slope threshold of only 12° being best suited for mapping debris-covered glaciers in the Himalaya [16] while 24° was suggested for the Swiss Alps [13]. Hence, the best slope threshold should be selected for each region separately. Combining slope with the thermal band improves classification to some degree, in particular when the supraglacial debris is thin enough to be cooled by the ice underneath [11], [40], [41]. However, it might also be possible that some clean ice pixels with their much lower temperature might be included, thus reducing the overall brightness temperature considerably. If a thick debris layer is present at the glacier surface, the cooling effect of the ice is impaired which hinders to differentiate it from the rest of the terrain around the glacier. Including such thick debris parts of the glacier based on the TIR layer is therefore much more challenging [13], [14]. Taken together, thermal and slope information in combination with the object-based approach has indeed increased mapping accuracy (e.g., by about 12% for the debris-covered glaciers in Khumbu Himalaya). In comparison to Bolch *et al.* (2007) [14], the OBIA classification is in particular better in regions with thick debris cover or stagnant ice close to the terminus. Moreover, the automatically generated outlines follow the outlines of the manual digitalization from the reference dataset quite closely. To obtain the best mapping results also the spatial resolution of the satellite imagery must be appropriate, the acquisition date of the DEM and satellite data should be close, and accurate geolocation of all input datasets is mandatory.

Some further issues need to be mentioned from the data processing point of view. Before image classification with OBIA started, the image has to be segmented into objects (Table II). This is critical, as the final classification is heavily dependent on this step. A careful selection of the segmentation parameters scale, shape and compactness is therefore mandatory. In our case a scale factor of 20 was applied for regions such as the Himalaya with extensive debris cover to include larger debris-covered glacier parts. The most typical errors resulting from the segmentation step are under- and over-segmentation [42]. The former results in an object that covers more than one class and thus introduce classification errors. This is a particular problem OBIA has when small details (at the extent of a few

TABLE IV
APPLIED THRESHOLDS OF THE FOUR DIFFERENT INPUT IMAGES FOR THE THREE TEST REGIONS. ECOGNITION MEMBERSHIP FUNCTIONS ARE SIGNED WITH AN ASTERISK*

	Thresholds OBIA				Best thresholds PBIA			
Region	Ratio (red/swir) (DN)	Temperature (K)	Slope (°)	DEM (m)	Ratio (red/swir) (DN)	Temperature (K)	Slope (°)	DEM (m)
Watkins range/Greenland	>2	273.5 - 283	0-12	0-10	2-255	270-280	0-12	0-10
Everest region (Himalaya)	*>20/24	273 – 284	*<9/10	-	60-500	273 – 282	0-12	-
Coast mountains /Canada	*>2.35/2.5	273 - 287	0-14	-	2-255	268 - 279.5	0-14	-

TABLE V
OVERVIEW OF THE ADVANTAGES AND DISADVANTAGES OF THE PBIA AND THE OBIA APPROACH

	Advantages	Disadvantages
PBIA	- lower sensitivity to selected threshold - low computational time - capture of details - large area mapping of several Landsat scenes in one step possible after mosaicing	- high amount of speckled pixels - limited post-processing possibilities - final result strongly related on additional input bands (DEM) - limited transferability - expert knowledge required
OBIA	- higher accuracy than PBIA due to initial high weighting of auxiliary data such as slope and brightness temperature - easy adjustable and applicable rule set - classification, post-processing & exporting in one rule set - many post-processing possibilities (Loop, neighborhood relationships, shape depended classification procedures) - high transferability - less dependent on additional input data like DEM due to post-processing possibilities	- strong dependency of mapping accuracy on initial segmentation procedure - expensive software - Software knowledge required - high computational costs and virtual memory allocation - process dependency on segment quantity -> scene subsetting necessary - Classical GIS or remote sensing software necessary for data pre-processing

pixels) have to be classified. For example, snow free mountain ridges in the Greenland test region were mapped as ice due to an initial under-segmentation and a high mean value of the objects in the ratio image. On the other hand, considering too small objects at the initial stage of segmentation reduces the possibility to map medial moraines or extended debris-covered glacier tongues with a selection on the shape. Such larger objects can only be considered using a high scale parameter with a high weighting of slope and the thermal band. In this case a higher scale parameter of 20 with a shape of 0.1 and a compactness of 0.5, as used in the Canadian and Everest region, provided the best results. Although the overall accuracy was better for OBIA, PBIA outperforms OBIA when detecting objects with single pixel size such as narrow ridges, nunataks (rock outcrops not covered with ice or snow within an ice field) and couloirs (narrow ditches on steep mountain slopes) in steep mountain terrain. Another advantage of PBIA is important when large amounts of data should be processed. In this case OBIA performs worse due to the long processing time of the initial image segmentation. Furthermore, OBIA commercial software packages are costly, whereas PBIA glacier mapping using ratio images can also be applied with freely available software. Moreover the pre-processing cannot be conducted with OBIA software. In CL_1 we compared the threshold selection for the different processing steps. We can clearly state, that using the same threshold for the input images with OBIA and PBIA was not successful (Table IV). This resulted in a large amount of commission errors in PBIA (Fig. 7(b), 8(b)) which would have to be corrected by manual editing. This is probably due to the different methodological approaches of OBIA and PBIA where the use of a mean threshold value refers to an object while in PBIA the threshold refers to individual pixels. Therefore, separate thresholds have to be chosen for each method.

Poor transferability is generally stated for many pixel-based remote sensing classifications, such as maximum likelihood or ISODATA clustering [6], with the exception of the robust results of ratio images (including the NDSI) [5], [43]. The robustness for OBIA is generally higher in this regard, since criteria such as object shape and neighbor-based classification rules, or the use of fuzzy rules is less dependent on absolute values of the image, or slope and temperature information [19], [44]. In this regard, we think that the OBIA "master rule set" for glacier mapping presented in this study is transferable and adjustable to other regions, because it combines the strengths of both PBIA and OBIA [45], [46]. In addition, Landsat and ASTER imagery and DEMs are freely available worldwide. Considering the specific mapping conditions in a region, the usage of OBIA for glacier mapping in spectrally and context-based challenging environments presents clear advantages.

VI. CONCLUSIONS

We investigated the differences of object (OBIA) and pixel-based (PBIA) approaches for glacier mapping in three test re-

gions with challenging conditions using optical satellite images and DEM data. In both approaches a band ratio for mapping clean snow and ice, as well as the combination of slope and brightness temperature was used to map debris on ice. Thresholds were chosen based on results from the literature and adjusted to scene conditions. In a second step, the possibilities of the specific object and context-based post-processing capabilities of OBIA were investigated qualitatively and quantitatively. While the accuracy of OBIA was slightly better than for PBIA at comparison level 1 (CL_1), a 12% higher accuracy in comparison level 2 (CL_2) for mapping debris on ice could be achieved with OBIA. The limitations of PBIA are mainly due to individual pixels, which can be seen as commission errors requiring manual corrections. On the other hand, OBIA misses tiny objects (ice couloirs or nunataks) but maps the larger ones much better (e.g., elongated medial moraines). The context-based mapping with OBIA allows removing objects that are not glaciers but correctly classified spectrally (e.g., icebergs), thus considerably reducing the workload for manual corrections. Overall, the application of OBIA can be recommended for glacier classification in regions where spectrally ambivalent mapping conditions are dominant.

ACKNOWLEDGMENT

Landsat ETM+ scenes were downloaded from http://glovis.usgs.gov/ website and the ASTER image was obtained from NASA within the framework of the Global Land Ice Monitoring from Space (GLIMS: http://www.glims.org/) initiative. The ASTER global digital elevation models (DEM) (GDEM II) were downloaded from the NASA web interface Reverb (http://reverb.echo.nasa.gov/reverb). The authors gratefully acknowledge R. Wheate for proofreading the paper, and M. Zebisch for providing the software E-cognition.

REFERENCES

[1] G. Kaser, J. G. Cogley, M. B. Dyurgerov, M. F. Meier, and A. Ohmura, "Mass balance of glaciers and ice caps: Consensus estimates for 1961–2004," *Geophys. Res. Lett.*, vol. 33, no. 19, p. L19501, 2006.

[2] L. Andreassen, F. Paul, A. Kääb, and J. Hausberg, "Landsat-derived glacier inventory for Jotunheimen, Norway, and deduced glacier changes since the 1930s," *The Cryosphere*, vol. 2, no. 2, pp. 131–145, 2008.

[3] T. Bolch, B. Menounos, and R. Wheate, "Landsat-based inventory of glaciers in western Canada, 1985–2005," *Remote Sens. Environ.*, vol. 114, no. 1, pp. 127–137, 2010.

[4] R. Le Bris, F. Paul, H. Frey, and T. Bolch, "A new satellite-derived glacier inventory for western Alaska," *Annals of Glaciology*, vol. 52, no. 59, pp. 135–143, 2011.

[5] F. Paul and A. Kaab, "Perspectives on the production of a glacier inventory from multispectral satellite data in Arctic Canada: Cumberland Peninsula, Baffin Island," *Annals of Glaciology*, vol. 42, no. 1, pp. 59–66, 2005.

[6] A. E. Racoviteanu, F. Paul, B. Raup, S. J. Khalsa, and R. Armstrong, "Challenges and recommendations in mapping of glacier parameters from space: Results of the 2008 Global Land Ice Measurements from Space (GLIMS) workshop, Boulder, Colorado, USA," *Annals of Glaciology*, vol. 50, no. 53, pp. 53–69, 2009.

[7] D. Scherler, B. Bookhagen, and M. R. Strecker, "Spatially variable response of Himalayan glaciers to climate change affected by debris cover," *Nature Geoscience*, vol. 4, no. 3, pp. 156–159, Jan. 2011.

[8] Y. Zhang, K. Fujita, S. Liu, Q. Liu, and T. Nuimura, "Distribution of debris thickness and its effect on ice melt at Hailuogou glacier, southeastern Tibetan Plateau, using in situ surveys and ASTER imagery," *J. Glaciology*, vol. 57, no. 206, pp. 1147–1157, 2011.

[9] C. Mihalcea, B. W. Brock, G. Diolaiuti, C. D'Agata, M. Citterio, M. P. Kirkbride, M. E. J. Cutler, and C. Smiraglia, "Using ASTER satellite and ground-based surface temperature measurements to derive supraglacial debris cover and thickness patterns on Miage Glacier (Mont Blanc Massif, Italy)," *Cold Regions Science and Technology*, vol. 52, no. 3, pp. 341–354, 2008.

[10] L. A. Foster, B. W. Brock, M. E. J. Cutler, and F. Diotri, "A physically based method for estimating supraglacial debris thickness from thermal band remote-sensing data," *J. Glaciology*, vol. 58, no. 210, pp. 677–691, 2012.

[11] M. Nakawo, T. Morohoshi, and S. Uehara, "Satellite data utilization for estimating ablation of debris covered glaciers," in *Proc. 1992 Kathmandu Symp.*, Kathmandu, Nepal, 1992, vol. 218, pp. 75–83.

[12] A. Shukla, M. K. Arora, and R. P. Gupta, "Synergistic approach for mapping debris-covered glaciers using optical-thermal remote sensing data with inputs from geomorphometric parameters," *Remote Sens. Environ.*, vol. 114, no. 7, pp. 1378–1387, Jul. 2010.

[13] F. Paul, C. Huggel, and A. Kääb, "Combining satellite multispectral image data and a digital elevation model for mapping debris-covered glaciers," *Remote Sens. Environ.*, vol. 89, no. 4, pp. 510–518, Feb. 2004.

[14] T. Bolch, M. F. Buchroithner, A. Kunert, and U. Kamp, "Automated delineation of debris-covered glaciers based on ASTER data," in *Proc. 27th EARSel Symp., Geoinformation in Europe*, Bozen, Italy, 2007, pp. 403–410.

[15] R. Bhambri, T. Bolch, and R. K. Chaujar, "Mapping of debris-covered glaciers in the Garhwal Himalayas using ASTER DEMs and thermal data," *Int. J. Remote Sens.*, vol. 32, no. 23, pp. 8095–8119, Sep. 2011.

[16] A. Racoviteanu and M. W. Williams, "Decision tree and texture analysis for mapping debris-covered glaciers in the Kangchenjunga Area, Eastern Himalaya," *Remote Sens.*, vol. 4, no. 10, pp. 3078–3109, Oct. 2012.

[17] J. Key, M. Drinkwater, and J. Ukita, "Cryosphere Theme report—For the monitoring of our environment from space and from earth," in *IGOS*, 2007.

[18] T. M. Lillesand, *Remote Sensing and Image Interpretation*. New York, NY, USA: Wiley, 2006.

[19] T. Blaschke and J. Strobl, "What's wrong with pixels? Some recent developments interfacing remote sensing and GIS," *Geo-Informations-Systems (GIS)*, vol. 6, pp. 12–17, 2001.

[20] S. Narumalani, Y. Zhou, and D. E. Jelinski, "Utilizing geometric attributes of spatial information to improve digital image classification," *Remote Sens. Rev.*, vol. 16, no. 4, pp. 233–253, Mai 1998.

[21] T. Blaschke, "Object based image analysis for remote sensing," *ISPRS J. Photogramm. Remote Sens.*, vol. 65, no. 1, pp. 2–16, 2010.

[22] M. Baatz and A. Schäpe, "Multiresolution segmentation—An optimization approach for high quality multi-scale image segmentation," in *Angewandte Geographische Informationsverarbeitung XII*. Heidelberg: Wichmann-Verlag, 2000, pp. 12–23.

[23] G. Willhauck, T. Schneider, R. De Kok, and U. Ammer, "Comparison of object oriented classification techniques and standard image analysis for the use of change detection between SPOT multispectral satellite images and aerial photos," in *Proc. XIX ISPRS Congress*, 2000, pp. 16–22.

[24] *"Definiens Imaging—eCognition User Guide 4,"* M. Baatz, U. C. Benz, S. Dehghani, M. Heynen, A. Höltje, P. Hofmann, I. Lingenfelder, M. Mimler, M. Solbach, M. Weber, and G. Willhauck, Eds., München, 2005.

[25] R. L. Wessels, J. S. Kargel, and H. H. Kieffer, "ASTER measurement of supraglacial lakes in the Mount Everest region of the Himalaya," *Annals of Glaciology*, vol. 34, no. 1, pp. 399–408, 2002.

[26] A. M. Johansson and I. A. Brown, "Adaptive classification of supraglacial lakes on the West Greenland Ice Sheet," *IEEE J. Sel. Topics Appl. Earth Observ. Remote Sens.*, pp. 1–10, 2013.

[27] T. Bolch, M. Buchroithner, T. Pieczonka, and A. Kunert, "Planimetric and volumetric glacier changes in the Khumbu Himal, Nepal, since 1962 using Corona, Landsat TM and ASTER data," *J. Glaciology*, vol. 54, no. 187, pp. 592–600, 2008.

[28] H. Frey, F. Paul, and T. Strozzi, "Compilation of a glacier inventory for the western Himalayas from satellite data: Methods, challenges, and results," *Remote Sens. Environ.*, vol. 124, pp. 832–843, Sep. 2012.

[29] T. Bolch, M. F. Buchroithner, J. Peters, M. Baessler, and S. Bajracharya, "Identification of glacier motion and potentially dangerous glacial lakes in the Mt. Everest region/Nepal using spaceborne imagery," *Natural Hazards and Earth System Sciences*, vol. 8, no. 6, pp. 1329–1340, 2008.

[30] J. A. VanLooy and R. R. Forster, "Glacial changes of five southwest British Columbia icefields, Canada, mid-1980s to 1999," *J. Glaciology*, vol. 54, no. 186, pp. 469–478, 2008.
[31] P. Rastner, T. Bolch, N. Mölg, H. Machguth, R. Le Bris, and F. Paul, "The first complete inventory of the local glaciers and ice caps on Greenland," *The Cryosphere*, vol. 6, pp. 1483–1495, 2012.
[32] ESRI, ArcGIS Desktop: Release 10. Redlands, CA: Environmental Systems Research Institute, 2013 [Online]. Available: http://web-help.esri.com/arcgisdesktop/9.2/index.cfm?TopicName=welcome, [Zugegriffen: 18-März-2013]
[33] J. Dozier, "Spectral signature of alpine snow cover from the Landsat thematic mapper," *Remote Sens. Environ.*, vol. 28, no. 0, pp. 9–22, Apr. 1989.
[34] *Landsat 7 Science Data Users Handbook*. Greenbelt, MD: Landsat Project Science Office, 2006, Landsat Project Science Office.
[35] T. Schmugge, A. French, J. C. Ritchie, A. Rango, and H. Pelgrum, "Temperature and emissivity separation from multispectral thermal infrared observations," *Remote Sens. Environ.*, vol. 79, no. 2, pp. 189–198, 2002.
[36] J. R. Anderson, US Government Printing Office, "A land use and land cover classification system for use with remote sensor data," , vol. 964, 1976.
[37] T. Bolch and U. Kamp, "Glacier mapping in high mountains using DEMs, Landsat and ASTER data," *Grazer Schriften der Geographie und Raumforschung*, vol. 41, pp. 37–48, 2006.
[38] U. Kamp, M. Byrne, and T. Bolch, "Glacier fluctuations between 1975 and 2008 in the Greater Himalaya Range of Zanskar, southern Ladakh," *J. Mountain Science*, vol. 8, pp. 374–389, 2011.
[39] A. Shukla, R. P. Gupta, and M. K. Arora, "Delineation of debris-covered glacier boundaries using optical and thermal remote sensing data," *Remote Sens. Lett.*, vol. 1, no. 1, pp. 11–17, März 2010.
[40] D. P. Dobhal, "DEAD ICE," *Encyclopedia of Snow, Ice and Glaciers*, vol. 16, no. 186, 2011.
[41] W. Tangborn and B. Rana, "Mass balance and runoff of the partially debris-covered Langtang Glacier, Nepal," *IAHS PUBLICATION*, pp. 99–108, 2000.
[42] D. Liu and F. Xia, "Assessing object-based classification: Advantages and limitations," *Remote Sens. Lett.*, vol. 1, no. 4, pp. 187–194, Dez. 2010.
[43] A. E. Racoviteanu, Y. Arnaud, M. W. Williams, and J. Ordonez, "Decadal changes in glacier parameters in the Cordillera Blanca, Peru, derived from remote sensing," *J. Glaciology*, vol. 54, no. 186, pp. 499–510, 2008.
[44] D. Flanders, M. Hall-Beyer, and J. Pereverzoff, "Preliminary evaluation of eCognition object-based software for cut block delineation and feature extraction," *Can. J. Remote Sens.*, vol. 29, no. 4, pp. 441–452, 2003.
[45] M. Möller, L. Lymburner, and M. Volk, "The comparison index: A tool for assessing the accuracy of image segmentation," *Int. J. Appl. Earth Observ. Geoinf.*, vol. 9, no. 3, pp. 311–321, Aug. 2007.
[46] D. Tiede, S. Lang, D. Hölblinga, and P. Füreder, "Transferability of Obia Rulesets for IDP Camp Analysis in Darfur," in *Proc. GEOBIA 2010 Conf., Geographic Object-Based Image Analysis*, Ghent, Belgium, 2010, vol. 29.

Philipp Rastner received his Diploma degree in geography from the University in Innsbruck, in 2006. From 2006 to 2010, he was working as a research assistant within the Institute of Applied Remote Sensing of the European Academy of Bozen/Bolzano (EURAC), Italy. His research concentrated in the mapping of soil and snow cover with high resolution optical satellite imagery. In 2010 he started his Ph.D. thesis at the Institute of Geography of the University of Zurich, Switzerland. During his Ph.D. he created the first inventory of the local glaciers and icecaps around Greenland. Currently he is analyzing their changing's of the last decades with reanalysis data.

Tobias Bolch obtained his Diploma degree in geography in 1999, his Ph.D. in 2006 from the University of Erlangen-Nuremberg, Germany, and the habilitation degree in physical geography at Dresden University of Technology, Dresden, Germany. He gained research and teaching experience in addition at Humboldt University zu Berlin, Germany, University of Bonn, Germany, and the University of Northern British Columbia, Canada. In 2009, he was substitute professor for GIS and remote sensing at University of Erlangen-Nuremberg. Since then, he is primarily working as senior scientist with the University of Zurich, Switzerland. His main research focus is the application of digital terrain models and remote sensing for glaciological applications. Additional research fields include creeping permafrost and glacial hazards. The regional focus includes the Canadian Cordilleran, the glaciers and ice caps on Greenland, and High Mountain Asia. Dr. Bolch is a member of the European Geosciences Union and the International Glaciological Society, among others.

Claudia Notarnicola (M'09) received the Physics Degree, summa cum laude, at the Physics Department of Università di Bari in 1995. From 1998 up to 2002 she was a Ph.D. student in the Remote Sensing Group of Physics Department, Bari, Italy, working on fusion techniques of radar and radiometric data for soil physical parameters extraction. From 2002 to 2004 she was with the Physics Department of Bari in the framework of a Nowcasting Project. In 2004 she worked with Politecnico di Bari in the framework of an Italian Government PON project for the application of data fusion techniques to degraded areas characterization. From 2005 to 2007 she worked at Compagnia Generale per lo Spazio (former Carlo Gavazzi Space) as project manager of projects funded by the Italian Space Agency (ASI). From 2008 she is with the EURAC-Institute of Applied Remote Sensing (Bolzano, Italy) working on biophysical parameters retrieval by using optical images and SAR images. Her research interests also include soil models, data fusion and inversion problems. She has been involved in numerous projects funded the ASI and ESA. Among them, she was the PI of **SNOX** "Snow cover and glacier monitoring in alpine areas by COSMO-SkyMed X-band data" funded by the Italian Space Agency and dedicated to the use of the X-band data for snow parameters monitoring and retrieval. From 2006 she is involved in the Cassini-Huygens Project, a NASA-ESA-ASI joint project, for the application of inversion procedure to the retrieval of Titan surface parameters.

Frank Paul received the master degree (diploma) in meteorology from the University of Hamburg in 1995 and a Ph.D. degree in physical geography from the University of Zurich in 2003, where he is currently working as a senior research scientist. He has worked in several national and international research projects related to glacier mapping and monitoring from space-borne optical sensors, distributed mass-balance modeling of glaciers, as well as geomorphometric analysis of DEMs and their application in glaciological studies. He is currently science leader of the ESA project Glaciers_cci and lead author in Working Group I of the Fifth Assessment Report of the Intergovernmental Panel on Climate Change (IPCC). He is a member of the European Geosciences Union, the International Glaciological Society and the Cryospheric Commission of the Swiss Academy of Sciences.

Paper III

Bolch, T., Sandberg Sørensen, L., Simonsen, S.B., Mölg, N., Machguth, H., Rastner, P., and Paul, F. (2013). Mass loss of Greenland's glaciers and ice caps 2003-2008 revealed from ICESat laser altimetry data. Geophysical Research Letters 40, 875–881.

Mass loss of Greenland's glaciers and ice caps 2003–2008 revealed from ICESat laser altimetry data

T. Bolch,[1,2] L. Sandberg Sørensen,[3] S. B. Simonsen,[4,5] N. Mölg,[1] H. Machguth,[1,6] P. Rastner,[1] and F. Paul[1]

Received 28 November 2012; revised 13 February 2013; accepted 18 February 2013.

[1] The recently finalized inventory of Greenland's glaciers and ice caps (GIC) allows for the first time to determine the mass changes of the GIC separately from the ice sheet using space-borne laser altimetry data. Corrections for firn compaction and density that are based on climatic conditions are applied for the conversion from volume to mass changes. The GIC which are clearly separable from the icesheet (i.e., have a distinct ice divide or no connection) lost 27.9 ± 10.7 Gt a^{-1} or 0.08 ± 0.03 mm a^{-1} sea-level equivalent (SLE) between October 2003 and March 2008. All GIC (including those with strong but hydrologically separable connections) lost 40.9 ± 16.5 Gt a^{-1} (0.12 ± 0.05 mm a^{-1} SLE). This is a significant fraction (~14 or 20%) of the reported overall mass loss of Greenland and up to 10% of the estimated contribution from the world's GIC to sea level rise. The loss was highest in southeastern and lowest in northern Greenland.
Citation: Bolch, T., L. Sandberg Sørensen, S. B. Simonsen, N. Mölg, H. Machguth, P. Rastner, and F. Paul (2013), Mass loss of Greenland's glaciers and ice caps 2003–2008 revealed from ICESat data, *Geophys. Res. Lett.*, *40*, doi:10.1002/grl.50270.

1. Introduction

[2] Glaciers and ice caps (GIC) are key indicators of climate change [e.g., *Lemke et al*., 2007], and their melt water could potentially make a substantial contribution to sea-level rise (SLR) during this century [*Meier et al*., 2007]. This is especially true for the GIC in Greenland which cover an area of about 89,000 km^2 when considering only ice bodies that are not or only weakly connected to the ice sheet [*Rastner et al*., 2012]. This area is up to twice as large as previously estimated (e.g., *Weidick and Morris*, 1998; *Radic and Hock*, 2010]) and comprises about 12% of the global GIC area as recorded in the Randolph Glacier Inventory [*Arendt et al*., 2012].

[3] A large number of studies have estimated the overall mass budget for Greenland (ice sheet including GIC to a varying degree) based on Gravity Recovery and Climate Experiment (GRACE) data (e.g., [*Velicogna*, 2009; *van den Broeke et al*., 2009]), altimetry data (e.g., [*Sørensen et al*., 2011; *Pritchard et al*., 2009]), or mass balance modeling [*Ettema et al*., 2009]. However, the contribution of the GIC alone has not been assessed so far despite their potentially high contribution to SLR. This was largely a consequence of a missing detailed glacier inventory that is needed to determine the GIC contribution precisely. The new inventory [*Rastner et al*., 2012] allowed us also to investigate the marine-terminating and land-terminating glaciers separately. The mass changes of the latter are a direct reaction to climate forcing while the interaction with the ocean alters the signal of the former.

[4] Existing mass balance studies on individual glaciers, such as Mittivakkat Glacier in southeast Greenland, suggest that glaciers are shrinking and losing mass [*Mernild et al*., 2011] like in most other parts of the world [*WGMS*, 2008] and that the majority of the non-surge-type glaciers continued to retreat during the last decades [*Bjørk et al*., 2012; *Citterio et al*., 2009; *Leclercq et al*. 2012] with larger retreats for the marine-terminating glaciers [*Jiskoot et al*., 2012]. However, altimetry data also revealed that Greenland's largest ice cap Flade Isblink (located in the north-east) had a mass budget close to zero [*Rinne et al*., 2011]. There is thus some spatial variability to be expected that can be determined from the Ice, Cloud, and land Elevation Satellite (ICESat) altimetry dataset. Here we report the elevation changes over the October 2003 to March 2008 period for the GIC on Greenland based on processed ICESat data [cf. *Sørensen et al*., 2011] and the new GIC inventory [*Rastner et al*., 2012]. Our focus is on the regional variability, a differentiation between marine and land-terminating glaciers, and an adequate consideration of firn compaction and density differences.

2. Data and Methods

2.1. Glacier Data

[5] The utilized glacier outlines were mainly derived semi-automatically from more than 70 Landsat Enhanced Thematic Mapper (ETM)+ scenes with a focus on the years 1999 to 2002 and the Greenland Ice Mapping Project (GIMP) digital elevation model (DEM) [*Rastner et al*., 2012]. The area north of the Landsat coverage (~80°N)

All Supporting Information may be found in the online version of this article.

[1]Department of Geography, University of Zurich, Winterthurer Str. 190, 8057, Zürich, Switzerland.
[2]Institute for Cartography, Technische Universität Dresden, 01069, Dresden, Germany.
[3]Geodynamics Department, DTU Space, Elektrovej, Building 328, 2800 Kgs. Lyngby, Denmark.
[4]Centre for Ice and Climate, NBI, University of Copenhagen, Juliane Maries Vej 30, 2100, Copenhagen, Denmark.
[5]Danish Climate Centre, DMI, Lyngbyvej 100, 2100, Copenhagen, Denmark.
[6]Geological Survey of Denmark and Greenland (GEUS), Voldgade 10, 1350, Copenhagen, Denmark.

T. Bolch, Department of Geography, University of Zurich, Winterthurer Str. 190, 8057 Zürich, Switzerland. (tobias.bolch@geo.uzh.ch)

0094-8276/13/10.1002/grl.50270

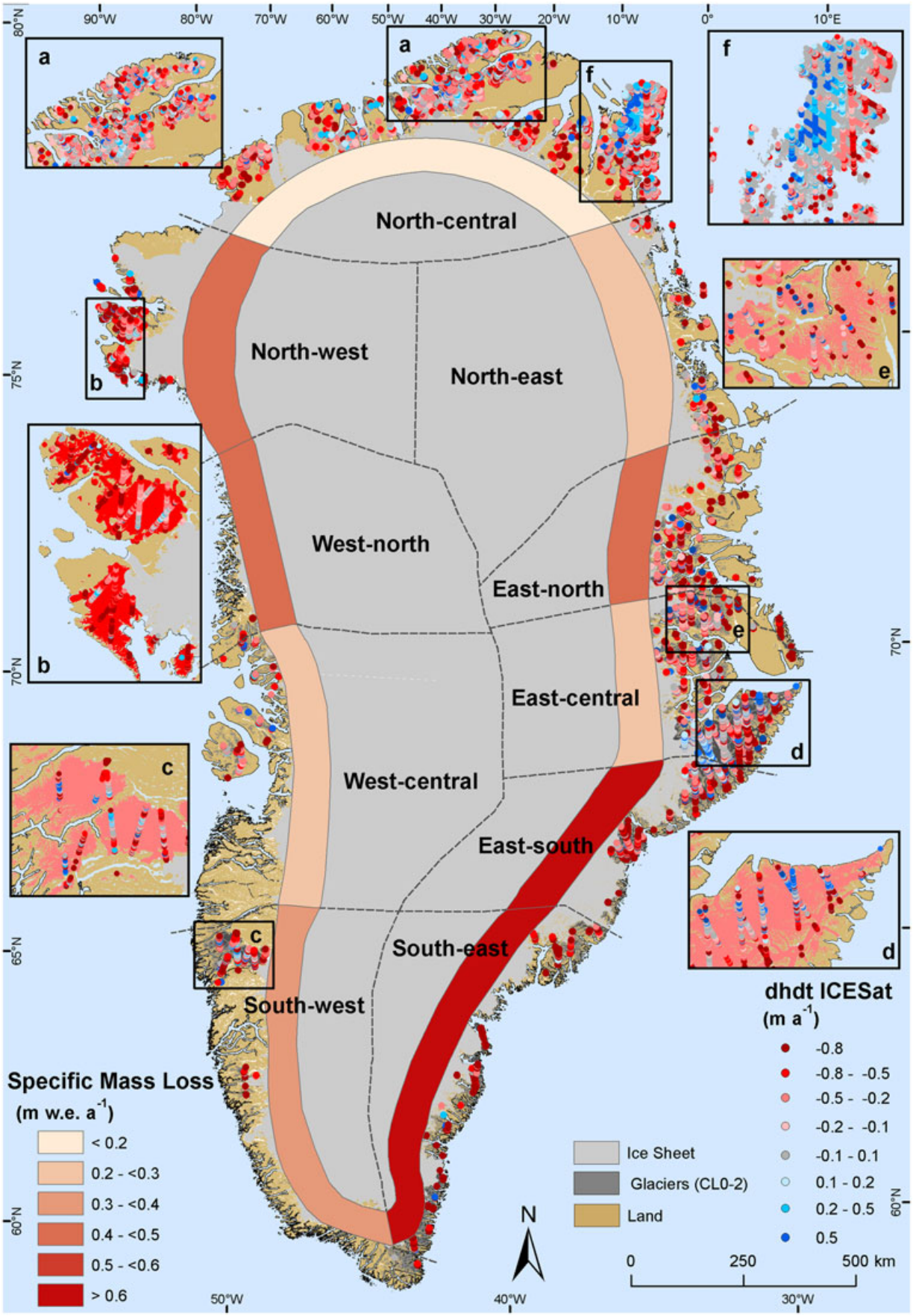

Figure 1. Mean mass changes for the 10 sectors and elevation changes for the GIC derived from ICESat points. The color of the GIC in the insets a–f represents the mean elevation change according to the legend for dh/dt ICESat.

was filled with the GIMP ice cover map (http://bprc.osu.edu/GDG/icemask.php) that was further adjusted with Moderate Resolution Imaging Spectroradiometer (MODIS) data. The inventory distinguishes three levels of connectivity to the ice sheet: CL0 has no connection to the ice sheet, CL1 has a weak connection, and CL2 has a strong connection to the ice sheet but is still hydrologically separable [*Rastner et al*., 2012]. The ice-covered area is ~89,000 km^2 for CL0 and CL1 and ~130,000 km^2 when including also CL2 areas. Here we present results separately for all GIC (CL0, 1, and 2) and those which are clearly separable from the ice sheet (CL0 and CL1). We divided Greenland in four major regions (north, east, south, and west) and 10 sectors (Figure 1) following *Rastner et al*. [2012] to derive a differentiated picture of the regional mass changes. All values are calculated and averaged for these sectors. The glacier hypsometry was derived from the GIMP DEM (http://bprc.osu.edu/GDG/gimpdem.php).

2.2. ICESat

[6] The elevation change data were obtained from the ICESat Geoscience Laser Altimeter System (GLAS) which was launched in January 2003. The laser system was operating at a wavelength of 1064 nm with footprints of about 70 m and a sampling frequency of about 170 m along track [*Zwally et al*., 2002]. The tracks are separated horizontally by ~30 km in southern and ~10 km in northern Greenland. The elevation changes are based on ICESat GLA12 data (release 531) and represent the mean of the time period from October 2003 to March 2008, taking into account all of the data available in this period. We performed the following data culling and correction procedures to reduce systematic errors and outliers (cf. [*Sørensen et al*., 2011], method M3, for full details): (a) a saturation correction to reduce elevation estimation errors originating from the saturation of the waveform as to reduce systematic errors in the measurements, (b) identification of thresholds of the so-called IceSvar parameter—showing the difference between the return signal and a Gaussian functional fit—to reject data with a large misfit (cf. [*Smith et al*., 2009]), and (c) identification and elimination of data with multiple peaks. The mean elevation change is derived by assuming that within 500 m the ice surface elevation can be represented by a rigid plane that varies linearly with time. A sine and cosine term describes the seasonal changes, which were consequently separated from the mean annual elevation change. The mean surface elevation changes were estimated at 500 m along track resolution and associated with variance from the regression procedure (cf. [*Sørensen et al*., 2011]). In addition, we assume that the error within each 500 m segment remains constant and, hence, the variances should reflect both the error of the measurements and the accuracy of the fit. For utilization of this dataset to the GIC and also to better approximate the assumption of a rigid plane, only data points lying at >250 m from the glacier margin are considered (glacier surfaces are usually having more constant slopes than the surroundings). Further filtering of the data is applied by rejecting implausibly high dh/dt values (>10 ma^{-1}), which corresponds roughly to

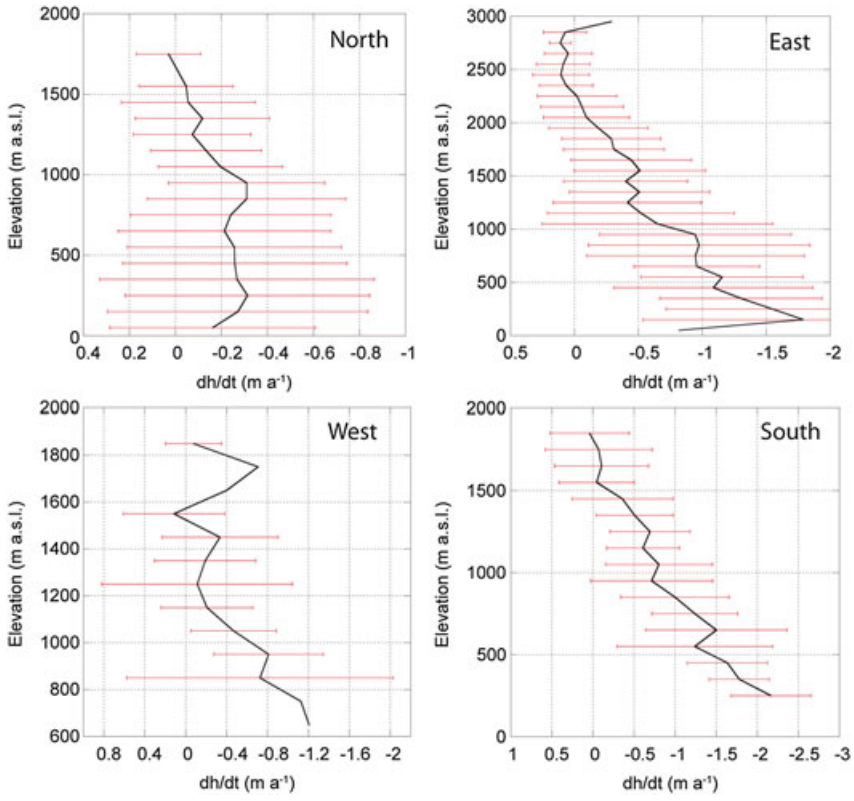

Figure 2. Mean annual elevation changes from 2003 to 2008 in 100 m bins vs. mean elevation for the four major regions as derived from the ICESat measurements. The red bars indicate the standard deviation for each interval but are only shown in case five or more ICESat measurements are available.

the highest/lowest 2.5% of the data. In addition, data points with high variances from the linear regression procedure (>1.0) were eliminated. In total 27,799 out of 40,475 data points were selected for elevation change analysis.

[7] The density of the ICESat points is large in the north (>20,000 ICESat points) so that most of the GIC are well covered, while the distance between tracks reaches about 30 km in the south and results in a low number of glaciers with sufficient coverage (~1750 points). We compared therefore the area-elevation distribution of the ICESat data points with the hypsometry for all glaciers in each sector as derived from the GIMP DEM (Figure S1 in Supporting Information). The deviation is for most altitudes and regions within ±10% with the highest deviation (+22%) occurring at elevations of about 1250 m a.s.l. in the western sectors. However, the lowest elevations, where most of the surface lowering occurred (except for the north, Figure 2), are well covered. To quantify the uncertainties due to varying track and thus point densities, we (a) randomly choose 50% of the points and (b) selected every second ICESat track. The deviations were around 4% for (a) and 5.5% for (b) with a maximum of 8% in Greenland's middle and middle-to-south latitudes. These values were considered in the uncertainty analysis. In order to estimate the volume loss for all GIC, we used the calculated along-track dh/dt-curves and applied them to the whole GIC area using the area-elevation distribution. The R^2 for the regression of dh/dt against elevation was up to 0.44 (east-south) but was low for sectors showing no clear trend with altitude (south-west, west, and north). For these sections, we calculated the elevation changes based on the mean dh/dt of all points below and above the ELA. This procedure was also performed for comparison and uncertainty estimation. The differences between these two procedures are about ±7% for most of the sections and highest (±25%) for the south-west section.

2.3. Density Determination

[8] Snow, firn, and ice densities and firn compaction must be taken into account when converting elevation changes into mass changes. We calculated the firn density based on an empirical relationship between snow density and mean firn temperature (at 10 m depth based on the mean annual air temperature, MAAT) by *Reeh et al*. [2005]. The MAAT is calculated as a function of surface elevation and geographical position according to *Fausto et al*. [2009]. The MAAT and the resulting firn density are derived for each sector. The dh/dt values above the equilibrium line altitude (ELA) are multiplied by the regional firn density and the values below the ELA are multiplied by the typical density of glacier ice (900 kg/m^3), resulting in average regional values between 528 kg m^{-3} (north-west sector) and 796 kg m^{-3} (east-south sector) (cf. Tables *S1* and *S2*). The ELA is approximated by the median elevation of each glacier (cf. [*Braithwaite and Raper*, 2009]). We estimate the uncertainty based on one standard deviation and assume that the uncertainty due to the rough estimate of the ELA is also considered by this conservative estimate of ±150 kg m^{-3}.

[9] The derivation of the firn compaction follows *Sørensen et al*. [2011], where the change in the air space of the top firn (top 15 annual layers) is estimated from a dynamic firn model based on the description of firn compaction by *Herron and Langway* [1980] and *Arthern et al*. [2010]. The dynamical firn model is forced by interpolated output fields from the HIRHAM5 regional climate model at a resolution of 5 × 5 km [*Lucas-Picher et al*., 2012]. The retention of melt water in the firn pack is assumed to be confined to the surface layer formed in the same period of time as the melt [*Reeh*, 2008]. The resolution of the model is too low to address each glacier individually, but it provides reasonable results for each sector. We estimated the uncertainty from the error in the linear fit of the interannual variability of the firn column and conservatively assumed the higher estimate of ~7.5% of the total mass change [cf. *Sørensen et al*., 2011]. The results revealed a mean change in firn densification of about -0.05 ± 0.01 m a^{-1} with the highest value in the warmer and wetter east-south sector (-0.22 m ± 0.02 m a^{-1}) and a slight expansion in the cold and dry north ($+0.09 \pm 0.01$ m a^{-1}) (Tables S1, S2).

[10] The potential overall uncertainty of the mass budget calculations is manifold and comprises especially the uncertainty in ICESat data itself (e_{ICESat}), the spatial interpolation of the ICESat samples (e_{Interp}), the density assumption (e_{Dens}), and the firn compaction model (e_{Firn}). Assuming that the sources are independent the total uncertainty would be as follows:

Table 1. Statistics and Derived Mass Changes for the GIC on Greenland that are Clearly Separable from the Ice Sheet (CL0, CL1)

	Land Terminating GIC Only				All GIC Including Marine Terminating			
Sector	Area (km^2)	Nr. points	Mean dh (m a^{-1})	Mass change (Gt a^{-1}]	Area (km^2)	Nr. points	Mean dh (m a^{-1})	Mass change (Gt a^{-1})
East-north	8,462	1,162	−0.61	-3.5 ± 1.5	8,795	1,191	−0.63	-3.8 ± 1.6
East-central	11,905	1,415	−0.40	-3.3 ± 1.4	13,757	3,104	−0.40	-3.9 ± 1.6
East-south	1,045	23	−0.86	-0.6 ± 0.2	3,080	1,352	−0.96	-2.2 ± 0.8
East total	21,411	2,600	*−0.50*	-7.4 ± 3.1	25,631	5,697	*−0.55*	-9.9 ± 4.0
South-east	2,354	68	−1.30	-2.2 ± 0.9	7,056	511	−1.37	-7.0 ± 2.9
South-west	5,481	560	−0.45	-2.1 ± 0.9	8,492	732	−0.43	-3.3 ± 1.4
South total	7,835	628	*−0.75*	-3.3 ± 1.8	15,548	1,243	*−0.90*	-10.3 ± 4.2
West-central	4,773	275	−0.28	-1.0 ± 0.4	5,045	285	−0.28	-1.0 ± 0.4
West-north	722	41	−0.77	-0.3 ± 0.1	729	42	−0.77	-0.4 ± 0.1
West total	5,495	316	*−0.35*	-1.3 ± 0.5	5,775	327	*−0.35*	-1.4 ± 0.5
North-west	2,699	797	−0.60	-1.1 ± 0.4	4,340	849	−0.60	-1.8 ± 0.7
North-central	18,116	7,788	−0.28	-3.8 ± 1.6	34,992	8,192	−0.18	-3.9 ± 1.7
North-east	2,667	580	−0.27	-0.5 ± 0.2	3,039	661	−0.29	-0.6 ± 0.3
North total	23,482	9,166	*−0.33*	-5.3 ± 1.8	42,370	9,702	*−0.23*	-6.30 ± 2.23
Total	*58,223*	*12,708*	**−0.45**	-18.5 ± 7.2	*89,324*	*17,009*	**−0.45**	-27.9 ± 10.7

Table 2. Statistics and Derived Mass Changes for the GIC on Greenland (CL0–Cl2)

	Land Terminating GIC Only				All GIC Including Marine Terminating			
Sector	Area (km^2)	Nr. points	Mean dh (m a^{-1})	Mass change (Gt a^{-1})	Area (km^2)	Nr. points	Mean dh (m a^{-1})	Mass change (Gt a^{-1})
East-north	10,038	1,338	−0.58	−3.9 ± 1.7	10,371	1,367	−0.60	−4.2 ± 1.8
East-central	15,075	1,819	−0.38	−4.0 ± 1.6	33,955	4,923	−0.38	−9.4 ± 3.9
East-south	1,294	29	−0.83	−0.7 ± 0.2	14,004	1,381	−0.67	−6.6 ± 2.4
East total	26,408	3,186	*−0.47*	−8.6 ± 3.5	58,330	7,671	*−0.48*	−20.3 ± 8.0
South-east	3,026	133	−1.23	−2.7 ± 1.1	12,114	645	−1.32	−11.3 ± 4.6
South-west	5,790	574	−0.45	−1.8 ± 0.7	8,843	746	−0.43	−3.4 ± 1.4
South total	8,816	708	*−0.76*	−4.4 ± 1.9	20,957	1,391	*−0.96*	−14.7 ± 6.0
West-central	4,919	279	−0.27	−0.9 ± 0.4	5,258	289	−0.28	−1.0 ± 0.4
West-north	765	41	−0.77	−0.4 ± 0.1	772	41	−0.77	−0.4 ± 0.1
West total	5,684	320	*−0.34*	−1.3 ± 0.5	6,030	330	*−0.34*	−1.4 ± 0.5
North-west	3,051	917	−0.62	−1.3 ± 0.5	6,368	1,766	−0.68	−2.9 ± 1.2
North-central	18,182	7,788	−0.28	−3.9 ± 1.7	35,059	15,980	−0.18	−3.9 ± 1.7
North-east	2,922	580	−0.27	−0.6 ± 0.2	3,294	661	−0.29	−0.7 ± 0.3
North total	24,155	9,285	*−0.33*	−4.4 ± 1.9	44,721	18,407	*−0.26*	−4.5 ± 1.9
Total	65,062	13,499	**−0.45**	−18.8 ± 7.9	130,037	27,799	**−0.48**	−40.9 ± 16.5

$$e = \sqrt{e^2_{ICESat} + e^2_{Interp} + e^2_{Dens} + e^2_{Firn}}. \quad (1)$$

[11] The accuracy of the ICESat elevation data is in the ideal case over flat terrain ±0.15 m, but still sufficiently accurate over glaciers and ice caps (about ±0.5 m, *Moholdt et al*. [2010]). Another uncertainty to consider, although small, is the ICESat intercampaign bias. We assume similar values (−0.013 m a^{-1}) for our data as calculated by *Sørensen et al*. [2011]. Hence, the estimated overall uncertainty of the ICESat data is 0.113 m a^{-1}. We did not explicitly correct the dh/dt for bedrock movement caused by glacio-istostatic adjustment, but assume that this is included in this conservative uncertainty estimate.

3. Results

[12] The GIC in Greenland showed a mean surface lowering of around 0.45 m a^{-1} for the period October 2003–March 2008 (Tables 1 and 2), resulting in an overall volume loss of about 40 km^3 a^{-1} for the CL0 and CL1 glaciers and about 60 km^3 a^{-1} for all local GIC. The resulting mass loss for the CL0 and CL1 glaciers is 27.9 ± 10.7 Gt a^{-1}, corresponding to 0.08 ± 0.03 mm a^{-1} SLE but only 18.5 ± 7.2 Gt a^{-1}, when excluding marine-terminating glaciers. This large difference can mainly be explained by the large overall area of marine-terminating glaciers (~31,000 km^2 or 34.5% of all GIC). The overall ice loss of all Greenland GIC was 40.9 ± 16.5 Gt a^{-1} (0.12 ± 0.05 mm a^{-1} SLE).

[13] The mass loss is not homogeneously distributed, but differs substantially among the regions (Figure 1). The highest average specific mass loss (average loss per unit area) for CL0 and CL1 glaciers occurred in the southeastern sector (1.0 ± 0.3 m w.e. a^{-1}) while the loss was lowest in the north-central sector (0.1 ± 0.05 m w.e. a^{-1}). The overall pattern of the regional mass change of all GIC is similar to those with CL0 and CL1. Overall, the total mass loss from marine and land-terminating glaciers is similar with a mean specific mass loss of 0.34 m w.e. a^{-1}. The largest contribution to the mass loss of marine-terminating glaciers with CL2 connectivity can be found in the south-east sector (~4 Gt a^{-1}), and the glaciers in the east, dominated by the Geikie Plateau, which adds another ~3 Gt a^{-1}. Somewhat special is Flade Isblink, the largest ice cap of Greenland (~7500 km^2) which is also marine-terminating (Figure 1f): It showed no mass loss at its northeastern margins and had an overall mass budget of about zero in close agreement with *Rinne et al*. [2011]. Other large ice caps like Sukkertoppen (West, Figure 1c) and Washington Land (North-central sector) had a clearly negative budget.

4. Discussion and Conclusions

[14] We applied ICESat data to estimate volume changes for Greenland's GIC after a rigorous quality check and several adjustments. The major problem is the large distance between the ICESat tracks especially in the southern sectors. Nevertheless, the ICESat points represent the hypsography of the glaciers quite well (Figure S1) and the observed surface lowering is significant even when assigning high-uncertainty ranges.

[15] We considered both the density of firn and ice and, in contrast to other studies which applied ICESat data on GIC (e.g., [*Gardner et al*., 2010; *Moholdt et al*., 2010; *Kääb et al*., 2012]), also the firn compaction for the conversion of volume to mass changes. The resolution of the compaction model is too coarse for individual glaciers but provided reasonable results and reflects the expected general pattern, e.g., high densification in the wetter and warmer south-east and little densification in the dryer and colder north. The applied dh corrections account for up to ¼ of the ICESat-derived elevation changes in the accumulation area and alter the overall volume changes by ~15% and are hence important to consider (cf. *Sørensen et al*. [2011]). However, these corrections are within the overall uncertainty range. Our estimated firn and ice densities are more at the lower bound. Taking estimates for glaciers like 600 kg m^{-3} for the accumulation and 900 kg m^{-3} for the ablation area used in other studies (cf. *Gardner et al*. [2010]) would result in a mass loss of 31.3 Gt a^{-1} for all CL0 and CL1 glaciers, i.e., 3.5 Gt a^{-1} larger than our estimate.

[16] The total and specific mass losses from marine and land-terminating glaciers are similar although one might expect a higher loss of the former due to enhanced melt from ice-water interaction and calving. This might be explained by the usually larger accumulation area at high elevations with slight mass gains (see insets in Figure 1), which offsets the higher mass loss at the tongues. *Gardner et al*. [2010] found a similar pattern for the Canadian Arctic. The specific mass

budget of about zero of the calving glaciers in the northern section in comparison to a mass budget of -0.20 m w.e. a^{-1} of the other glaciers is mainly caused by the Flade Isblink. In-situ mass balance measurements of Mittivakkat Glacier in the southeast, the only one with longer-term data, revealed a mean mass loss of ~0.82 m w.e. a^{-1} for 2003–2008 [*Mernild et al*., 2011] which is within the range of our results for the south-east sector (-1.0 ± 0.3 m w.e. a^{-1}).

[17] The mass loss of the Greenland ice sheet according to different methods is slightly higher than 200 Gt a^{-1} for a similar period as investigated here [*Schrama et al*., 2011; *Rignot et al*., 2011]. In general, these studies do not clearly separate between GIC and ice sheet, so it is difficult to determine if GIC are included in the estimates. Apart from the formerly missing inventory, this is also due to the coarse resolution of the mass change estimates from GRACE (e.g., [*Velicogna*, 2009]) which do not resolve individual glaciers. Assuming a 200 Gt a^{-1} loss for all of Greenland, the CL0 and CL1 GIC contributed ~14% to the loss, while this would amount to 20% when considering also the CL2 GIC. Hence, the specific mass loss of the GIC is about 2.5 times higher than for the ice sheet as the GIC area (CL0-CL2) is only about 7% of the area of the ice sheet (~1,680,000 km^2, *Rastner et al*. [2012]).

[18] The regional pattern of the GIC mass loss seems to be similar for the ice sheet [*Schrama et al*., 2011]. Most negative mass budgets are found in the southeastern sectors and only limited change is found in the northern sector (Figure 1). Interestingly, the highest mass loss takes place in regions which receive most precipitation and vice versa. Hence, it might be possible that mass changes are correlated to mean annual precipitation amounts. However, further investigations of this hypothesis are needed for clarification.

[19] The obtained mass loss of Greenland's GIC is higher than from the glaciers on Svalbard (4.3 Gt a^{-1} [*Moholdt et al*., 2010]) and in the Russian Arctic (9.1 ± 2.0 Gt a^{-1} [*Moholdt et al*., 2012]), but lower than in the Canadian Arctic Archipelago (61 ± 7 Gt a^{-1} [*Gardner et al*., 2010]). However, the ice-covered area in the latter region is with ~148,000 km^2 significantly larger, yielding a mean specific mass budget of -0.41 ± 0.05 m w.e. a^{-1}. The mass loss for all Greenland GIC (CL0-CL2) is 40.9 ± 16.5 Gt a^{-1} resulting in a less negative specific mass budget of -0.31 ± 0.12 m w.e. a^{-1}.

[20] The published estimates of the contribution of the world's GIC to the sea level rise in the early 21st century vary around 1 mm a^{-1} (e.g., 0.95 mm a^{-1} for 2002–2006 [*Dyurgerov*, 2010], 1.12 mm a^{-1} during 2001–2005 [*Cogley*, 2009]). In this regard, the contribution revealed here for the GIC on Greenland (0.12 ± 0.05 mm a^{-1} for all GIC and 0.08 ± 0.03 mm a^{-1} for the GIC with CL0 and CL1) is significant.

[21] **Acknowledgments.** This work was supported by funding from the ice2sea program from the European Union 7th framework program, grant 226375. Ice2sea contribution 136. F.P. and N.M. acknowledge the funding by the ESA project Glaciers_cci (4000101778/10/I-AM). H.M. acknowledges funding from the Programme for Monitoring of the Greenland Ice Sheet (PROMICE).

References

Arendt, A., et al. (2012), Randolph Glacier Inventory, 2.0: A dataset of global glacier outlines, Global Land Ice Measurements from Space, Boulder Colorado, USA. Digital Media.

Arthern, R. J., D. G. Vaughan, A. M. Rankin, R. Mulvaney, and E. R. Thomas (2010), In situ measurements of Antarctic snow compaction compared with predictions of models. *J. Geophys. Res. (Earth Surface) 115*, F03011. doi:10.1029/2009JF001306.

Bjørk, A. A., K. H. Kjær, N. J. Korsgaard, S. A. Khan, K. K. Kjeldsen, C. S. Andresen, J. E. Box, N. K. Larsen, and S. Funder (2012), An aerial view of 80 years of climate-related glacier fluctuations in southeast Greenland, *Nature Geosci. 5*(6), 427–432.

Braithwaite, R., and S. Raper (2009), Estimating equilibrium-line altitude (ELA) from glacier inventory data, *Ann. Glaciol. 50*(53), 127–132.

Citterio, M., F. Paul, A. P. Ahlstrøm, H. F. Jepsen, and A. Weidick (2009), Remote sensing of glacier change in West Greenland: Accounting for the occurrence of surge-type glaciers, *Ann. Glaciol. 50*(53), 70–80.

Cogley, J. (2009), Geodetic and direct mass-balance measurements: Comparison and joint analysis, *Ann. Glaciol. 50*, 96–100.

Dyurgerov, M. B. (2010), Reanalysis of glacier changes: From the IGY to the IPY, 1960–2008, *Data of Glaciological Studies 108*, 1–116.

Ettema, J., van den Broeke M. R., E. van Meijgaard, W. J. van de Berg, J. L. Bamber, J. E. Box, and R. C. Bales (2009), Higher surface mass balance of the Greenland ice sheet revealed by highresolution climate modeling, *Geophys. Res. Lett. 36*, L12501, doi:10.1029/2009GL038110.

Fausto, R. S., A. P. Ahlstrøm, D. van As, C. E. Bøggild, and S. J. Johnson (2009), A new present-day temperature parameterization for Greenland, *J. Glaciol. 55*(189), 95–105.

Gardner, A. S., G. Moholdt, B. Wouters, G. J. Wolken, D. O. Burgess, M. J. Sharp, C. Cogley, C. Braun, and C. Labine (2010), Sharply increased mass loss from glaciers and ice caps in the Canadian Arctic Archipelago, *Nature 473*, 357–460.

Herron, M. M., and C. C. Langway (1980), Firn densification: An empirical model. *J. Glaciol. 25* (93), 373–385.

Jiskoot, H., D. Juhlin, H. St Pierre, and M. Citterio (2012), Tidewater glacier fluctuations in central East Greenland coastal and fjord regions (1980s–2005), *Ann. Glaciol. 53*(60), 35–44.

Kääb, A., E. Berthier, C. Nuth, J. Gardelle, and Y. Arnaud (2012), Contrasting patterns of early twenty-first-century glacier mass change in the Himalayas, *Nature*, *488*(7412), 495–498.

Leclercq, P. W., A. Weidick, F. Paul, T. Bolch, M. Citterio, and J. Oerlemans (2012), Historical glacier length changes in West Greenland, *Cryosphere 6*, 1339–1343.

Lemke, P., et al. (2007), Observations: Changes in snow, ice and frozen ground, in *Climate Change 2007: The Physical Science Basis. Contribution of Working Group I to the Fourth Assessment Report of the Intergovernmental Panel on Climate Change* edited by S. Solomon, D. Qin, M. Manning, C. Chen, M. Marquis, K.B. Averyt, M. Tignor, and H.L. Miller, 337–384, Cambridge University Press, Cambridge.

Lucas-Picher, P., M. Wulff-Nielsen, J. H. Christensen, G. Aðalgeirsdóttir, R. Mottram, and S. B. Simonsen (2012), Very high resolution regional climate model simulations over Greenland: Identifying added value, *J. Geophys. Res.*, *117*, D02108, doi:10.1029/2011JD016267.

Meier, M. F., M. B. Dyurgerov, U. K. Rick, S. O'Neel, W. T. Pfeffer, R. S. Anderson, S. P. Anderson, and A. F. Glazovsky (2007), Glaciers dominate eustatic sea-level rise in the 21st century, *Science 317*(5841), 1064–1067.

Mernild, S. H., N. T. Knudsen, W. H. Lipscomb, J. C. Yde, J. K. Malmros, B. Hasholt, and B. H. Jakobsen (2011), Increasing mass loss from Greenland's Mittivakkat Gletscher, *Cryosphere 5*(2), 341–348.

Moholdt, G., C. Nuth, J. O. Hagen, and J. Kohler (2010), Recent elevation changes of Svalbard glaciers derived from ICESat laser altimetry, *Remote Sens. Environ. 114*, 2756–2767.

Moholdt, G., B. Wouters, and A. S. Gardner (2012), Recent mass changes of glaciers in the Russian High Arctic, *Geophys. Res. Lett. 39*(10). doi: 10.1029/2012GL051466.

Pritchard, H. D., R. J. Arthern, D. G. Vaughan, and L. A. Edwards (2009), Extensive dynamic thinning on the margins of the Greenland and Antarctic ice sheets, *Nature 461*, 971–975.

Radic, V., and R. Hock (2010), Regional and global volumes of glaciers derived from statistical upscaling of glacier inventory data, *J. Geophys. Res. 115*, F01010. doi:10.1029/2009JF001373

Rastner, P., Bolch, T., Mölg, N., Machguth, H., Le Bris, R., and Paul, F. (2012), The first complete inventory of the local glaciers and ice caps on Greenland. *Cryosphere 6*, 1483–1495.

Reeh, N. (2008), A nonsteady-state firn-densification model for the percolation zone of a glacier. *J. Geophys. Res. 113*. doi:10.1029/2007JF000746.

Reeh, N., D. A. Fisher, R. M. Koerner, and H. B. Clausen (2005), An empirical firn-densification model comprising ice lenses, *Ann. Glaciol. 42*, 101–106.

Rignot, E., I. Velicogna, M. R. van den Broeke, A. Monaghan, and J. Lenaerts (2011), Acceleration of the contribution of the Greenland and Antarctic ice sheets to sea level rise, *Geophys. Res. Lett*. 38(5). doi: 10.1029/2011GL046583.

Rinne, E., A. Shepherd, S. Palmer, M. van den Broeke, A. Muir, J. Ettema, and D. Wingham (2011), On the recent elevation changes at the Flade Isblink Ice Cap, northern Greenland, *J. Geophys. Res. 116*. F03024, doi:10.1029/2011JF001972.

Schrama, E., B. Wouters, and B. Vermeersen (2011), Present Day Regional Mass Loss of Greenland Observed with Satellite Gravimetry, *Surv. Geophys. 32*(4–5), 377–385.

Smith, B. E., H. A. Fricker, I. R. Joughin, and S. Tulaczyk (2009), An inventory of active subglacial lakes in Antarctica detected by ICESat (2003–2008), *J. Glaciol. 55*(192), 573–595.

Sørensen, L. S., S. B. Simonsen, K. Nielsen, P. Lucas-Picher, G. Spada, G. Adalgeirsdottir, R. Forsberg, and C. S. Hvidberg (2011), Mass balance of the Greenland ice sheet (2003–2008) from ICESat data–the impact of interpolation, sampling and firn density, *Cryosphere 5*(1), 173–186.

van den Broeke, M., J. Bamber, J. Ettema, E. Rignot, E. Schrama, and B. Wouters (2009), Partitioning recent Greenland mass loss, *Science 326*, 984–986.

Velicogna, I. (2009), Increasing rates of ice mass loss from the Greenland and Antarctic ice sheets revealed by GRACE, *Geophys. Res. Lett. 36*, L19503. doi: 10.1029/2009GL040222.

Weidick, A., and E. Morris (1998), Local glaciers surrounding the continental ice sheets, in Into the Second Century of World-Wide Glacier Monitoring - Prospects and Strategies, edited by W. Haeberli et al., pp. 197–207, UNESCO, Paris.

WGMS (2008), Global glacier changes: Facts and figures, Zemp, M., Roer, I., Kääb, A., Paul, F., Hoelzle, M., Haeberli, W. pp. 88, UNEP/DIWA/GRID, Geneva.

Zwally, H., et al. (2002), ICESat's laser measurements of polar ice, atmosphere, ocean, and land, *J. Geodyn. 34*(3–4), 405–445.

Mass loss of Greenland's glaciers and ice caps 2003-2008 revealed from ICESat data

T. Bolch (1,2), L. Sandberg Sørensen (3), S. B. Simonsen (4, 5), N. Mölg (1), H. Machguth (1,6), P. Rastner (1), F. Paul (1)

(1) Department of Geography, University of Zurich, Winterthurer Str. 190, 8057 Zürich, Switzerland
**Corresponding author, email: tobias.bolch@geo.uzh.ch*
(2) Institute for Cartography, Technische Universität Dresden, 01069 Dresden, Germany
(3) Geodynamics Department, DTU Space, Elektrovej, Building 328 2800 Kgs. Lyngby, Denmark
(4) Centre for Ice and Climate, NBI, University of Copenhagen, Juliane Maries Vej 30, 2100 Copenhagen, Denmark
(5) Danish Climate Centre, DMI, Lyngbyvej 100, 2100 Copenhagen, Denmark
(6) Geological Survey of Denmark and Greenland (GEUS), Voldgade 10, 1350 Copenhagen, Denmark

Auxillary Material

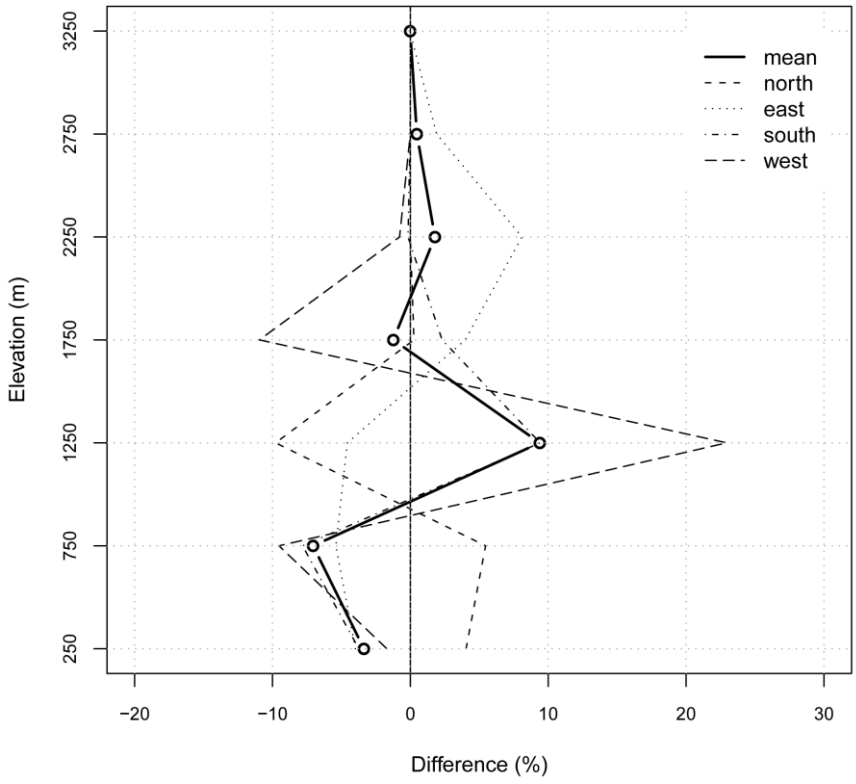

Supplementary Figure 1: Difference of the area-elevation distribution of entire glacier area and the ICESat tracks and for the different regions. Negative values indicate that the elevation interval is underrepresented with ICESat points while positive values indicate an above average representation.

Supplementary Table 1: Mean ICESat derived elevation changes, the modeled firn densification adjustments and mean snow, firn and ice density for Greenland's GIC that are clearly separable from the ice sheet (CL0, CL1).

	Land terminating GIC only					all GIC incl. marine terminating				
Sector	Mean dh >= ELA [m a^{-1}]	dh firn densification adjustment	Mean dh >= ELA. adjusted [m a^{-1}]	Mean dh < ELA [m a^{-1}]	Mean snow. ice and firn density [kg m^{-2}]	Mean dh >= ELA [m a^{-1}]	dh firn densification adjustment	Mean dh >= ELA. adjusted [m a^{-1}]	Mean dh < ELA [m a^{-1}]	Mean snow. ice and firn density [kg m^{-2}]
east-north	-0.38	-0.11	-0.27	-0.84	590	-0.38	-0.11	-0.27	-0.88	599
east-central	-0.2	-0.10	-0.10	-0.59	577	-0.2	-0.10	-0.10	-0.6	585
east-south	-0.64	-0.22	-0.43	-1.08	712	-0.74	-0.22	-0.53	-1.18	796
East total	***-0.29***	***-0.11***	***-0.19***	***-0.71***	***589***	***-0.33***	***-0.12***	***-0.21***	***-0.77***	***615***
south-east	-1.03	-0.09	-0.94	-1.57	666	-1.09	-0.09	-1.00	-1.64	699
south-west	-0.35	-0.01	-0.34	-0.68	665	-0.29	-0.01	-0.28	-0.73	662
South total	**-0.55**	**-0.03**	***-0.52***	**-0.95**	***665***	**-0.65**	**-0.05**	***-0.60***	**-1.14**	***679***
west-central	-0.16	-0.04	-0.12	-0.41	633	-0.17	-0.04	-0.13	-0.4	625
west-north	-0.78	-0.06	-0.72	-0.77	625	-0.78	-0.06	-0.72	**-0.77**	625
West total	**-0.24**	**-0.04**	***-0.20***	**-0.46**	***632***	**-0.25**	**-0.04**	***-0.21***	**-0.45**	***625***
north-west	-0.42	-0.04	-0.38	-0.78	532	-0.4	-0.04	-0.36	-0.79	528
north-central	-0.20	0.09	-0.29	-0.40	441	-0.19	0.09	-0.28	-0.18	551
north-east	-0.17	0.09	-0.25	-0.35	562	-0.2	0.09	-0.29	-0.36	592
North total	***-0.22***	***0.08***	***-0.30***	***-0.44***	***465***	***-0.21***	***0.08***	***-0.29***	***-0.26***	***552***
Total	**-0.30**	***-0.02***	***-0.28***	**-0.61**	***553***	**-0.32**	***-0.01***	***-0.31***	**-0.57**	***597***

Supplementary Table 2: Mean ICESat derived elevation changes, the modeled firn densification adjustments and mean snow, firn and ice density for all Greenland's GIC (CL0, CL1, CL2).

	Land terminating GIC only					all GIC incl. marine terminating				
Sector	Mean dh >= ELA [m a^{-1}]	dh firn densification adjustment	Mean dh >= ELA. adjusted [m a^{-1}]	Mean dh < ELA [m a^{-1}]	Mean snow. ice and firn density [kg m^{-2}]	Mean dh >= ELA [m a^{-1}]	dh firn densification adjustment	Mean dh >= ELA. adjusted [m a^{-1}]	Mean dh < ELA [m a^{-1}]	Mean snow. ice and firn density [kg m^{-2}]
east-north	-0.34	-0.11	-0.23	-0.81	559	-0.35	-0.11	-0.24	-0.84	566
east-central	-0.19	-0.10	-0.09	-0.56	562	-0.15	-0.10	-0.05	-0.60	565
east-south	-0.59	-0.22	-0.38	-1.06	719	-0.33	-0.22	-0.12	-1.01	602
East total	***-0.27***	***-0.11***	***-0.16***	***-0.68***	***569***	***-0.23***	***-0.13***	***-0.10***	***-0.74***	***574***
south-east	-0.92	-0.09	-0.83	-1.54	639	-1.00	-0.09	-0.91	-1.60	674
south-west	-0.35	-0.01	-0.34	-0.68	658	-0.29	-0.01	-0.28	-0.71	662
South total	**-0.55**	**-0.04**	***-0.51***	**-0.97**	***651***	**-0.70**	**-0.06**	***-0.64***	**-1.23**	***669***
west-central	-0.14	-0.04	-0.10	-0.4	626	-0.17	-0.04	-0.13	-0.39	604
west-north	-0.81	-0.06	-0.75	-0.76	612	-0.81	-0.06	-0.75	-0.76	599
West total	**-0.23**	**-0.04**	***-0.19***	**-0.45**	***624***	**-0.25**	**-0.04**	***-0.21***	**-0.44**	***603***
north-west	-0.44	-0.04	-0.40	-0.79	544	-0.46	-0.04	-0.42	-0.91	616
north-central	-0.2	0.09	-0.29	-0.4	440	-0.19	0.09	-0.28	-0.18	546
north-east	-0.16	0.09	-0.25	-0.35	551	-0.19	0.09	-0.28	-0.36	571
North total	***-0.23***	***0.07***	***-0.30***	***-0.44***	***467***	***-0.23***	***0.07***	***-0.30***	***-0.30***	***557***
Total	**-0.29**	***-0.03***	***-0.26***	**-0.61**	***547***	**-0.30**	***-0.04***	***-0.26***	**-0.66**	***585***

Supplementary Table 3: Specific mass changes for the different sectors for Greenland's GIC that are clearly separable from the ice sheet (CL0, CL1)

Sector	Mass loss (Gt a^{-1})	Area (km^2)	Specific mass budget (m w.e. a^{-1})
east-north	-3.8 ± 1.6	8795	-0.43 ± 0.18
east-central	-3.9 ± 1.6	13757	-0.28 ± 0.12
east-south	-2.2 ± 0.8	3080	-0.71 ± 0.25
East total	**-9.9 ± 4.0**	***25632***	***-0.39 ± 0.16***
south-east	-7.0 ± 2.9	7056	-0.99 ± 0.30
south-west	-3.3 ± 1.4	8492	-0.39 ± 0.16
South total	**-10.3 ± 4.2**	***15548***	***-0.66 ± 0.27***
west-central	-1.0 ± 0.4	5045	-0.20 ± 0.08
west-north	-0.4 ± 0.1	729	-0.50 ± 0.20
West total	**-1.4 ± 0.5**	***5774***	***-0.24 ± 0.09***
north-west	-1.8 ± 0.7	4340	-0.41 ± 0.17
north-central	-3.9 ± 1.7	34992	-0.11 ± 0.05
north-east	-0.6 ± 0.3	3039	-0.20 ± 0.08
North total	**-6.30** ± 2.23	***42371***	***-0.15 ± 0.05***
Total	***-27.9 ± 10.7***	***89325***	***-0.31 ± 0.12***

Paper IV

Rastner, P., Machguth, H., Bolch, T. and Paul, F. (subm). Climate sensitivity of Greenland's local glaciers and ice caps. Journal of Glaciology.

Climate sensitivity of Greenland's local glaciers and ice caps

P. Rastner[1], H. Machguth[2], T. Bolch[1,3], F. Paul[1]
[1]*Department of Geography, University of Zurich, Switzerland*
[2] *Arctic Technology Centre, Technical University of Denmark*
[3] *Institute for Cartography, Technische Universität Dresden, Germany*

Abstract

Glaciers and ice caps (GIC) react differently to the same climatic change as they have different geometries (size, slope, hypsometry), response times, topographic settings and climatic regimes. The latter governs their climate and mass balance sensitivities which both provide a means to determine their response to climate change. In this study, we assessed the climate and mass balance sensitivity of the GIC on Greenland from mass balance and climate observations. We used surface elevation and mass changes derived from the Ice, Cloud, and Land Elevation Satellite (ICESat) laser altimetry data, and temperature (*T*) and precipitation (*P*) from re-analysis driven RACMO2 regional climate model data. Greenland was divided into ten sectors to analyze to what degree mass and volume changes are correlated with mean annual *T* and *P* or changes in *T* and *P* on a regional scale. We found a correlation with mean annual *T* of 69% and with mean annual *P* of 56%. The relationship of annual T_{change} of nearly 2 K for some sectors with ICESat mass changes appears also significant but the regressions of P_{change} not. A reasonable mass-balance sensitivity could be derived to a change in *T* using the observed values. However, the correlation with changes in *P* was small. High sensitivities are found in the south-east sectors (-1.23 m w.e. yr^{-1} K^{-1}) and much smaller ones (< -0.28 m w.e. yr^{-1} K^{-1}) for the remaining parts of Greenland. We conclude that the observed regional variability in mass changes can be best explained with the climate sensitivity, i.e. the prevailing climatic regime rather than its recent trends.

1. Introduction

Glaciers and ice caps (GIC) are important components of the Earth's hydrological system and are particularly sensitive to climate change (e.g. Vaughan and others, 2013). Thereby, 'sensitive' has a range of different meanings. From a more general point of view it means that very small changes in climate (e.g. a temperature increase of 0.1 K per decade that is hardly measurable) translate in very large changes in glacier geometry, i.e. changes in length (or front variations) that are well visible for a large public and measure in (tens of) metres per year. From a more scientific point of view, glacier changes are highly variable due to their vastly different geometries (e.g. size, slope, hypsometry), their topographic setting, and the rather different climatic regimes (from warm/wet to cold/dry) they are located in (Kuhn, 1984). The latter is also responsible for what can be seen as the climatic sensitivity: the more humid the climate is, the higher can the temperatures be to sustain a glacier, i.e. the higher is the mass turnover and hence the mass balance gradient γ of a glacier (i.e. the change in mass balance with elevation) or activity index (Kuhn, 1980). There is a large body of literature related to this climatic sensitivity, either analyzing observed mass balance profiles (e.g. (Kuhn, 1984; Braithwaite and Zhang, 2000; Hock and others, 2007) or past and future glacier

behavior using models (e.g. Leclercq and Oerlemans, 2011; Oerlemans, 2005). In the latter studies, γ is directly derived from mean annual precipitation sums, i.e. a long-term climate parameter.

Yet there is another kind of sensitivity, the mass balance sensitivity (MBS). Though closely related to the climatic sensitivity (via γ), it describes how the mass balance of a glacier changes for given changes in temperature *T* and precipitation *P*. The MBS depends on γ but also on glacier hypsometry (e.g. Furbish and Andrews, 1984), i.e. its value changes when the geometry of a glacier strongly changes (Paul, 2010). The MBS is an important parameter, as its value allows to determine the contribution of glacier melt to sea-level change for given climate changes by just multiplying the glacier area with the *T*/*P* change and the respective MBS (e.g. Braithwaite and Raper, 2002; Hock and others, 2009). In general, the MBS is derived from a numeric mass/energy balance or degree-day model, allowing easy determination of the change in mass balance due to a change in *T* or *P.* Most of the time, the MBS is expressed by the static sensitivity, which neglects changes in glacier size and geometry (e.g. Anderson and others, 2010; Braithwaite and Zhang, 1999; Oerlemans and Fortuin, 1992; De Woul and Hock, 2005). Formerly, also analytical studies have revealed the mass change of glaciers due to climate change (Kuhn, 1980). With the long-term records of mass balance and climate data being available today, it is also possible to derive the MBS directly by dividing observed changes in mass balance by observed changes in *T* or *P* (e.g. Braithwaite and others, 2013).

A recent study by Bolch and others (2013) has derived mass changes of the GIC in Greenland over the 2003-2008 period using ICESat data and revealed high mass losses in the south-east and much lower changes towards the north. This pattern might be related to the climatic sensitivity of the glaciers in these regions but also to their MBS. Both sensitivities are expected to change from the more wet and relatively warm south of Greenland to the dry and cold north (Hanna and others, 2012). However, this has not been analyzed so far as long-term measurements of mass balance and modeling studies were missing apart from Mittivakkat Glacier in southeastern Greenland where measurements are available since 1995 (Mernild and others, 2011).

The aim of this study is to determine whether the variability in climate can explain the spatial variability of the observed mass changes over the 2003-2008 period, i.e. if a correlation with long-term means and/or changes in *T* and *P* exist. The special challenge is to obtain useful data of *T* and *P* for all of Greenland. As weather stations (WS) are sparse and mainly located along the coast in low-lying regions (Mernild and others, 2013), they cannot be used for the GIC. We thus extracted *T* and *P* over all glacierized regions (with the Greenland Glacier Inventory by Rastner and others, 2012) from physically downscaled ERA-Interim re-analysis data for the 1980-2011 period using the RACMO2 Regional Climate Model (RCM) (Van Meijgaard and others, 2008). We further calculated annual, summer and winter mean values of *T* and *P* as an average for each of the ten sectors as used by Bolch and others (2013) for a direct comparison with the mass changes in each sector. Though this regional scale averaging per sector can be seen as a strong smoothing of the local scale variability (e.g. Anderson and Mackintosh, 2012), it is justified for the purpose of analyzing the large-scale variability for entire Greenland. It helps also to overcome the resolution gap between the RCM grid cells (11 km) and the size of individual glaciers (that are often smaller).

2. Study region

Greenland is located between 59° and 83° N and 11° and 74° W. The region is dominated by its large ice-sheet that is surrounded by numerous glaciers and ice caps (Citterio and Ahlstrøm, 2013; Rastner

and others, 2012; Weidick and Morris, 1998). This study focuses on the GIC's of Greenland that are either completely disconnected or only weakly connected to the ice sheet according to Rastner and others (2012). The largest number of GICs is found in the East of Greenland (~58'000 km²) and the smallest in the North West (~6'000km²) (Fig. 1). The area distribution of the glaciers is rather uneven: those smaller than 0.5 km² contribute only 1.5% to the total area (~2000 km²), but more than 50% to the total number, while the 24 largest (all > 500 km^2) contribute 38% to the total area (~36'800 km^2), but only 0.1% to the total number. In the East sector most of the ice is located at elevations around 1700 m a.s.l. and around 1000 m a.s.l. in all other sectors (Rastner and others, 2012).

Greenland's climate is polar to sub-polar (Dahl-Jensen and others, 2009). Owing to the large latitudinal extension, glaciers exist in different thermal regimes. Whereas in the north of Greenland most GIC are cold, they are polythermal in the central part and in the south also temperate (Bull, 1963; Hammer, 2001). The earliest monitored temperature time series started in 1880 and two stations exist with a measuring record exceeding 100 years: Nuuk (old name: Gothåb) and Tasiilaq (Ammassalik) (Chylek and others, 2006). A more dense weather station network was initiated in the 1970s (Cappelen and others, 2011). Temperature measurements demonstrate a recent warming trend of about 2-4°C (over the last three decades) particularly in West Greenland, primarily driven by winter temperature anomalies (Hanna and others, 2012). At the same altitude and latitude the climate at the eastern coast of Greenland is colder compared to the western side (Fausto and others, 2009; Steffen and Box, 2001). This difference is related to the cooling effect of the sea ice that is present along the north and northeast of Greenland, the cold East Greenland Current (Holfort and others, 2008), and the advection of cold air by down-slope winds from the ice sheet (Cappelen, 2001; Ettema and others, 2010; Scorer, 1988). During winter time, the absence of sunlight results in very low mean temperatures (< -30°C) in northern regions whereas in the summer temperature rises above the freezing point in all regions. The accumulation pattern shows high precipitation rates in the South-east (2000-2500 mm/a^{-1}) that decline towards higher latitudes reaching only 100-200 mm in the north-east. A decrease of precipitation from the sea towards the inland can be assumed from the steadily increasing median elevation of individual glaciers (Rastner and others, 2012). However, precipitation information in Greenland is uncertain as it is only roughly captured by the sparse measurements having a biased distribution (Bales and others, 2009; Burgess and others, 2010) and regional climate modeling (Box and others, 2006; Ettema and others, 2009; Fettweis and others, 2008; Fettweis and others, 2013).

3. Data

3.1 Glacier Data

From the newly established Greenland glacier inventory we only used the glaciers with a connectivity level (CL) 0 (not connected to the ice sheet) and CL1 (weakly connected). Marine and land terminating glaciers were not distinguished as their average mass losses were similar (Bolch et al., 2013) and only smaller marine terminating glaciers are included in the CL0 and CL1 sample. The glacier outlines were resampled with a nearest neighbor interpolation to 1 km resolution and reprojected to the polar stereographic projection for the appropriate geolocation of all input data. As a result, 1519 local GIC with a too small area were removed, so that finally 17'804 glaciers were included in the calculations.

Volume and mass change data of the local GIC around Greenland were obtained from the elevation change (Δh) measurements of the ICESat Geoscience Laser Altimeter System (GLAS) in combination with the glacier outlines and represent mean values for the period from October 2003 to March 2008 (Δt) (Bolch and others, 2013). The point data from ICESat were up-scaled to the entire glacier area using elevation dependent Δh curves and the area-elevation distribution of the glaciers. For the conversion from volume changes (ΔV) to mass changes (ΔM), a specific correction for firn compaction and density was applied for each of the ten sectors (cf. Bolch and others, 2013).

3.2 Climate data

The RCM RACMO2 was used to downscale ERA-Interim data and obtain daily values of *T* and *P* over Greenland for the 32 years from 1980 to 2011. The model has a horizontal resolution of 11 km and considers sea surface temperature and sea ice extent at the lower boundary (cf. Van Meijgaard and others, 2008). RACMO2 is currently one of the most sophisticated RCMs for Greenland as a physical snow model is included that considers surface albedo as a function of snow/firn/ice properties, as well as melt water percolation, retention and refreezing (Bougamont and others, 2005).

Additionally, data from 25 long-term (covering at least more than 20 years) synoptic weather stations (WS) from the Danish Meteorological Institute (DMI) were selected with at least one station being present in each sector) to validate the RACMO2 temperature data (Fig. 1). Unfortunately, only two WS (Dye 1 and Renland) with short measuring periods (< 9 years) are available for mountainous regions. All other stations are located directly at the coast.

Fig. 1: The local GIC (CL0 & CL1) and the defined sectors with their weather stations.

3.3 Digital elevation model (DEM)

We used the DEM of the Greenland Ice Mapping Project (GIMP) as provided by Howat and others (2014) and a supplementary tile from the website viewfinderpanoramas.org in the far north of Greenland, which was not covered by the GIMP DEM. The version of the GIMP DEM that was used here has a resolution of 90 m and a reported vertical accuracy of 10 m. It was merged from several datasets acquired between the years 2000 and 2009 and mostly derived with photogrammetric techniques from optical satellite data (the ASTER GDEM). Hence, it provides accurate results only in regions with good optical contrast and is less accurate above the snowline (Howat and others, 2014; Rastner and others, 2012). However, all calculations are performed at a resolution of 1 km so that the internal errors of the GIMP DEM are negligible. Additionally, the RACMO2 internal 11 km resolution DEM has been used to adjust elevation-dependent variables. Due to the coarser cell size, the topography of the RACMO2 DEM is stronger smoothed and elevation values are different from the GIMP DEM.

4. Methods

4.1 Climate data

Annual, summer (June to August) and winter (September to May) averages of mean temperature and precipitation sums were calculated for all ten sectors under the glacier mask (see Fig. 5 for processing flow chart). This calculation included a resampling (nearest neighbor) from 11 km to 1 km resolution

of the daily RACMO2 data and a reprojection from geographic coordinates to polar stereographic projection.

Specific lapse rates were calculated for each sector and the three time periods as a fixed standard lapse rate (e.g. of 6.5 K km^{-1}) would likely cause poor results (Marshall et al., 2007). We first selected only RACMO2 *T* values where the elevation difference to the GIMP DEM (also resampled to 1 km) was within ±80 m. This eliminated 18% of the cells with glaciers. Subsequently the GIMP DEM was re-classified into 100 m elevation bands and a mean temperature value was derived for all selected grid cells in each elevation bin, time period and sector. Finally, a regression analysis was applied to obtain the specific lapse rate for each sector from the respective regression coefficient (Table 1).

Table 1: Retrieved specific lapse rates per sectors in K/km.

This specific temperature lapse rate was used to adjust the original RACMO2 temperature data to the elevation of the GIMP DEM. We restricted the application of the correction to elevation differences of ±200 m to reduce the impact of a wrong lapse rate for larger DEM differences.

Precipitation data from RACMO2 has not been corrected due to its likely high spatial and temporal variability at a regional scale and the well-known uncertainties of the measurements in rough topography (Braithwaite and Raper, 2002; Sevruk and others, 2009). Moreover, the distances from the coastal stations to the glaciers were too large and much of the precipitation more inland is of orographic origin and hence underestimated by the WS near sea level (Ettema and others, 2010). Also wind and avalanches have a strong impact on the snow distribution in rough topography and influence accumulation patterns and amounts (Machguth and others, 2006; Plattner and others, 2004; Escher-Vetter et al., 2009). Taken together, these uncertainties result in unknown rules to be applied for correcting the data. We also compared RACMO2 *P* was compared to in-situ WS data from DMI. Due to limited data availability only 11 out of 25 WS were considered for this inter-comparison. The results reveal a mean difference of only 55 mm, however, with a standard deviation of 200.6 mm.

The RACMO2 temperature values were also compared to WS data (mean values and trends) using the specific lapse rates to compensate for the elevation differences. For the overlapping time period (1980- end of WS data) the mean values and the trends were compared. All WS data have been checked for outliers, data gaps and repeated dates. These WS values were masked out and not considered for the calculation of the mean for each period from all WS available in each sector. If several stations were available in one sector, we calculated the mean of all the WS and compared the mean value to the obtained RACMO2 mean *T* of all coinciding pixels.

The comparison of RACMO2 to WS data revealed a mean annual bias for *T* of 1.19 K (σ: 1.16 K), for summer of -2.46 K (σ: 0.96 K) and for winter of 2.77 K (σ: 1.46 K). The bias for the two high altitude WS (Dye 1 and Renland) is higher compared to the low lying WS. The annual, summer and winter bias for Dye 1 is 4.1°C, 9.1°C and 1.9°C whereas for Renland it is 1.1°C, 4.6°C and -3.1°C. Figure 2 shows the observed and modeled 2 m annual mean temperature value (1980 – 2011) for four selected long term DMI WS representing different climatological settings. Regarding the temperature trend analysis (cf. next section for the defined time intervals) of the two datasets, only a small difference was found for the slope of each regression analysis. This implies that the model closely follows the observed temperature over the measurement period.

Fig. 2: Observed and modeled T for four weather stations in Greenland.

4.2 Temperature and precipitation for GICs in Greenland obtained from RACMO2

Mean annual and seasonal *T* and *P* values and their changes for all sectors are listed in Table 2 and annual values are visualized in Figs. 3 and 4. The highest mean annual *T* and winter *T* values are found in the two southeast sectors (-7 °C) whereas during the summer the West-north sector is the warmest. Comparing precipitation in the three time periods, in all sectors most of it falls in winter (up to 87% in sector East-south). During summer, only two regions (South-west and South-east) receive amounts above 300 mm, whereas in winter, they receive more than 1000 mm (South-east >1700 mm) and all others receive less than 400 mm.

Fig. 3: Mean annual temperatures and precipitation from 1980-2011 per sector.

Trends in mean annual temperature are visualized in Fig. 4a. As can be seen from the values in Table 2, the warming trend is much larger for winter (about ~ 1.8 °C) than for summer temperatures (about 1 °C). This positive temperature trend is also confirmed by other studies (Mernild and others, 2012; Yde and Knudsen, 2007). The trend is particularly notable in the West (Van As, 2011; Box and others, 2009; Hanna and others, 2012) along the Baffin Bay coast. The increase in *T* is larger by a factor of two (0.2 °C a^{-1} since the beginning of the measurements in 1981) than recorded at the more northerly Pittufik and Daneborg WS on the east coast (Van As, 2011). Precipitation increased, especially in the winter months, by more than 15% in the west and by about 10% in three other sectors (Table 2). Summer precipitation decreased in the two southeastern sectors (> -5%) and in North-central (-10%), but all changes are statistically not significant and a clear pattern for the annual changes does not emerge (Fig. 4b). This missing trend in mean annual precipitation for all regions in Greenland has also been obtained by several other studies (e.g. Box and others, 2013; Burgess and others, 2010; Shen and others, 2012).The strong latitudinal gradient of precipitation with a decrease from South-east to North-west (Shen and others, 2012) has also a longitudinal trend where the west side receives less precipitation in southern Greenland while it is the east side in the north.

Fig. 4: Mean annual temperature and precipitation change in percent between time int_a (1980-1995) and int_b (1996-2011) for all sectors.

Table 2: Mean temperatures, temperature change, precipitation sum and precipitation change for all sectors and periods.

4.3 Statistical analysis of the climate and mass-balance sensitivity

Changes in *T* and *P* over the 32-year period were derived by calculating mean values for two distinct time intervals 1980-1995 (int_a) and 1996-2011 (int_b) and subtracting them. The “statistical significance“ of the change was determined according to Chylek and others (2006), stating that the difference in *T* and *P* of int_a and int_b is higher than the sum of the standard deviations of the two means in the respective periods.

Relations of *T* and *P* to observed mass (and volume) changes were investigated for all three temporal averaging periods (annual: index a, summer: jja, winter: s-m) by linear regression of the sectorial RACMO2 mean temperature (T_{mean}), temperature change (T_{change}), mean precipitation (P_{mean}), and

precipitation change (P_{change}) to the ICESat volume (ΔICE_{vol}) and mass changes (ΔICE_{mas}) obtained by Bolch and others (2013). Mass-balance sensitivity per 1 K temperature increase was derived by dividing the specific ΔICE_{mas} obtained by ICESat with the T_{change} and P_{change} per sector. This assumes that mass balance was about zero in int_a, which was probably not the case as Kjaer and others (2012) indicate. The already negative mass balances in this period imply that the derived MBS are upper bound values.

Fig. 5: Flow chart of the applied steps performed in this study.

5. Results

5.1 Correlation analysis und sensitivities

The changes in glacier mass and volume can be best explained by T_{mean}, followed by P_{mean} (Fig. 6), T_{change} and P_{change} (Fig. 7) according to the regressions with the climate data described above. While T_{mean} explains 69% (R^2 = 0.69) of the spatial variability in glacier volume change, P_{mean} explains 56% (R^2 = 0.56). The null hypothesis of insignificant correlations can be rejected for T_{mean} by P of 4.5^{-18} and P_{mean} by P of 0.003 (confidence interval 95%). Due to their particular characteristics the two sectors South-east and East-south exhibit a strong influence on the regression line and the correlation coefficient. Without these two sectors, correlations would be close to zero and might even have opposite trends (Fig. 7a). The interpretation of correlation and trends should thus not be overestimated. The lower correlation of P_{mean} (Fig. 6 b) is largely a result of the extreme value of the sector South-west. The correlation of T_{change} with ΔICE_{vol} is also significant (Fig. 7 a), but the conclusion the higher annual temperature change the *lower* the volume loss, is reversed when excluding both sectors to the more reasonable the higher the annual temperature change (T_{change}) the *higher* the mass loss. The regression of P_{change} against ΔICE_{vol} results in a sensible positive correlation but is statistically not significant. The correlation with ΔICE_{vol} would be close to zero without the two south-eastern sectors. The low coefficient for P_{change} has been expected because precipitation changes are not very pronounced (from -3.1% to +7.1%) and need to be considerably larger to have a similar impact on mass balance as the observed changes in T. Differences in P_{change} might also explain some of the residuals in the significant correlations.

Fig. 6: Linear regression analysis for T_{mean} and P_{mean} with ΔICE_{vol}.

Fig. 7: Linear regression analysis for T_{change} and P_{change} with ΔICE_{vol}.

Correlation coefficients for summer temperatures and their changes with volume changes are small (Fig. 8). The correlation of $T_{change\text{-}jja}$ against ΔICE_{vol} does not result in a significant correlation as it is the case when analyzing T_{change}. The reason is that summer warming in Greenland is quite uniform (Fig. 4b) whereas differences in T_{change} are mainly subject to a north-south gradient in winter warming. Although correlation of $T_{change\text{-}jja}$ to ΔICE_{vol} is insignificant, regional differences in $T_{change\text{-}jja}$ might be useful to explain some of the residuals in the regressions T_{mean}-ΔIce_{vol} and P_{mean}-ΔIce_{vol}. The correlation for winter temperatures $T_{mean\text{-}s\text{-}m}$ (R= -0.83) and its changes $T_{change\text{-}s\text{-}m}$ (R= 0.68) is much higher (Figs. 9a, b). The plots however, are highly similar to the annual plots in Fig. 6 due to the allocation of 9 months to represent winter. As mentioned above, the East-south and South-east sector have also here rather extreme values with a rather strong influence on the regression.

Fig. 8: Mean summer temperature and temperature change in °C between time int_a (1980-1995) and int_b (1996-2011) for all sectors.

Fig. 9: Mean winter temperature and temperature change in °C between time int_a (1980-1995) and int_b (1996-2011) for all sectors.

The mass-balance sensitivity to a temperature increase of 1 K is high in the sectors South-east (-1.23 m w.e. yr^{-1} K^{-1}) and East-south (-0.77 m w.e. yr^{-1} K^{-1}) and much lower for all other sectors (Table 3 and Fig.10). The MBS is particular low in the North-east and North-central sectors (which was expected from the dry and cold climate in this region, see Fig. 3), but interestingly the West-central sector also has a very low sensitivity. The mean value for all sectors is -0.35 m w.e. yr^{-1} K^{-1} with a standard deviation of 0.37 m w.e. yr^{-1} K^{-1}. The MBS in regard to a 10% precipitation change derived from the observed P_{change} values has not been retrieved as P_{change} were not significant in the last three decades on Greenland.

Table 3: Changes in observed mass balance and T for the period 1980 -2011 for CL0-CL1 GIC. Δb is the change in mass-balance observed by ICESat, ΔT is the change in average T per period, Δb/ΔT is the MBS.

Fig. 10: Mass balance sensitivity to a 1 K temperature increase per sector.

Correlations between ΔICE_{vol} and T and P were in general higher for ΔICE_{vol} than for ΔICE_{mas} (Table 4, Fig. 6-9). This might be related to the conversion from volume to mass change using some uncertain assumptions for the density of firn and ice and for firn compaction (Bolch and others, 2013).

Table: 4 Correlation results for each period of $\Delta ICE_{vol}/T_{mean}$ and $\Delta ICE_{mas} / T_{mean}$ versus $\Delta ICE_{vol} / P_{mean}$ and $\Delta ICE_{mas} / P_{mean}$ per period.

5.2 Residuals of individual regions

West-central has the largest residual from the T_{mean}-ΔIce_{vol} regression with a comparably low loss in volume and a relatively high T_{mean} (Fig. 6a). Furthermore, volume changes of West-central and North-east are almost identical. However, increase in $T_{change\text{-}jja}$ is more pronounced at West-central than in the North-east. The latter one is expected to react less sensitive to higher temperature because of lower T_{mean}. The similarity of the mass loss in the two regions and the relatively large residual of West-central might be related to the largest precipitation increase of all regions (Fig. 7b). The residual of South-west is similar to West-central and again there is a region (East-central) that shows almost the same ΔIce_{vol} at a lower T_{mean}. The difference here might be explained by $T_{change\text{-}jja}$ being clearly more pronounced at East-central (Fig. 8b).

Climatological P_{mean} (Fig. 6b) achieves a lower score in explaining volume changes compared to T_{mean}. This is mainly the case because of one strong outlier, South-west, where a large P_{mean} coincides with a comparably low ΔIce_{vol}. An explanation might be the second lowest $T_{change\text{-}jja}$ observed for the same region (Fig. 7a). Following this argumentation one might also expect East-south to be an outlier due to similar P_{mean} and changes in $T_{change\text{-}jja}$. However, East-south is the region with the lowest P_{change} which might explain the larger volume loss compared to South-west.

6. Discussion

6.1 Glacier sensitivity

All regression coefficients and the represented correlations (Figs. 6 to 8) are influenced by special values of two rather particular sectors, namely the South-east and East-south. These two sectors have always more extreme values than the other sectors in Greenland. Removing the two sectors from the calculation would result in rather different regression equations and - coefficients. The equations are thus most of the time not suitable for any statistical interpolations.

The higher correlation with climatic mean values appear to contradict the experience that changes in summer *T* are the major force of glacier mass changes (Oerlemans and Reichert, 2000). While $T_{change\text{-}jja}$ was in the range of 1 K between 1980 and 2011 (Table 2), it had virtually no correlation with the observed mass and volume changes (R=0.06, Fig. 8). Summer warming on Greenland was rather uniformly distributed while the changes in glacier volume and mass were not. Although summer warming is a major driving force for glacier changes, the non-uniform distribution of the latter is due to differing climate-sensitivities of the glaciers in the different regions of Greenland. This interpretation is in line with previous modeling studies showing that changes in glacier volume are best explained from annual precipitation (Oerlemans and Fortuin, 1992) or continentality (temperature amplitude of the maximum and minimum value in one mass balance year) (Schneeberger and others, 2003). Changes in annual or winter *P* could also have an impact, but they were small and not significant (Table 2). We thus propose that the climate sensitivities of the glaciers are controlling the observed mass change pattern in Greenland. This interpretation was also shown in other modeling studies using mass balance gradients derived from annual precipitation sums for modelling of volume changes (Oerlemans, 2005) and it confirms the assumption by Bolch and others (2013) that the pattern of the high mass (and volume) losses observed in Greenland could be related to P_{mean}.

As mentioned above, the MBS derived here for a 1 K temperature increase must be seen as an upper bound value as the mass balance in the first period (int_a) was possibly already negative. In this regard our results are comparable to other studies, like Dyurgerov (2003) who derived a mean MBS of -0.7 m w.e. yr^{-1} K^{-1} for the northern hemisphere and De Woul and Hock (2005) who obtained values of -0.44 m w.e. yr^{-1} K^{-1} for glaciers in Svalbard and -1.63 m w.e. yr^{-1} K^{-1} for (the much more maritime) Icelandic glaciers. Comparing our results for entire sectors to an individual glacier like Mittivakkat Glacier can be seen as a far stretch but the MBS of -1.2 m w.e. yr^{-1} K^{-1} (using an annual net loss of -0.97 ±0.75 m w.e. yr^{-1} for the 1995/96–2010/11 period; Mernild and others, 2013) in good agreement with the -1.23 m w.e. yr^{-1} K^{-1} derived in this study for the South-east sector. Finally, we have to note that the observed changes in mass and volume over the 2003 to 2008 period are, of course, related to the climatic conditions over the same period. This increases the risk of incorporating individual warm or cold summers (dry or wet years) covering the impact of a general trend in *T* or *P*. This is of particular relevance because in the last decades several meteorological records were documented for Greenland, for example nine of the ten warmest summers have occurred since the year 2000 (Hanna and others, 2013). We thus performed a statistical analysis to investigate the difference of the 32 years time period and the short time period (2003-2008) of $T_{\text{-(2003-2008)-mean-jja}}$, $T_{\text{-(2003-2008)-mean}}$ and $P_{\text{-(2003-2008)-mean}}$ with ΔICE_{vol} which revealed only small changes in the correlation coefficients ($T_{\text{-(2003-2008)-mean-jja}}$ R= -0.29, $T_{\text{-(2003-2008)-mean}}$ R= -0.82, $P_{\text{-(2003-2008)-mean}}$ R= -0.70). The

mean temperature bias of the short time period ($T_{\text{-(2003-2008)-mean}}$) to the long time period (T_{mean}) is 1.48 K higher. Hence, explaining the spatial pattern of their variability (not the absolute values) with the prevailing climatic conditions is likely only an intermediate option before more detailed studies are becoming available.

The obtained climate- and mass-balance sensitivities in this study have to be interpreted with care as they rely on static sensitivities (Braithwaite and Zhang, 1999; De Woul and Hock, 2005). For example, a temperature increase is likely accompanied by a change in the glacier geometry. Geometry changes influence the results also from another aspect as they vary between the regions and might blur the investigated relationship of glacier changes and climate. The most pronounced contrast exists between the east and north where ice caps dominate and the South-east where mostly valley-type glaciers are found. The latter are more independent of the accumulation regime as they will have an accumulation area as long the equilibrium line altitude (ELA) is not above the maximum elevation of the mountain range. Ice caps on the other hand, are more prone to self-reinforcing negative mass balances once the ELA is above their highest elevation since mass loss would result in a general surface lowering that might lead to a complete loss of accumulation area and down wasting (the mass-balance elevation feedback) (Evans and Cox, 2005; Raymond and others, 2005; Paul, 2010). Observations of the ice caps indicate stable or even growing elevations in the accumulation areas (Bolch and others, 2013; Rinne and others, 2011) indicating that the above scenario can currently be excluded.

6.2 Input data and sectors

Strong precipitation gradients from the coast towards the ice sheet are confirmed by several studies (Burgess and others, 2010; Bales and others, 2009; Rastner and others, 2012) but were not considered in this analysis due to sector averaging. This might influence the signal in two ways. On the one hand, sectors can reinforce the signal, by smoothing out individual glacier sensitivities. On the other hand, local patterns are not addressed. For this reason we have not compared the sector averages to results from individual glaciers.

The correlations in this study revealed better results with Δ_{vol} than Δ_{mas} suggesting that the conversion from volume to mass using firn and ice density assumptions as well as densification modeling introduces additional errors. The determination of a density value for converting Δ_{vol} into Δ_{mas} is a well-known problem as it depends on the time period, the climatic regime and its location (Escher-Vetter and others, 2009; Huss, 2013; Zemp and others, 2013). So for instance a higher densification can be expected in the wetter and warmer south-east and a lower one in the dryer and colder north. The latter problem is also confirmed by the two independent studies of Bolch et al. 2013 and (Gardner and others, 2013) which analyzed volume and mass changes of the local GIC in Greenland. The results of both studies are in accordance for Δ_{vol} however for Δ_{mas} they are not.

A main limitation of RACMO2 is its resolution of 11 km, which is too coarse for resolving the local GIC on Greenland. This also impacts on the internal land cover map where GIC are often treated as land surface, leading to higher T values in the model. A related large T bias at the margin of the ice sheet is also mentioned in the study of Ettema and others (2010), reporting deviations of more than 4 K.

The application of the here calculated specific lapse rates increased the correlation coefficient, for example between Δ_{vol} and T_{mean} from R=0.74 (using a standard lapse rate) to R=0.83. This underlines,

406 that our method to retrieve specific lapse rates is promising. However, specific lapse rates have to be
407 treated with care, as cold air pooling and temperature inversions (Minder and others, 2010) are
408 common in Greenland (and thus not considered). Notwithstanding our values are in line with other
409 studies from the Arctic (Marshall and others, 2007; Minder and others, 2010) revealing a significant
410 change throughout the year.

411 7. Conclusion

412 We analyzed time series of *T* and *P* (physically downscaled re-analysis data) from 1980 to 2011 above
413 the GIC in Greenland, to determine whether their mean values or trends are correlated with the
414 observed mass and volume losses (mean values for ten sectors) obtained by ICESat data. Mean
415 values in *T* and *P* show clear north-south and east-west patterns with extreme values often found in
416 two south-eastern sectors. Comparably high correlations (linear regression) of 0.69 for *T* and 0.56 for
417 *P* confirm the assumption that the large-scale variability in climatic mean values impact on the
418 observed volume changes (correlations were less good with mass changes). A strong temperature
419 increase during the winter months (dominating the annual signal), in particular for regions in the
420 north of Greenland, and only small changes in precipitation without a clear spatial pattern has been
421 observed. By dividing the mean mass balance by the observed temperature increase we derived
422 mass balance sensitivities that compare well to other regions, but need to be interpreted with care
423 as they refer to sector mean values and assume a zero mass balance before the temperature
424 increase took place. It is expected that in the future more regional studies using longer time series of
425 input data can add to the more general results obtained here and provide a more detailed picture of
426 the response of the GIC in Greenland to climate change.

427 8. Acknowledgements

428 This work was supported by the ESA project Glaciers_cci (4000101778/10/I-AM) and funding from
429 the ice2sea programme from the European Union 7th Framework Programme, grant number 226375.
430 Ice2sea contribution number 169. H. M. acknowledges funding from the Programme for Monitoring
431 of the Greenland Ice Sheet (PROMICE). We thank Michiel van den Broeke, IMAU, Utrecht for having
432 provided the RACMO2 RCM. P. R. acknowledges the marine and glaciology group from GEUS in
433 Copenhagen for enabling a research exchange and thus building the base for this study.

434

435 9. REFERENCES:

436 Anderson, B., and Mackintosh, A., 2012, Controls on mass balance sensitivity of maritime glaciers in
437 the Southern Alps, New Zealand: The role of debris cover. Journal of Geophysical Research, 117,
438 F01003.

439 Anderson, B., Mackintosh, A., Stumm, D., George, L., Kerr, T., Winter-Billington, A., and Fitzsimons, S.,
440 2010, Climate sensitivity of a high-precipitation glacier in New Zealand. Journal of Glaciology, 56, 195,
441 114–128.

Van As, D., 2011, Warming, glacier melt and surface energy budget from weather station observations in the Melville Bay region of northwest Greenland. Journal of Glaciology, 57, 202, 208–220.

Bales, R.C., Guo, Q., Shen, D., McConnell, J.R., Du, G., Burkhart, J.F., Spikes, V.B., Hanna, E., and Cappelen, J., 2009, Annual accumulation for Greenland updated using ice core data developed during 2000–2006 and analysis of daily coastal meteorological data. Journal of Geophysical Research, 114, D06116.

Bolch, T., Sandberg Sørensen, L., Simonsen, S.B., Mölg, N., Machguth, H., Rastner, P., and Paul, F., 2013, Mass loss of Greenland's glaciers and ice caps 2003-2008 revealed from ICESat laser altimetry data. Geophysical Research Letters, 40, 875–881.

Bougamont, M., Bamber, J.L., and Greuell, W., 2005, A surface mass balance model for the Greenland Ice Sheet. Journal of Geophysical Research: Earth Surface, 110, F4, F04018.

Box, J.E., Bromwich, D.H., Veenhuis, B.A., Bai, L.S., Stroeve, J.C., Rogers, J.C., Steffen, K., Haran, T., and Wang, S.H., 2006, Greenland Ice Sheet Surface Mass Balance Variability (1988-2004) from Calibrated Polar MM5 Output*. Journal of Climate, 19, 12, 2783–2800.

Box, J.E., Cressie, N., Bromwich, D.H., Jung, J.-H., van den Broeke, M., van Angelen, J.H., Forster, R.R., Miège, C., Mosley-Thompson, E., Vinther, B., and McConnell, J.R., 2013, Greenland Ice Sheet Mass Balance Reconstruction. Part I: Net Snow Accumulation (1600–2009). Journal of Climate, 26, 11, 3919–3934.

Box, J.E., Yang, L., Bromwich, D.H., and Bai, L.-S., 2009, Greenland Ice Sheet Surface Air Temperature Variability: 1840–2007*. Journal of Climate, 22, 14, 4029–4049.

Braithwaite, R.J., and Raper, S.C.B., 2002, Glaciers and their contribution to sea level change. Physics and Chemistry of the Earth, Parts A/B/C, 27, 32, 1445–1454.

Braithwaite, R.J., Raper, S.C.B., and Candela, R., 2013, Recent changes (1991–2010) in glacier mass balance and air temperature in the European Alps. Annals of Glaciology, 54, 63, 139–146.

Braithwaite, R.J., and Zhang, Y., 1999, Modelling changes in glacier mass balance that may occur as a result of climate changes. Geografiska Annaler Series a-Physical Geography, 81A, 4, 489–496.

Braithwaite, R.J., and Zhang, Y., 2000, Sensitivity of mass balance of five Swiss glaciers to temperature changes assessed by tuning a degree-day model. Journal of Glaciology, 46, 152, 7–14.

Bull, C., 1963, Glaciological reconnaissance of the Sukkertoppen ice cap, south-west Greenland. Journal of Glaciology, 21, 813–817.

Burgess, E.W., Forster, R.R., Box, J.E., Mosley-Thompson, E., Bromwich, D.H., Bales, R.C., and Smith, L.C., 2010, A spatially calibrated model of annual accumulation rate on the Greenland Ice Sheet (1958–2007). Journal of Geophysical Research, 115, F2, F02004.

Cappelen, J., 2001, The observed climate of Greenland, 1958-99: with climatological standard normals, 1961-90. Danish Meteorological Institute.

Cappelen, J., Laursen, E.V., Jørgensen, P.V., and Kern-Hansen, C., 2011, DMI monthly Climate Data Collection 1768-2006, Denmark, The Faroe Islands and Greenland. Technical Report 07-06.

Chylek, P., Dubey, M.K., and Lesins, G., 2006, Greenland warming of 1920–1930 and 1995–2005. Geophysical Research Letters, 33, 11.

Citterio, M., and Ahlstrøm, A.P., 2013, Brief communication "The aerophotogrammetric map of Greenland ice masses:" The Cryosphere, 7, 2, 445–449.

Dahl-Jensen, D., Bamber, J., Boeggild, C.E., Buch, E., Christensen, J.H., Dethloff, K., Fahnestock, M., Marshall, S., Rosing, M., Steffen, K., Thomas, R., Truffer, M., Van Den Broeke, M., and Van Der Veen, C.J., 2009, The Greenland ice sheet in a changing climate: snow, water, ice and permafrost in the Arctic (SWIPA) 2009. Artic Monitoring and Assessment Programme, Oslo, 121 p.

Dyurgerov, M., 2003, Mountain and subpolar glaciers show an increase in sensitivity to climate warming and intensification of the water cycle. Journal of Hydrology, 282, 1-4, 164–176.

Escher-Vetter, H., Kuhn, M., and Weber, M., 2009, Four decades of winter mass balance of Vernagtferner and Hintereisferner, Austria: methodology and results. Annals of Glaciology, 50, 87–95.

Ettema, J., van den Broeke, M.R., van Meijgaard, E., van de Berg, W.J., Box, J.E., and Steffen, K., 2010, Climate of the Greenland ice sheet using a high-resolution climate model – Part 1: Evaluation. The Cryosphere, 4, 4, 511–527.

Ettema, J., Van Den Broeke, M.R., Van Meijgaard, E., Van De Berg, W.J., Bamber, J.L., Box, J.E., and Bales, R.C., 2009, Higher surface mass balance of the Greenland ice sheet revealed by high-resolution climate modeling. Geophysical Research Letters, 36, L12501, L12501.

Evans, I.S., and Cox, N.J., 2005, Global variations of local asymmetry in glacier altitude: separation of northsouth and eastwest components. Journal of Glaciology, 51, 174, 469–482.

Fausto, R.S., Ahlstrom, A.P., Van As, D., Boggild, C.E., and Johnsen, S.J., 2009, A new present-day temperature parameterization for Greenland. Journal of Glaciology, 55, 189, 95–105.

Fettweis, X., Franco, B., Tedesco, M., van Angelen, J.H., Lenaerts, J.T.M., van den Broeke, M.R., and Gallée, H., 2013, Estimating the Greenland ice sheet surface mass balance contribution to future sea level rise using the regional atmospheric climate model MAR. The Cryosphere, 7, 2, 469–489.

Fettweis, X., Hanna, E., Gallée, H., Huybrechts, P., and Erpicum, M., 2008, Estimation of the Greenland ice sheet surface mass balance for the 20th and 21st centuries. The Cryosphere, 2.

Furbish, D.J., and Andrews, J.T., 1984, The use of hypsometry to indicate long term stability and response of valley glaciers to changes in mass transfer. Journal of Glaciology, 30, 105.

Gardner, A.S., Moholdt, G., Cogley, J.G., Wouters, B., Arendt, A.A., Wahr, J., Berthier, E., Hock, R., Pfeffer, W.T., Kaser, G., Ligtenberg, S.R.M., Bolch, T., Sharp, M.J., Hagen, J.O., and others, 2013, A reconciled estimate of glacier contributions to sea level rise: 2003 to 2009. Science, 340, 6134, 852–857.

514 Hammer, C.U., 2001, The Hans Tausen Ice Cap. Glacialogy and glacial geology.. Geoscience,
515 Meddelelser om Grønland, Copenhagen, 165.

516 Hanna, E., Jones, J.M., Cappelen, J., Mernild, S.H., Wood, L., Steffen, K., and Huybrechts, P., 2013, The
517 influence of North Atlantic atmospheric and oceanic forcing effects on 1900-2010 Greenland summer
518 climate and ice melt/runoff. International Journal of Climatology, 33, 4, 862–880.

519 Hanna, E., Mernild, S.H., Cappelen, J., and Steffen, K., 2012, Recent warming in Greenland in a long-
520 term instrumental (1881–2012) climatic context: I. Evaluation of surface air temperature records.
521 Environmental Research Letters, 7, 4, 045404.

522 Hock, R., Radić, V., and De Woul, M., 2007, Climate sensitivity of Storglaciaren, Sweden: an
523 intercomparison of mass-balance models using ERA-40 re-analysis and regional climate model data.
524 Annals of Glaciology, 46, 1, 342–348.

525 Hock, R., de Woul, M., Radić, V., and Dyurgerov, M., 2009, Mountain glaciers and ice caps around
526 Antarctica make a large sea-level rise contribution. Geophysical Research Letters, 36, 7, L07501.

527 Holfort, J., Hansen, E., Østerhus, S., Dye, S., Jonsson, S., Meincke, J., Mortensen, J., and Meredith, M.,
528 2008, Freshwater fluxes east of Greenland, *in* Arctic–Subarctic Ocean Fluxes, Springer, 263–287.

529 Howat, I.M., Negrete, A., and Smith, B.E., 2014, The Greenland Ice Mapping Project (GIMP) land
530 classification and surface elevation datasets. The Cryosphere Discussions, 8, 1, 453–478.

531 Huss, M., 2013, Density assumptions for converting geodetic glacier volume change to mass change.
532 The Cryosphere, 7, 3, 877–887.

533 Kjaer, K.H., Khan, S.A., Korsgaard, N.J., Wahr, J., Bamber, J.L., Hurkmans, R., van den Broeke, M.,
534 Timm, L.H., Kjeldsen, K.K., Bjork, A.A., Larsen, N.K., Jorgensen, L.T., Faerch-Jensen, A., and Willerslev,
535 E., 2012, Aerial photographs reveal late-20th-century dynamic ice loss in northwestern Greenland.
536 Science, 337, 6094, 569–573.

537 Kuhn, M., 1980, Climate and glaciers. IAHS Publication, 131, 3–20.

538 Kuhn, M., 1984, Mass budget imbalances as criterion for a climatic classification of glaciers.
539 Geografiska Annaler, 66, 3, 229–238.

540 Leclercq, P.W., and Oerlemans, J., 2011, Global and hemispheric temperature reconstruction from
541 glacier length fluctuations. Climate Dynamics, 38, 5-6, 1065–1079.

542 Machguth, H., Eisen, O., Paul, F., and Hoelzle, M., 2006, Strong spatial variability of snow
543 accumulation observed with helicopter-borne GPR on two adjacent Alpine glaciers. Geophysical
544 Research Letters, 33, 13, L13503.

545 Machguth, H., Rastner, P., Bolch, T., Mölg, N., Sørensen, L.S., Aðalgeirsdottir, G., van Angelen, J.H.,
546 van den Broeke, M.R., and Fettweis, X., 2013, The future sea-level rise contribution of Greenland's
547 glaciers and ice caps. Environmental Research Letters, 8, 2, 025005.

548 Marshall, S.J., Sharp, M.J., Burgess, D.O., and Anslow, F.S., 2007, Near-surface-temperature lapse
549 rates on the Prince of Wales Icefield, Ellesmere Island, Canada: implications for regional downscaling
550 of temperature. International Journal of Climatology, 27, 3, 385–398.

551 Van Meijgaard, E., Van Ulft, L.H., Van de Berg, W.J., Bosveld, F.C., Van den Hurk, B., Lenderink, G.,
552 and Siebesma, A.P., 2008, The KNMI regional atmospheric climate model RACMO version 2.1.
553 Koninklijk Nederlands Meteorologisch Instituut, 50 p.

554 Mernild, S.H., Knudsen, N.T., Hoffman, M.J., Yde, J.C., Hanna, E., Lipscomb, W.H., Malmros, J.K., and
555 Fausto, R.S., 2013, Volume and velocity changes at Mittivakkat Gletscher, southeast Greenland.
556 Journal of Glaciology, 59, 216, 660–670.

557 Mernild, S., Knudsen, N., Lipscomb, W., Yde, J., Malmros, J., Hasholt, B., and Jakobsen, B., 2011,
558 Increasing mass loss from Greenland's Mittivakkat Gletscher. The Cryosphere, 5, 341–348.

559 Mernild, S.H., Malmros, J.K., Yde, J.C., and Knudsen, N.T., 2012, Multi-decadal marine- and land-
560 terminating glacier recession in the Ammassalik region, southeast Greenland. The Cryosphere, 6, 3,
561 625–639.

562 Minder, J.R., Mote, P.W., and Lundquist, J.D., 2010, Surface temperature lapse rates over complex
563 terrain: Lessons from the Cascade Mountains. Journal of Geophysical Research, 115, D14, D14122.

564 Oerlemans, J., 2005, Extracting a Climate Signal from 169 Glacier Records. Science, 308, 5722, 675–
565 677.

566 Oerlemans, J., and Fortuin, J.P.F., 1992, Sensitivity of glaciers and small ice caps to greenhouse
567 warming. Science, 258, 115–117.

568 Oerlemans, J., and Reichert, B.K., 2000, Relating glacier mass balance to meteorological data by using
569 a seasonal sensitivity characteristic. Journal of Glaciology, 152, 46, 1–6.

570 Paul, F., 2010, The influence of changes in glacier extent and surface elevation on modeled mass
571 balance. The Cryosphere, 4, 4, 569–581.

572 Plattner, C., Braun, L.N., and Brenning, A., 2004, Spatial variability of snow accumulation on
573 Vernagtferner, Austrian Alps, in winter 2003/2004. Zeitschrift für Gletscherkunde und
574 Glazialgeologie, 39, 43–57.

575 Rastner, P., Bolch, T., Mölg, N., Machguth, H., Le Bris, R., and Paul, F., 2012, The first complete
576 inventory of the local glaciers and ice caps on Greenland. The Cryosphere, 6, 1483–1495.

577 Raymond, C., Neumann, T.A., Rignot, E., Echelmeyer, K., Rivera, A., and Casassa, G., 2005, Retreat of
578 Glaciar Tyndall, Patagonia, over the last half-century. Journal of Glaciology, 51, 173, 239–247.

579 Rinne, E.J., Shepherd, A., Palmer, S., van den Broeke, M.R., Muir, A., Ettema, J., and Wingham, D.,
580 2011, On the recent elevation changes at the Flade Isblink Ice Cap, northern Greenland. Journal of
581 Geophysical Research, 116, F3, F03024.

582 Schneeberger, C., Blatter, H., Abe-Ouchi, A., and Wild, M., 2003, Modelling changes in the mass
583 balance of glaciers of the northern hemisphere for a transient 2×CO2 scenario. Journal of Hydrology,
584 282, 1-4, 145–163.

585 Scorer, R.S., 1988, Sunny Greenland. Quarterly Journal of the Royal Meteorological Society, 114, 479,
586 3–29.

587 Sevruk, B., Ondrás, M., and Chvíla, B., 2009, The WMO precipitation measurement intercomparisons.
588 Atmospheric Research, 92, 3, 376–380.

589 Shen, D., Liu, Y., and Huang, S., 2012, Annual accumulation over the Greenland Ice Sheet interpolated
590 from historical and newly compiled observation data. Geografiska Annaler: Series A, Physical
591 Geography, 94, 3, 377–393.

592 Steffen, K., and Box, J., 2001, Surface climatology of the Greenland ice sheet: Greenland climate
593 network 1995-1999. Journal of Geophysical Research - Atmospheres, 106, D24, 33951–33964.

594 Vaughan, D.G., Comiso, J.C., Allison, J., Carrasco, J., Kaser, G., Kwok, R., Mote, P., Murray, T., Paul, F.,
595 Ren, J., Rignot, E., Solomina, O., Steffen, K., and Zhang, T., 2013, Observations: Cryosphere, *in* Climate
596 Change 2013: The Physical Science Basis. Contribution of Working Group I to the Fifth Assessment
597 Report of the Intergovernmental Panel on Climate Change [Stocker, T.F., D. Qin, G.-K. Plattner, M.
598 Tignor, S.K. Allen, J. Boschung, A. Nauels, Y. Xia, V. Bex and P.M. Midgley (eds.)], Cambridge
599 University Press, Cambridge University Press, Cambridge, United Kingdom and New York, USA, 317–
600 382.

601 Weidick, A., and Morris, E., 1998, Local glaciers surrounding the continental ice sheets: In: Haeberli,
602 W, Hoelzle, M., and Suter, S. (eds.), Into the second century of world glacier monitoring- prospects
603 and strategies. A contribution to the IHP and the GEMS. Prepared by the World Glacier Monitoring
604 Service UNESCO (Chapter 12), 197–207.

605 De Woul, M., and Hock, R., 2005, Static mass-balance sensitivity of Arctic glaciers and ice caps using a
606 degree-day approach. Annals of Glaciology, 42, 217–224.

607 Yde, J.C., and Knudsen, N.T., 2007, 20th-century glacier fluctuations on Disko Island (Qeqertarsuaq),
608 Greenland. Annals of Glaciology, 46, 209–214.

609 Zemp, M., Thibert, E., Huss, M., Stumm, D., Rolstad Denby, C., Nuth, C., Nussbaumer, S.U., Moholdt,
610 G., Mercer, A., Mayer, C., Joerg, P.C., Jansson, P., Hynek, B., Fischer, A., and others, 2013, Reanalysing
611 glacier mass balance measurement series. The Cryosphere, 7, 4, 1227–1245.

612

613

10. TABLES:

Table 1: The calculated specific temperature lapse rates for each sector in K/km (derived from RACMO2).

Zone	annual lapse rate	summer lapse rate	winter lapse rate
North-central	6.5	3.4	7.8
North-west	6.5	3.4	7.8
North-east	6.7	4.0	7.4
West-north	6.7	4.0	7.4
East-north	3.6	3.4	3.5
West-central	3.6	3.4	3.5
East-central	4.0	2.0	3.8
East-south	4.0	2.0	3.8
South-west	5.4	1.6	6.9
South-east	5.4	1.6	6.9

Table 2: Mean temperature, temperature change, precipitation and precipitation change for all sectors and summer and winter periods (derived from RACMO2). Annual values are depicted in the Figs. 3 and 4.

	Mean temperature [°C]		Temperature change [°C]		Mean Precipitation [mm]		Precipitation change [%]	
Zone	Winter	Summer	Winter	Summer	Winter	Summer	Winter	Summer
North-central	-33.6	2.4	2.0	0.9	162	98	12.9	-12.0
North-west	-30.4	3.8	2.2	1.0	229	189	16.5	-1.5
North-east	-30.9	4.0	1.9	0.6	206	71	8.2	-2.7
West-north	-26.3	7.0	2.4	1.3	277	157	16.1	0.3
East-north	-29.6	4.7	1.8	1.0	223	81	-3.5	4.2
West-central	-26.4	6.5	2.1	1.3	377	164	16.5	-0.2
East-central	-29.9	2.6	1.7	1.2	378	129	-0.4	2.3
East-south	-21.2	4.8	1.0	0.9	1171	168	-1.5	-8.0
South-west	-25.4	3.6	2.4	0.9	1077	325	9.9	-1.8
South-east	-18.6	4.9	0.9	0.9	1772	302	2.6	-6.8
Mean	-27.2	4.4	1.8	1.0	587	168	7.7	-2.6
SD	4.6	1.5	0.5	0.2	553	86	7.9	5.0

625

626 Table 3: Changes in observed mass balance and *T* for the period 1980 -2011 for CL0-CL1 GIC
627 (RACMO2). Δb is the change in mass-balance observed by ICESat, ΔT is the change in average *T* per
628 period, Δb/ΔT is the *T* sensitivity of observed mass balance and SD is the standard deviation of
629 observed mass balance.

		Annual
Zone	Δb (CL0-CL1) m yr^{-1}	Δb/ΔT m w.e. yr^{-1} K^{-1}
North-central	-0.11	-0.07
North-west	-0.41	-0.24
North-east	-0.2	-0.13
West-north	-0.5	-0.27
East-north	-0.43	-0.28
West-central	-0.2	-0.12
East-central	-0.28	-0.19
East-south	-0.71	-0.78
South-west	-0.39	-0.22
South-east	-0.99	-1.23
Mean	-0.42	-0.35
SD	0.26	0.37

630

631

632 Table 4: Linear regression analysis results for T_{mean} and P_{mean} with the ΔICE_{vol} ΔICE_{mas} averaged over
633 the 32 year time period.

	$\Delta ICE_{vol}/T_{mean}$	$\Delta ICE_{mas}/T_{mean}$	$\Delta ICE_{vol}/P_{mean}$	$\Delta ICE_{mas}/P_{mean}$
Summer	-0.34	-0.41	-0.49	-0.42
Winter	-0.83	-0.33	-0.76	-0.61
Annual	-0.82	-0.66	-0.74	-0.60

634

11 FIGURES

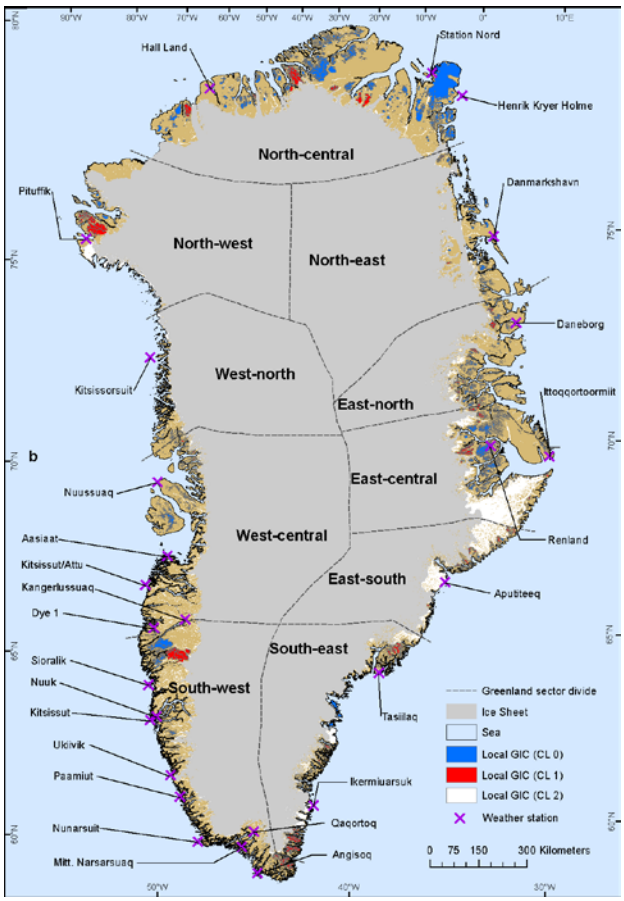

Fig. 1: The local GIC (CL0 & CL1) and the defined sectors with their weather stations.

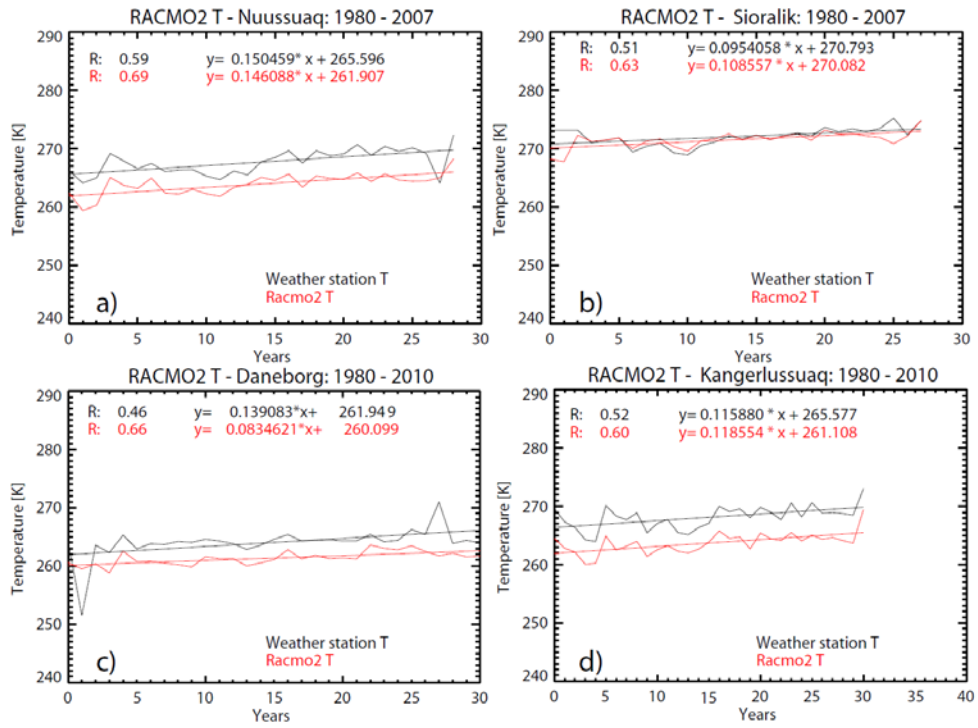

Fig. 2: Observed and modeled annual *T* for four weather stations in Greenland.

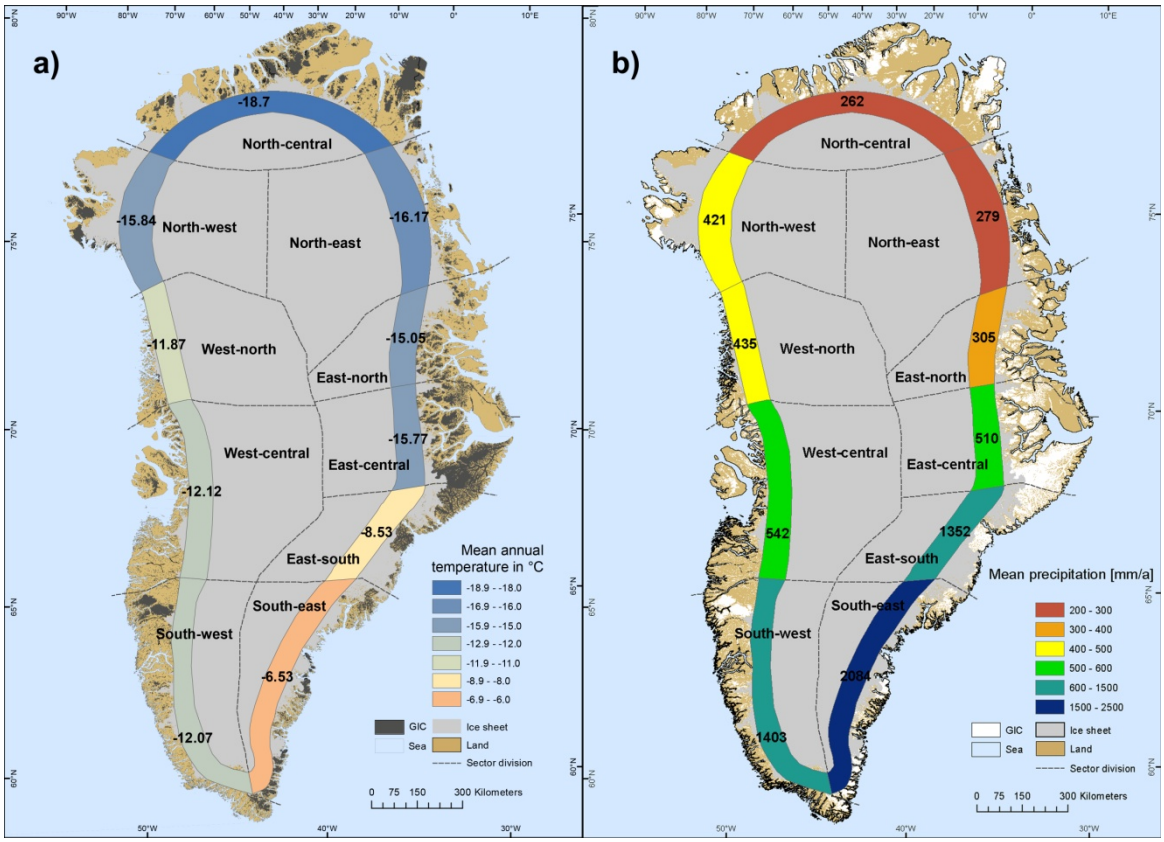

640

641 Fig. 3: Mean annual temperature (left) and precipitation (right) per sector as derived from RACMO2.

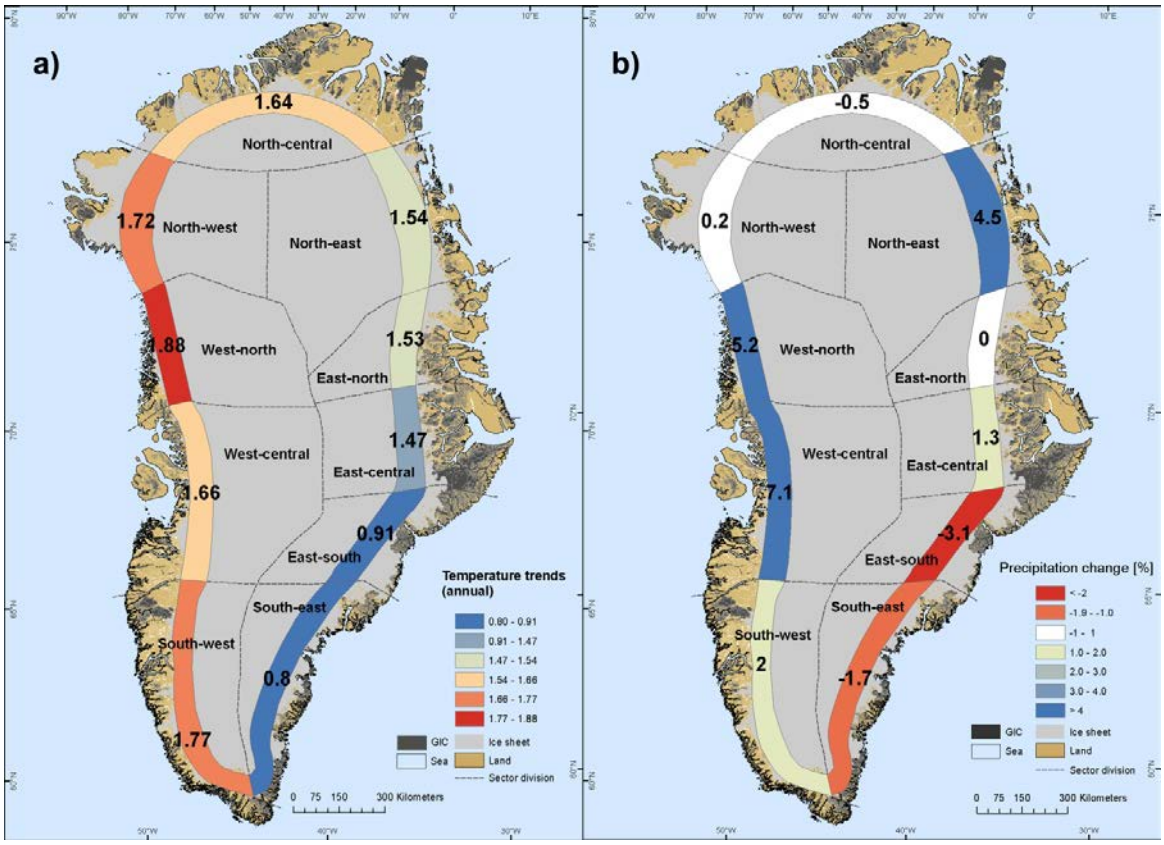

642

643 Fig. 4: Annual temperature and precipitation change for the two periods investigated as derived from
644 RACMO2.

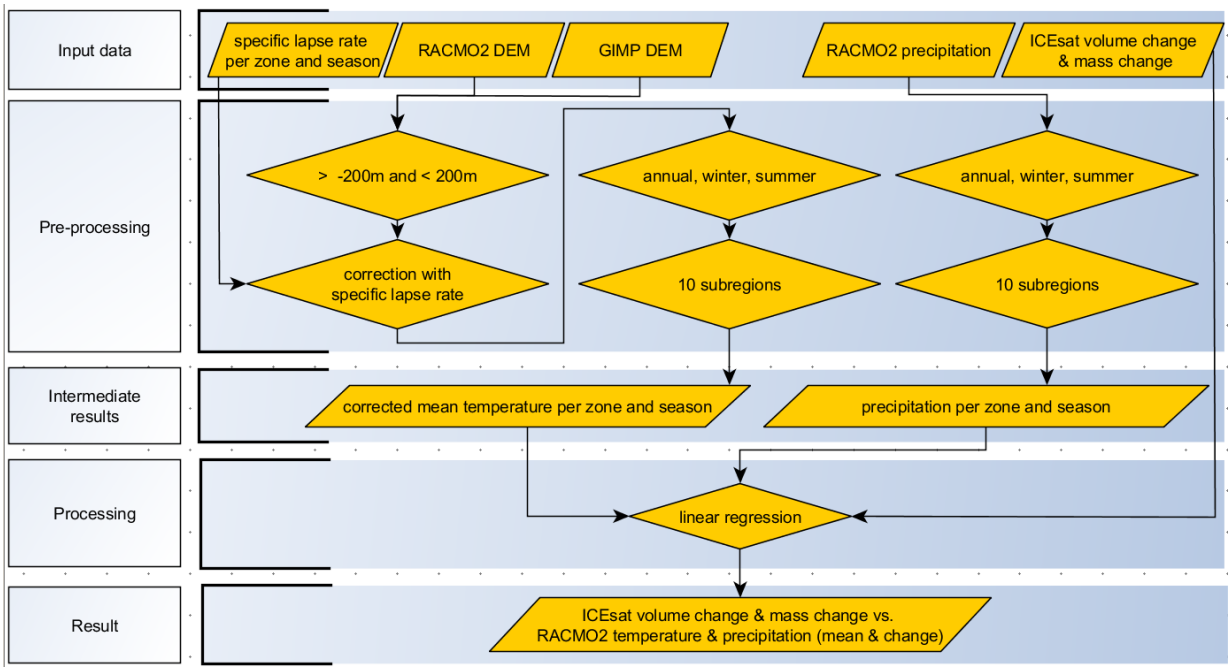

Fig. 5: Flow chart of the applied steps performed in this study.

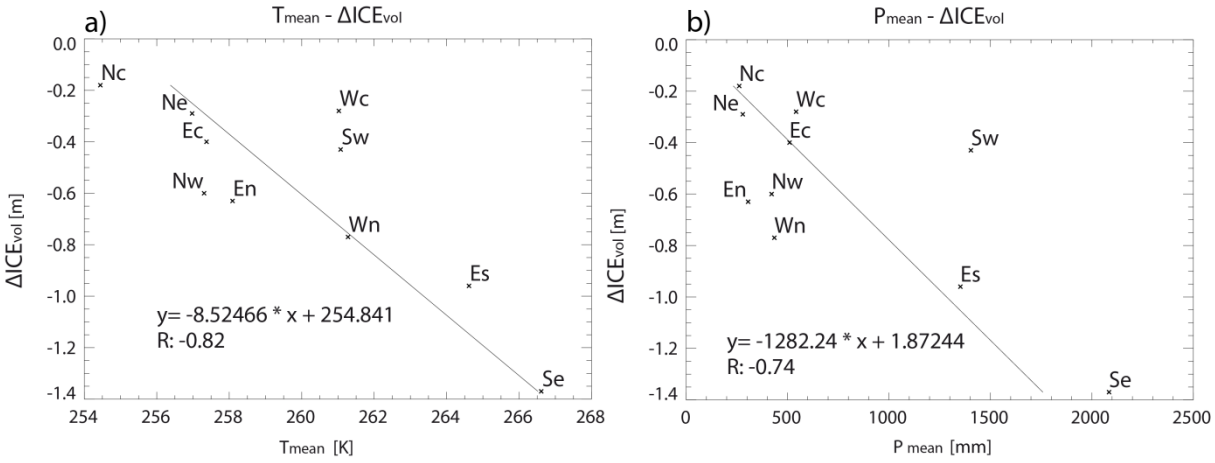

Fig. 6: Linear regression analysis for T_{mean} and P_{mean} with ΔICE_{vol}.

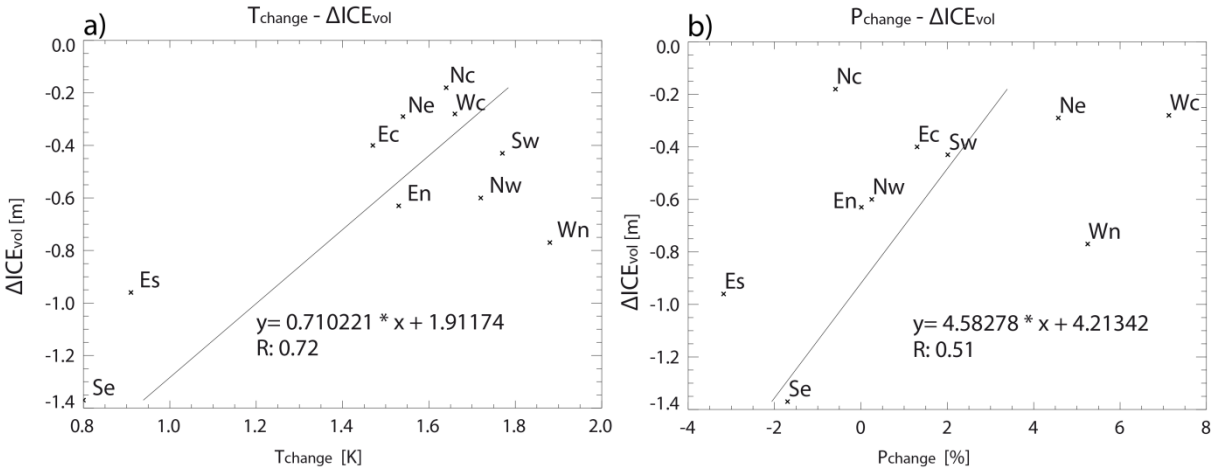

651

652 Fig. 7: Linear regression analysis for T_{change} and P_{change} with ΔICE_{vol}.

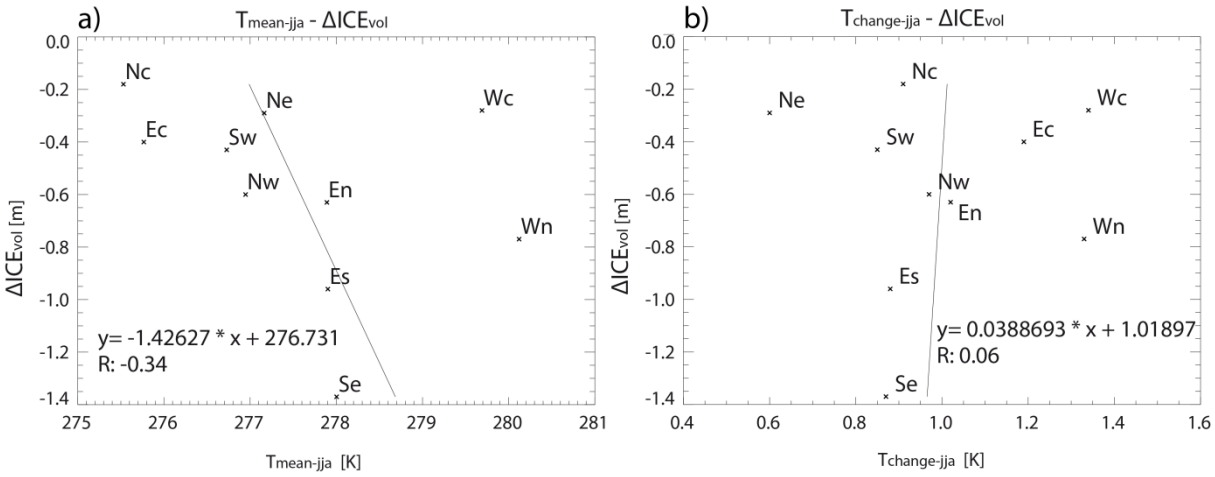

653

654 Fig. 8: Linear regression analysis of $T_{mean\text{-}jja}$ and $T_{change\text{-}jja}$ with the ΔICE_{vol}

655

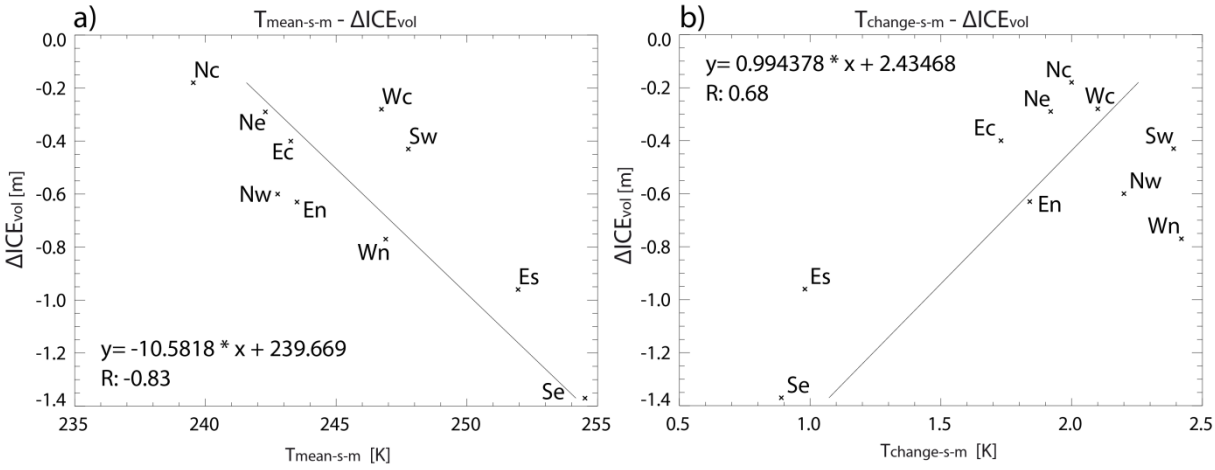

656

657 Fig. 9: Linear regression analysis of $T_{mean\text{-}s\text{-}m}$ and $T_{change\text{-}s\text{-}m}$ with the ΔICE_{vol}.

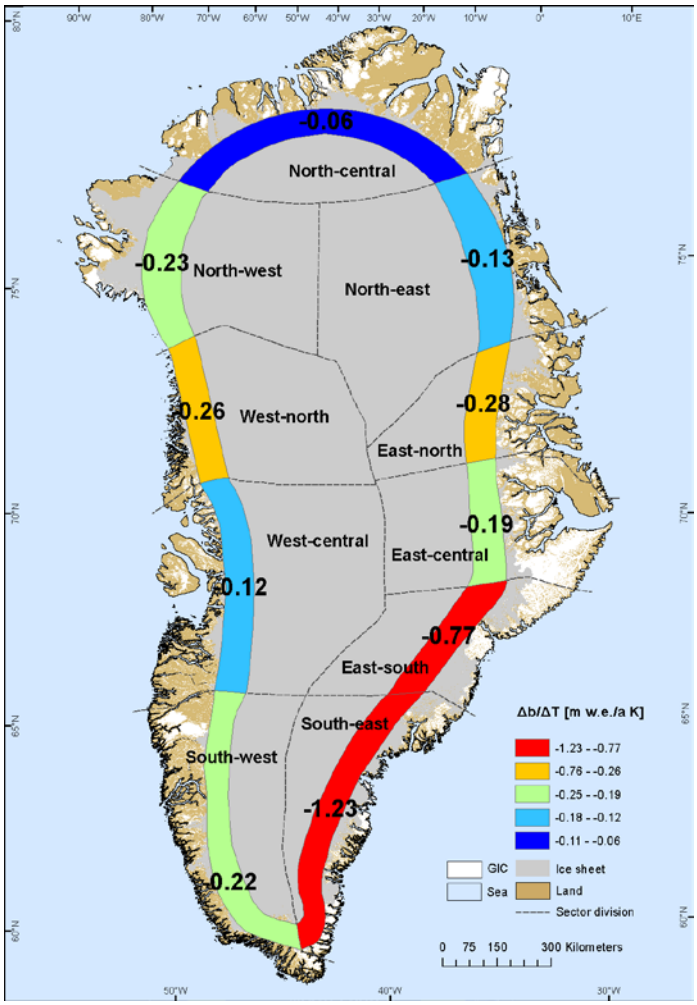

658

659 Fig. 10: Mass balance sensitivity to a 1 K temperature change as derived from RACMO2.

Part III

Appendix

Personal bibliography

Peer reviewed

Rastner, P., Machguth, H., Bolch, T. and Paul, F. (subm). Climate sensitivity of Greenland's local glaciers and ice caps. Journal of Glaciology.

Rastner, P., Bolch, T., Notarnicola, C., and Paul, F. (2014). A comparison of pixel- and object-based glacier classification with optical satellite images. IEEE Journal of Selected Topics in Applied Earth Observations and Remote Sensing 7, 853–862.

Rastner, P., Bolch, T., Mölg, N., Machguth, H., Le Bris, R., and Paul, F. (2012). The first complete inventory of the local glaciers and ice caps on Greenland. The Cryosphere 6, 1483–1495.

Bolch, T., Sandberg Sørensen, L., Simonsen, S.B., Mölg, N., Machguth, H., **Rastner, P.**, and Paul, F. (2013). Mass loss of Greenland's glaciers and ice caps 2003-2008 revealed from ICESat laser altimetry data. Geophysical Research Letters 40, 875–881.

Machguth, H., **Rastner, P.**, Bolch, T., Mölg, N., Sørensen, L.S., Aðalgeirsdottir, G., van Angelen, J.H., van den Broeke, M.R., and Fettweis, X. (2013). The future sea-level rise contribution of Greenland's glaciers and ice caps. Environmental Research Letters 8, 025005.

Paul, F., Barrand, N. E., Baumann, S., Berthier, E., Bolch, T., Casey, K., Frey, H., Joshi, S. P., Konovalov, V., Bris, R. L., Mölg, N., Nosenko, G., Nuth, C., Pope, A., Racoviteanu, A., **Rastner, P.**, Raup, B., Scharrer, K., Steffen, S. and Winsvold, S. (2013). On the accuracy of glacier outlines derived from remote-sensing data. Annals of Glaciology 54, 171–182.

Pfeffer, W. T., Arendt, A. A., Bliss, A., Bolch, T., Cogley, J. G., Gardner, A. S., Hagen, J. O., Hock, R., Kaser, G., Kienholz, C., Miles, E. S., Moholdt, G., Mölg, N., Paul, F., Radić, V., **Rastner, P.**, Raup, B. H., Rich, J., Sharp, M. J. and Randolph, C. (in press). The Randolph Glacier Inventory: a globally complete inventory of glaciers. Journal of Glaciology.

Carturan, L., Filippi, R., Seppi, R., Gabrielli, P., Notarnicola, C., Bertoldi, L., Paul, F., **Rastner, P.**, Cazorzi, F., Dinale, R., et al. (2013). Area and volume loss of the glaciers in the Ortles-Cevedale group (Eastern Italian Alps): controls and imbalance of the remaining glaciers. The Cryosphere 7, 1339–1359.

Knoll, C., Kerschner, H., Heller, A. and **Rastner, P.** (2009). A GIS-based reconstruction of little ice age glacier maximum extents for South Tyrol, Italy. Transactions in GIS 13, 449–463.

Conference proceedings

Mölg, N., **Rastner, P.**, Irsara, L., Notarnicola, C., Steurer, C., and Zebisch, M. (2010). Multi-temporal MODIS snow cover monitoring over the alpine regions for civil protection applications. In Remote Sensing for Science, Education, and Natural and Cultural Heritage, (Paris France), pp. 669–676.

Rastner, P., Irsara, L., Schellenberger, T., Della Chiesa, S., Bertoldi, G., Endrizzi, S., Notarnicola, C., Steurer, C., and Zebisch, M. (2009). Monitoraggio del manto nevoso in aree alpine con dati MODIS multi-temporali e modelli idrologici. In 13th ASITA National Conference, Bari (Italy), pp. 1657–1662.

Rastner, P., Irsara, L., Schellenberger, T., Della Chiesa, S., Bertoldi, G., Endrizzi, S., Notarnicola, C., and Zebisch, M. (2009). Snow cover monitoring and modelling in the Alps using multi temporal MODIS data. In International Snow Science Workshop, J. Schweizer, and A. VanHerwijnen, eds. Davos (Switzerland), pp. 214–218.

Notarnicola, C., Frick, A., Kass, S., **Rastner, P.**, Pulighe, G., and Zebisch, M. (2009). Semiautomatic classification procedure for updating landuse maps with high resolution optical images. In Geoscience and Remote Sensing Symposium, Cape Town (South Africa), pp. 975–978.

Fritsch, U., Lichtenegger, J., Mair, E., **Rastner, P.**, and Steurer, C. (2009). EURAC junior Earth observation schoollab at the European Academy in Bolzano/Italy. In Workshop on Education and Training", Chania (Greece), pp. 132–139.

Books

Cattadori, M., Fritsch, U., **Rastner, P.**, Steurer, C., and Taponecco, F. (2010). Views from space. In Polar Science and Global Climate: An International Resource for Education and Outreach, (Hampshire: Pearson Custom Publishing), pp. 117–118.

Rastner, P., and Knoll, C. (2010). Die Vergletscherung der Südtiroler Alpen. In Südtirol: eine Landschaft auf dem Prüfstand; Entwicklungen - Chancen - Perspektiven, (Lana: Tappeiner), pp. 45–53.

Rastner, P. (2008). Die Gletscher im Tauferer Ahrntal. In Tauferer Ahrntal: Geschichte und Zukunft, (Lana: Tappeiner), pp. 52–59.

Other

Arendt, A., Bolch, T., Cogley, J. G., Gardner, A. S., Hagen, J. O., Hock, R., Kaser, G., Pfeffer, W. T., Moholdt, G., Paul, F., Radic, V., Andreassen, L. M., Bajracharya, S., Beedle, M. J., Berthier, E., Bhambri, R., Bliss, A., Brown, I., Burgess, D. O., Burgess, E. W., Cawkwell, F., Chinn, T., Copland, L., Davies, B., De Angelis, H., Dolgova, H., Filbert, K., Forester, R., Fountain, A., Frey, H., Giffen, B., Glasser, N., Gurney, S., Hagg, W., Hall, D., Haritashya, U. K., Hartmann, G., Helm, C., Herreid, S., Howat, I. M., Kapustin, G., Khromova, T., Kienholz, C., Koenig, M., Kohler, J., Kriegel, D., Kutuzov, S., Lavrentiev, I., Le Bris, R., Lund, J., Manley, W. F., Mayer, C.,

Miles, E. S., Li, X., Menounos, B., Mercer, A., Mölg, N., Mool, P., Nosenko, G., Negrete, A., Nuth, C., Pettersson, R., Racoviteanu, A., Ranzi, R., **Rastner, P**., Rau, F., Raup, B. H., Rich, J., Rott, H., Schneider, C., Seliverstov, Y., Sharp, M. J., Sigurosson, O., Stokes, C. R., Wheate, R., Wolken, G. J., Wyatt, F. and Zheltyhina, N. (2012). Randolph Glacier Inventory [v2.0]: A Dataset of Global Glacier Outlines., [online] Available from: http://www.glims.org/RGI/RGI_Tech_Report_V2.0.pdf (Accessed 18 January 2014), Digital Media.

Zemp, M., Paul, F., Andreassen, L. M., Arino, O., Bippus, G., Bolch, T., Braithwaite, R. J., Braun, L. Cáceres, B.E., Casassa, G., Casey, K.A., Ceballos, C.L., Citterio, M., Delgado, H., Demuth, M., Espizua, L.E., Farokhnia, A., Fischer, A., Foppa, N., Frey, H., Fujita, K., Gärtner-Roer, I., Glowacki, P., Haeberli, W., Hagen, J.O., Hoelzle, M., Holmlund, P., Giesen, R.H., Kääb, A., Khromova, T., Kotlarski, S., Le Bris, R., Li, Z., Meier, M., Meneghel, M., Mool, P., Nussbaumer, S.U., Peduzzi, P., Plummer, S., Popovnin, V.V., Prinz, R., Rack, W., **Rastner, P.**, Raup, B., Rinne, E., Seifert, F.M., Seiz, G., Severskiy, I., Shepherd, A., Sigurðsson, O., Strozzi, T., Vincent, C., Wheate, R., Yakovlev, A. (2011). Summary of International Glacier Monitoring Summit, Earth Observer - NASA, August.

Rastner, P. (2006). Visualisierung hochauflösender Fernerkundungsdaten aus Hochgebirgsräumen, Diploma thesis, University of Innsbruck, Innsbruck - Austria.

Outreach activities

Glacier stand Axporama (2013). Scientific visualization of Findelen glacier retreat from 1862 – 2010.

Globglacier Promotional DVD (2011). Scientific visualization of the results from GLOBGLACIER-ESA project. (Available online: http://globglacier.ch/docs/dvd/index.html)

Mumien (Mummies) (2009). Visualizations with remote sensing data related to the Iceman recovery site. Archeological museum Bolzano - Italy.

Gletscherwelten (The world of glaciers) (2007). Exhibition (computer animations) in the mountain station of the "Schnalstaler Gletscherbahnen" - Italy.

Gletscher im Treibhaus (Glaciers and the greenhouse effect) (2007). Exhibition (computer animations) natural museum Bolzano. Diploma thesis animations.

.

Curriculum Vitae

First name	Philipp
Last name	Rastner
Date of birth	16 February 1980
Place of birth	Bruneck
Citizenship	Italian

Education

Since 2010	PhD studies at University of Zurich, Switzerland
Certificate: 10. Nov. 2006	Mag.rer.nat – Diploma of Geography Leopold – Franzens – University Innsbruck Thesis: 'Visualization of high resolution remote sensing data in high Alpine regions' In collaboration with the German Space Center (DLR) – Austria, Germany.
2002 – 2003	Geography studies at the University of Aberdeen (Erasmus exchange year) – Scotland.
1999 – 2004	Studies of Geography at the Leopold – Franzens – University of Innsbruck – Austria.
1991 – 1999	High school, Bruneck – Italy
1986 – 1991	Primary school, Gais - Italy

Work experience

Nov. 2006- Feb. 2010	EURAC research – Institute of Applied Remote Sensing – Bolzano – Italy
Nov. 2005 – Feb. 2006	Geoville - GIS and Remote Sensing Innsbruck– Austria
Aug. – Oct. 2005	Development Project (Computer Instructor) - Kenya
Feb. – Jul. 2004	Geoville – GIS and Remote Sensing – Innsbruck - Austria

Internships

Aug. – Oct. 2011	Marine Geology and Glaciology, Geological Survey of Denmark and Greenland – GEUS København – Denmark
Aug. – Sept. 2003	German Aerospace Center (DLR), Department: Remote Sensing Data Centre (DFD), Oberpfaffenhofen - Germany
Summer 1998-2002	Texas Instruments, Department: Customer Service, Freising - Germany

Summer schools and workshops

Feb. 2013	Workshop: Regional Climate Models – ETH Zurich - Switzerland

Aug. 2012	Summer school: ESA Summer School – Frascati - Italy
Jul. 2011	Summer school: Remote Sensing for Polar Scientists – Reading – United Kingdom
Sep. 2010	Summer school: Karthaus Summer School, Karthaus – Italy
Aug. 2010	Workshop: Technologia satelital para reducir la incertidumbre de los scenarios climaticos e hidrologicos. Identificacion y monitoreo de glaciares. ESA/CONAE workshop - Argentina

Languages: German (mother tongue), English, Italian

Acknowledgements

The successful conclusion of this PhD wouldn't have been possible without great social surroundings.

While some people are mentioned explicitly, my sincere thanks also go to all the people who are not listed individually; their help is nevertheless remembered and very much appreciated.

First of all, I want to thank my family (Monika, Gabi, Lukas und Walter) and my girlfriend Bianca for supporting me and giving me the freedom to fully dedicate my time to the PhD. They were always there whenever I needed them.

I have to give a thousand thanks to my supervisors Frank Paul, Tobias Bolch, Horst Machguth, Wilfried Haeberli and Andreas Vieli who were always available to answer my many questions and queries. Thanks to Frank, I had the opportunity to earn my PhD in the framework of the ice2sea project that funded this thesis. In particular, I also want to say thank you to Horst, who enabled me to perform a research exchange with the GEUS in Copenhagen. In addition I have to emphasize the help I received from Claudia Notarnicola and Nico Mölg.

Furthermore, I want to say thank you to Karen Edelvang, the head of the marine geology and glaciology department in Copenhagen for the efficient organisation of the research exchange. Of course the stay in Copenhagen wouldn't have been the same without: Andreas Peter Ahlstrøm, Dirk van As, Michele Citterio, Morten Langer Anderson, Signe Hillerup Larsen, Robert Schjøtt Fausto, Signe Bech Andersen, Anker Weidick and Jason Eric Box.

Moreover, I appreciate the help, fun and support from all my colleagues from the physical geography department here in Zurich. Thank you for the warm welcome at the beginning of my stay and the nice coffee breaks, parties, barbecues, field work activities and sport events.

Thanks are extended also to my former colleagues from EURAC research in Bolzano/Bozen. You motivated me to stay in the field of research and to start a PhD. In particular I want to say thanks to Claudia Notarnicola, Marc Zebisch, Christian Steurer, Stefan Schneiderbauer, Daniela Dellantonio and Lydia Pedoth for their help and support in particular regarding the provision of eCognition which was essential for the second paper.

I mustn't forget to thank Nadine Salzman, Roberto Dinale, Isabelle Gärtner-Roer and Johann Müller for giving me the opportunity to join in some field-work activities. This experience was a great motivation for my research activities and facilitated a quicker process understanding.

In addition, I want to say thank you to Michael Zemp, Philip Claudio Jörg and Matthias Huss for the great collaboration regarding the activities of the Axporama exhibition. This enabled me to observe other research activities in glaciology and in particular the public communication of science.

I also want to mention some of my friends who helped in the proofreading of this thesis. Pierre Dalban, Yvonne Schaub, Johann Müller, Nico Mölg and Steve Kass for their scientific comments and my English teachers Marc de Souza, Sarah Packford, Manuela Czech and Jeremy Mossop.

Of course, good work wouldn't be possible without old friends who help you to clear your mind from scientific topics. I therefore greatly appreciate their warm welcome and fun whenever I was at home.